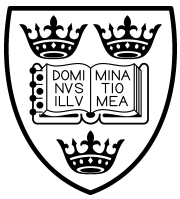
Mathematics of Crimping



Warrick Cooke
St Catherine's College
University of Oxford

A thesis submitted for the degree of
Doctor of Philosophy

June 2000

To my parents, who showed me the importance of love

Acknowledgements

Thanks to my supervisors, John and Hilary Ockendon, for the many worthwhile discussions on the subject of crimping. I would also like to give thanks to V. Saward, K. Gillow and J. Lawry for help with the layout of this document. I have also appreciated the assistance of Philip Baggot and Ifor Griffiths for helpful insights to the operation of the stuffer box. Finally I would like to acknowledge the funding given by the EPSRC and Courtaulds PLC.

Abstract

The aim of this thesis is to investigate the mathematics and modelling of the industrial crimper, perhaps one of the least well understood processes that occurs in the manufacture of artificial fibre.

We begin by modelling the process by which the fibre is deformed as it is forced into the industrial crimper. This we investigate by presuming the fibre to behave as an ideal elastica confined in a two dimensional channel. We consider how the arrangement of the fibre changes as more fibre is introduced, and the forces that are required to confine it. Later, we apply the same methods to a fibre confined to a three dimensional channel.

After the fibre has undergone a preliminary deformation, a second process known as secondary crimp can occur. This involves the "zig-zagged" material folding over. We model this process in two ways. First as a series of rigid rods joined by elastic hinges, and then as an elastic with a highly oscillatory natural configuration compressed by thrusts at each end. We observe that both models can be expressed in a very similar manner, and both predict that a buckle can occur from a nearly straight initial condition to an arched formation. We also compare the results to experiments performed on the crimped fibre.

Throughout much of the process, the configuration of the fibre does not alter. This part of the process we call the block, and model the material in this region in two ways : as a series of springs; and as an isotropic elastic material. We discuss the coupling between the different regions and the process that occurs in the block, and consider both the steady state and stability of the system.

Contents

1 Introduction **1**

1.1 1997 : The Year of the Man-made fibre 1

1.2 The fibre manufacturing process 2

1.2.1 The stuffer box crimper 3

1.2.2 Terminology and length scales of the stuffer box crimper . . . 5

1.3 Structure of this thesis 5

1.4 Statement of originality 7

1.5 Experimental Observations and Results 8

1.5.1 Observations of crimp formation 8

1.5.2 Quantitative results 9

1.5.3 General observations on the fibre crimper 9

2 Primary Crimp **13**

2.1 Previous work on related contact problems 15

2.2 2D Confined Fibre 27

2.2.1 Boundary Conditions 29

2.2.2 Non-dimensionalisation 30

2.2.3 Linearisation 31

2.2.3.1 Linearisation of the boundary and free boundary conditions 32

2.2.3.2 Summary of Linearised equations 33

2.2.4 Methodology 33

2.2.5 Example 1a : The rectangular channel 35

2.2.5.1 Section Types 35

2.2.5.2 Types of Solution 41

2.2.5.3 Choice of Solution 45

2.2.5.4 Degeneracy 50

2.2.6 Example 1b : Rectangular channel fed midway 51

2.2.6.1 Section types . . . 52
2.2.6.2 Summary of the types of Solution . . . 55
2.2.6.3 Results . . . 57
2.2.7 Example 2: Fibre confined in a narrow wedge . . . 60
2.2.8 Section Types . . . 61
2.2.9 Results . . . 63
2.3 3D Confined Fibre . . . 65
2.3.1 The equations of an elastica in three dimensions . . . 65
2.3.2 Relationship with the co-ordinates in fixed space . . . 69
2.3.3 Boundary conditions . . . 69
2.3.4 Non-dimensionalisation . . . 69
2.3.5 Linearisation . . . 70
2.3.6 Boundary Condition at $s = 1 + 2t$ . . . 72
2.3.7 Summary of Linearized Equations . . . 73
2.3.8 3D Confined Fibre : Results . . . 74
2.3.8.1 Normal contact $\phi = 0$ . . . 75
2.3.8.2 Energy in three dimensions . . . 76
2.3.8.3 General Fibre Orientation - Single contact Point . . . 76
2.4 Conclusions . . . 84
2.4.1 Two dimensional fibre . . . 84
2.4.2 Three dimensional crimp . . . 85

3 Secondary Crimp **86**
3.1 Introduction . . . 86
3.2 Hinged Rods : Model . . . 89
3.2.1 Derivation . . . 89
3.2.2 Non-dimensionalization . . . 91
3.2.3 Asymptotics . . . 92
3.2.3.1 $O(1)$ . . . 92
3.2.3.2 $O(\kappa)$ . . . 93
3.2.3.3 $O(\kappa^2)$ . . . 94
3.2.4 A reformulation of the problem . . . 94
3.2.5 Results of the asymptotic analysis . . . 99
3.2.6 Numerical solution of the hinged rods model . . . 100
3.2.6.1 Comparisons and Observations . . . 100
3.3 Hinged Rods : Fitting Experimental Curves . . . 108

3.3.1 Fitting Experimental Data . . . 109
3.3.1.1 Typical Results . . . 110
3.3.2 Extensible, Unbending rods . . . 111
3.3.3 Fitting the data . . . 112
3.3.3.1 Large Tension . . . 112
3.3.3.2 Small Tension ($\theta = \pi/2 - \phi/2 - \epsilon$) . . . 113
3.3.3.3 Numerical Fitting . . . 113
3.4 Naturally-curved Fibres . . . 115
3.4.1 Multiple scales analysis . . . 116
3.4.2 Hinged Rods revisited . . . 117

4 Modelling the Block Motion 120
4.1 Introduction . . . 120
4.2 Concept . . . 121
4.2.1 Models for the amount of material entering the block . . . 125
4.2.2 Models for the micro-structure of the block . . . 127
4.2.2.1 Loops of Elastica . . . 127
4.2.2.2 Loop touching others above and below . . . 131
4.2.2.3 Loop touching others above, below and to the sides . 131
4.2.2.4 A folded Elastica touching others above and below . 133
4.2.3 Stress, strain and nondimensionalisation . . . 136
4.2.4 The primary crimp length and the force applied to the block . 137
4.3 First model of the Block : Vertical Springs . . . 138
4.3.1 Contact . . . 139
4.3.2 Time varying Parameters . . . 140
4.3.3 Non-dimensionalization . . . 140
4.3.4 Linearization . . . 141
4.3.5 Closing the model . . . 141
4.3.6 Uniform equilibrium states and their stability . . . 143
4.3.6.1 Finding the roots . . . 145
4.3.7 Predicting the equilibrium state . . . 149
4.3.7.1 Steady State Solutions . . . 150
4.3.7.2 A new model for secondary crimp . . . 154
4.3.7.3 Nondimensionalisation . . . 156
4.4 The Block as an Isotropic Elastic Material . . . 157
4.4.1 Constitutive relations . . . 157

4.4.1.1 Nondimensionalisation . . . 158
4.4.1.2 Steady State Solution . . . 161
4.4.1.3 Relationship between micro-structure and elastic properties . . . 161
4.4.2 Stability of the stuffer box . . . 164
4.4.2.1 Stability of the stuffer box with a nearly horizontal upper plate . . . 165
4.4.2.2 Stability of the Alternative Stuffer box design . . . 167
4.4.3 Springs model revisited . . . 171
4.5 Summary . . . 173

5 Conclusions **174**
5.1 Primary Crimp . . . 174
5.1.1 Crimp in three dimensions . . . 175
5.2 Secondary Crimp . . . 176
5.2.1 The hinged rods model . . . 177
5.2.2 Curved fibre model . . . 178
5.3 The Block . . . 178
5.3.1 Stability of the stuffer box . . . 180
5.4 Open Problems . . . 181

Bibliography **184**

List of Figures

1.1 Crimped fibres 2
1.2 The flat plated stuffer box 3
1.3 Schematic of the Hinged Plate Crimper 4
1.4 Photograph of the hinged plate paper crimper 5
1.5 Video still of a section of the block. 8
1.6 Secondary crimp occuring in the paper crimper 9
1.7 Time Series showing how the angle made by the top plate changes with time 10
1.8 Variation in Crimp Length along the crimped paper strip 10
1.9 Angle Against Applied Moment 11
1.10 Crimp Length against Applied Moment 11

2.1 Model problem for the industrial drier [1] 16
2.2 Folding of paper fed vertically onto a table [11] 17
2.3 Infinite elastica confined to a channel [15] 18
2.4 Buckling in a wide channel [3] 19
2.5 Buckling in a curved channel [13] 20
2.6 Contact problem for an elastica [16] 22
2.7 Contact problem for a freely supported elastica [9] 23
2.8 Section types for constrained Euler buckling [8] 25
2.9 A general geometry for a fibre confined in a 2d box. 27
2.10 Example 1a : The rectangualr box 35
2.11 The unconfined fibre 36
2.12 The starting sections 37
2.13 The ending sections 38
2.14 The Middle sections 39
2.15 Dimple 40
2.16 Key for figures 2.17 and 2.18 42
2.17 $\bar{t}$ vs. λ 46

2.18 Energy vs. $\bar{t}$ 48
2.19 A_i vs. $\bar{t}$ for the first dimple. Transition from solid to dashed line indicates transition from physical to unphysical (outside the box) solution. 49
2.20 Three possible solutions that are indistinguishable energetically . . . 50
2.21 Example 1b: The rectangular box fed midway 51
2.22 Unconfined fibre being fed into a rectangular box midway up the lefthand wall. 52
2.23 The fibre confined only by the bottom wall 53
2.24 The starting section for fibre fed into a rectangular box midway up the lefthand wall 54
2.25 Key to figures 2.26 and 2.27 showing the types of solutions found . . 56
2.26 $\bar{t}$ vs. λ for a fibre entering midway 58
2.27 Energy vs. $\bar{t}$ for a fibre entering midway 59
2.28 Geometry for a fibre in a wedge 60
2.29 The unconfined fibre in a wedge 61
2.30 The fibre confined by the bottom surface of a wedge 61
2.31 Starting section for a fibre in a wedge 62
2.32 The mid section for a wedge 62
2.33 The ending section for a wedge 63
2.34 λ against $\bar{t}$ for a fibre in a wedge 64
2.35 Observed 3d crimp formations 66
2.36 A three dimensional elastica confined in a narrow channel 67
2.37 λ vs. $\bar{t}$ for a 3d elastica, $\sigma_2 = \sqrt{2}/5$ 77
2.38 *Energy* vs. $\bar{t}$ for a 3d elastica, $\sigma_2 = \sqrt{2}/5$ 78
2.39 Typical path for a 3d crimped fibre, $\sigma_2 = 0.25$ 79
2.40 3d configurations for a confined fibre with increasing λ. $\phi = \pi/4$, $\sigma_2 = 0.25$ 83

3.1 The two ways of seeing secondary crimp 87
3.2 Hinged Rod configuration for an even number of rods (N) 90
3.3 Comparison of asymptotics and Numerical Solution for $N = 20$ and $N = 21$ 101
3.4 Comparison of asymptotics and Numerical Solution for $N = 100$ and $N = 101$ 102
3.5 Σ_0 against κ in the case $N = 20$, $\phi = 0.9$ 104
3.6 Key to Figure 3.5 105

3.7 Σ_0 against κ in the case $N = 21$, $\phi = 0.9$ 106
3.8 Key to Figure 3.7 107
3.9 Fitting Data 110
3.10 A comparison of a theoretical and experimental curve 114
3.11 A smoothly curved fibre 116
3.12 s and s' for the hinged rods model 118

4.1 Video still of a section of the block. 122
4.2 Diagram of the stuffer box, showing movement of material from A to A' 124
4.3 Formation of the block through secondary crimp 125
4.4 Two possible fibre arrangements 128
4.5 Comparison of loop microstructure with the material from the block . 130
4.6 Strain vs. stress for a loop of elastica 130
4.7 Strain vs. stress for a loop of elastica touching similar loops above and below 132
4.8 A loop touching others at four points 133
4.9 Strain vs. stress for a loop of elastica touching similar loops on four sides 134
4.10 Structure of the folded Elastica 135
4.11 Strain vs. Stress for a folded elastica touching similar loops above and below 136
4.12 An idealized view of the crimped material in the stuffer box 138
4.13 Forces acting on an elemental section of the block 139
4.14 Closing the springs model 142
4.15 Regions of stability (black) and instability (white) for the springs model, with $x_0 = 1.0$ and 0.9 146
4.16 Regions of stability (black) and instability (white) for the springs model, with $x_0 = 0.8$ and 0.7 147
4.17 Closing the springs model 149
4.18 Geometry for the new model for secondary crimp 154
4.19 The nip as a wedge 155
4.20 The block composed of an isotropic elastic solid 157
4.21 An alternative design of stuffer box 165
4.22 Stability contours for the stuffer box crimper with isotropic elastic block and nearly flat top plate 168
4.23 Stability contours for the stuffer box crimper with isotropic elastic block and nearly flat top plate 169

4.24 The different models considered in this chapter 173

5.1 Tow being removed from a box 182

Chapter 1

Introduction

1.1 1997 : The Year of the Man-made fibre

Over the last century there has been a silent revolution in the textile industry. Up until the end of the 19th century, fabrics were limited to the small number of naturally occuring fibres. However, over the next few decades, spurred on in part by the wartime economies, chemists began to perfect the techniques of manufacturing artificial fibres. Large scale production brought novel fabrics into the lives of the many. For many years, the emphasis was on producing low cost replacements for naturally occurring fibres such as wool, cotton and silk, which artificial filaments could achieve with only limited success.

The technology of weaving had not stood still over these years. Fundamental research into how fibres behaved when woven into fabrics meant that textile engineers could at last begin to tailor the properties of the cloth to the use. These so called "designer fabrics" required fibres with particular properties, and artificial filaments were soon produced to fulfil this need. Outdoor pursuits were one of the first beneficiaries, where new *micropore* jackets gave superior warmth and wind protection, whilst allowing the body to lose moisture and hence maintain comfort. Fashion, always to the forefront of textile revolution, began to experiment with novel materials, that allowed designers to work with a greater range of textures and styles than was possible before.

Artificial fibres have a great impact in areas outside the textile industry. New fibre chemistry and coatings have improved the efficiencies of filters. In addition, filaments are often used as precursors to other industrial products (for example to make the carbon fibre brake pads for large jets). In all these applications, the ability to control the properties of the fibres is crucial. Much work had been done ensuring



Figure 1.1: Crimped fibres

the correct concentrations in the polymers from which the fibre is formed, and careful control of the spinning process ensures an even thickness of filament. However the three-dimensional structure of the fibre (its **crimp**- see figure 1.1) has proved much more problematic. Indeed, the design of the **stuffer box crimper** (the part of the production line that turns straight filaments into crimped filaments) has always been regarded as a black art. It is this subject that this thesis will attempt to investigate.

1.2 The fibre manufacturing process

To understand the design of the stuffer box crimper, one must first understand the process by which fibres are manufactured. Artificial fibres begin as polymer melts, liquids formed from large chain polymers and solvents. This solution is extruded (either into water or air) through plates containing thousands of holes[1] to form the tow[2]. Once in the air or water, the polymer begins to lose solvent, and hence solidify. At this point, the filaments are much thicker than required, and so the next process is to stretch them, thus making them thinner. Two techniques are typically used. Fibres extruded into water are taken across a pair of rollers, running at different speeds. This provides the stretch. Air spun filaments are blown with high speed gas jets as

[1]The shape of the holes determines the cross-section of the fibres, typical examples include circular, square or triangular.

[2]The tow is the name given to the collection of filaments that is being manufactured. It is typically 1000 filaments wide by 20 deep.

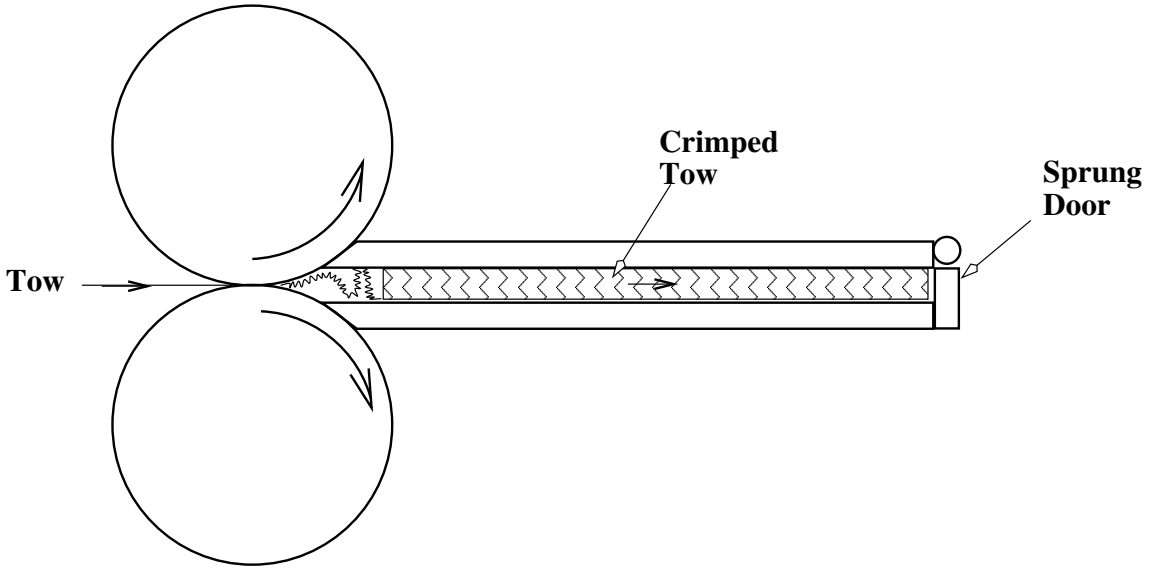


Figure 1.2: The flat plated stuffer box

they leave the extruding plate, which both dries and tensions the fibres.

The fibres are now washed and dried, to remove all traces of solvents. Depending on the eventual destination, they may also be dyed to the appropriate hue. Up until now the filaments have remained straight[3]. The final process before packaging is to introduce the permanent crimp. Conceptually, it is easy to describe how this happens. The tow is fed into a small box, and must fold up many times in order to fit. This fold becomes permanent to form crimp. Implementing this idea as part of a continuous production line is where the fun begins.

1.2.1 The stuffer box crimper

The main problem to overcome is having a design that forces the fibre to buckle while still forming part of a continuous process. There are two main methods used to achieve this. The easiest to understand is the *flat plated stuffer box (figure 1.2)*. This forces the fibres into a rectangular tube, the far end of which is blocked by a sprung door. Fibre fills the tube until the force required to add more fibre is sufficient to force open the door, allowing crimped fibre to escape.

The more common design of stuffer box, on which we shall concentrate in this thesis, uses a hinged top plate rather than a sprung door. The plate supports a large

[3]Except for a limited type of polymer which crimps during solidification due to instabilities

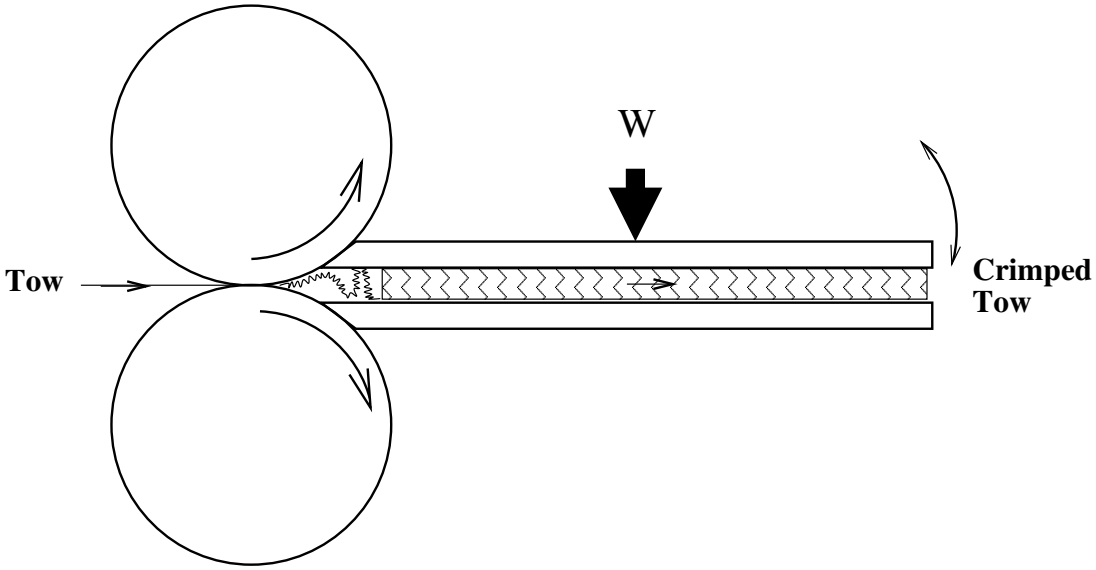


Figure 1.3: Schematic of the Hinged Plate Crimper

weight, and as more fibre is forced in, the buckled tow lifts the plate, allowing tow to escape. Figure 1.3 shows a schematic of the hinged plate crimper, whilst 1.4 is a photograph of a modified model that crimps paper (see section on experimental work 1.5).

Construction of a stuffer box crimper is a difficult undertaking. The individual filaments are very thin, so construction tolerances must be high lest the fibre escape and jam the machine. Unfortunately, as we wish to make as much fibre as possible, we require the crimper to operate at high speeds and under large loads. This makes the engineering of such a device an expensive job. When a new fibre comes into production, it will need a modified crimper, in order to cope with its particular properties. Hence the motivation behind this thesis is to predict how properties of the crimped fibre depend on the parameters of the machine and polymer.

At this point, it is worth discussing the history of the modelling of the crimping process. Courtaulds first brought the crimping problem to the 26th European Study Group with Industry, in 1993 [2]. The participants modelled the primary crimp formation as an Euler strut, but the model contained many unknown parameters, and hence was of little use in making predictions. This thesis, which was partly funded by Courtaulds (as a Case award) aims to improve and extend those early ideas to give a unified model for the stuffer box crimper.

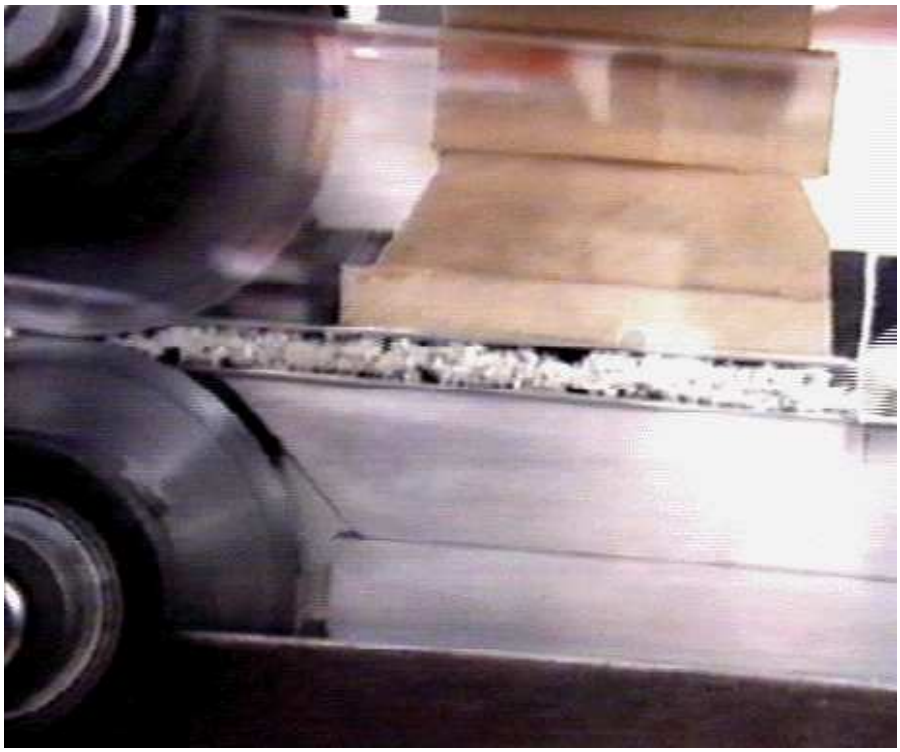


Figure 1.4: Photograph of the hinged plate paper crimper

1.2.2 Terminology and length scales of the stuffer box crimper

When we observe the stuffer box crimper in action[4], and examine closely the output, we see structures on a number of length scales. The smallest ($\sim 2mm$) is referred to as *primary crimp*. This is the main permanent deformation that occurs. When the fibre exits the stuffer box, it is folded a second time ($\sim 15mm$), in the arrangement we call *secondary crimp*. For comparison, the stuffer box is about $200mm$ long, and has rollers $100mm$ in diameter. The region between the rollers we will refer to as the *nip*.

1.3 Structure of this thesis

In section 1.5 we shall introduce experimental observations made using the paper crimper. Although this does not exhibit all the features of the fibre crimper, there is sufficient similarity to gain an understanding of the basic processes involved. These observations will help focus our investigation into the mathematics of crimp. Included in this section will be details of the limited quantitative results obtained from exper-

[4]See section 1.5 on experimental observations

iments, and a brief discussion of the difficulties in carrying out experiments.

Chapter 2 will discuss the formation of primary crimp. We begin with a brief review of the literature on contact problems for two dimensional elastic rods, and then proceed to describe a technique to solve the problem of a elastica confined within a narrow channel, which is applicable to a range of different geometries. In particular, we present results for three shapes of channel: two for comparison with another paper on a similar subject (that used a different methodology), and one which is new (the fibre in a wedge).

The remainder of chapter 2 extends these techniques to the problem of a three-dimensional elastica confined to a channel. The aim is to gain understanding as to if/when the fibres of elliptic cross-section adopt a helical form. We find that for small deflections, the deformations in each of the principal directions of the fibre uncouple. This allows us to solve the problem using results from the early part of the chapter. Unfortunately, although the fibre adopts a three-dimensional shape, we do not predict any helical crimp.

Secondary crimp involves the deformation of highly "concertinaed" fibres. In chapter 3, we will describe two models for such a system (in two dimensions). The first models the crimped fibre as a series of rigid rods coupled by elastic hinges. We first derive the difference equation for the orientation of the rods, then attempt to solve it asymptotically for small applied force. The solution we find is not valid when the number of rods is large, and we therefore have to reformulate the problem in terms of rapidly and slowly varying terms. We then seek a solution that is uniformly valid for all numbers of rods. This predicts a critical value of the force for which there is a change in behaviour from a nearly flat configuration to an arched shape. The equation for this force is observed to be different depending if there are an even or odd number of rods present. This feature is observed numerically. We then discuss experiments to determine values of the parameters in the model.

Our second model for secondary crimp treats the crimped fibre as an elastica with a rapidly varying shape. We carry out a multiple scales analysis for the problem, and find that the fibre behaves as an Euler strut of lower stiffness than the fibre from which it is composed. We then make comparisons between this result and that for

the hinged rods model.

Chapter 4 looks at the stuffer box crimper as a complete system. We present two models for the material between the plates, treating it as either a system of springs or as an isotropic elastic material. We derive equations in each case that describe the force needed to move the material in terms of the current properties of the material. In particular, we relate elastic constants to the microstructure of the block, and hence to the primary crimp length. We also relate the secondary crimp length model described in chapter 3 to the height of the material between the plates. We then discuss methods of closing the model to describe how the global behaviour of the crimping machine changes with time. As well as the models discussed in chapter 3, we also discuss a second model for the coupling between the force required to move the material and the properties of the incoming fibre. The advantage of this model is that it takes into account the geometry of the region between the rollers.

As well as discussing steady states, we also examine the stability of these states to small perturbations. We find that the "springs" model predicts that the stuffer box is almost always stable. In order to examine the stability of the "elastic material" model, we choose to study a simpler system, and find that the system can go unstable if there is much friction between fibre and plates, and the equilibrium height of the material is large.

To compare the stability of the two models, we also look at the much simpler horizontal plate stuffer box design. We observe that this is less stable than the hinged plate version, and that the springs model is more stable in general than the elastic model.

In the final chapter, we bring these results together, and also present some open problems.

1.4 Statement of originality

In chapter 2, the results of the work carried out on a fibre confined to 3 dimensional channel is original work. All of chapter 3 is original, as are the models and results for the stuffer box discussed in chapter 4.

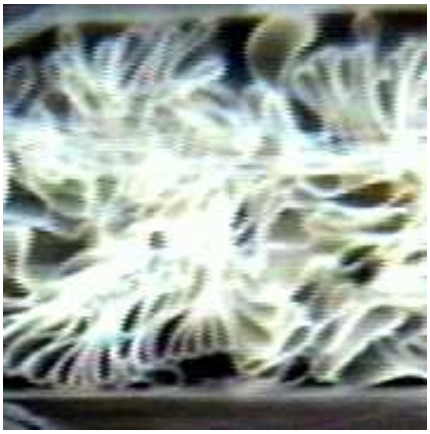


Figure 1.5: Video still of a section of the block.

1.5 Experimental Observations and Results

In order to improve their understanding of the crimping process, Courtaulds built a paper crimper. This works the same way as the hinged plate stuffer box crimper, but instead of a tow, uses a continuous sheet of paper as its input. As the paper cannot escape from the sides, the walls of the crimper can be made of perspex, and hence it is easy to observe the crimp occuring. It is also much smaller (as the fibre comes from a roll, not a production line!) and therefore allows experiments to be carried out much more easily.

1.5.1 Observations of crimp formation

- **Primary Crimp**
  Even when using the paper crimper, primary crimp is difficult to observe, as it happens in the small gap between the rollers. When running the crimper very slowly, we observe that contact occurs first at one surface, then the other.

- **Secondary Crimp**
  Secondary crimp occurs relatively infrequently. Primary crimped fibre builds up until it suddenly folds, and moves towards the plates (see figure 1.6).

- **The material between the plates**
  The material between the plates does not move continuously, but rather in jerks as more fibre is added through secondary crimp. The structure of the material is very complicated (see figure 1.5), with many gaps. This makes modelling the properties difficult. Thankfully, as it moves along the gap, the orientation of

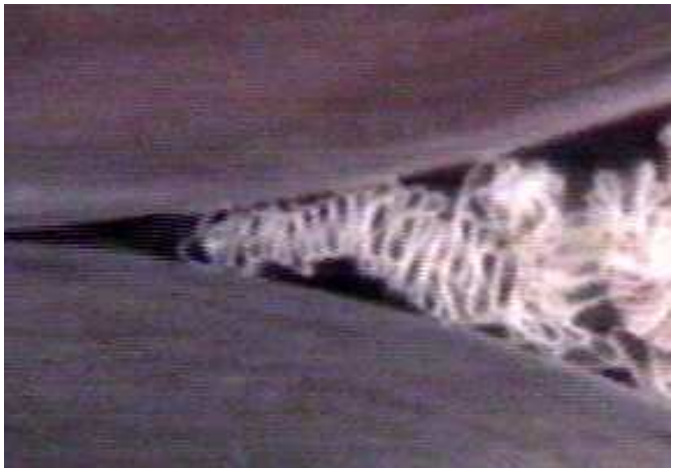


Figure 1.6: Secondary crimp occuring in the paper crimper

the fibre does not change much. We shall make use of this fact in chapter 4 when we model the fibre in this area.

Under certain circumstances, especially when the applied load is large, the block may buckle, lifting the angle of the top plate. This is a feature of the paper crimper, and is not observed in the industrial process.

1.5.2 Quantitative results

Quantitative results were hard to come by with the paper crimper. Over a period of a week, numerous experimental runs were performed with different loadings on the upper plate of the crimper. The angle of the plate was recorded at regular intervals, and after the experiment was concluded, the primary crimp length was measured at regular points along the paper. Figures 1.7 and 1.8 show typical data sets. Notice the large variations in both quantities. The graphs 1.9 and 1.10 show how the arithmetic means of these properties changed with the applied load. Note that "trends" are difficult to observe.

1.5.3 General observations on the fibre crimper

Observation of the industrial crimper shows a number of differences to the paper version studied. First is the relative stability of the fibre crimper. Unless the plates are close to requiring replacement, the crimper is relatively stable, and exhibits none of the large variations in angle oberverved with paper. Secondly, the crimp of the fibre

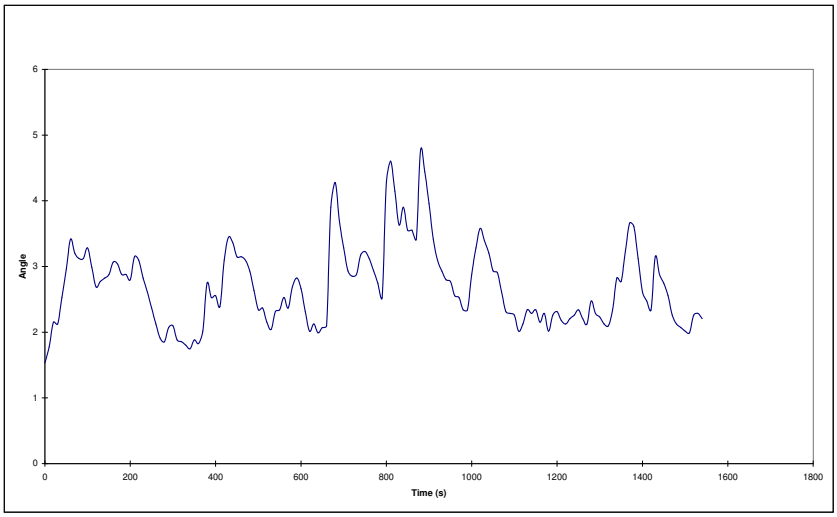


Figure 1.7: Time Series showing how the angle made by the top plate changes with time

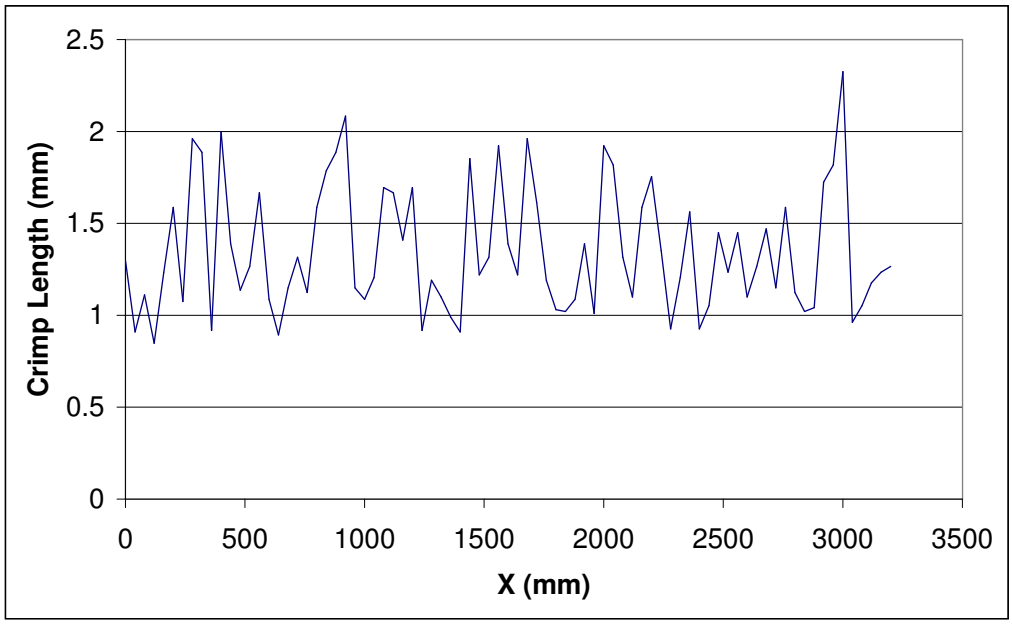


Figure 1.8: Variation in Crimp Length along the crimped paper strip

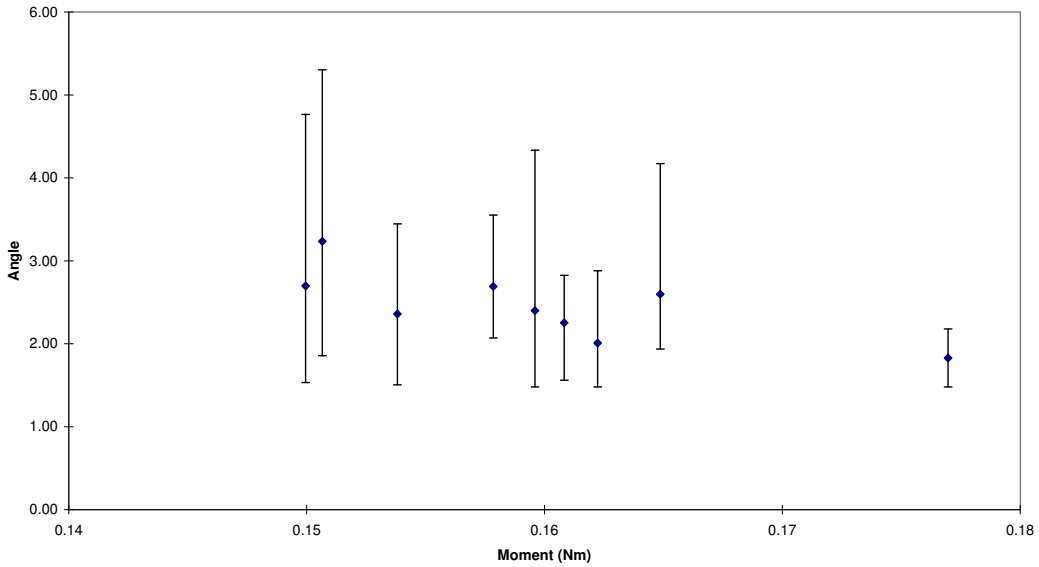


Figure 1.9: Angle Against Applied Moment

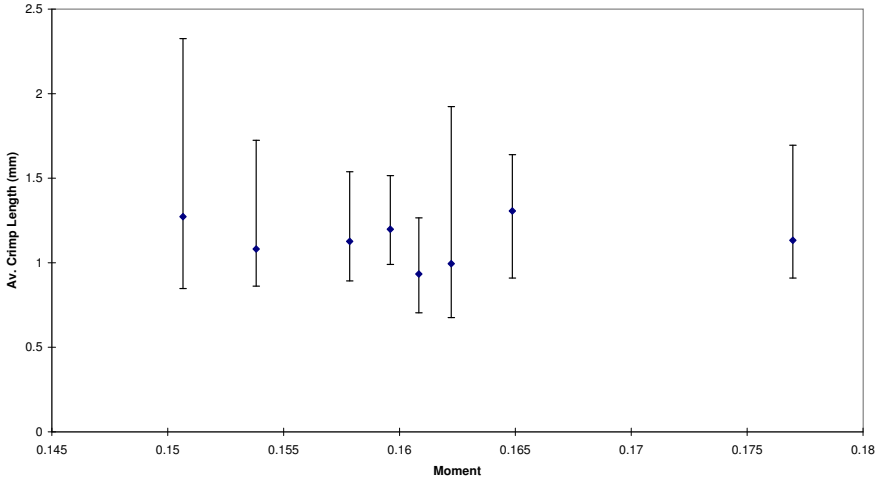


Figure 1.10: Crimp Length against Applied Moment

emerging from the industrial process is much more uniform (these observations may well be related).

The fibre crimper also has some features that arise only due the nature of the material being fed in. Unlike a sheet of paper, the fibre can easily deform in three dimensions. This is an important feature of the industrial process that cannot be understood through studying the paper crimper alone.

Chapter 2

Primary Crimp

In this chapter we will discuss how the primary crimp forms as the fibre enters the crimping machine between the rollers. We believe that the processes that occur at formation and the length scale of the crimp are two of the major factors that determine the properties of the fibre. To gain a better understanding of what is happening when the fibre first enters the machine, we will model it as an elastica[1] being forced into a long, thin box. The fibre must bend to allow more to enter, and so we expect it to touch the walls at many points. This gives rise to a contact problem. Let us begin our discussion with a brief outline of other appropriate contact problems that can be found in the literature.

Consider a fibre confined to two dimensions. The full problem is nonlinear and it is possible, but difficult, to make some progress in this case. However, for the sake of simplicity we will concentrate on the linearised model for the elastica. To do so, we will have to confine ourselves to small displacements of the fibre. Due to this linearisation we find that the equations can be solved exactly in the regions between the contact points. These segments can then be joined together by applying suitable conditions at the contact points. Finally, we can apply conditions on the fibre as a whole to find a solution to the full problem. In the best traditions of applied mathematics in OCIAM we will start by applying this to the simplest problem of a thin, rectangular box. This will illustrate both the advantages and limitations of the method. We will end the discussion of the two-dimensional fibre by briefly looking at the results for a fibre in a wedge.

[1] Elastic beam

Armed with the knowledge and experience of the confined two-dimensional fibre, we will then begin to look at the effect of giving the fibre a third direction into which to deform. Our hope is to explain the observations about the three-dimensional nature of crimp. The equations for a three-dimensional elastica are numerous and nonlinear, so we will again make a start by limiting ourselves to small deflections and hence linearising the equations. Under these circumstances, we will see that the deformations in each of the principle axes of inertia of the cross-section are independent. This will allow us to exploit many of the techniques we developed for the two dimensional fibre. Once again, we consider only the simplest geometries.

2.1 Previous work on related contact problems

Contact problems between elasticas and surfaces are very common in industrial problems. One particularily rich source has been modelling the handling of sheets of material (be they paper or tow). At the 22nd Study Group with Industry [1], Courtaulds brought a problem they encountered when fibre was being transfered between the rollers on an industrial drier. Under certain operating conditions, the tow would buckle as it was being laid down on the second cylinder. The model problem considered was that of feeding paper onto a table at twice the rate that the feeder moved along the table (see figure 2.1). This resulted in an excess of fibre, and hence a compressive force. The rate of motion and feeding was assumed sufficiently small that inertia effects could be ignored. A brief outline of the equations and some details of the solution can be found in Ockendon [6]. Starting from the steady state equations of an elastica acted on by both a compressive force (due to the overfeeding) and a normal body force (from gravity), the linearized equations give a fourth order equation relating the height of the fibre (y) as a function of position (x),

$$y^{(4)} + \lambda y'' + \gamma = 0, \qquad d < x < t.$$

where λ is the nondimensional compressive force and γ the nondimensional gravity term. At the contact point with the table ($x = d$) the boundary conditions are

$$y = y' = y'' = 0$$

and at the feeder ($x = t$)

$$y = 1 \qquad y' = 0$$

(which is fixing the height and direction of the fibre). The overfeed condition is that

$$\text{Total length} - \text{Distance moved along table} = \text{Excess Fibre}$$

which can be rewritten as

$$\int_0^t \left(\frac{dy}{dx}\right)^2 dx = 2t.$$

Solving this free boundary problem involved solving a pair of trancendental equations, and there are multiple possible shapes the fibres could take up. In [1] use was made of energy arguments to determine which was most likely. The result was believed not to be valid for large times due to steepening effects making the nonlinear terms ignored in the derivation important.

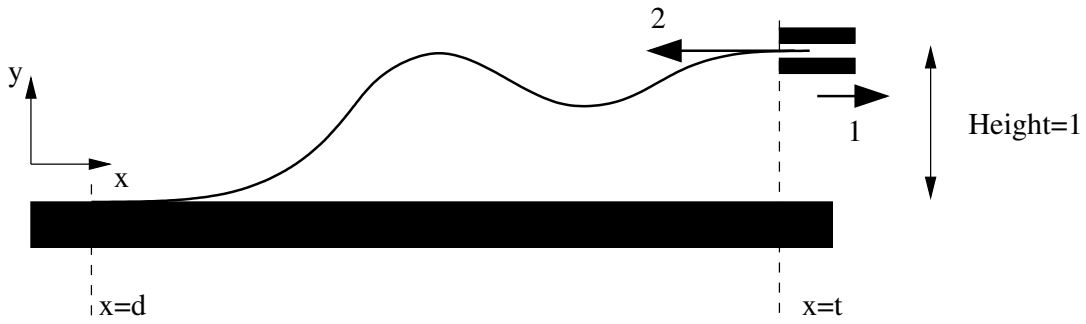


Figure 2.1: Model problem for the industrial drier [1]

Certain problems will always require one to consider nonlinear effects. Mahadevan and Keller [11] [12] have modelled the problem of thin sheets and ropes being fed vertically onto a horizontal table (see figure 2.2). During the evolution of a fold the angle must change by $\pi/2$; it will never be possible to ignore the geometrical nonlinearity. Mahadevan and Keller began with the dynamic equations for an elastica acted on by a body force (gravity). They then focussed their attention on situations when the inertia terms were negligible. At the feeder they specified both the position and angle made by the sheet. The boundary conditions made at the other end depended on which configuration they expected to see. Experimental observations suggested that the folding began with no contact with the surface, followed by touching line contact. As more sheet is added, the angle between the sheet and the table decreases towards zero. After this is reached, a second contact line forms, which moves as more fibre is added. Eventually, the weight of fibre causes it to form a third contact line (figure 2.2). Mahadevan and Keller solved the problem numerically using a "homotopy method." Their solution agreed qualitatively with experimental results. The authors then considered a free standing fold of paper, and applied the same techniques to predict the width and height. These were found to agree well with experimental results made for different paper types.

Vaillette and Adams [15] looked at the problem of paper crumpling in photocopiers. They modelled this as an infinite, periodic elastica confined within a channel between two rigid walls. The only forces acting on the elastica came from a compressive thrust delivered along the undeformed length, and reaction forces at the contact points (see figure 2.3a). They made the assumption that, through symmetry, each section was identical, and that contact could only occur at points, not over a continuous region. This reduced the problem to the equivalent situation of a cantilever (as shown in figure 2.3b). The equations for this are well known, and because of the simple geometry, they were able to solve the full nonlinear problem using elliptic

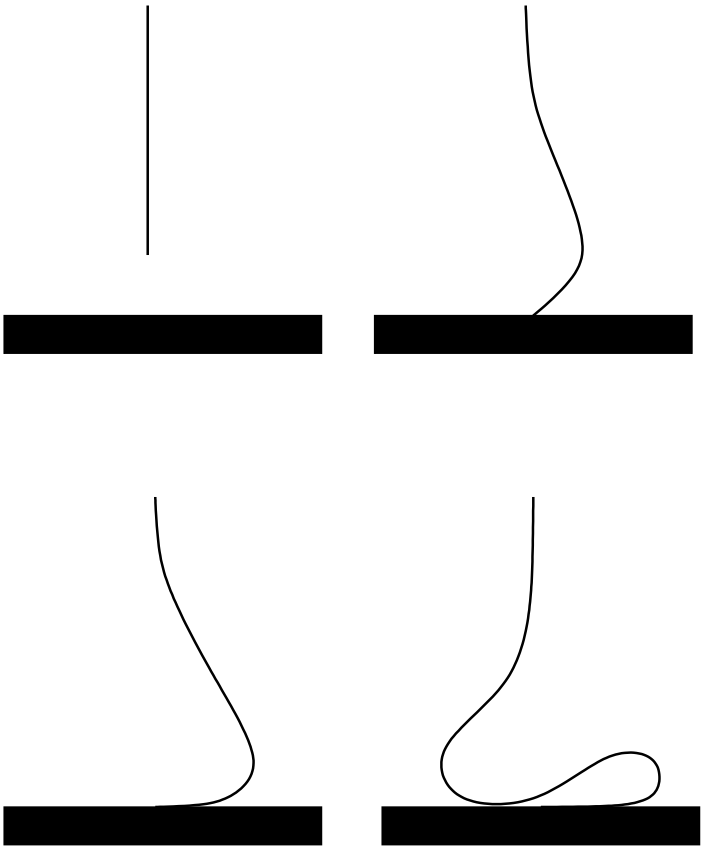


Figure 2.2: Folding of paper fed vertically onto a table [11]

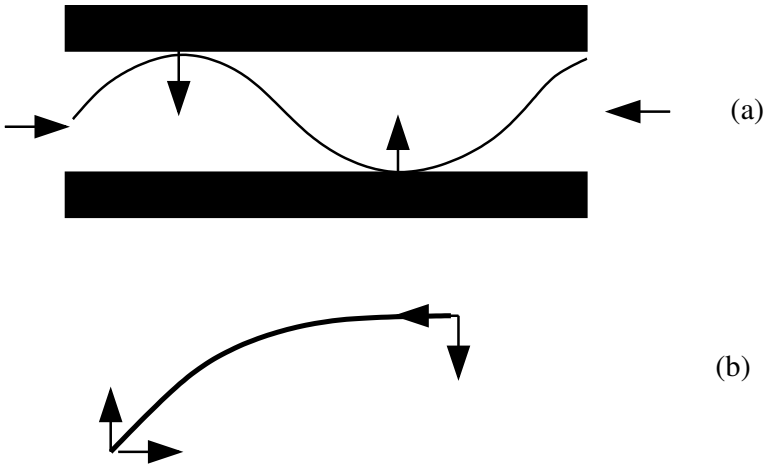


Figure 2.3: Infinite elastica confined to a channel [15]

integrals. This gave multiple solutions, and the authors resorted to energy arguments to determine which were stable for a given applied force. They found that regular solutions were only stable for a limited range of forces, above which the elastica "folded over" and was considered unstable.

In a follow-up paper, Adams and Benson [3] discussed the postbuckling of a finite elastica confined between two parallel plates. This time the length of the elastica was finite, although once again the only forces acting were the equal and opposite thrusts applied to each end and reaction forces with the walls. The aspect ratio of the channel was O(1), and hence it was necessary for them to solve the full, nonlinear model for the elastica. At the feeding end, they fixed the position and angle of the elastica, and at the other end the position was fixed and it was assumed that there was no applied moment. Their method was to divide the beam into a series of sections, and solve the problem in each region exactly using elliptic integrals. This required them to make assumptions as to what was occuring between the contact points. They proposed a sequence of events that began with the buckled fibre, which then made contact at the upper surface. The curvature at the contact point decreased as more fibre was added until a flat section (where the fibre is in contact over a region) formed. This grew until a critical condition was met when the fibre folded over (see figure 2.4). Clearly the nature of the contact set is crucial to the modelling and analysis, and we will discuss this from a mathematical viewpoint shortly.

Soong and Choi [13] looked at the problem of an elastica being fed round a curved channel (see figure 2.5). They applied a very general technique to solve the problem that would be applicable to channels where the curvature was discontinuous. Beginning with the nonlinear equations for the elastica, they assumed the number of

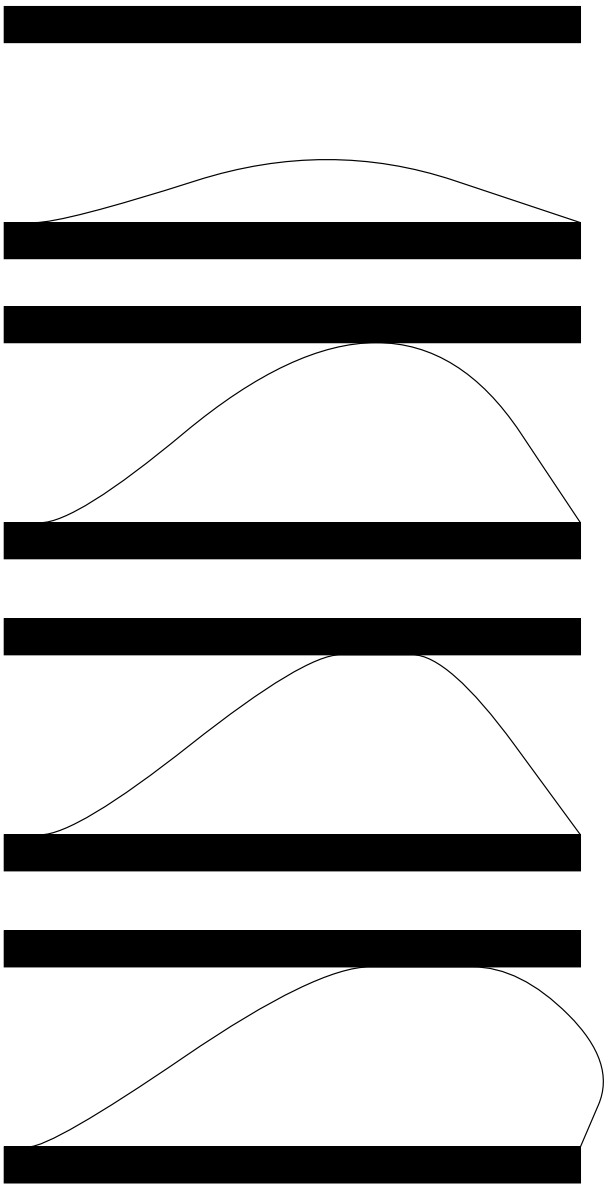


Figure 2.4: Buckling in a wide channel [3]

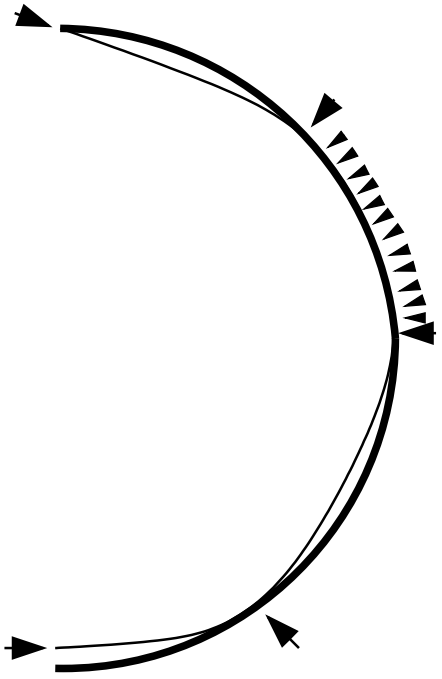


Figure 2.5: Buckling in a curved channel [13]

contact points present. They then attempted to solve the problem by a shooting method, where they used numerical integration to find the shape of the elastica and to improve on initial guesses to unknown parameters (such as forces and position of contact points). They then attempted to improve the accuracy by adding another contact point. The close proximity of many contact points sugguested that continuous contact was possible and we shall make use of this idea of trying different numbers of contact points in the next section.

Variational techniques are very popular to solve contact problems for elasticas. Westbrook [17] [16] looked at beams and plates loaded non-uniformly. He considered a beam of stiffness $B(x)$ held a distance δ above a flat surface. The beam was acted on by a body force $f(x)$ which is normal to the undeformed beam and such that $f > 0$ imples a force lifting the beam away from the surface (see figure 2.6). Starting from the linearised equations of the elastica, and letting $u(x)$ be the displacement from the surface, Westbrook looked for solutions to the problem

$$\begin{aligned} u(x) &\geq 0, \\ \left(B(x)u''(x)\right)'' - f &\geq 0, \\ u(x)\left\{\left(B(x)u''(x)\right)'' - f\right\} &= 0 \\ -1 \leq x \leq 1 & \end{aligned}$$

with boundary conditions

$$u(\pm 1) = \delta \qquad B(\pm 1)u''(\pm 1) = M,$$

where M is the moment applied to the ends. He then rewrote it in the weak formulation as a variational inequality. Defining a convex cone of functions

$$K = \left\{u | u - \delta \in H_0^2(-1,-1), u \geq 0\right\}$$

and

$$\begin{aligned} a(u,v) &= \int_{-1}^{1} B(x)u'' \cdot v'' dx, \\ l(w) &= \int_{-1}^{1} fw dx + M(w'(1) - w'(-1)), \end{aligned}$$

then u is the unique solution of

$$u \in K, \qquad a(w-u,u) - l(w-u) \geq 0 \qquad \forall w \in K.$$

He proceeded to find this solution using a finite element method and to compare for simple cases with exact solutions. The examples given in [16] are confined to the special cases of

$$B(x) = 1 \qquad \text{and} \qquad f(x) = A + Cx^2$$

for constant A and C. For $C = 0$, four types of contact are observed to occur:

1. No contact.
2. Point contact at $x = 0$.
3. Line contact in the region $-\rho \leq x \leq \rho$.
4. Point contact at $x = \pm\rho$.

with the type of contact observed depending on the relative sizes and signs of A and M.

Hodges and Bless [9] approached the problem of a loaded beam constrained by a rigid boundary using techniques from optimal control (see figure 2.7). Their notation is quite different[2] from that presented elsewhere in this chapter, and so we shall go through the derivation in more detail. They used $u(x)$ and $v(x)$ to denote the displacment of the elastica from its initial line. The orientation of the cross-section

[2]But does reduce to ours under the appropriate assumptions

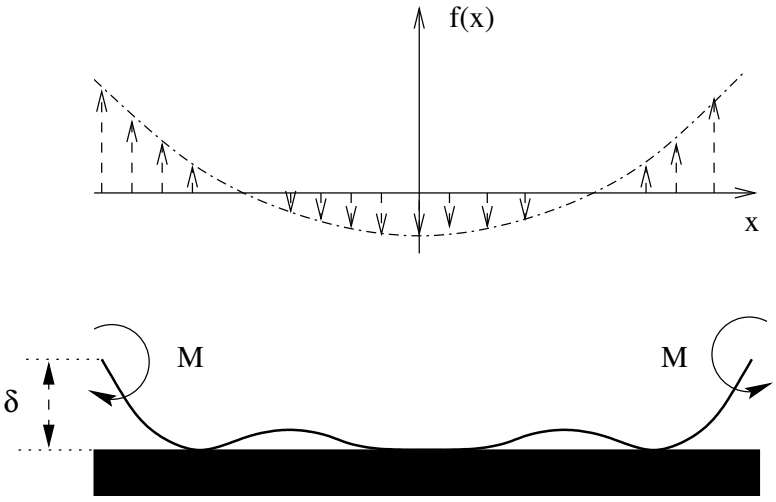


Figure 2.6: Contact problem for an elastica [16]

of the elastica was written $\theta(x)$. The three strain measures associated with the deformation of the beam were $\epsilon(x)$ (the stretching of the reference line), $\gamma(x)$ (the transverse shear strain measure) and $\kappa(x)$ (the bending strain measure), and these took the part of the "control parameters" in the formulation of the problem. They used the equations

$$\begin{aligned} u' &= (1+\epsilon)\cos\theta - \gamma\sin\theta - 1 \\ v' &= (1+\epsilon)\sin\theta + \gamma\cos\theta \\ \theta' &= \kappa \end{aligned}$$

as the equations of state. The constraint that the elastica remain above the boundary was written as

$$S = -(v+h) \leq 0 \qquad \forall x.$$

They first made the assumption that the ends of the elastica were simply supported such that the reference line was unstretched ($\epsilon = 0$). The optimisation involved minimising the total of the strain and potential energy, which in nondimensional terms is

$$J = \frac{1}{2}\int_0^1 \left(\kappa^2 + g\gamma^2 + 2\mu v\right) dx$$

where g and μ are given by

$$\begin{aligned} g &= \frac{GJl^2}{EI} \\ \mu &= \frac{ql^3}{EI} \end{aligned}$$

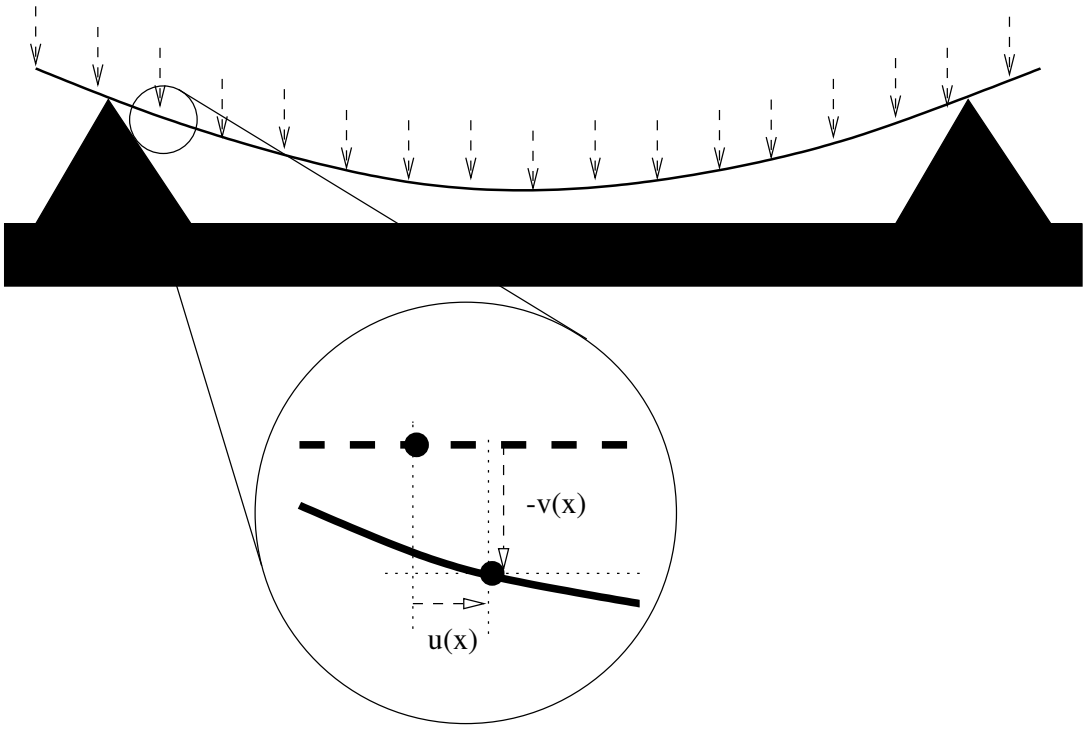


Figure 2.7: Contact problem for a freely supported elastica [9]

and EI is the bending rigidity of the beam, GK the transverse shear rigidity, l the length of the beam and q the body force per unit length. g therefore determines the relative importance of bending to shear, whilst μ indicates the balance between gravity and bending stiffness.

The solution of this problem was performed numerically using commercially available software. Two important cases were considered. The first, labelled in the paper the Timoshenko model, had general values of g and μ. The authors found that the shear force acting on the fibre was continuous, and that the fibre made contact over a region. This was in contrast to the second model they examined, labelled Euler-Bernoulli, where in addition to assuming $\epsilon = 0$ they also chose $\gamma = 0$[3]. In this case, they found that the shear force acting was discontinuous, which the authors considered unphysical. However, for the purposes of this thesis we shall ignore this question and continue to use the Euler-Bernoulli equations, under the assumption that the transverse shear rigidity is sufficiently large that these effects are minimised.

[3]This is equivalent to setting g infinite, i.e. a beam with infinite transverse shear rigidity

Domokos, Holmes and Boyce [8] have studied the problem of constrained Euler buckling as it applies to the stuffer box crimper. This work is the most relavent to the model of primary crimp that we shall proceed to develop, and was first reported in a simple form in [4][4]. They worked with the nonlinear equations of a two dimensional elastica, and assumed that inertial and gravity terms were not significant. The technique they used to examine the problem was very similar to that employed by [3] in that they divided the fibre into regions between contact points and solved the equations exactly in this region using elliptic integrals. Their solutions encompassed the following contact/boundary conditions (see figure 2.8):

1. Pinned-pinned (no contact)
2. Clamped-pinned without contact
3. Pinned-contact
4. Clamped-contact
5. Contact-contact (same wall)[5]

They then used continuity arguments to form full solutions, and plotted load against displacement of the end. They observed that flat solutions could occur (where the elastica was in continuous contact with the walls, but forces only acted at the ends of the fibre).

In later parts of the paper, Domokos, Holmes and Boyce also approached the problem using both numerical and experimental techniques. The experimental technique duplicated where possible the conditions modelled in the theoretical part. The channel walls were made as smooth as possible to reduce the amount of friction present, the displacement of the end was carefully controlled, and as uniform a beam as possible was used. Numerically, a shooting technique was used to locate values of the unknown parameters, and the resulting plots of load against displacement compared with the experimentally obtained curves.

The technique we shall discuss in the next section has some similarities and many differences to the important pieces of work we have summarised above. The geometries we shall consider include the two parallel plates discussed by Vaillette and

[4]Note that the paper [8] was published at the same time that the work we present was being undertaken.

[5]The authors did not consider the case of contact-contact which went between the walls.

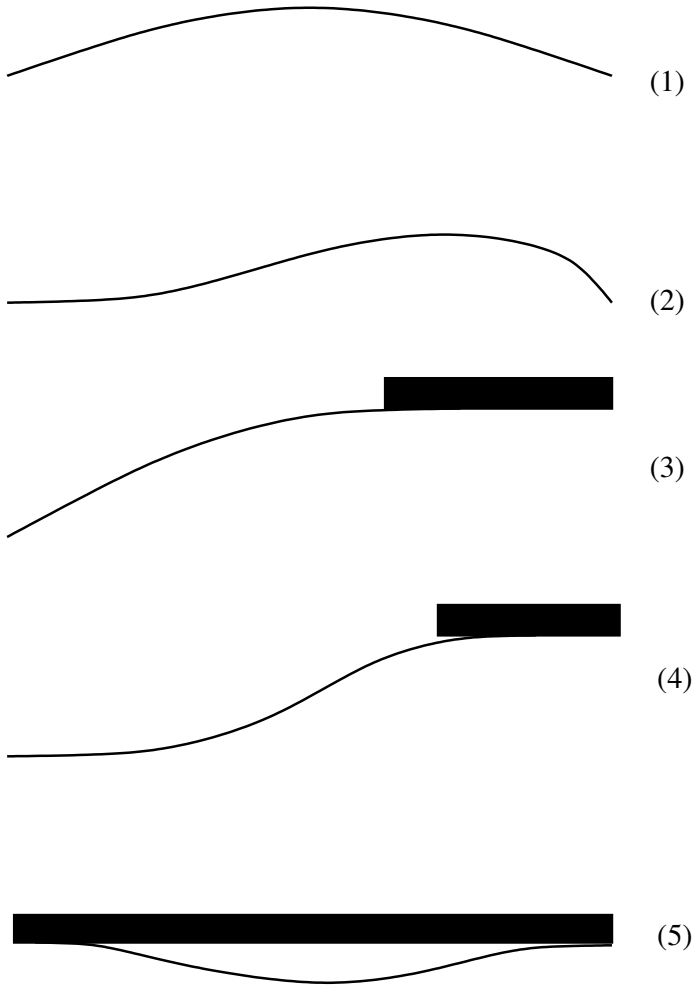


Figure 2.8: Section types for constrained Euler buckling [8]

Adams [15], Adams and Benson [3] and Domokos, Holmes and Boyce [8]. Unlike these authors, we shall limit our discussion to situations where the aspect ratio is small, and hence where we can use the linearised equations for the elastica. Despite this, we shall observe a similar bifurcation diagram to that reported for the wide channel [8]. We shall also expand our methodology to describe a stuffer box in the shape of a thin wedge.

Unlike the cases considered by Westbrook [17] [16] and Hodges and Bless [9], there will be no advantage in using variational techniques to solve the problem. This is because of the potential existence of multiple solutions when a compressive force is added. In their discussion of the variational technique for moving boundary problems, Elliott and Ockendon [5] show that a unique solution exists if the energy operator is *coercive*. This requirement is not satisfied if we apply a compressive force to the elastica. Hence we lose the advantages of formulating the problem as a variational inequality.

The technique we will adopt is most similar to that employed by Soong and Choi [13] where we try different numbers of contact points until we find a solution. Note that we extend their method to cases when there are two surfaces to which we can make contact. We also have the advantage that we can write down an exact solution to the linearised elastica equations in the region between contact points, and hence do not need to use numerical integration to solve the problem.

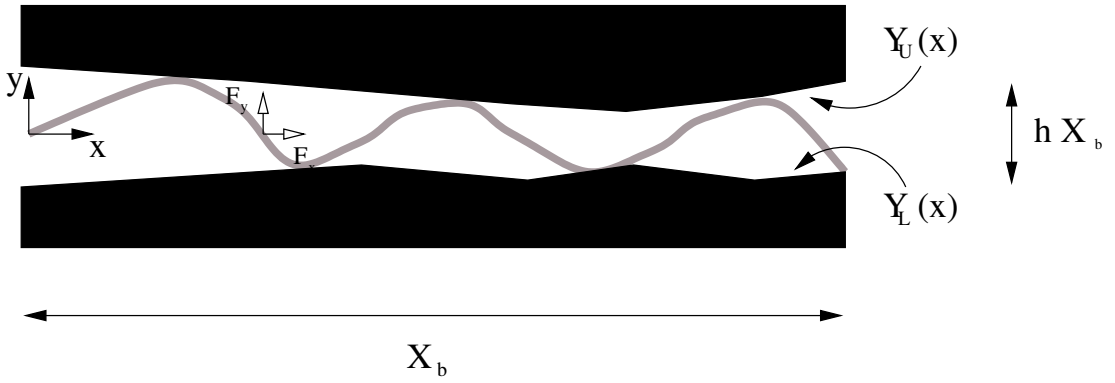


Figure 2.9: A general geometry for a fibre confined in a 2d box.

2.2 2D Confined Fibre

Let us begin our discussion of the problem by setting out a typical configuration we may expect to see. Figure 2.9 shows a fibre confined between two general surfaces. In all the examples we shall consider, the wall geometry will be much simpler than that shown here, but the methods we shall discuss will be applicable to many possible geometries. As we expect the weight of the fibre to be unimportant, we will not consider the effect of allowing any body forces to act on the fibre. Instead, we will suppose that the fibre is acted on by reaction forces whenever it touches the walls, and by a thrust along its undeformed direction, applied at the ends of the fibre. Before we begin to discuss the equations that govern the shape, let us begin by introducing the notation. Throughout, the distance along the fibre will be denoted by s, where

$$0 \leq s \leq L.$$

We will write $x(s)$ and $y(s)$ to describe the position of the fibre, and $\theta(s)$ to denote its orientation and say that the undeformed fibre lies along the line $y(s) =$ constant. The walls of the box are given by $x \in (0, X_b)$, $y = Y_U(x)$ and $y = Y_L(x)$, where the subscripts U and L refer to upper and lower boundaries. Later, we will need a quantity h that gives a typical height of the box. The internal forces that act on the fibre are written as $F_x(s)$ and $F_y(s)$ where the subscript defines the direction in which they act.

Throughout this thesis, we shall limit ourselves to the case when there are no body forces acting on the fibre. If this is the case then we have when the fibre is not touching the walls

$$\frac{dF_y}{ds} = 0, \tag{2.1}$$

$$\frac{dF_x}{ds} = 0, \tag{2.2}$$

and $\theta(s)$, $x(s)$ and $y(s)$ unknown functions. Alternatively, if the fibre is in contact with the walls, $\theta(s)$, $x(s)$ and $y(s)$ are known, and the forces exerted by the walls on the fibre have to be found.[6]

In both contact and non-contact cases, balancing the moments acting on the fibre gives

$$EI\frac{d^2\theta}{ds^2} + F_x \sin\theta - F_y \cos\theta = 0. \tag{2.3}$$

If the fibre is in contact with the walls, this equation describes the relationship between $F_x(s)$ and $F_y(s)$, without determining either. In addition, if the walls are flat (as we will limit ourselves in this thesis), this equation can be interpreted as requiring that the internal force in a fibre in the contact region acts along the boundary. If we further assume that the walls are smooth, and hence able to exert forces only perpendicular to themselves, we can also deduce that, when the fibre is in contact, F_x and F_y are constant. From equation (2.3) the forces can only change when $\theta''(s)$ changes discontinuously. This can occur when

- the fibre changes from being in contact with the surface to being free of the surface; or
- the fibre touches the surface at a point.

We shall call these points boundary points denote them as s_i $(i = 1, \cdots N+1)$. We shall mostly be interested in the behaviour of the fibre in between these points, and for that reason s_1, the first boundary point, is always at the leftmost end of the fibre $s = 0$ and the last s_{N+1} at $s = L$. The reaction forces that act in the x and y directions at these points are given by $f_{x,i}$ and $f_{y,i}$ respectively, and change the forces acting on the fibre as

$$\frac{dF_y}{ds} = \sum_{i=1}^{N} f_{y,i}\delta(s - s_i), \tag{2.4}$$

$$\frac{dF_x}{ds} = -\sum_{i=1}^{N} f_{x,i}\delta(s - s_i). \tag{2.5}$$

[6]We shall discuss the boundary conditions necessary when the fibre goes from contact to free shortly

We also have from the geometry of the fibre in the channel

$$\frac{dy}{ds} = \sin\theta, \tag{2.6}$$

$$\frac{dx}{ds} = \cos\theta. \tag{2.7}$$

The free boundary conditions between equations (2.4) and (2.5) will depend on the model of contact that we use. We will only assume a frictionless contact.[7]
Here we assume that the walls of the box are smooth. If this is the case then the total reaction force, which has the direction

$$\begin{pmatrix} f_{x,i} \\ f_{y,i} \end{pmatrix}$$

must be normal to the surface. In particular, if the wall is at an angle ψ to the horizontal then

$$\begin{pmatrix} f_{x,i} \\ f_{y,i} \end{pmatrix} \cdot \begin{pmatrix} \cos\psi \\ \sin\psi \end{pmatrix} = 0. \tag{2.8}$$

Equation (2.8) is an example of a free boundary condition. We will make use of this and others like it when joining together solutions between the contact points.

2.2.1 Boundary Conditions

There are two types of place where we will need to apply boundary conditions. Firstly, we must model the ends of the fibre. Depending on the geometries involved, we may need to specify position, direction of the fibre and/or and moment (or lack thereof) applied. Note that prescribing the moment is equivalent to prescribing θ'. We shall need to apply free boundary conditions at the boundary points. Most of these will be self evident : as the contact point is on a surface, we know a relationship between $x(s_i)$ and $y(s_i)$; the fibre must also be tangent to the surface at the contact point, and hence θ is determined; the fibre cannot penetrate the surface so we can also say for certain that $\theta' \leq 0$ at the upper surface, and conversely $\theta' \geq 0$ at the lower.[8] It is important to realise what effect the boundary points have on the fibre. Firstly, the fibre is always continuous, hence

$$[x(s_i)]^+_- = [y(s_i)]^+_- = 0.$$

[7] Frictional contact
A second assumption is to have friction acting at the contact points. This makes solution of the problem considerably more complex, and we will not discuss this option further.

[8] In the case of non-flat walls, these become $\theta' \leq \psi'$ and $\theta' \geq \psi'$ respectively

Secondly, we assume that the boundary points do not introduce any kinks in the fibre, so

$$[\theta(s_i)]^+_- = 0.$$

Finally, we assume the boundary points do not apply a moment to the fibre, so

$$[\theta'(s_i)]^+_- = 0$$

Note that, as yet, the position of the boundary points is not known, nor the magnitude of the contact forces $f_{h,i}$ and $f_{v,i}$.

2.2.2 Non-dimensionalisation

We shall now choose suitable scalings for our equations. We are interested in the behaviour of the fibre as it fills the channel, so it is natural to non-dimensionalise all lengths with X_b. Unfortunately, we have no prior knowledge of the magnitude of the forces involved. Thankfully, there is a natural force scaling that arises from (2.3):

$$\frac{EI}{X_b^2}.$$

These lead us to the following variables

$$\begin{aligned}
x &= x' X_b \\
y &= y' X_b \\
s &= s' X_b \\
s_i &= s_i' X_b \\
L &= X_b(1+2t) \\
F_y &= \frac{EI}{X_b^2}\lambda_i p_i \\
F_x &= \frac{EI}{X_b^2}\lambda_i \\
f_{x,i} &= \frac{EI}{X_b^2} f'_{x,i} \\
f_{y,i} &= \frac{EI}{X_b^2} f'_{y,i}
\end{aligned}$$

At this point, we should note that F_y and F_x are both constant between boundary points, and so we have written them in terms of quantities (λ_i and $p_i\lambda_i$) that are constant for each section. These subscripts are written such that p_i is the quantity

that corresponds to the section from boundary point i to $i+1$. Inserting into our equations (2.4), (2.5) and (2.3) and dropping the primes (') gives

$$[p_i\lambda_i]_{s_i-}^{s_i+} = f_{v,i}, \tag{2.9}$$

$$[\lambda_i]_{s_i-}^{s_i+} = f_{h,i}, \tag{2.10}$$

$$\frac{d^2\theta}{ds^2} + \lambda_i \sin\theta = p_i\ \lambda_i \cos\theta. \tag{2.11}$$

where $[\ \ ]_{s_i-}^{s_i+}$ denotes the change across the boundary point s_i.

It is perfectly possible to begin solving these equations as written. The results are difficult to interpret as they involve many elliptic integrals. Instead, we shall now seek a suitable linearisation.

2.2.3 Linearisation

Looking at the typical geometry we are interested in, we realise that the channel is much longer than it is wide (i.e. h, the aspect ratio $\ll 1$). Let us attempt to make use of this in linearising the equations. Firstly, let us scale all vertical distances with this parameter.

$$\begin{aligned} y &= h\,\bar{y} \\ Y_u &= hX_b\,\bar{Y_u} \\ Y_l &= hX_b\,\bar{Y_l} \end{aligned}$$

Equation (2.6) becomes

$$h\bar{y}' = \sin\theta$$

and in order to balance, we will need either a rapid variation as we move along the fibre, or

$$\theta = h\,\bar{\theta}.$$

It is this latter case that we shall consider here. Bearing this in mind, and inserting the scalings into (2.11) requires that

$$p_i = h\,\bar{p_i}$$

in order that the term does not dominate. Finally, for reasons that will become clear later, we need to write that

$$t = h^2\,\bar{t}.$$

Inserting these into (2.11), gives

$$\frac{d^2\bar{\theta}}{ds^2} + \lambda_i \bar{\theta} = \bar{p}_i \lambda_i + O(h^2) \tag{2.12}$$

In addition, the equations for the position become

$$\begin{aligned} \frac{d\bar{y}}{ds} &= \bar{\theta} + O(h^2) \\ \frac{dx}{ds} &= 1 + O(h^2) \end{aligned} \tag{2.13}$$

2.2.3.1 Linearisation of the boundary and free boundary conditions

We shall now see the effect of these scalings on the boundary conditions we apply both at the ends of the fibre and the boundary points. Firstly, we will assume that the right hand end is at $x = 1$:

$$x(1 + 2h^2\bar{t}) = \int_0^{1+2h^2\bar{t}} \cos h\bar{\theta} ds = 1$$

and hence one condition is

$$\int_0^1 \bar{\theta}^2 = 4\bar{t}. \tag{2.14}$$

At the boundary points, we will still require that $\bar{\theta}$, $\bar{\theta}'$, x and y are all continuous. The condition that the fibre be tangent to the wall can be expressed, in dimensional variables, as

$$\tan\theta = \frac{dY_u}{dx}$$

Making the scalings for these quantities, this becomes

$$\bar{\theta} = \frac{d\bar{Y}_u}{dx}. \tag{2.15}$$

Once again, for the upper surface $\bar{\theta}' \leq 0$.

Finally, we must consider the changes in λ_i and $\lambda_i\bar{p}_i$ that occur across the boundary point. Remembering our continuity condition (2.8) and changing variables gives

$$\begin{pmatrix} [\lambda_i]_{s_{i-}}^{s_{i+}} \\ h[\bar{p}_i\lambda_i]_{s_{i-}}^{s_{i+}} \end{pmatrix} \cdot \begin{pmatrix} \cos\psi \\ \sin\psi \end{pmatrix} = 0,$$

where

$$\psi = \tan^{-1}\left(h\frac{d\bar{Y}_u}{dx}\right) \quad \text{or} \quad \tan^{-1}\left(h\frac{d\bar{Y}_l}{dx}\right)$$

as required. Expanding this to $O(1)$ gives,

$$[\lambda_i]_{s_i-}^{s_i+} = 0. \tag{2.16}$$

This is an important result, as it means that the each section will feel the same thrust, λ. For this reason, we can treat λ as a global parameter rather than determining it for each section in turn.

2.2.3.2 Summary of Linearised equations

The linearised equations for the poisition of the fibre within the channel are

$$\begin{aligned} \bar{y}'(s) &= \bar{\theta} \\ x'(s) &= 1 \qquad\qquad s \in 0, 1 \\ \bar{\theta}''(s) + \lambda_i \bar{\theta} &= \bar{p_i} \lambda_i. \end{aligned}$$

At the extreme ends of the fibre we fix the position, and either apply no moment (in which case $\bar{\theta}' = 0$ or fix the angle ($\bar{\theta}$ fixed). The length of fibre within the box leads to the global boundary condition

$$\int_0^1 \bar{\theta}^2 = 4\bar{t}.$$

At the boundary points, we assume no friction, and hence

$$[\lambda_i]_{s_i-}^{s_i+} = 0.$$

In addition, we assume that x, $\bar{y}$, $\bar{\theta}$ and $\bar{\theta}'$ are all continuous.

2.2.4 Methodology

We shall now attempt to make use of the fact that equation (2.12) is simple to solve analytically in the regions where $\bar{p_i}$ is fixed. For $s_i < s < s_{i+1}$ it has the general solution

$$\bar{\theta} = A_i \sin \sqrt{\lambda} s + B_i \cos \sqrt{\lambda} s + \bar{p_i}. \tag{2.17}$$

Problems arise because the position and number of the boundary points, as well as the changes they make to $\bar{p_i}$ are not specified as part of the problem. Below we will discuss a methodology that can partially overcome these problems by making use of the symmetries present in the solutions of (2.12).

Our method will be to construct candidate solutions to the problem. These will be built out of a series of exact solutions in the regions between boundary points. By requiring that all the necessary quantities are continuous, we can join these sections together. Finally, we can look at global parameters to ensure that the solution solves the problem as a whole. Let us begin by noting that each part of the elastica is defined by five constants, A_i, B_i, λ,$\bar{p_i}$ and d_i, which is the length of the section and is given by

$$d_i = (s_{i+1} - s_i).$$

The values of these constants are fixed by the requirements that $\bar{\theta}$ and $\bar{\theta}'$ are continuous, and that each end of the section should be a boundary point. This gives four boundary conditions for four unknowns in each section. Also λ is a global parameter, and we have the global boundary condition that

$$\sum_i d_i = 1 \tag{2.18}$$

To find a solution,we select a particular number and type[9] of boundary points, and start by choosing trial values for λ and the free initial condition at the start (either $\bar{\theta}$ or $\bar{\theta}'$). The remaining parameters are fixed by requiring that the section satisfies the condition at the first boundary point. The continuity conditions are then applied, and the next section generated so that it goes to the next point. This continues until the end of the fibre is reached. We then check to see if a solution has been found, based on the global condition (2.18). If not, new values of our shooting parameters are tried.

We also need to check that the solution is physically acceptable, namely that at each contact point (1) $\bar{\theta}'$ has the correct sign, and (2) the change in the force $\lambda\bar{p_i}$ has the correct sign[10]. Given that this is confirmed, we can then calculate the length of fibre that is contained in the channel from equation (2.14). It is important to note that the method we have just described will generate solutions to the problem as formulated. It does not distinguish between solutions that are possible and those that actually occur in practice. For this, we need to discuss a selection criteria such as seeking solutions that minimise the elastic potential energy. This point will be discussed in section 2.2.5.3 for the example of a fibre confined to a rectangular channel.

[9]The type of boundary point refers to its position at either the top or bottom boundary.

[10]For the top boundary, this force must act inwards, hence $[\lambda\bar{p_i}]^+_- \geq 0$. Equivalently, we can say that $[\bar{\theta}'']^+_- \geq 0$



Figure 2.10: Example 1a : The rectangualr box

2.2.5 Example 1a : The rectangular channel

Let us now put these ideas into practice. We will start with a very simple geometry for the channel, a rectangle (with boundaries at $y = 0$ and $y = h$). In addition, we will apply the same boundary conditions of no applied moment ($\bar{\theta}' = 0$) and $y = 0$ at each end of the fibre. Our first task will be to identify what can happen to the fibre between the contact points. The solutions of these "prototype" sections will then be written down, and any undetermined parameters identified. These will be fixed when we come to join the sections together. The solutions to the full problem will be classified depending on the types of section they contain. We will then plot a diagram showing how λ varies with the amount of fibre in the channel ($\bar{t}$) for different classes of solution. These will show that there can be more than one solution for a particular value of $\bar{t}$. Hence we will need to introduce criteria to select which solution is observed in practice.

We will now introduce two points of notation. Firstly, as the position along the channel makes no difference to the boundary conditions (because the height of the channel is constant), we will write down all of the solutions in terms of the distance from the contact point r_i where

$$r_i = s - s_i.$$

Secondly, we will define the quantity $\bar{\delta x}_i$,

$$\bar{\delta x}_i = \int_0^{d_i} \frac{\bar{\theta}_i^2}{2} dr_i.$$

Hence the global boundary condition (2.14) becomes

$$\sum_i \bar{\delta x}_i = 2\bar{t}.$$

2.2.5.1 Section Types

We now consider the solution of the problem for all possible "sections" between two contact points. By joining these sections together, we can construct the complete solution.

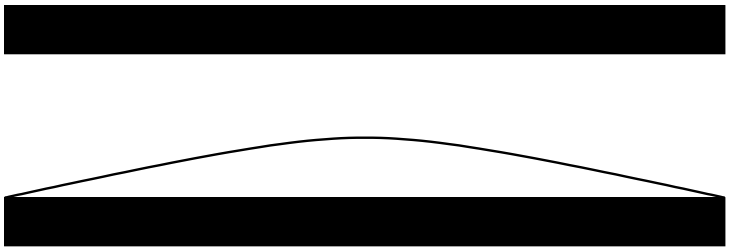


Figure 2.11: The unconfined fibre

1. *Unconfined Fibre (figure 2.11)*
   The fibre only has contact points at the start and end, and does not touch the top boundary at all. The boundary conditions for this type of section are:

$$\begin{aligned} \bar{\theta}' &= 0 \text{ at } r_i = 0, 1 \\ \bar{p_i} &= 0 \\ \max \bar{y}(r) &< 1 \qquad (2.19) \\ \min \bar{y}(r) &\geq 0. \qquad (2.20) \end{aligned}$$

   Applying these requires that

$$\bar{\theta} = B_i \cos \sqrt{\lambda} r_i \quad \text{and} \quad \sqrt{\lambda} = m\pi \qquad (2.21)$$

   for some integer m. The amplitude of the fibre, B_i, is determined by the boundary conditions on the length of the fibre in the channel (2.14).

   In addition, we can also calculate the additional quantities $y(r_i)$ and $\bar{\delta x_i}$.

$$\begin{aligned} \bar{y}(r_i) &= \frac{B_i}{m\pi} \sin m\pi r_i \\ \bar{\delta x_i} &= \frac{B_i^2}{4} \end{aligned}$$

   If we now specify that $y(0) = 0$, it becomes clear that in order for the equation (2.20) to hold, $\sin m\pi r_i$ must remain positive. This implies that $m = 1$. We can now summarise that, for the unconfined fibre,

$$\begin{aligned} \bar{\theta}(r) &= B_i \cos \pi r_i \\ \bar{y}(r) &= \frac{B_i}{\pi} \sin \pi r_i \end{aligned}$$

   where $B_i^2 = 8\bar{t}$. In order to satisfy (2.19), $B_i < \pi$, which implies that the total length of the fibre in the box is less than

$$1 + \frac{h^2\pi^2}{4}$$



Figure 2.12: The starting sections

for this type of solution to be possible.

2. *Starting Section (figure 2.12)*
   The starting section goes from the base to the first contact point at $\bar{y} = 1$ The boundary conditions we apply are:

$$\begin{aligned} \bar{\theta}'(0) &= 0, \\ \bar{\theta}(d_i) &= 0, \\ \bar{\theta}'(d_i) &\leq 0, \\ \bar{p}_i &< 0, \\ \bar{y}(0) &= 0, \\ \bar{y}(d_i) &= 1. \end{aligned} \tag{2.22}$$

   These can then be applied to solution (2.17) to solve for the coefficients A_i and B_i. Hence

$$\bar{\theta}(r_i) = \bar{p}_i \left(1 - \frac{\cos\sqrt{\lambda} r_i}{\cos\sqrt{\lambda} d_i} \right) \tag{2.23}$$

$$\bar{y}(r_i) = \frac{\bar{p}_i}{\sqrt{\lambda}} \left(r_i\sqrt{\lambda} - \frac{\sin r_i\sqrt{\lambda}}{\cos\sqrt{\lambda} d_i} \right) \tag{2.24}$$

$$\bar{\delta x}_i = \frac{{\bar{p}_i}^2}{8\sqrt{\lambda}} \left(4\sqrt{\lambda} d_i - \frac{8\sin\sqrt{\lambda} d_i}{\cos\sqrt{\lambda} d_i} + \frac{2\sqrt{\lambda} d_i + \sin 2\sqrt{\lambda} d_i}{\cos^2\sqrt{\lambda} d_i} \right). \tag{2.25}$$

   The condition that this section goes from the base to the top plate allows us to fix $\bar{p}_i$ through use of equations (2.22) and (2.24), if we assume that d_i is known

$$\bar{p}_i = -\frac{\sqrt{\lambda}}{d_i\sqrt{\lambda} - \tan\sqrt{\lambda} d_i}. \tag{2.26}$$

   The requirements that $\bar{p}_i \leq 0$ and $\theta'(d_i) \leq 0$ mean that

$$\frac{\pi}{2} < \sqrt{\lambda} d_i \leq \pi. \tag{2.27}$$



Figure 2.13: The ending sections

At this point we introduce the variable z_i where

$$z_i = \sqrt{\lambda} d_i$$

the importance of which will become apparent later.

3. *End Section (figure 2.13)* The end section is the mirror image of the start section, and has the boundary conditions

$$\begin{aligned} \bar{\theta}'(d_i) &= 0 \\ \bar{\theta}(0) &= 0 \\ \bar{\theta}'(0) &\leq 0 \\ \bar{p_i} &> 0 \\ \bar{y}(0) &= 1 \\ \bar{y}(d_i) &= 0. \end{aligned}$$

Having applied these we find that

$$\bar{\theta}(r_i) = \bar{p_i} \left(1 - \frac{\cos \sqrt{\lambda}(d_i - r_i)}{\cos \sqrt{\lambda} d_i} \right). \tag{2.28}$$

Once again, we can integrate this to obtain the position within the channel

$$\bar{y}(r_i) = 1 + \frac{\bar{p_i}}{\sqrt{\lambda}} \left(\sqrt{\lambda} r_i + \frac{\sin \sqrt{\lambda}(d_i - r_i) - \sin \sqrt{\lambda} d_i}{\cos \sqrt{\lambda} d_i} \right) \tag{2.29}$$

$$\bar{\delta x}_i = \frac{\bar{p_i}^2}{8\sqrt{\lambda}} \left(4\sqrt{\lambda} d_i - \frac{8 \sin \sqrt{\lambda} d_i}{\cos \sqrt{\lambda} d_i} + \frac{2\sqrt{\lambda} d_i + \sin 2\sqrt{\lambda} d_i}{\cos^2 \sqrt{\lambda} d_i} \right). \tag{2.30}$$

As the section joins one plate to the other, we can use equation (2.29) and $\bar{y}(d_i) = 0$ to calculate $\bar{p_i}$ in terms of d_i and $\sqrt{\lambda}$

$$\bar{p_i} = \frac{\sqrt{\lambda}}{\sqrt{\lambda} d_i - \tan \sqrt{\lambda} d_i}. \tag{2.31}$$

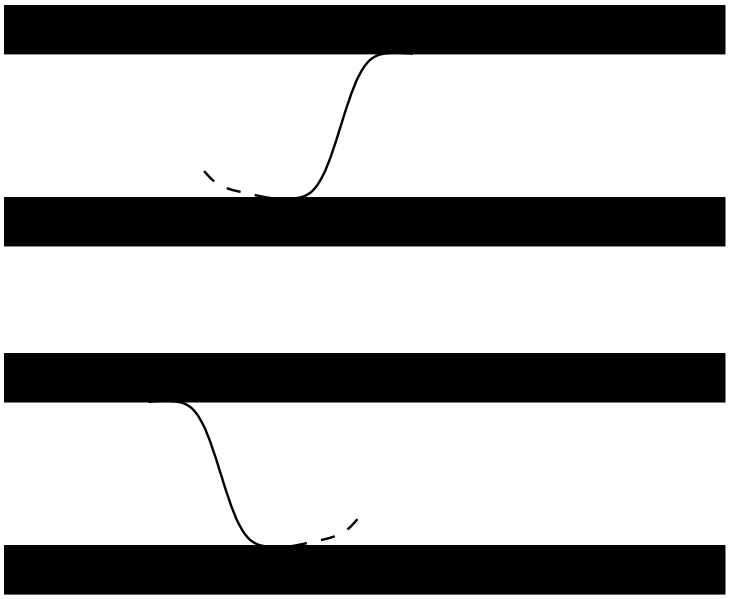


Figure 2.14: The Middle sections

The requirement that $\bar{p}_i \geq 0$ means that

$$\frac{\pi}{2} \leq z_i \leq \pi \tag{2.32}$$

where again $z_i = \sqrt{\lambda} d_i$. The value of z_i will be determined by applying the continuity conditions for the fibre.

4. *Middle Section (figure 2.14)*
   The middle section goes from top plate to bottom plate (or vice versa). The boundary conditions are

$$\begin{aligned} \bar{\theta}(0) &= 0 \\ \bar{\theta}(d_i) &= 0 \\ \bar{y}(0) &= 0 \text{ or } 1 \\ |\bar{y}(d_i) - \bar{y}(0)| &= 1. \end{aligned} \tag{2.33}$$

   Applying these gives

$$\bar{\theta}(r_i) = \bar{p}_i \left(1 - \cos\sqrt{\lambda} r_i - F(z_i) \sin\sqrt{\lambda} r_i\right), \tag{2.34}$$

   where once again $z_i = \sqrt{\lambda} d_i$ and

$$F(z_i) = \frac{1 - \cos z_i}{\sin z_i}. \tag{2.35}$$

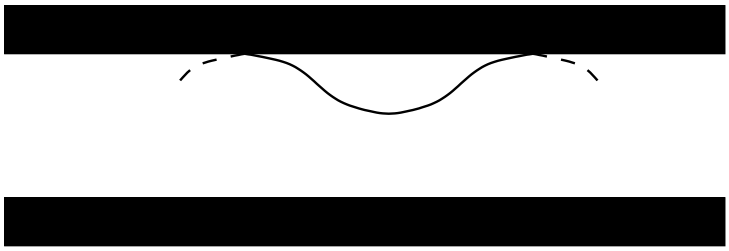


Figure 2.15: Dimple

We can now proceed to integrate this to find the coordinates of the fibre in the box

$$\bar{y}(r_i) = \bar{y}(0) - \frac{\bar{p}_i}{\sqrt{\lambda}}\left(F(z_i)(1-\cos\sqrt{\lambda}r_i) - (r_i\sqrt{\lambda} - \sin\sqrt{\lambda}r_i)\right) \quad (2.36)$$

$$\begin{aligned}\bar{\delta x}_i &= \frac{\bar{p_i}^2}{8\sqrt{\lambda}}(6z_i - 6F(z_i) + 8F(z_i)\cos z_i - 2F(z_i)\cos 2z_i + \\ &\quad 2z_iF^2(z_i) - 8\sin z_i + \sin 2z_i - F^2(z_i)\sin 2z_i). \end{aligned} \quad (2.37)$$

Applying the boundary condition on $\bar{y}(d_i) - \bar{y}(0)$ (2.33) and making use of half angle identities we arrive at the following equation for $\bar{p}_i$

$$\bar{p}_i = G_i\frac{\sqrt{\lambda}}{z_i - 2\tan\frac{z_i}{2}} \quad (2.38)$$

where G_i is 1 if the fibre goes from base to top and -1 if it goes from top to base. As we wish $\bar{p}_i$ to be positive as it goes from base to top, and that $\bar{\theta}'(d_i) \leq 0$ we also require that

$$\pi \leq z_i \leq 2\pi \quad (2.39)$$

Once again, z_i must be determined by use of the continuity conditions

5. *Dimple (figure 2.15)*

The dimple is one of two solutions that go from one plate to the same plate (the other being a flat section). The boundary conditions are

$$\begin{aligned} \bar{\theta}(0) &= 0 \\ \bar{\theta}(d_i) &= 0 \\ \bar{p}_i &= 0 \\ \max|(\bar{y}(r_i) - \bar{y}(0))| &< 1 \\ y(0) = y(d_i) = 0 \quad &\text{and} \quad \theta'(0) = \theta'(d_i) \geq 0 \\ \text{or} \quad y(0) = y(d_i) = 1 \quad &\text{and} \quad \theta'(0) = \theta'(d_i) \leq 0. \end{aligned}$$

Application of these leads to

$$\begin{aligned} \bar{\theta}(r_i) &= A_i \sin\sqrt{\lambda} r_i \\ d_i &= \frac{m\pi}{\sqrt{\lambda}} \end{aligned} \tag{2.40}$$

for some integer m. If we require that $y(0) = y(d_i)$ then we can deduce that m must be even. Note that A_i has still not been determined. Instead, this will need to be calculated from the continuity of $\bar{\theta}'$. The position of the fibre within the channel can be found simply by integration to give

$$\begin{aligned} \bar{y}(r_i) &= \bar{y}(0) + \frac{A_i}{\sqrt{\lambda}}(1 - \cos\sqrt{\lambda} r_i) \\ \bar{\delta x}_i &= \frac{A_i^2 d_i}{4}. \end{aligned} \tag{2.41}$$

The limit on the height of the dimple requires that

$$\begin{aligned} |\bar{y}(r_i) - \bar{y}(0)| &\leq 1 \\ \text{and} \qquad |A_i| &\leq \frac{\sqrt{\lambda}}{2}. \end{aligned}$$

6. *Flat section*

   We also have the possibility of a flat section, where

   $$\bar{\theta} = 0.$$

   By multiplying (2.12) by θ' and integrating, we can readily see that the magnitude of θ' is directly related to θ, and hence if $theta'$ is 0 at one end of the section, it must be 0 at the other (and hence $theta' = 0$ at all contact points where $theta = 0$. We will discuss the special treatment required for these solutions shortly.

2.2.5.2 Types of Solution

We can now begin to combine the above sections to form solutions to the full problem. First let us note that the free boundary conditions are dependent on the parameter $\sqrt{\lambda}$ only through the quantity $z_i = \sqrt{\lambda} d_i$. Hence we can make use of the global conditions on d_i (2.18) to write[11]

$$\sqrt{\lambda} = \sum_i z_i. \tag{2.43}$$

[11] This is true if there are no flat sections present. If this is not the case then

$$\sqrt{\lambda} = \frac{1}{1-\sigma} \sum_i z_i \tag{2.42}$$

where $\sigma < 1$ is the total length of flat fibre.

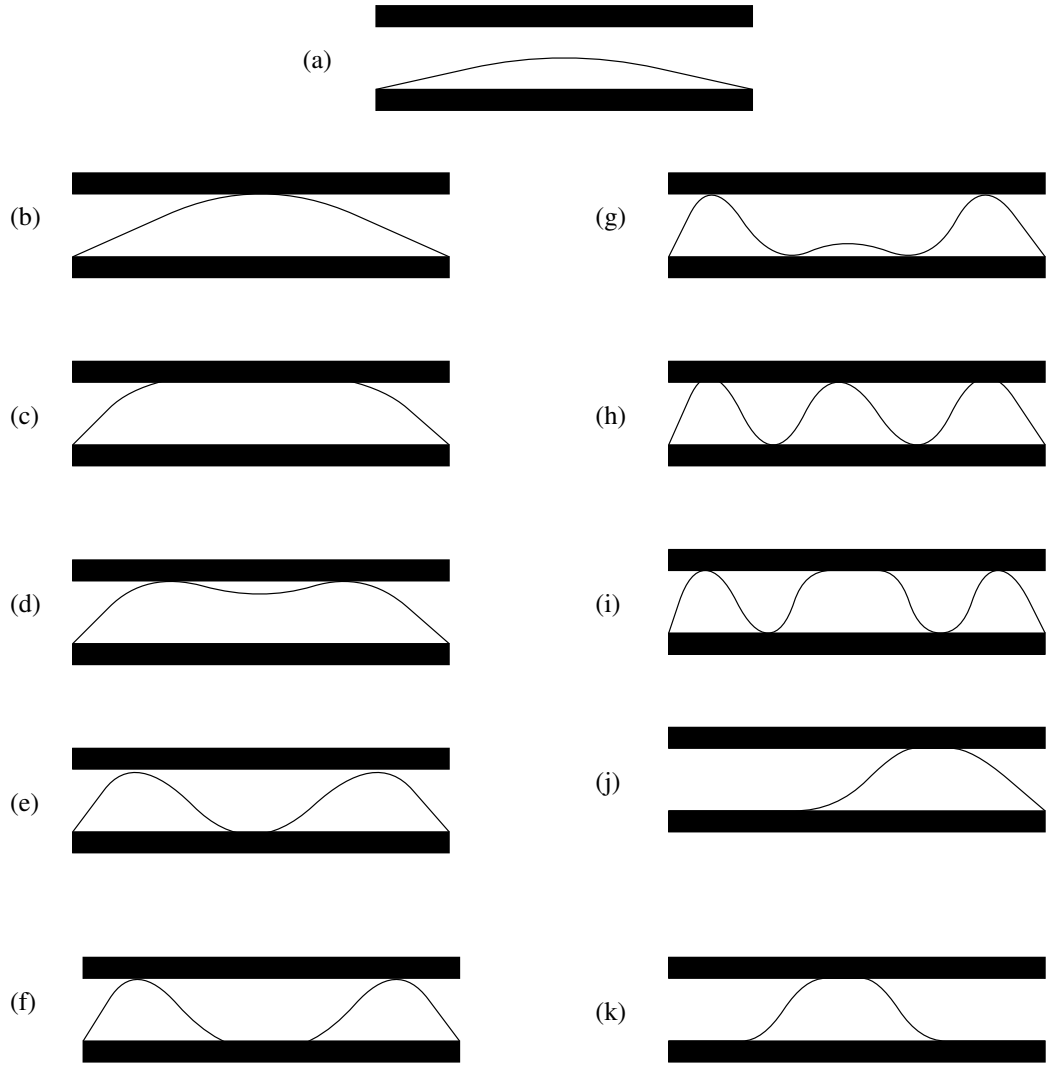


Figure 2.16: Key for figures 2.17 and 2.18

Secondly, in order to satisfy the boundary conditions, we require that :

Either	The only section present is the unconfined fibre
Or	The solution begins with a starting section and finishes with an ending section.
Or	The solution has $\bar{\theta}' = 0$ at each end of all the sections

The third of these is the only way the fibre can contain a flat section.

The method outlined above produces many different solutions (see figure 2.16). However they can be classified into a small number of different categories depending on how they are constructed.

1. *Unconfined Fibre (a)*

   The fibre has not yet touched the top plate, and hence encounters no vertical

force. As shown in section 1 this will occur for $B_i < \pi$ and for a constant force. Explicitly we have that

$$\begin{aligned} \sqrt{\lambda} &= \pi \\ \bar{t} &= \frac{B_i^2}{4}. \end{aligned}$$

When $B_i = \pi$ the fibre just touches the top and a new category of solution is needed.

2. *Point Contact (b), (e) and (h)*
These solutions occur after a dimple or unconfined fibre just touches one of the plates. They always begin with a starting section, finish with an ending section, and may have an even number of middle sections.
If there are only the two sections present, then the symmetry of the start and end types requires that $z_1 = z_2$ and hence

$$\begin{aligned} \sqrt{\lambda} &= 2z_1 \\ \bar{t} &= \bar{\delta x}_1(z_1). \end{aligned}$$

In the presence of middle sections, we can still say that, by symmetry

$$\begin{aligned} z_1 &= z_N \\ z_i &= z_j \quad i, j \neq 1, N \end{aligned}$$

and in addition the continuity of $\bar{\theta}'$ requires that (from (2.23), (2.26) , (2.34), and (2.38)

$$\begin{aligned} \frac{\tan z_1}{z_1 - \tan z_1} &= \frac{\tan \frac{z_2}{2}}{z_2 - 2\tan \frac{z_2}{2}} \\ \frac{\pi}{2} < z_1 &< \pi \\ \pi < z_2 &< 2\pi. \end{aligned} \tag{2.44}$$

If the number of middle sections is $2M$ then

$$\begin{aligned} \sqrt{\lambda} &= z_1 + Mz_2 \\ \bar{t} &= \bar{\delta x}_1 + M\bar{\delta x}_2 \end{aligned}$$

where $\bar{\delta x}_1$ is the $\bar{\delta x}$ for sections 1 and N, and $\bar{\delta x}_2$ is the $\bar{\delta x}$ for the middle sections. As z_1 approaches π the curvature at the contact point tends to zero, at which point a flat section is possible.

3. *Flat Sections (c), (f) and (i)*

   These have the same sections present as before, but with the additional option of flat sections. The presence of these greatly simplifies the calculation of $\sqrt{\lambda}$ and $\bar{t}$. As the $\bar{\theta}' = 0$ at the contact points, we require that

$$\begin{aligned} z_1 = z_N &= \pi \\ z_i &= 0 \quad \text{if section is flat} \\ z_i &= 2\pi \quad \text{otherwise} \end{aligned}$$

   (This arises from the symmetry of the different sections, in particular that the curvature at one end of a middle section is the opposite to that at the other end.) In addition as $\bar{\delta x}_i = 0$ for the flat section, and again writing $2M$ to be the number of middle sections we can see from (2.25), (2.26), (2.37) and (2.38) that

$$\bar{t} = \frac{3}{8\pi}(2 + M)\sqrt{\lambda} \tag{2.45}$$

   The growth of the flat section is limited only by the requirement that the total flat length (σ) is less than 1 for the linearised case. As will be seen later, this limit is never reached in a stable configuration.

4. *Flat sections (j) and (k)*

   It is not necessary for flat sections to begin with a starting section and end with an ending section. Instead these can be replaced by equivalent middle sections. Most of the above discussion holds true, except the values for z_1 and z_i are altered, and if P is the number of start or end sections then

$$\bar{t} = \frac{3}{16\pi}(P + 2M + 2)\sqrt{\lambda}$$

   which reduces to (2.45) for the case $P = 2$.

5. *Dimple Solutions (d) and (g)*
   Dimple solutions are similar to the point contact described above except that they also include a dimple section. Once again, symmetry simplifies greatly the problem of determining the properties $\sqrt{\lambda}$ and $\bar{t}$, and we can immediately write that :

$$\begin{aligned} z_N &= z_1 \\ z_{dimple} &= 2\pi \\ z_i &\quad \text{is found from the solution of (2.44),} \end{aligned}$$

   where z_{dimple} refers to the dimple section and z_i applies to all the middle-type sections. We can now apply the continuity condition for $\bar{\theta}'$ and use the equations for $\bar{\theta}$ ((2.23), (2.26) and (2.40)) to determine the value for A_i, the amplitude of the dimple :

$$A_i = \pm\frac{\sqrt{\lambda}\tan z_1}{z_1 - \tan z_1} \tag{2.46}$$

$$\text{and} \qquad |A_i| \leq \frac{\sqrt{\lambda}}{2}.$$

   Note that the ambiguity over the sign of A_i arises because of the possibility of the dimple forming at the top or the bottom. It is now trivial to insert these quantities in order to calculate $\bar{t}$ and λ.

Figure 2.17 shows the calculated values of $\bar{t}$ and λ for the configurations discussed above and drawn in figure 2.16. Note the presence of kinks in the curves. These can be classified into two types. The first occur when a dimple begins to form. This is a bifurcation. The second occur when a dimple touches the base and begins to flatten. These are not bifurcations. For each of these curves, all valid values of z_1 were used. Looking at this graph we see immediately the problem of non-uniqueness of the solutions if we specify $\bar{t}$ or λ alone. We must now apply energy minimisation arguments to determine which configuration is stable for each of these cases.

2.2.5.3 Choice of Solution

The problem we are solving can be attacked in a number of different ways. The approach used so far has been based on equilibrium conditions for elemental sections of the fibre. However an alternative method is to seek configurations that minimise the energy of the system. Explicitly, we can write that the solution minimises :

Strain Energy – Work Done by External Forces

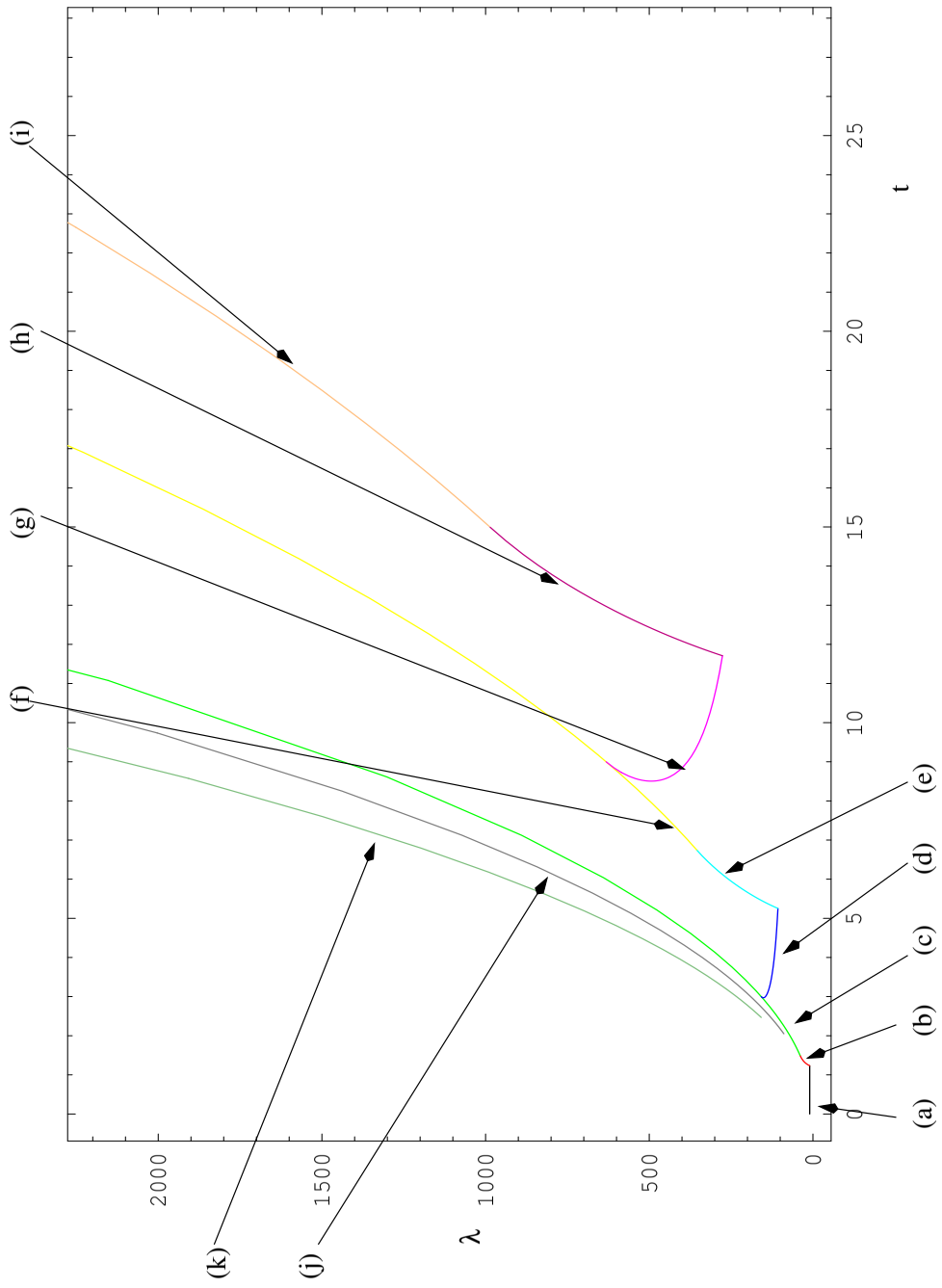


Figure 2.17: $\bar{t}$ vs. λ

where the strain energy is given by

$$\text{Strain Energy} = EI \int_0^l \frac{\text{Curvature}^2}{2} ds$$

In the non-dimensional, linearised system this becomes

$$\int_0^1 \frac{\bar{\theta}'^2}{2} ds. \tag{2.47}$$

The work done depends on the particular boundary conditions we choose. If the force is controlled (equivalent to prescribing λ) then it acts as an external part of the system and work is done

$$\text{Work Done} = \int_0^l F_h(1 - \cos\theta) ds$$

or (in linear, non-dimensional terms)

$$\begin{aligned} \text{Work Done} &= \lambda \int_0^1 \frac{\bar{\theta}^2}{2} ds + \quad O(h^2) \\ &= 2\lambda \bar{t} + \quad O(h^2). \end{aligned} \tag{2.48}$$

For the situation where the length is specified ($\bar{t}$ is prescribed) there is no external work done to the system, hence the only contribution to the energy is due to strain in the fibre.

We now apply the latter condition for the case of increasing amounts of fibre being fed into the box. Plotting $\log(Energy)$ vs the control variable $\bar{t}$ we obtain figure 2.18 From this we can see the progression of the solution as more fibre is fed into the box:

The fibre begins to buckle as soon as $\bar{t}$ is positive (a). The amplitude increases steadily until the fibre just touches the top. It then begins to flatten (b). When the curvature at the contact point reaches zero, the flat solution begins to grow (c). This it does until it is energetically feasable for a dimple (d) to form. Note that the amplitude of the dimple is *not* zero. The dimple grows until it reaches the base, at which point a second flattening occurs (e). This then forms a flat solution (f) which again forms a dimple when it is able. The cycle of dimple to touching to flat to dimple continues indefinitely.

The dimple in this arrangement is favoured energetically. However, the transition from flat to dimple is not straightforward. Looking at figure 2.17 we see that for each dimple, the plot of $\bar{t}$ against $\sqrt{\lambda}$ curves back on itself. This is also visible on the

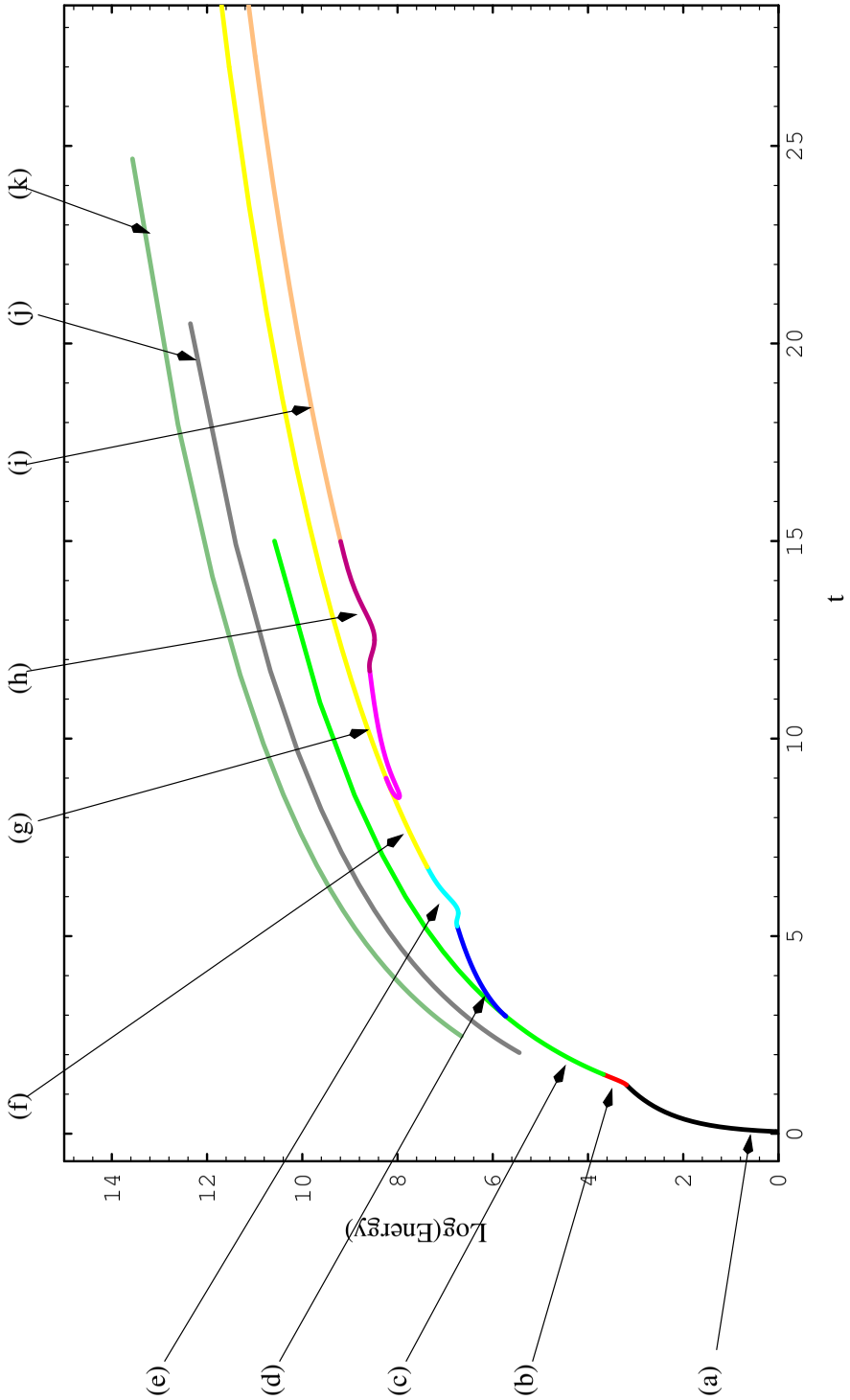


Figure 2.18: Energy vs. $\bar{t}$

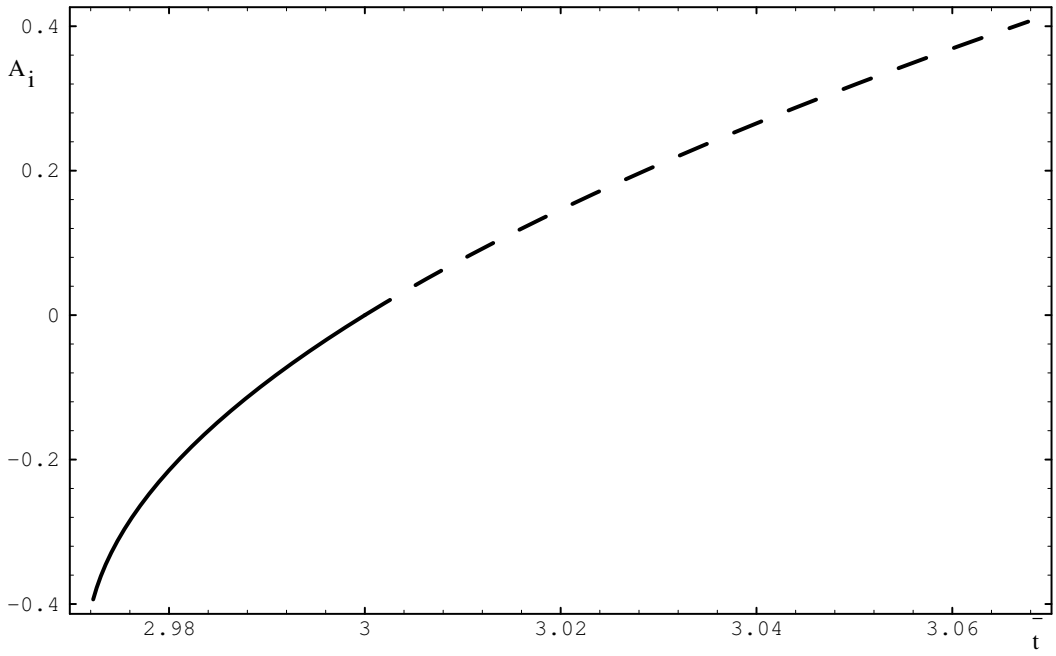


Figure 2.19: A_i vs. $\bar{t}$ for the first dimple. Transition from solid to dashed line indicates transition from physical to unphysical (outside the box) solution.

energy - $\bar{t}$ plot (figure 2.18). The effect is clearer if we examine the variation of the dimple amplitude (A_i) with $\bar{t}$.

The case where A_i is zero marks the intersection of the flat and dimple curves. When this happens, we must have $z_1 = \pi$ If we therefore write that for the first dimple solution (d)

$$\begin{aligned} z_1 &= \pi + \epsilon \\ \bar{t} &= \frac{1}{2}\sum_{i=0}^{2} \delta\bar{x}_i \\ A_i &= \sqrt{\lambda}\frac{\tan z_1}{z_1 - \tan z_1} \end{aligned}$$

and expand in powers of ϵ we get that

$$\begin{aligned} \bar{t} &= 3 + \frac{3}{2\pi}\epsilon + 2\epsilon^2 + O(\epsilon^3) \\ A_i &= 4\epsilon + \frac{2}{\pi}\epsilon^2 + O(\epsilon^3) \end{aligned}$$

Note that for physical solutions, $\epsilon < 0$ This can be plotted to give figure 2.19

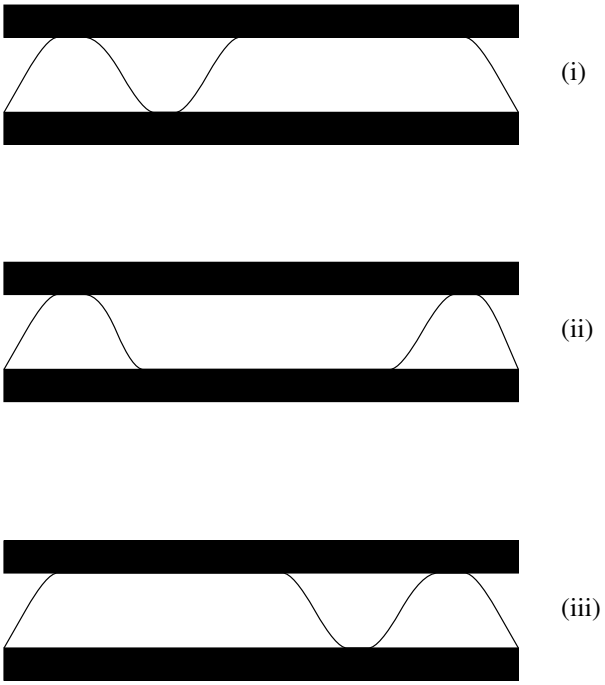


Figure 2.20: Three possible solutions that are indistinguishable energetically

Notice that the gradient is positive at $A_i = 0$, and hence the dimple exists locally for $\bar{t}$ less than the critical value. We would therefore expect that there is a fold in the curve for a smaller value of $\bar{t}$, which is the energetically favourable branch. This is in contrast to the case for an unconfined, non-linear Euler strut.

2.2.5.4 Degeneracy

Our method is successful in that it predicts solutions for different values of the control parameters, λ or $\bar{t}$. However in many circumstances there exist solutions with the same energy . Consider the situation where the fibre begins with a starting section, has two middle sections, a flat section and an end section. The process by which λ and $\bar{t}$ are calculated involves the sum of various quantities, and hence does not take into account the exact order of the sections. Hence there are three different versions of the fibre described above that are indistinguishable in terms of $\bar{t}$, λ and $Energy$ (see figure 2.20)

This occurs as there is no energy penalty for moving the points of contact. If we include a frictional force this would change, and the arrangement would become dependent on the past history of the fibre, in such a way as to minimise the movement of the contact points.



Figure 2.21: Example 1b: The rectangular box fed midway

2.2.6 Example 1b : Rectangular channel fed midway

The simple rectangular box we have just considered showed how our method can work in practice. Unfortunately, the boundary conditions on the fibre are a long way from those we would expect in the industrial crimper. Let us therefore move one step closer by feeding fibre into the box at one end, whilst leaving the other free to rotate (see figure 2.21). Mathematically, we will specify that at $s = 0$

$$\bar{\theta} = 0 \qquad \text{and} \qquad y = \frac{1}{2},$$

and at $s = 1$

$$\bar{\theta}' = 0.$$

It will be natural to then progress to a fibre confined to a wedge.

Once again, we begin by considering the types of section that will make up our final solution. Thankfully, we have only changed the boundary conditions at $s = 0$. So, except for the starting section and unconfined fibre, we can make use of the results from example 1a. Having discussed the changes that must be made, we will join the sections together in the same way as before, and hence produce our graph of $\sqrt{\lambda}$ against $\bar{t}$. Energy minimisation arguments will again be needed to select the solutions that will be observed.

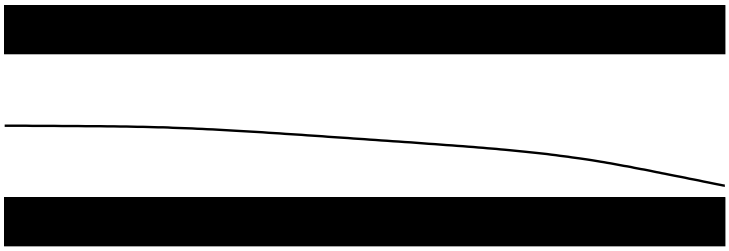


Figure 2.22: Unconfined fibre being fed into a rectangular box midway up the lefthand wall.

2.2.6.1 Section types

1. *Unconfined Fibre (1) (figure 2.22)*

   Once again we will solve equation (2.12) but now we consider a fibre which touches neither the top nor the bottom wall (figure 2.22). Physically, we are treating the right-hand end as free to move vertically as more fibre enters, until it reaches the lower wall. This means that there can be no vertical forces on the fibre and so $\bar{p}_i = 0$. Hence the boundary conditions we will apply are

$$\begin{aligned} \bar{\theta}(0) &= 0 \\ \bar{\theta}'(1) &= 0 \\ \bar{y}(0) &= \frac{1}{2} \\ 0 \leq \bar{y}(r_i) \leq 1 \quad &\text{for} \quad 0 \leq r_i \leq 1 \\ \bar{p}_i &= 0. \end{aligned} \tag{2.49}$$

   Applying these gives

$$\bar{\theta} = A_i \sin \sqrt{\lambda} r_i \qquad \text{and} \qquad \sqrt{\lambda} = \frac{\pi}{2}$$

   Solving (2.13) for $\bar{y}$ we find

$$\bar{y} = \frac{1}{2} + \frac{2A_i}{\pi}\left(1 - \cos \sqrt{\lambda} r_i\right)$$

   and hence in order to satisfy (2.49) we place limits on A_i such that

$$\frac{-\pi}{4} \leq A_i \leq \frac{\pi}{4}$$

   When $A_i = -\pi/4$, the fibre is touching the bottom righthand corner of the box and[12] $\bar{t}$ is trivially found to be $\frac{A_i^2}{8}$. Thus A_i is determined by the amount of fibre that has been fed into the box.

[12] and when $A_i = \pi/4$ the fibre touches the top right hand corner

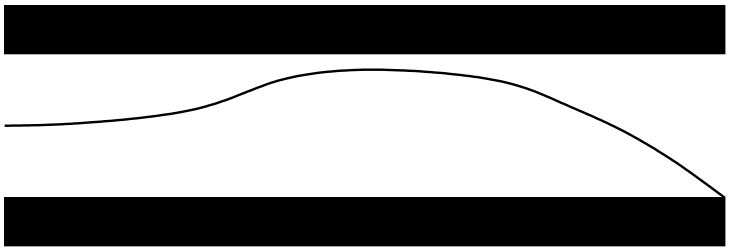


Figure 2.23: The fibre confined only by the bottom wall

2. *Fibre confined by the bottom wall (figure 2.23)*

   This section has the fibre confined only by the bottom wall (see figure 2.23). Now we have another parameter $\bar{p}_i$ to determine, but there is an extra boundary condition at $r_i = 1$ The boundary conditions are

$$\begin{aligned} \bar{\theta}(0) &= 0 \\ \bar{\theta}'(1) &= 0 \\ \bar{y}(0) &= \frac{1}{2} \\ \bar{y}(1) &= 0 \\ \text{with} \quad 0 \le \bar{y}(r_i) \le 1 \quad &\text{for} \quad 0 \le r_i \le 1. \end{aligned} \tag{2.50}$$

   Solving (2.12) for $\bar{\theta}$ we find

$$\bar{\theta} = -\bar{p}_i(\tan\sqrt{\lambda} \cdot \sin\sqrt{\lambda}r_i + \cos\sqrt{\lambda}r_i - 1)$$

   for $\sqrt{\lambda} \ge \frac{\pi}{2}$. Integrating up, we find

$$\bar{y} = \frac{1}{2} - \frac{\bar{p}_i}{\sqrt{\lambda}}\left(\tan\sqrt{\lambda}(1 - \cos\sqrt{\lambda}r_i) + \sin\sqrt{\lambda}r_i - \sqrt{\lambda}r_i\right).$$

   The boundary conditions on $\bar{y}(1)$ fix the value of $\bar{p}_i$ to be

$$-\frac{1}{2}\frac{\sqrt{\lambda}}{\sqrt{\lambda} - \tan\sqrt{\lambda}}$$

   whilst the requirement that the fibre remain in the box (2.50) places an upper bound on λ.[13] Finally, we can calculate $\bar{t}$ as

$$\frac{\sqrt{\lambda}}{4}\frac{4\sqrt{\lambda} + 2\sqrt{\lambda}\cos 2\sqrt{\lambda} - 3\sin 2\sqrt{\lambda}}{16(\sqrt{\lambda}\cos\sqrt{\lambda} - \sin\sqrt{\lambda})^2}$$

   so that in this case λ is determined by the length of fibre in the box.

[13] This comes from solving

$$\bar{y}(r_{max}) = 1$$

where $0 \le r_{max} \le 1$ solves $\bar{\theta}(r_{max}) = 0$

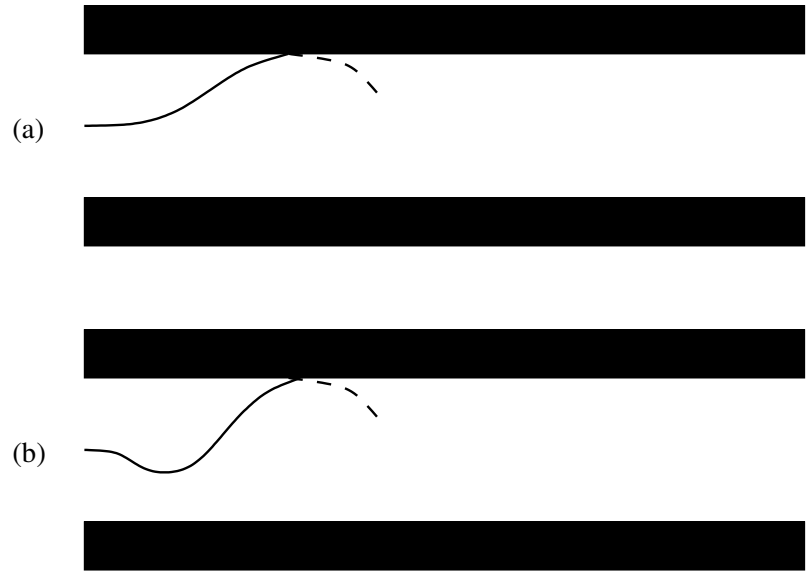


Figure 2.24: The starting section for fibre fed into a rectangular box midway up the lefthand wall

3. *Starting section (figure 2.24)*

   In order to solve a starting section of the type shown in figure 2.24 we apply the boundary conditions

$$\begin{aligned} \bar{\theta}(0) &= 0 \\ \bar{\theta}(d_i) &= 0 \\ \bar{y}(0) &= 0.5 \\ \bar{y}(d_i) &= 0 \text{ or } 1 \\ 0 \leq \bar{y}(r_i) \leq 1 &\qquad 0 \leq r_i \leq d_i. \end{aligned}$$

   The solution depends on how many zeros $\bar{\theta}$ has between the contact points. If none, then the solution is equivalent to a midsection of half the height, analysed as on page 37, so that

$$\bar{\theta} = \bar{p_i} \left(1 - \cos \sqrt{\lambda} r_i - \frac{1 - \cos z_i}{\sin z_i} \sin \sqrt{\lambda} r_i \right),$$

   where $\bar{p_i}$[14] is

$$\pm \frac{1}{2} \left(\frac{\sqrt{\lambda}}{z_i - 2 \tan \frac{z_i}{2}} \right)$$

[14]The positive value correspnds to the solution going to the bottom plate.

as $z_i = \sqrt{\lambda} d_i$. If one now allows the fibre to go downwards before going upwards as shown in (2.24b) (or vice versa), another solution is possible which is

$$\begin{aligned} \bar{\theta} &= \bar{p_i}(1 - \cos\sqrt{\lambda} r) - \alpha\sqrt{\lambda}\sin\sqrt{\lambda} r \\ z_i &= 2\pi \end{aligned} \tag{2.51}$$

where α is an unknown constant ($\alpha \geq 0$). We can integrate to find $\bar{y}$

$$\bar{y}(r_i) = \frac{1}{2} + \frac{\bar{p_i}}{\sqrt{\lambda}}\left(\sqrt{\lambda} r_i - \sin\sqrt{\lambda} r_i\right) - \alpha(1 - \cos\sqrt{\lambda} r_i) \tag{2.52}$$

and $\bar{\delta x}$

$$\bar{\delta x} = \int_0^{d_i} \frac{\bar{\theta}^2}{2} dr_i = \frac{\sqrt{\lambda}}{2}\left(\frac{3}{16\pi} + \pi\alpha^2\right)$$

The requirement that the fibre remains within the box places limits on the values of α allowed. In addition, the equation for $\bar{y}$ allow us to determin $\bar{p_i}$ as

$$\bar{p_i} = \frac{\sqrt{\lambda}}{4\pi}.$$

The value of α will be determined by the global boundary conditions.

2.2.6.2 Summary of the types of Solution

Once again, we can form solutions by piecing together the different sections discussed above and in section 2.2.5.1. They are shown in figure 2.25.

1. *Unconfined Fibre (a)*
   The fibre has touched neither plate, and we have that

   $$\begin{aligned} \sqrt{\lambda} &= \frac{\pi}{2}, \\ \bar{t} &= \frac{A_i^2}{8}. \end{aligned}$$

   This is valid for

   $$-\frac{\pi}{4} \leq A_i \leq 0.$$

2. *Fibre confined at the base (b)*
   The fibre is touching only the lower plate. Varying λ gives various values of $\bar{t}$, with

   $$\frac{\pi}{2} \leq \sqrt{\lambda} \leq \sqrt{\lambda}_{max}$$

   where $\sqrt{\lambda}_{max}$ satisfies the equation

   $$\pi = \frac{3}{2}\sqrt{\lambda}_{max} - \tan\sqrt{\lambda}_{max}.$$

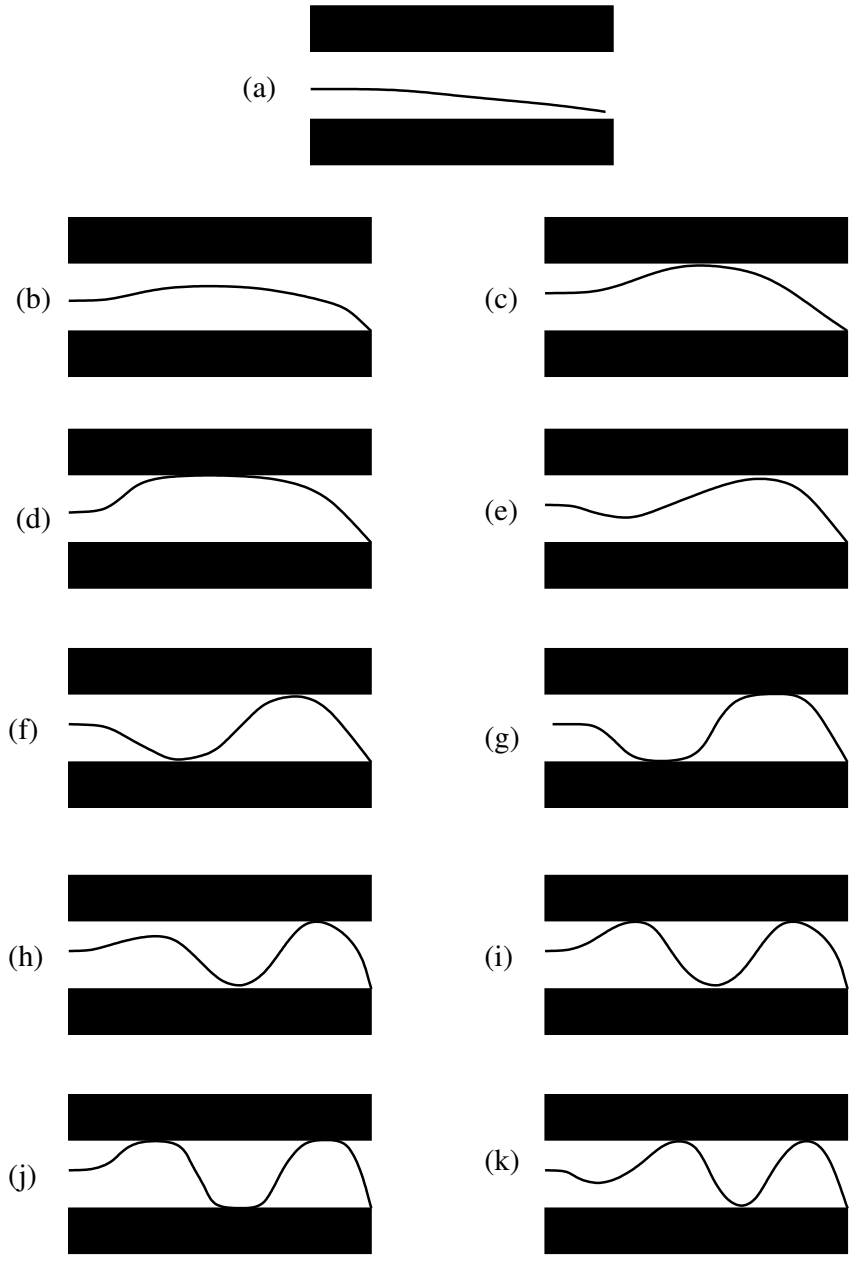


Figure 2.25: Key to figures 2.26 and 2.27 showing the types of solutions found

3. *Fibre with point contact (c), (f) and (i)*
   The fibre is in point contact with the surfaces, and in the first section $\bar{\theta}$ has no zeros between the contact points. If one or more middle sections are present, then
   $$\frac{1}{2}\frac{\tan\frac{z_1}{2}}{z_1 - 2\tan\frac{z_1}{2}} = \frac{\tan\frac{z_{mid}}{2}}{z_{mid} - 2\tan\frac{z_{mid}}{2}}.$$
   The continuity condition at the end is
   $$\frac{1}{2}\frac{\tan\frac{z_1}{2}}{z_1 - 2\tan\frac{z_1}{2}} = \frac{\tan z_N}{z_N - \tan z_N}.$$

4. *Fibre with point contact (e), (h) and (k)*
   The fibre is again in point contact with the surfaces, and $\bar{\theta}$ has a single zero within the starting section. We vary the solution with the parameter α, use the continuity conditions
   $$\alpha = \frac{-\tan z_N}{z_N - \tan z_N}$$
   to match with the end section, and
   $$\alpha = \frac{\tan\frac{z_{mid}}{2}}{z_{mid} - 2\tan\frac{z_{mid}}{2}}$$
   to match with the middle sections.

5. *Fibre containing flat sections (d), (g) and (j)*
   If σ again represents the total flat length, and there are M middle sections then
   $$\sqrt{\lambda} = \frac{(3+2M)\pi}{1-\sigma}$$

2.2.6.3 Results

Figure 2.26 plots $\bar{t}$ against λ for the different types of solution discussed above. Notice the similarity with figure 2.17 which is the same plot for the original geometry. Firstly, see the similarity between dimple solutions in the first geometry and those where the first section has a zero in θ between the contact points.

Once again, we need to resort to energy arguments to decide which solution will be observed in practice. Figure 2.27 shows a plot of energy against $\bar{t}$. Note that, in contrast to example 1a, solutions with a flat section are never energetically favoured.

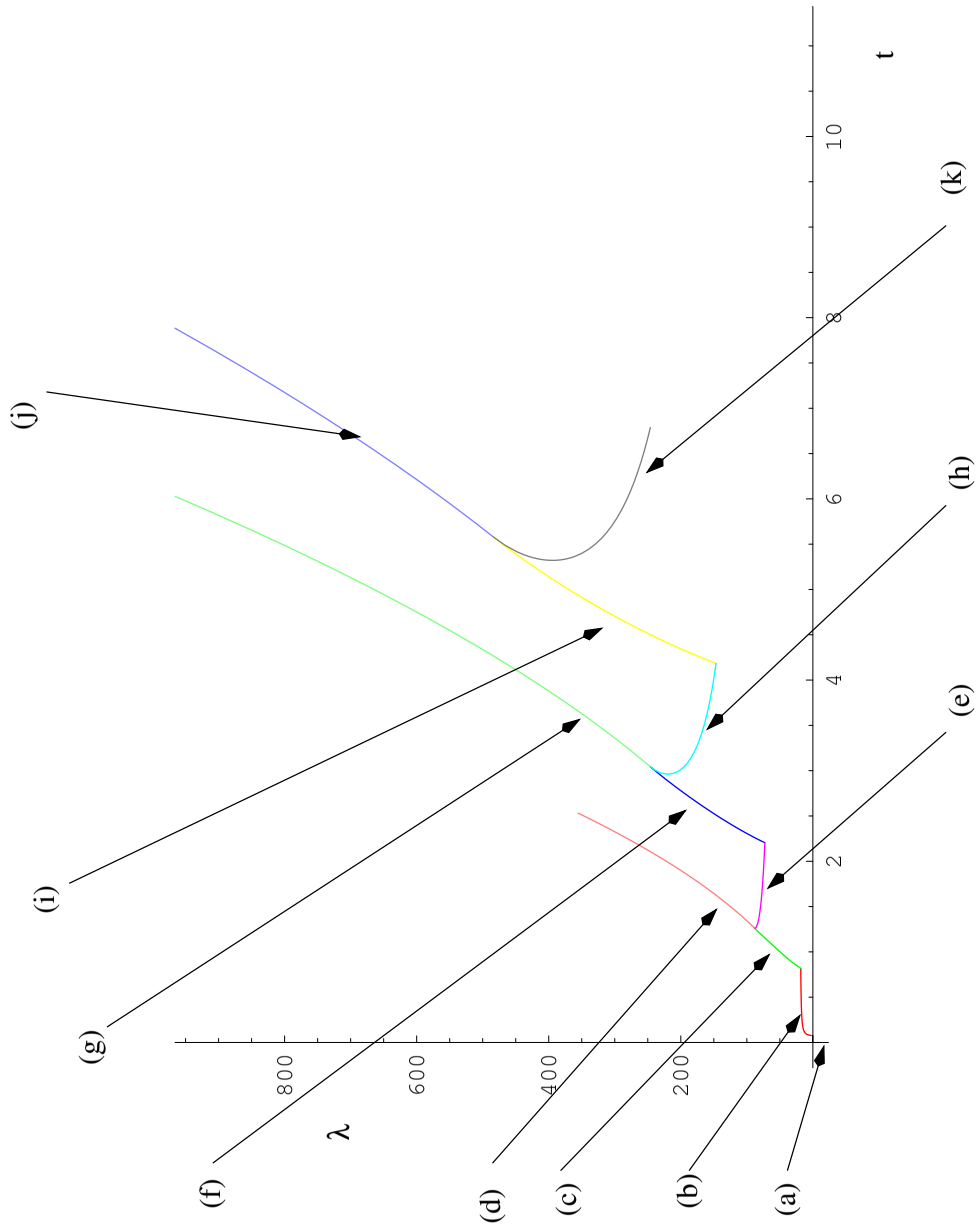


Figure 2.26: $\bar{t}$ vs. λ for a fibre entering midway

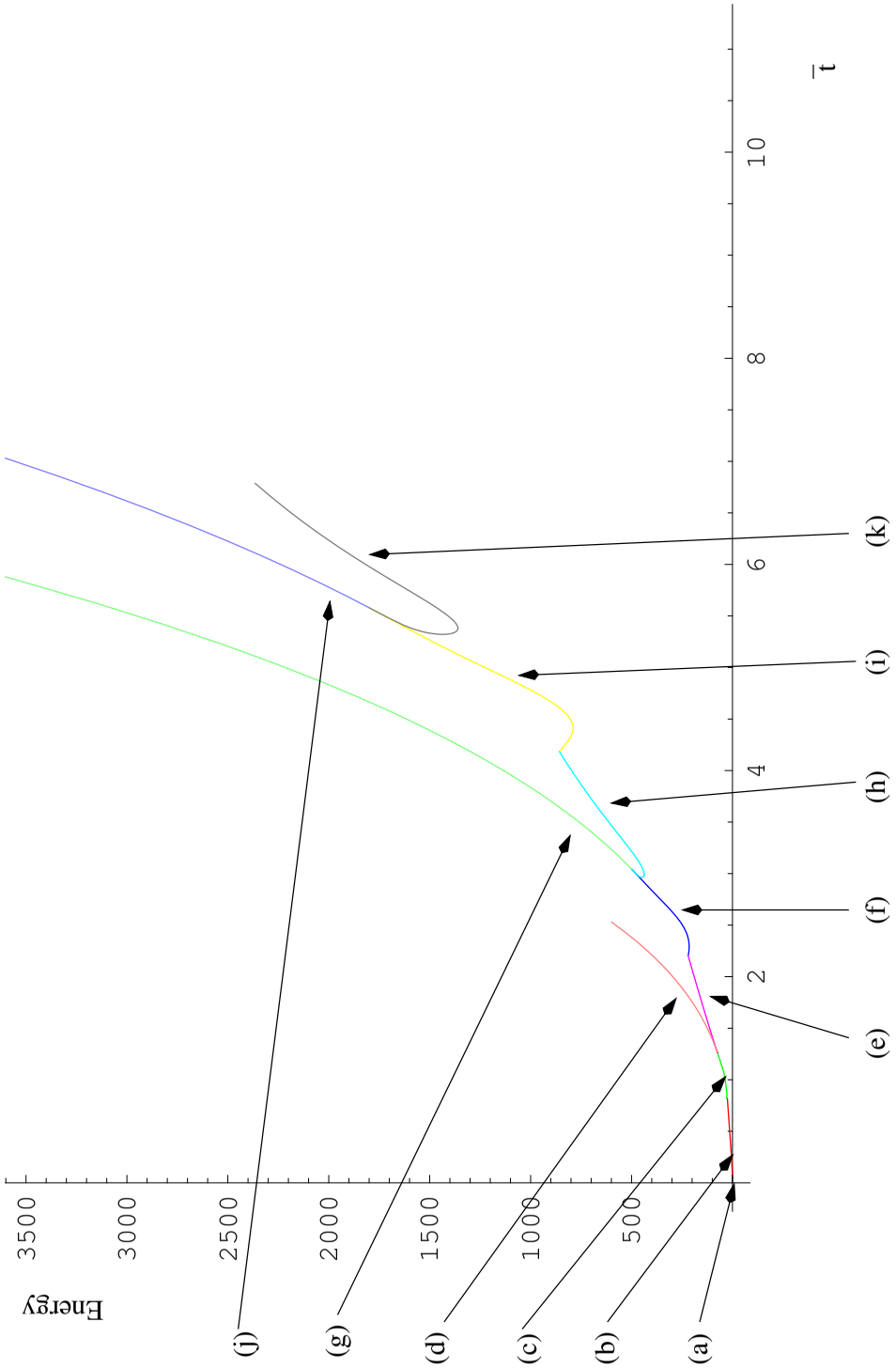


Figure 2.27: Energy vs. $\bar{t}$ for a fibre entering midway

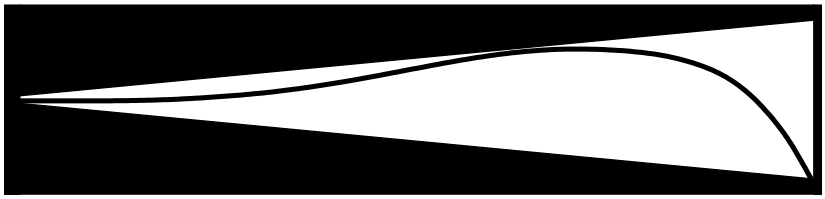


Figure 2.28: Geometry for a fibre in a wedge

2.2.7 Example 2: Fibre confined in a narrow wedge

We will now consider the more relevant geometry of a fibre entering a wedge, as shown in figure 2.28. This is a similar configuration to that encountered in the crimping machine, where fibre enters into the nip region between the two rollers. We will begin by discussing the types of behaviour possible between the contact points. From these, we will form solutions in much the same way as before, once again making use of any symmetry to simplify the problem. Finally we will discuss the results for this model and compare them to those for the rectangular box geometries.

We use the same scalings as before and take the walls of the wedge to be at

$$y = \frac{1}{2} \pm \frac{1}{2}x;$$

thus the wedge is of small angle and we can continue to use the linear approximation.

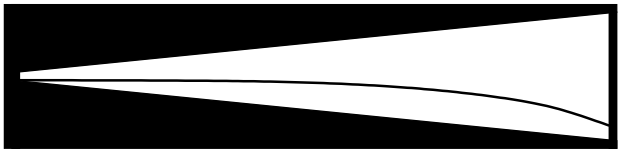


Figure 2.29: The unconfined fibre in a wedge

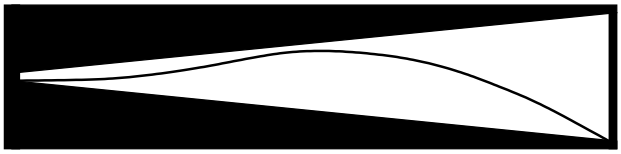


Figure 2.30: The fibre confined by the bottom surface of a wedge

2.2.8 Section Types

We will now consider the types of behaviour that can be exhibited by the fibre between contact points.

1. *Unconfined Fibre (figure 2.29)*
   See figure 2.29. The boundary conditions and equations are the same as for the unconfined fibre for example 1b (see page 52).

2. *Fibre confined by the base (figure 2.30)*
   The boundary conditions are the same as for example 1b, page 53 except that the upper bound on λ needs to be changed. To do so, we must first realise that for contact just to occur, $\bar{\theta} = 1/2$. If this occurs at the point $\sqrt{\lambda} r_i = \zeta_{1/2}$, then we wish to solve

   $$\frac{\zeta_{1/2}}{2} = \bar{p}_i \left(\tan\sqrt{\lambda} \cdot (1 - \cos\zeta_{1/2}) + \sin\zeta_{1/2} + \zeta_{1/2} \right)$$

   to find the maximum $\sqrt{\lambda}$. When this is reached, the fibre has touched the the top surface, and we shall need a new type of solution.

3. *Starting section (figure 2.31)*
   The starting wedge has the following boundary conditions:

   $$\begin{aligned} \bar{\theta}(0) &= 0 \\ \bar{\theta}(d_i) &= \frac{1}{2} \\ \bar{y}(0) &= \frac{1}{2} \\ \bar{y}(d_i) &= \frac{1}{2} + \frac{d_i}{2} \end{aligned}$$

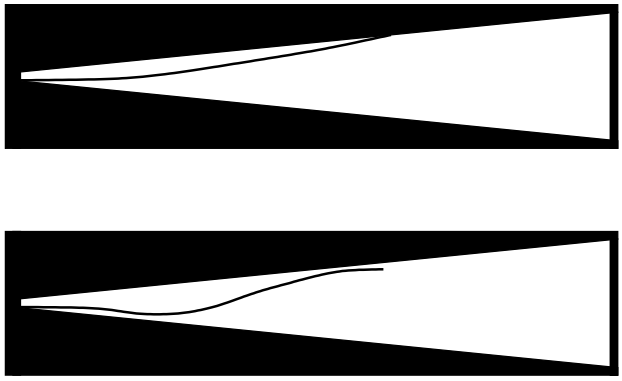


Figure 2.31: Starting section for a fibre in a wedge

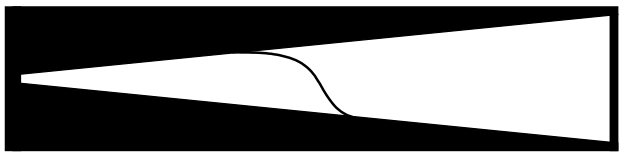


Figure 2.32: The mid section for a wedge

$$\frac{1}{2} - \frac{r_i}{2} \leq \bar{y}(r_i) \leq \frac{1}{2} + \frac{r_i}{2} \qquad 0 \leq r_i \leq d_i.$$

The boundary condition for $\bar{y}(d_i)$ fixes the value of $\bar{p_i}$ to be

$$\bar{p_i} = \frac{1}{2} \frac{\tan z_i/2 - z_i}{z_i - 2\tan z_i/2}.$$

The condition that the fibre remains within the wedge will fix the maximum value of z_i. As with the fibre confined only by the bottom plate, we need to find the point of contact with the wedge wall, which occurs at position c_i where $\bar{\theta} = 1/2$. The maximum value of z_i satisfies the condition

$$\bar{y}(c_i) = \frac{1}{2} + \frac{c_i}{2}.$$

4. *Middle section (see figure 2.32)*

   The mid section has the following boundary conditions

$$\begin{aligned} \bar{\theta}(0) &= -\frac{1}{2} \\ \bar{\theta}(d_i) &= \frac{1}{2} \\ \bar{y}(0) &= -y_0 \\ \bar{y}(d_i) &= 2y_0 + \frac{d_i}{2} \end{aligned}$$

   and the analysis proceeds much as before.

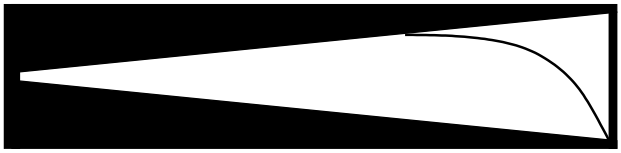


Figure 2.33: The ending section for a wedge

5. *End Section (see figure 2.33)*
   The end section has the following boundary conditions applied

$$\begin{aligned} \bar{\theta}(0) &= \frac{1}{2} \\ \bar{\theta}'(d_i) &= 0 \\ \bar{y}(0) &= y_0 \\ \bar{y}(d_i) &= -\left(2y_0 + \frac{d_i}{2}\right) \end{aligned}$$

   and the analysis is similar to the earlier end section.

2.2.9 Results

The analysis of these section types, and the continuity conditions, proceed much as before. Once again, the symmetry present means that λ can be determined at the end, as

$$\sqrt{\lambda} = \sum_i z_i.$$

In addition, we can eliminate λ from both the joining conditions and boundary conditions on the section types. Figure 2.34 shows the results of this analysis with a plot of applied force against excess fibre. Note that there is less of a drop in λ as $\bar{t}$ is increased at the transition points (see figure 2.26).

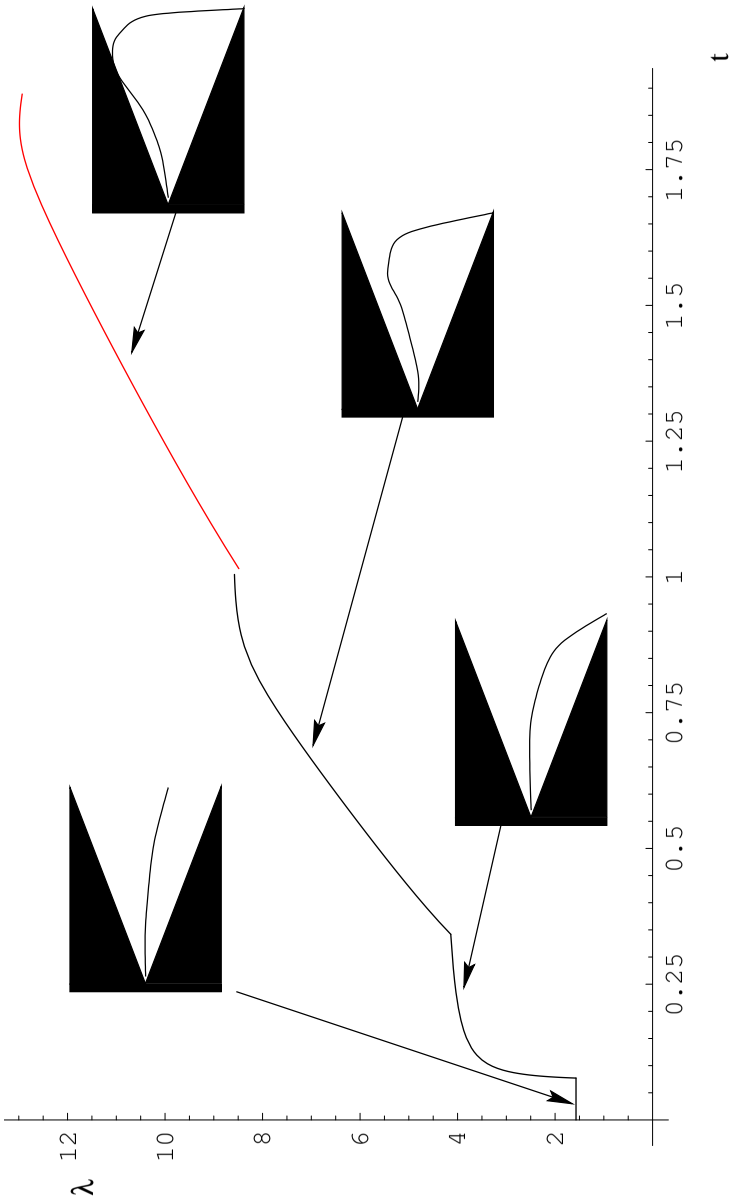


Figure 2.34: λ against $\bar{t}$ for a fibre in a wedge

2.3 3D Confined Fibre

So far, our models for the fibre as it enters the crimper have concentrated on the relationship between the forces exerted on the fibre and the extra length we have added. They have not given any insight into another important physical property, the three-dimensional nature of crimp. That is observed experimentally. If you take a selection of tow as it comes out of the industrial crimper and examine a number of fibres, you will see sections where the crimp is vertical, others where it is at some slanted angle and still more when it forms a helix (see figure 2.35). The different types of crimp may even be seen on the same fibre. For many applications, it is important to know the amount of three dimensional crimp.[15] Therefore some understanding as to what causes the different configurations would be useful. To this end, we shall attempt to extend the ideas we used to discuss two dimensional crimp and apply them when the fibre has an extra direction in which to deform.

Our model problem will be a fibre confined between two horizontal plates. These it can touch at multiple points (or over a region). At each end of the fibre we will apply no moments, just equal and opposite thrusts along the undeformed direction (see figure 2.36). The idea in this is to be as close to the configuration of the two-dimensional example 1a (page 35) as is possible. We will begin by discussing the equations of an elastica in three dimensions. We will then linearise these for the case of small deflections. Under these circumstances the deformations in each of the principle directions of the fibre are independent. This will allow us to use a very similar method to solve the problem as we employed for the two-dimensional crimp. Once again, we will produce plots of how the force varies with the amount of fibre entering and discuss which configurations are observed in practice.

2.3.1 The equations of an elastica in three dimensions

[16] Let the position of the fibre in the channel be denoted by $\mathbf{r}(s)$ where s is the distance along the elastica. The orientation of the cross-section of the fibre is given by the orthonormal vector pair $\mathbf{d}_1(s)$ and $\mathbf{d}_2(s)$, where $\mathbf{d}_1$ and $\mathbf{d}_2$ point along the directions of the principle axes of the cross-section. We obtain the following relationship between

[15] One use of crimped fibre is to make the filters for cigarettes. The more three dimensional the crimp, the more tortuous the path through the filter and the more chemicals removed.

[16] From Love[10]

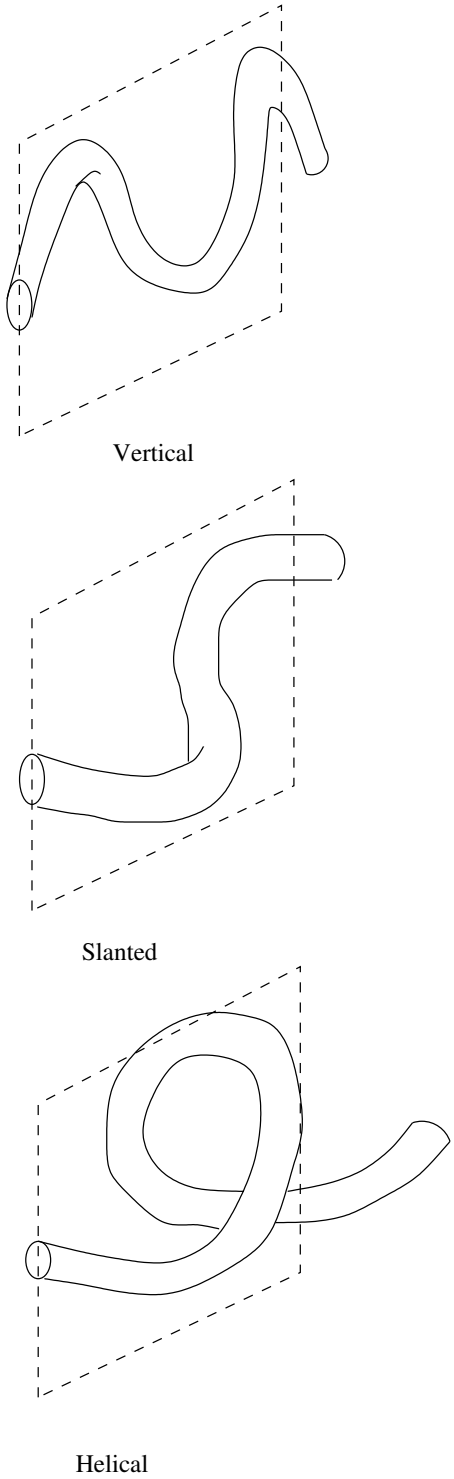


Figure 2.35: Observed 3d crimp formations

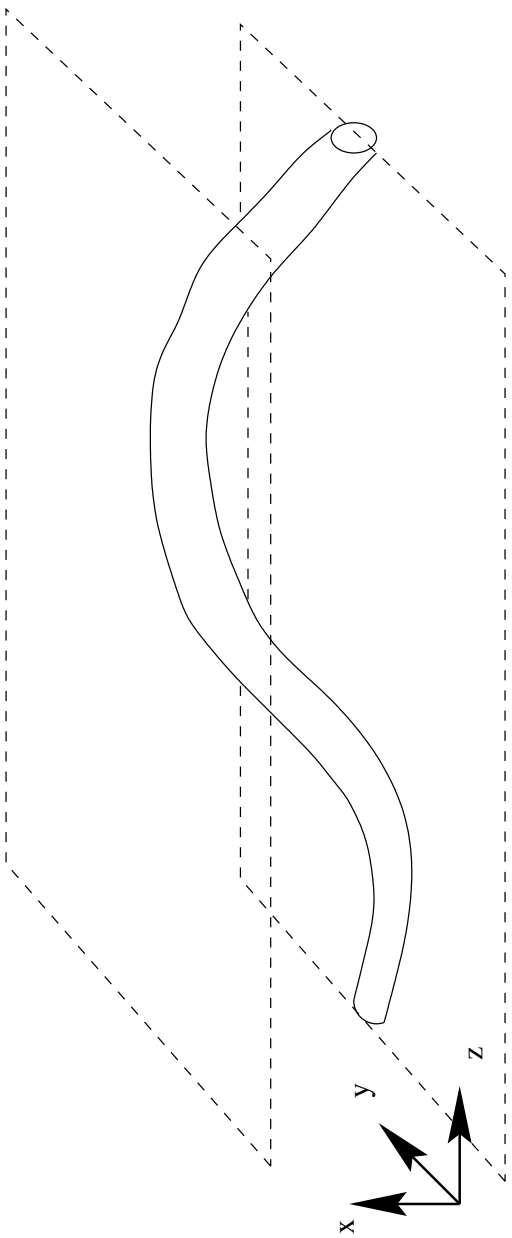


Figure 2.36: A three dimensional elastica confined in a narrow channel

the position of the fibre and the orientation

$$\mathbf{r}'(s) = \mathbf{d}_3(s) = -\mathbf{d}_1 \times \mathbf{d}_2. \tag{2.53}$$

As the triad $\{\mathbf{d}_k\}$ is orthonormal, there exists a vector $\mathbf{u}$, called the curvature vector, such that

$$\mathbf{d}_k' = \mathbf{u} \times \mathbf{d}_k$$

and we choose to write this vector in the form

$$\mathbf{u} = u_k \mathbf{d}_k.$$

Let $\mathbf{m}(s)$ be the internal moment within the fibre at point s, and $\mathbf{n}(s)$ the internal force. By balancing forces and moments, and in the absence of body forces and applied moment loads we find

$$\begin{aligned} \mathbf{m}' + \mathbf{r}' \times \mathbf{n} &= \mathbf{0} \\ \mathbf{n}' &= \mathbf{0} \end{aligned} \tag{2.54}$$

The last equation shows that $\mathbf{n}$ is determined by the external forces. We now choose to write that

$$\mathbf{m} = m_k \mathbf{d}_k$$

and assume the following linear constitutive relations

$$\begin{aligned} u_1 &= \sigma_1 m_1, \\ u_2 &= \sigma_2 m_2, \\ u_3 &= \sigma_3 m_3 \end{aligned}$$

where the σ_i are constant[17]. For an arbitrary cross section, these constants may all be different. Rearranging and combining with (2.54) we find

$$m_1' + (\sigma_2 - \sigma_3) m_2 m_3 - \mathbf{n} \cdot \mathbf{d}_2 = 0, \tag{2.55}$$

$$m_2' + (\sigma_3 - \sigma_1) m_3 m_1 + \mathbf{n} \cdot \mathbf{d}_1 = 0, \tag{2.56}$$

$$m_3' + (\sigma_1 - \sigma_2) m_1 m_2 = 0. \tag{2.57}$$

A similar set of substitutions gives that

$$\mathbf{d}_1' = -\sigma_2 m_2 \mathbf{d}_3 + \sigma_3 m_3 \mathbf{d}_2 \tag{2.58}$$

$$\mathbf{d}_2' = -\sigma_3 m_3 \mathbf{d}_1 + \sigma_1 m_1 \mathbf{d}_3 \tag{2.59}$$

$$\mathbf{d}_3' = -\sigma_1 m_1 \mathbf{d}_2 + \sigma_2 m_2 \mathbf{d}_1. \tag{2.60}$$

We therefore have 6 vector quantities ($\mathbf{r}$, $\mathbf{d}_1$, $\mathbf{d}_2$, $\mathbf{u}$, $\mathbf{m}$ and $\mathbf{n}$) and six vector equations describing their evolution.

[17] In Love's Notation, $\sigma_1^{-1} = EI_A$, $\sigma_2^{-1} = EI_B$ and $\sigma_3^{-1} = C$

2.3.2 Relationship with the co-ordinates in fixed space

Let the fixed coordinates be denoted by $\{x, y, z\}$ where the z-axis lies along the undeformed fibre. The position of the fibre in the channel is hence written as

$$\mathbf{r} = \begin{pmatrix} x \\ y \\ z \end{pmatrix}.$$

Let the undeformed fibre be aligned such that

$$\mathbf{d}_1 = \begin{pmatrix} \sin\phi \\ \cos\phi \\ 0 \end{pmatrix} \quad \mathbf{d}_2 = \begin{pmatrix} \cos\phi \\ -\sin\phi \\ 0 \end{pmatrix} \quad \mathbf{d}_3 = \begin{pmatrix} 0 \\ 0 \\ 1 \end{pmatrix}.$$

2.3.3 Boundary conditions

We will assume the boundary conditions that are equivalent to those used to describe example 1a, a fibre confined to a box (see page 35) whose walls are located at $x = 0,\ \epsilon Z_b$, where ϵ is small. Firstly, we will assume that the ends of the fibre are both free to rotate, such that they exert no moment on the fibre. Hence

$$m_1(s) = m_2(s) = m_3(s) = 0 \ \text{ when } \ s = 0, L.$$

Secondly, we will require that at the contact points, $\mathbf{m}$ and $\mathbf{d}$ are continuous. Finally, at a boundary point, the fibre lies along the boundary, so

$$x'(s) = 0.$$

2.3.4 Non-dimensionalisation

We choose similar non-dimensionalisations as for the 2d problem (see page 30), choosing Z_b (the length of the box) as a typical length scale, σ_1 as a typical beam constant and obtaining other typical dimensions from suitable combinations of these such that

$$\begin{aligned} L &= Z_b(1+2t) \\ \mathbf{n} &= \frac{1}{\sigma_1 Z_b^2}\hat{\mathbf{n}} \\ m_k &= \frac{1}{\sigma_1 Z_b}\hat{m_k} \\ \sigma_2 &= \sigma_1\hat{\sigma_2} \\ \sigma_3 &= \sigma_1\hat{\sigma_3}. \end{aligned}$$

We will also assume that the fibre has only a small deflection from its original direction so

$$\begin{aligned} x &= \epsilon Z_b \hat{x} \\ y &= \epsilon Z_b \hat{y} \\ z &= Z_b \hat{z}. \end{aligned}$$

Our equations (2.55)-(2.60) become

$$\begin{aligned} \hat{m_1'} + (\hat{\sigma_2} - \hat{\sigma_3})\hat{m_2}\hat{m_3} - \hat{\mathbf{n}} \cdot \mathbf{d}_2 &= 0, \\ \hat{m_2'} + (\hat{\sigma_3} - 1)\hat{m_3}\hat{m_1} + \hat{\mathbf{n}} \cdot \mathbf{d}_1 &= 0, \\ \hat{m_3'} + (1 - \hat{\sigma_2})\hat{m_1}\hat{m_2} &= 0, \end{aligned}$$

and

$$\begin{aligned} \frac{d\mathbf{d}_1}{d\hat{s}} &= -\hat{\sigma_2}\hat{m_2}\mathbf{d}_3 + \hat{\sigma_3}\hat{m_3}\mathbf{d}_2 \\ \frac{d\mathbf{d}_2}{d\hat{s}} &= -\hat{\sigma_3}\hat{m_3}\mathbf{d}_1 + \hat{m_1}\mathbf{d}_3 \\ \frac{d\mathbf{d}_3}{d\hat{s}} &= -\hat{m_1}\mathbf{d}_2 + \hat{\sigma_2}\hat{m_2}\mathbf{d}_1. \end{aligned} \tag{2.61}$$

2.3.5 Linearisation

We will now seek to solve these equations with an externally applied compressive force (of non-dimensional magnitude λ) and with a small component in the x direction. Writing this in non-dimensional terms (having droped the $\hat{}$s) as

$$\mathbf{n} = \begin{pmatrix} -\epsilon a \lambda \\ 0 \\ -\lambda \end{pmatrix}$$

we now expand each property as a series around the undeformed state of the rod. Hence

$$\begin{aligned} m_1 &= \epsilon m_{11} + O(\epsilon^2) \\ m_2 &= \epsilon m_{21} + O(\epsilon^2) \\ m_3 &= \epsilon m_{31} + O(\epsilon^2) \\ \mathbf{d}_1 &= \begin{pmatrix} \sin\phi \\ \cos\phi \\ 0 \end{pmatrix} + \epsilon \mathbf{d}_{11} + O(\epsilon^2) \end{aligned}$$

$$\begin{aligned}
\mathbf{d}_2 &= \begin{pmatrix} \cos\phi \\ -\sin\phi \\ 0 \end{pmatrix} + \epsilon \mathbf{d}_{21} + O(\epsilon^2) \\
\mathbf{d}_3 &= \begin{pmatrix} 0 \\ 0 \\ 1 \end{pmatrix} + \epsilon \mathbf{d}_{31} + \epsilon^2 \mathbf{d}_{32} + O(\epsilon^3)
\end{aligned}$$

Substituting into the equations for m_k and d_k we find that, to order ϵ

$$\begin{aligned}
m'_{11} + \lambda\gamma_{21} + a\lambda\cos\phi &= 0 \qquad (2.62) \\
m'_{21} - \lambda\gamma_{11} - a\lambda\sin\phi &= 0 \qquad (2.63) \\
m'_{31} &= 0
\end{aligned}$$

and

$$\begin{aligned}
\mathbf{d}'_{11} &= -\sigma_2 m_{21}\mathbf{d}_{30} + \sigma_3 m_{31}\mathbf{d}_{20} \\
\mathbf{d}'_{21} &= -\sigma_3 m_{31}\mathbf{d}_{10} + m_{11}\mathbf{d}_{30} \\
\mathbf{d}'_{31} &= -m_{11}\mathbf{d}_{20} + \sigma_2 m_{21}\mathbf{d}_{10}
\end{aligned}$$

where

$$\mathbf{d}_{k1} = \begin{pmatrix} \alpha_{k1} \\ \beta_{k1} \\ \gamma_{k1} \end{pmatrix}$$

As m_{31} is constant along the section and continuous at contact points we can immediately see that $m_{31} = 0$ everywhere. This in turn implies that

$$\alpha'_{11} = \beta'_{11} = \alpha'_{21} = \beta'_{21} = 0 \qquad (2.64)$$

and hence the equations simplify further to :

$$\begin{aligned}
\gamma'_{11} &= -\sigma_2 m_{21} \qquad (2.65) \\
\gamma'_{21} &= +m_{11} \qquad (2.66) \\
\mathbf{d}'_{31} &= -m_{11}\mathbf{d}_{20} + \sigma_2 m_{21}\mathbf{d}_{10} \qquad (2.67)
\end{aligned}$$

Realising from (2.53) that

$$\mathbf{d}'_{31} = -\left(\mathbf{d}'_{11} \times \mathbf{d}_{20} + \mathbf{d}_{10} \times \mathbf{d}'_{21}\right)$$

and hence integrating and making the substitutions $\mathbf{d}_{11} = \gamma_{11}\mathbf{d}_{30}$, $\mathbf{d}_{21} = \gamma_{21}\mathbf{d}_{30}$[18] we find

$$\mathbf{d}_{31} = -\gamma_{11}\mathbf{d}_{30} \times \mathbf{d}_{20} - \gamma_{21}\mathbf{d}_{10} \times \mathbf{d}_{30}$$

[18]This comes from integrating (2.64)

As $\{\mathbf{d}_k\}$ are orthogonal, this in turn simplifies to

$$\mathbf{d}_{31} = -\gamma_{11}\mathbf{d}_{10} - \gamma_{21}\mathbf{d}_{20} \tag{2.68}$$

Writing that

$$\mathbf{r}' = \mathbf{r}'_0 + \epsilon\mathbf{r}'_1$$

and remembering the relationship to the fibre orientation (2.53) we find

$$\frac{dx_0}{ds} = 0, \quad \frac{dy_0}{ds} = 0, \quad \frac{dz_0}{ds} = 1.$$

$$\begin{pmatrix} x'_1 \\ y'_1 \\ z'_1 \end{pmatrix} = -\gamma_{11}\begin{pmatrix} \sin\phi \\ \cos\phi \\ 0 \end{pmatrix} - \gamma_{21}\begin{pmatrix} \cos\phi \\ -\sin\phi \\ 0 \end{pmatrix}. \tag{2.69}$$

2.3.6 Boundary Condition at $s = 1 + 2t$

As with the two dimensional fibre, we require that at $s = 1 + 2t$, $z = 1$ (i.e. the fibre fills the box). We can rewrite this as

$$\int_0^{1+2t} \mathbf{d}_3 \cdot \begin{pmatrix} 0 \\ 0 \\ 1 \end{pmatrix} ds = 1.$$

Now let us use the series expansion for $\mathbf{d}_3$, and write

$$\int_0^{1+2t} \left(\mathbf{d}_{30} - \epsilon\gamma_{21}\mathbf{d}_{20} - \epsilon\gamma_{11}\mathbf{d}_{10} + \epsilon^2\mathbf{d}_{32}\right) \cdot \begin{pmatrix} 0 \\ 0 \\ 1 \end{pmatrix} ds = 1.$$

Collecting terms, we see that this can only be satisfied if

$$t = \epsilon^2\bar{t}$$

and

$$\int_0^1 \mathbf{d}_{32} \cdot \begin{pmatrix} 0 \\ 0 \\ 1 \end{pmatrix} ds = -2\bar{t}. \tag{2.70}$$

Consider the second order expansion of (2.61). This can be written as

$$\mathbf{d}'_{32} = -m_{11}\mathbf{d}_{21} - m_{12}\mathbf{d}_{20} + \sigma_2 m_{21}\mathbf{d}_{11} + \sigma_2 m_{22}\mathbf{d}_{10}.$$

Taking the dot product of each side with the unit vector in the z direction and using the results for $\mathbf{d}_{21}$ and $\mathbf{d}_{11}$ this simplifies to

$$\mathbf{d}'_{32} \cdot \begin{pmatrix} 0 \\ 0 \\ 1 \end{pmatrix} = -\gamma_{21}\gamma'_{21} - \gamma_{11}\gamma'_{11}.$$

Integrating twice and substituting into (2.70) we arrive at

$$2\bar{t} = \int_0^1 \frac{\gamma_{11}^2}{2} + \frac{\gamma_{21}^2}{2} ds.$$

2.3.7 Summary of Linearized Equations

Hence using (2.65) to eliminate m_{11} and m_{21} from (2.62) and (2.63) we reach the linearized equations we will be solving for γ_{11}, γ_{21}, x_1' and y_1':

$$\gamma_{21}'' + \lambda\gamma_{21} + a\lambda\cos\phi = 0, \tag{2.71}$$

$$\gamma_{11}'' + \sigma_2\lambda\gamma_{11} + a\sigma_2\lambda\sin\phi = 0, \tag{2.72}$$

and

$$x_1' = -\gamma_{11}\sin\phi - \gamma_{21}\cos\phi, \tag{2.73}$$

$$y_1' = -\gamma_{11}\cos\phi + \gamma_{21}\sin\phi. \tag{2.74}$$

At the free ends, we apply no moments, but will apply sufficient twist to fix the angle of inclination. At the contact point, the fibre must be tangent to the surface, and there will be no moment applied. Hence at $s = 0, 1$

$$\gamma_{11}' = \gamma_{21}' = 0 \tag{2.75}$$

and at the contact points

$$\gamma_{11}\sin\phi + \gamma_{21}\cos\phi = 0, \tag{2.76}$$

$$[\gamma_{k1}']_-^+ = 0, \tag{2.77}$$

$$[\gamma_{k1}]_-^+ = 0. \tag{2.78}$$

In addition, we have the global boundary condition

$$\bar{t} = \frac{1}{4}\int_0^1 \gamma_{11}^2 + \gamma_{21}^2 ds. \tag{2.79}$$

We will now solve these equations for simple geometries.

2.3.8 3D Confined Fibre : Results

We will now consider solutions of equations (2.71)-(2.74) with boundary conditions at the ends of no applied moments (2.75). If contact points exist, they will satisfy the conditions on tangency and continuity (2.76)-(2.78). Without loss of generality, we can choose that

$$\sigma_2 \leq 1.$$

Let us begin by considering the initial deformation of the fibre before it makes contact with any surface. This has no normal force acting on it, so $a = 0$. In addition, we imagine that we are prescribing $\bar{t}$ (the amount of excess fibre fed into the box), but not the compressive force λ. First consider the equation for γ_{21}. This has the general solution (with $a = 0$) of

$$\gamma_{21} = A \sin \sqrt{\lambda} s + B \cos \sqrt{\lambda} s.$$

In order to satisfy the boundary conditions (2.75) non-trivially we require that

$$A = 0 \quad \text{and} \quad B \sin \sqrt{\lambda} = 0.$$

Similarily for γ_{11} (2.72)

$$\gamma_{11} = \alpha \sin \sqrt{\bar{\lambda}} s + \beta \cos \sqrt{\bar{\lambda}} s$$

with

$$\alpha = 0 \quad \text{and} \quad \beta \sin \sqrt{\bar{\lambda}} = 0$$

where

$$\bar{\lambda} = \sigma_2 \lambda.$$

These conditions have three possible outcomes, depending on the value of σ_2:

$\sigma_2 = 1$	The elastica has no prefered direction in which to buckle. Any direction will be the consequence of inhomogeneities in the enviroment or the elastica itself. The amplitude is determined by the value of $\bar{t}$.
$\sigma_2 = m^2/n^2$	for some pair of integers m,n ($m < n$). Buckles can occur in both directions, and $\lambda = n^2\pi^2$. As for the Euler-strut, the amplitudes of the buckles are again determined by the value of $\bar{t}$. Once again, the values are not unique (as $\bar{t} \propto B^2 + \beta^2$).
Otherwise	The elastica will buckle in only one direction. As $\sigma_2 < 1$, the most energetically favourable buckle will be that which occurs for the lowest λ, and hence the fibre will buckle in the "easiest" direction (hence $\beta = 0$). Again, the amplitude of the buckle must be determined by the value of $\bar{t}$.

2.3.8.1 Normal contact $\phi = 0$

We will now consider what happens when contact has occured. Our first case considered will be that of normal contact between the fibre and the plate, that is $\phi = 0$. We shall also assume that $\sigma_2 < 1$, so that we imagine that the fibre has buckled in the x direction until it has touched the top surface. It is now necessary to determine the value of a, but as we know that the fibre is touching the top surface we can can use the equations for the position of the fibre in the channel (2.73) to fix its value[19].

We will be solving the following pair of equations

$$\begin{aligned} \gamma_{21}'' + \lambda\gamma_{21} + a\lambda &= 0 \\ \gamma_{11}'' + \sigma_2\lambda\gamma_{11} &= 0 \end{aligned} \tag{2.80}$$

with boundary conditions

$$\begin{aligned} \gamma_{21}'(0) = \gamma_{21}'(1) &= 0 \\ \gamma_{11}'(0) = \gamma_{11}'(1) &= 0 \end{aligned} \tag{2.81}$$

at the ends, and at the contact point the free boundary conditions

$$\gamma_{21} = 0 \tag{2.82}$$

$$[\gamma_{21}']_-^+ = [\gamma_{21}]_-^+ = 0 \tag{2.83}$$

$$[\gamma_{11}']_-^+ = [\gamma_{11}]_-^+ = 0$$

Now let us make use of the work we have already done for the two dimensional elastica. Look at equations (2.80), (2.81), (2.82) and (2.83). These describe the same system as for example 1a on page 35. We will therefore make full use of these solutions in solving the problem. The remaining equations describe an unconfined euler strut, whose solutions are once again well known. Realising that if $\bar{t}_{confined}$ and $\bar{t}_{Free}$ are the values of $\bar{t}$ for the two dimensional confined elastica and the two dimensional Euler strut respectively, then

$$\begin{aligned} \bar{t}_{3d} &= \int_0^1 \tfrac{\gamma_{11}^2}{2} ds + \int_0^1 \tfrac{\gamma_{21}^2}{2} ds, \\ &= \bar{t}_{Free} + \bar{t}_{confined} \end{aligned} \tag{2.84}$$

It is simple to modify the plots of λ vs. $\bar{t}$ to include this effect, as shown in figure 2.37 (for which we have taken $\sigma_2 = \sqrt{2}/5$) Two curves are plotted. The first (black, dashed

[19]This is the same technique we used to calculate the value of $\bar{p}_i$ for the starting section for example 1a (see page 37)

line), has deformation only in the y direction, and hence corresponds to the first mode of buckle for the second direction. The second curve (red, dashed) is the same mode superimposed on the solution of the two dimensional problem.

2.3.8.2 Energy in three dimensions

We have created a new type of solution. Now we need to find out if it is energetically favoured. In section 2.2.5.3 we noted that the energy stored in the two dimensional elastica was given by

$$Energy = EI \int_0^L \frac{\theta'^2}{2} ds.$$

In a similar manner, and making the connection that $EI = \sigma_1^{-1}$ we have for the three dimensional elastica

$$Energy = \sum_{k=1}^{3} \sigma_k \int_0^L \frac{m_k^2}{2} ds.$$

Rewriting this in terms of the non-dimensional, linearised quantities we have

$$Energy = \int_0^1 \frac{{\gamma'_{21}}^2}{2} ds + \frac{1}{\sigma_2} \int_0^1 \frac{{\gamma'_{11}}^2}{2} ds. \tag{2.85}$$

Again, this has the components from the confined elastica and free elastica added together, and it is therefore simple to modify our plots of $\log(Energy)$ vs. $\bar{t}$ to show this (see figure 2.38). Note how, for $\sigma_2 = 0.25$ the 3d configuration is energetically favoured. This suggests that for even moderately non-circular cross-sections the fibre adopts a crimp with components in the third direction.

We can also plot the position of the fibre as shown in figure 2.39. Notice how the fibre is slanted rather than helical.[20]. We will now look more closely at this type of configuration for a more general orientation of the fibre ($0 < \phi < \pi/2$).

2.3.8.3 General Fibre Orientation - Single contact Point

We will now solve the model, (2.71)-(2.78), for the case of a single contact point ($\lambda > \pi^2$). In the same way as we solved the earlier, two-dimensional, problems, we will divide the fibre into sections before and after the contact point and solve in these regions separately. We will then apply the matching conditions to produce a solution.

[20]This would not be the case if we had observed the second buckling mode for γ_{11}, however this occurs for higher λ

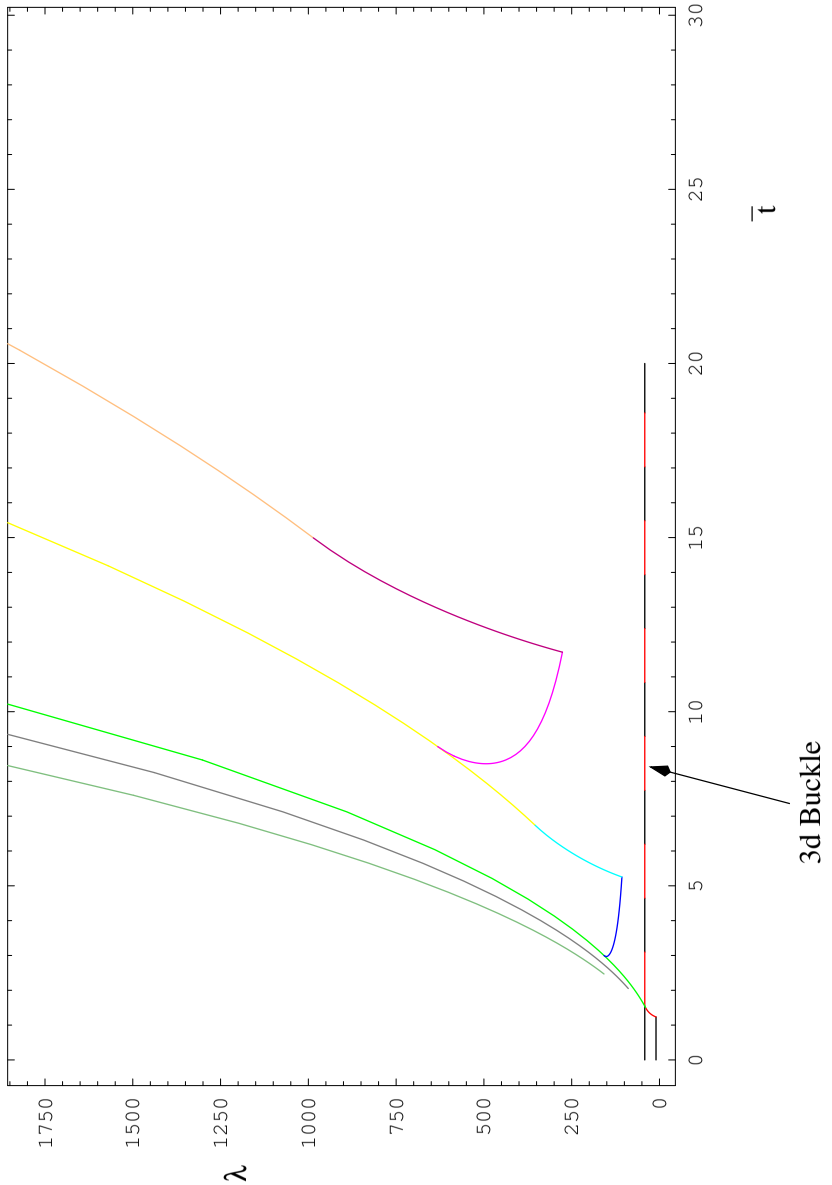


Figure 2.37: λ vs. $\bar{t}$ for a 3d elastica, $\sigma_2 = \sqrt{2}/5$

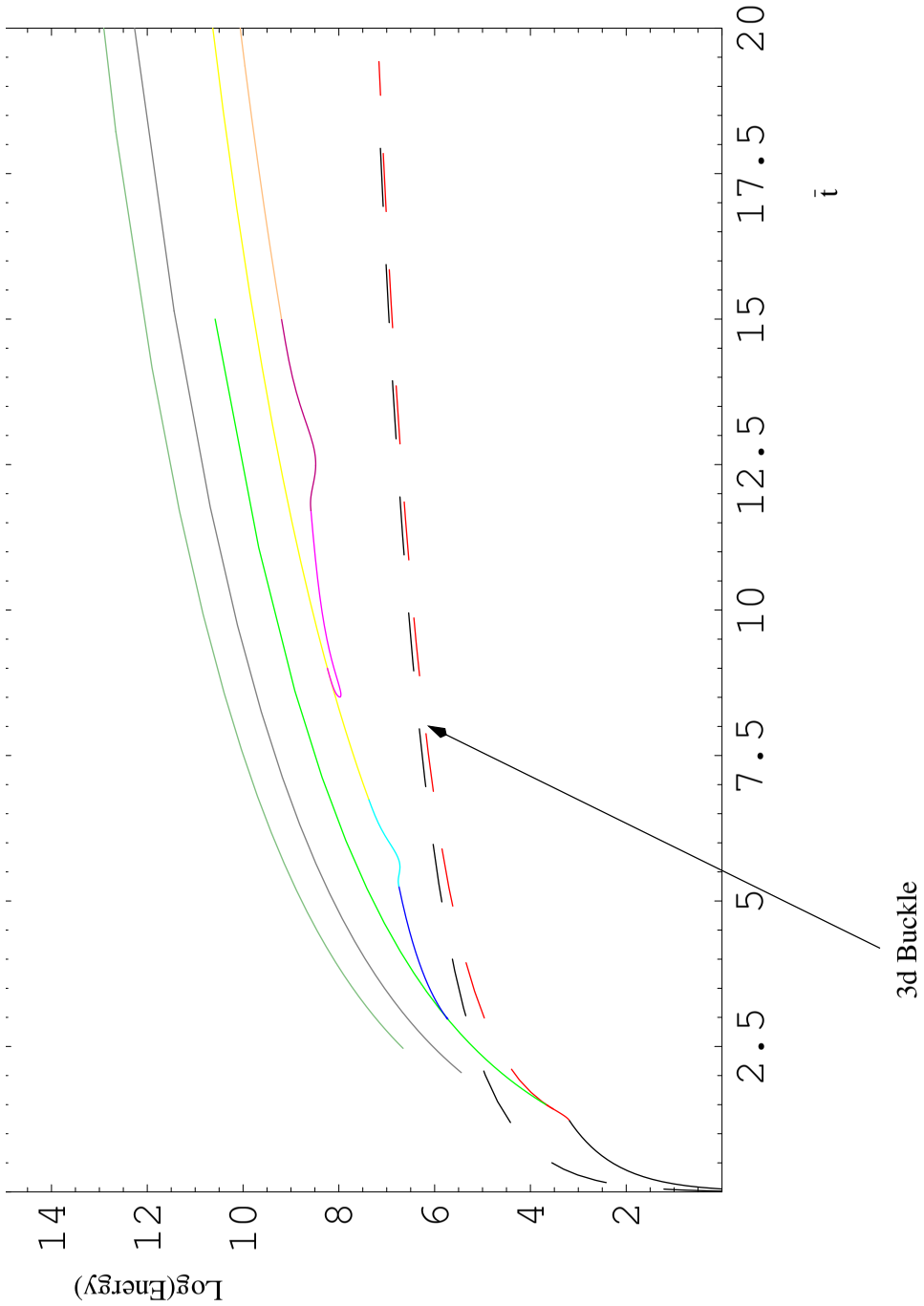


Figure 2.38: *Energy* vs. $\bar{t}$ for a 3d elastica, $\sigma_2 = \sqrt{2}/5$

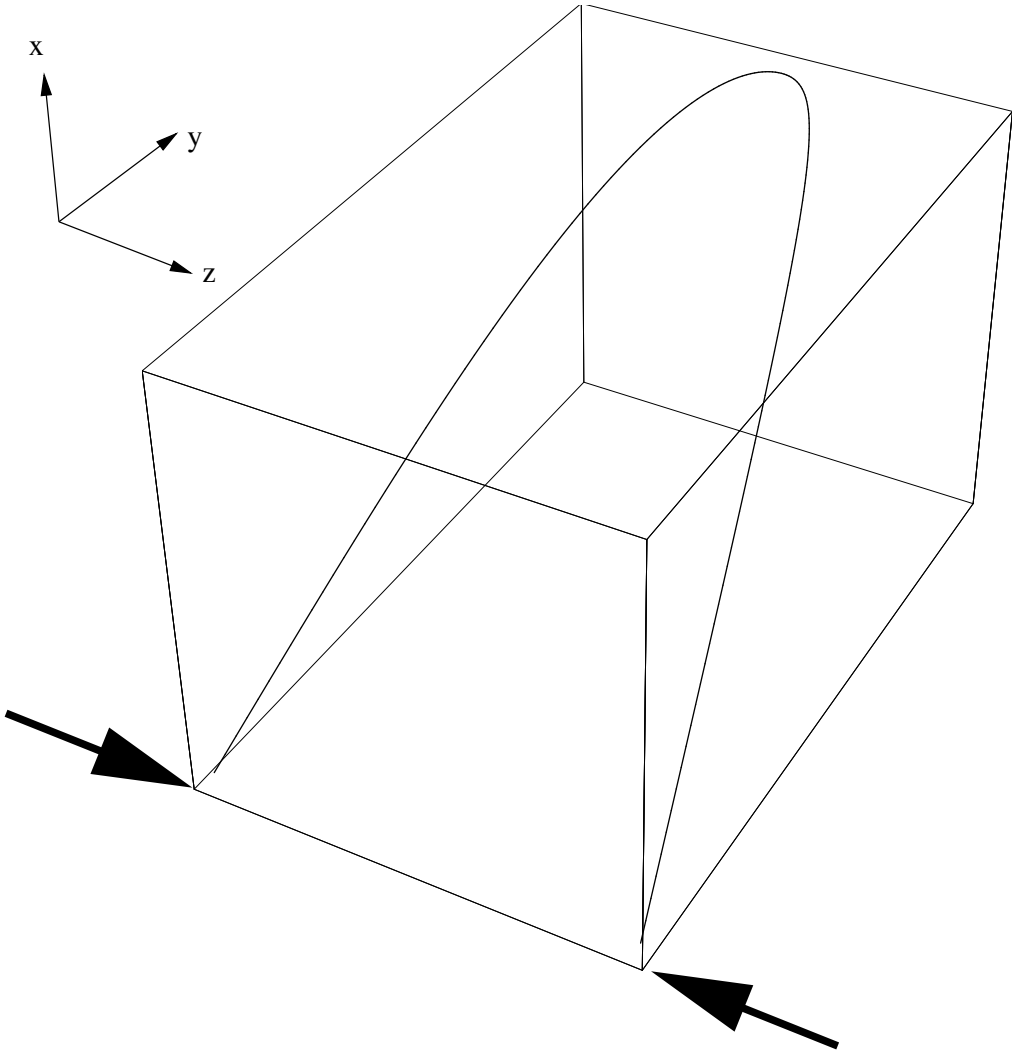


Figure 2.39: Typical path for a 3d crimped fibre, $\sigma_2 = 0.25$

.

1. *First section*

   We have the boundary conditions

$$\gamma'_{11} = \gamma'_{21} = 0,$$

   at the start of the fibre ($s = 0$), and

$$\gamma_{11} \sin\phi + \gamma_{21} \cos\phi = 0$$

   at $s = 1/2$. Note that we have three boundary conditions for two second order ODE's, with one unknown parameter a (which we will denote a_1 to associate it with the first section). We can use equation (2.69) and the boundary conditions

$$x_1(0) = 0 \quad \text{and} \quad x_1\left(\frac{1}{2}\right) = 1 \tag{2.86}$$

   to fix the value of a_1, but we are still short of one boundary condition. We will overcome this by introducing a new parameter that is constant between the sections and use the joining conditions to obtain its value. To this end let us write that

$$\gamma_{21}\left(\frac{1}{2}\right) = \frac{\Gamma}{\cos\phi}$$

   for some yet-undetermined constant Γ. By (2.76)

$$\gamma_{11}\left(\frac{1}{2}\right) = -\frac{\Gamma}{\sin\phi}$$

   Solving the equations and applying the boundary conditions gives

$$\begin{aligned} \gamma_{21} &= B_1 \cos\sqrt{\lambda}s + a_1 \cos\phi \\ \gamma_{11} &= \beta_1 \cos\sqrt{\bar{\lambda}}s + a_1 \sin\phi \end{aligned}$$

   where

$$\begin{aligned} B_1 &= -\frac{1}{\cos\sqrt{\lambda}/2}\left(a_1\cos\phi - \frac{\Gamma}{\cos\phi}\right) \\ \beta_1 &= -\frac{1}{\cos\sqrt{\bar{\lambda}}/2}\left(a_1\sin\phi + \frac{\Gamma}{\sin\phi}\right) \\ \sqrt{\bar{\lambda}}^2 &= \sigma_2\sqrt{\lambda}^2 \end{aligned}$$

   Integrating (2.69) between $s = 0$ and $s = 1/2$ and applying (2.86) gives

$$1 + \frac{a_1}{2} = -\frac{\beta_1 \sin\phi}{\sqrt{\bar{\lambda}}} \sin\frac{\sqrt{\bar{\lambda}}}{2} - \frac{B_1\cos\phi}{\sqrt{\lambda}} \sin\frac{\sqrt{\lambda}}{2}. \tag{2.87}$$

2. *End section*

For the end section, we apply the boundary conditions

$$\gamma_{11}'(1) = \gamma_{21}'(1) = 0,$$

at the end, and by continuity of γ_{k1}

$$\begin{aligned} \gamma_{11} &= -\frac{\Gamma}{\sin\phi} \\ \gamma_{21} &= \frac{\Gamma}{\cos\phi} \end{aligned}$$

at $s = 1/2$. Applying these, we find

$$\begin{aligned} \gamma_{21} &= B_2\left(\tan\sqrt{\lambda}\sin\sqrt{\lambda}s + \cos\sqrt{\lambda}s\right) + a_2\cos\phi, \\ \gamma_{11} &= \beta_2\left(\tan\sqrt{\bar{\lambda}}\sin\sqrt{\bar{\lambda}}s + \cos\sqrt{\bar{\lambda}}s\right) + a_2\sin\phi, \end{aligned}$$

where

$$\begin{aligned} B_2 &= -\frac{1}{\cos\phi}\left(\frac{a_2\cos^2\phi - \Gamma}{\tan\sqrt{\lambda}\cdot\sin\sqrt{\lambda}/2 + \cos\sqrt{\lambda}/2}\right) \\ \beta_2 &= -\frac{1}{\sin\phi}\left(\frac{a_2\sin^2\phi + \Gamma}{\tan\sqrt{\bar{\lambda}}\cdot\sin\sqrt{\bar{\lambda}}/2 + \cos\sqrt{\bar{\lambda}}/2}\right). \end{aligned}$$

The value of a_2 is found in the same way as for the start section by requiring that

$$x(1) - x\left(\frac{1}{2}\right) = -1.$$

This gives

$$\begin{aligned} \frac{a_2}{2} - 1 &= -\frac{\beta_2\sin\phi}{\sqrt{\bar{\lambda}}}\cos\frac{\sqrt{\bar{\lambda}}}{2}\left[\tan\sqrt{\bar{\lambda}} - \tan\frac{\sqrt{\bar{\lambda}}}{2}\right] \\ &\quad -\frac{B_2\cos\phi}{\sqrt{\lambda}}\cos\frac{\sqrt{\lambda}}{2}\left[\tan\sqrt{\lambda} - \tan\frac{\sqrt{\lambda}}{2}\right]. \end{aligned} \tag{2.88}$$

In (2.87) and (2.88) we have two equations from which we can deduce $a_1(\Gamma)$ and $a_2(\Gamma)$. If we now apply

$$\left[\gamma_{21}'\left(\frac{1}{2}\right)\right]_-^+ = 0$$

we find that

$$B_2\left(\tan\sqrt{\lambda}\cdot\cot\frac{\sqrt{\lambda}}{2} - 1\right) = -B_1. \tag{2.89}$$

Combining (2.87), (2.88) and (2.89) we obtain

$$\frac{2\Gamma\sqrt{\lambda}\sec\phi\tan\sqrt{\lambda}/2\left(\sqrt{\bar{\lambda}}-2\tan\sqrt{\bar{\lambda}}/2\right)}{-2\sqrt{\bar{\lambda}}\cos^2\phi\tan\sqrt{\lambda}/2+\sqrt{\lambda}(\sqrt{\bar{\lambda}}-2\sin^2\phi\cdot\tan\sqrt{\bar{\lambda}}/2)} \tag{2.90}$$

This has the solution

$$\Gamma = 0$$

unless

$$\sqrt{\bar{\lambda}} = 2\tan\frac{\sqrt{\bar{\lambda}}}{2}$$

or

$$\tan\frac{\sqrt{\lambda}}{2} = 0.$$

The first exception will only occur for $\sqrt{\lambda} > 2\pi$, and hence we can ignore this case. $\sqrt{\lambda} = 2\pi$ is more promising, as we know that this is an important parameter in the two-dimensional case. Unfortunately, if we find Γ using the continuity condition

$$\left[\gamma'_{11}\left(\frac{1}{2}\right)\right]^{+}_{-} = 0$$

we find

$$\frac{2\Gamma\sqrt{\bar{\lambda}}\csc\phi\tan\sqrt{\bar{\lambda}}/2\left(\sqrt{\lambda}-2\tan\sqrt{\lambda}/2\right)}{-2\sqrt{\bar{\lambda}}\cos^2\phi\tan\sqrt{\lambda}/2+\sqrt{\lambda}(\sqrt{\bar{\lambda}}-2\sin^2\phi\cdot\tan\sqrt{\bar{\lambda}}/2)} = 0$$

which requires that $\Gamma = 0$ for $\sqrt{\lambda} = 2\pi$. From this, we conclude that Γ must always be zero. The consequence of this is that the fibre never enters a helical configuration. Figure 2.40 show typical configurations of the fibre for increasing force (with constants $\phi = \pi/4$, $\sigma_2 = 0.25$).

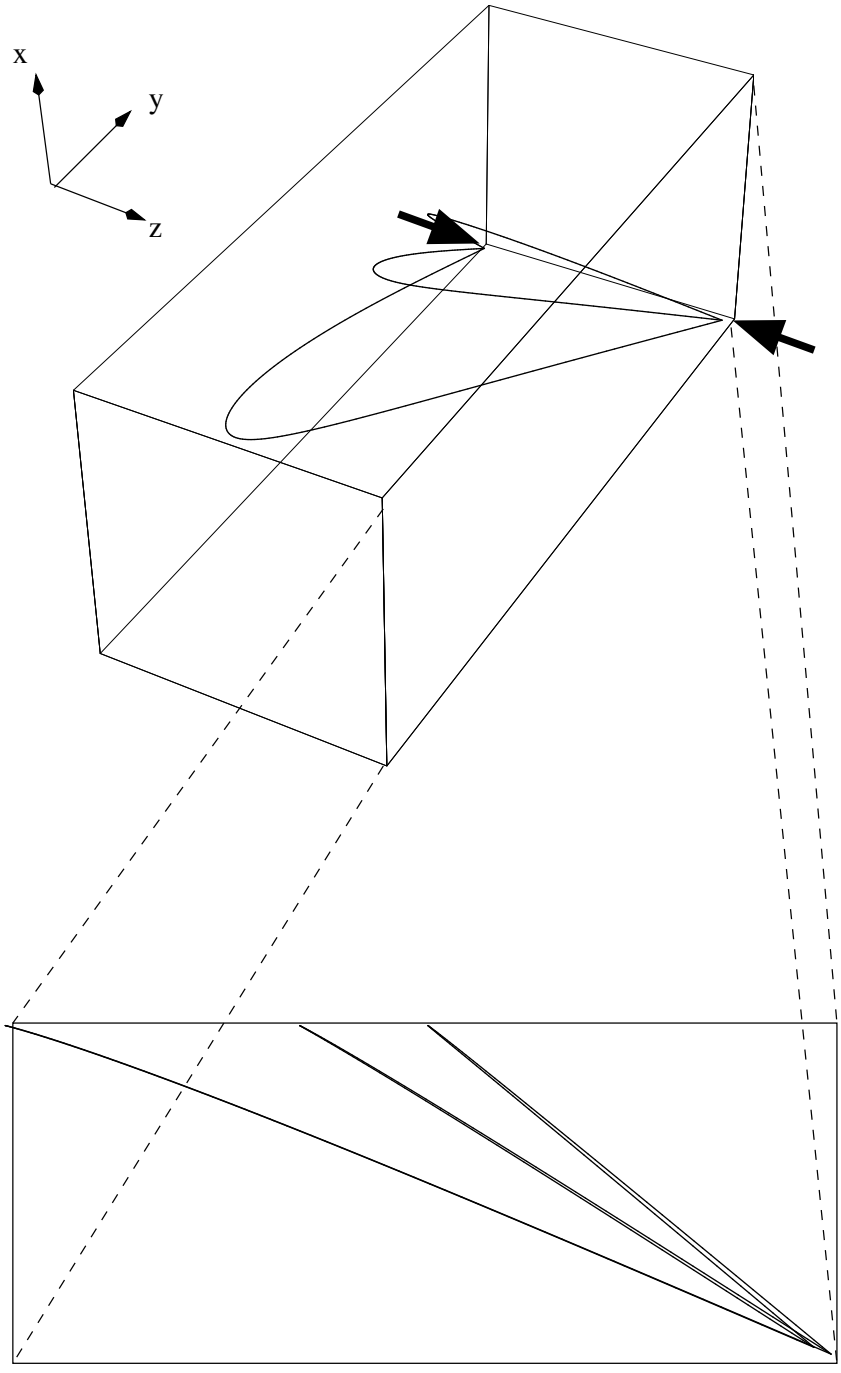


Figure 2.40: 3d configurations for a confined fibre with increasing λ. $\phi = \pi/4$, $\sigma_2 = 0.25$

2.4 Conclusions

In this chapter we have discussed models for the deformation of the fibre as it first enters the stuffer box. We chose to model the fibre as an elastica contained in a box of fixed length, and allowed the fibre to make multiple contacts with the sides. To gain understanding of the problem, we concentrated on special case when the aspect ratio of the box was small, and hence when we could use the linearised equations for the elastica.

2.4.1 Two dimensional fibre

When we treated the fibre as a two-dimensional elastica, we were left with equations that were simple to solve between the contact points. We then proceeded to discuss a methodology for joining these solutions together to produce a full solution. This was done for a simple rectangular box, a rectangular box fed midway and a wedge. Different types of solution were observed in each case. We then applied energy arguments to determine which configuration was energetically favoured, although we also discussed the possible non-uniqueness of solutions created by this methodology.

We must also consider the results of this work on primary crimp formation as part of an understanding of the machine as a whole. Firstly, we saw how the force exerted by the fibre on the walls that confine it at the ends changes as more fibre is forced in. Secondly, we saw that, for a given number of contact points, the force reaches a maximum as more fibre enters, after which point the fibre will begin to form a new contact point. For the rectangular box we can see that the maximum force is quadratic in the number of contact points. In particular, when we apply no moment to either end we had

$$F_x = \frac{EI}{X_b^2}\left(M+1\right)^2 4\pi^2 \tag{2.91}$$

where M is the number of contact points (not counting the ends). In addition there were $(M+1)/2$ crimps,[21] hence the crimp length was, on average

$$\frac{2X_b}{M+1}. \tag{2.92}$$

Note that for these boundary conditions, M had to be an odd number.

[21] where one crimp goes from bottom to top to bottom again

For a rectangular box fed midway, the solutions containing sections with flat fibre were seen to be energetically unfavoured. The maximum force was found to be

$$F_x = \frac{EI}{X_b^2}\left(2M+1\right)^2\pi^2$$

and the average length of the crimp

$$\frac{2X_b}{M+1}.$$

For the wedge, this is much less clear. In particular, the force is not exactly quadratic in the number of contact points, nor is it as clear where the maximum force occurs. However, for large numbers of sections, each contributes approximately the same amount to the force, and has the same length, hence

$$F_x \propto \frac{EI}{X_b^2}M^2$$

and the crimp length

$$\sim \frac{2X_b}{M}$$

Note that all these results are only valid for the small amplitude crimp. Although the maximum force is likely to be similar, if there are large deflections the crimp length may be very different.

2.4.2 Three dimensional crimp

Experimentally, we have seen that the fibre can be deformed into a three dimensional crimped shape, especially a helix. Starting from the equations for a three dimensional elastica, we showed that, for small deflections, the deformations in each of the principal directions were independent except where they were coupled at the contact points. We considered the geometry of a fibre confined between two plates. When the principle axis of the fibre was parallel to the two plates, the fibre behaved as the two-dimensional elastica until a critical force was reached when it adopted a three-dimensional form. When the axis was at a general angle, the fibre was not confined to a plane for any force once contact had been achieved. In neither case did the fibre adopt a helical configuration.

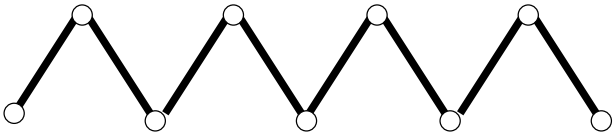
Chapter 3

Secondary Crimp

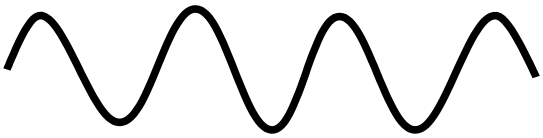
3.1 Introduction

Having modelled the primary deformation that occurs as the material first enters between the rollers, it is now time to turn our attention to the subsequent behaviour and secondary crimp formation. To this end, we need to consider the behaviour of the crimped tow as it is compressed.

- **Hinged Rods Model**
  Looking at typical primary crimped material, we see a fairly uniform small scale structure. We also see that much of the fibre is straight, with large changes in angle occurring at the corners where the material has undergone an irreversible plastic deformation. A similar structure can be formed by folding a piece of paper in alternate directions to form a concertina shape. When we compress such a structure, we see that as the force increases, the angle between adjacent rods decreases. This observation leads us to propose our first model for the crimped tow. We will describe the fibre as a series of rigid rods, joined by hinges. These hinges will exert both reaction forces and torques on the rods and in the absence of any applied force the tow will have a "concertina" shape (figure 3.1a).
  By considering the forces and moments acting on such a system, we will derive a second-order difference equation for the orientation of each rod. In order to gain a better understanding of the behaviour of this model, we will look for an asymptotic solution when the ratio of the couple exerted by external forces to that exerted by the elastic hinges is small. The form of the solution thus found is not valid for a sufficiently large numbers of rods, and we will then require a different expansion.



(a) Hinged Rods



(b) Naturally Curved Fibre

Figure 3.1: The two ways of seeing secondary crimp

We show that the dependent variable in the equations derived for the "concertina" can be rewritten as a sum of two angles that vary over different length scales. This enables us to seek solutions where the change in these angles between one hinge and the next is very small, and leads to a more convenient asymptotic procedure that is uniformly valid for large numbers of rods. Unlike the first expansion, this procedure will predict a bifurcation of the "concertina" from a nearly flat configuration to an arched shape similar to the Euler strut under certain circumstances. Both of these asymptotic solutions are also compared with the numerical response diagrams calculated from solving the full problem.

The hinged rods model has a number of parameters which are unknown. In order to find these, experiments have been carried out by Acordis[1] by stretching[2] a crimped tow and measuring the force and extension[3]. The model's predictions were compared with these, and a fit taken to obtain the parameters.

- **Multiple Scale model**

  A second model for the crimped fibre is to think of it as an elastica that has a curved shape when unstressed as in figure 3.1b. Starting from the equations of such a fibre, and, using the small scale of the crimp in comparison to its length, we will again carry out an analysis to derive an expression for the slow modulations that occur along the fibre; now however this analysis can be achieved by the method of multiple scales. This predicts a buckling when a critical condition is satisfied, which is similar to that for the classical Euler strut. We also

[1] Formerly Courtaulds.

[2] Pull rather than push.

[3] Here we use extension as experimentally observed, i.e. the change in the macroscopic length of the sample.

compare this result with that obtained from the above mentioned continuum limit for the hinged rods model, and show the similarities in the structure of the solutions.

3.2 Hinged Rods : Model

3.2.1 Derivation

Our model will make the following assumptions

- The tow consists of N rods, numbered $n = 1 \cdots N$ (see figure 3.2)
- The rods are rigid and inextensible.
- The only external forces acting on the rods are $\pm\mathbf{F}$ applied at the end rods. Thus each rod is acted on by forces $\pm\mathbf{F}$ at the ends due to the internal reaction in the hinges.
- All the rods are of the same length Λ.
- The hinges joining the rods exert a torque which resists deviation from the equilibrium angle ϕ and is given by

  $$K(\Theta_n - \phi)$$

  where Θ_n is the acute angle between rod n and $n+1$ and K is a spring constant (units Nm).

Consider the equilibrium of a single rod denoted by $n(\neq 1)$. It has two torques acting on it due to hinges $n-1$ and n. The externally applied force, transmitted to the rod by the hinges, gives rise to a couple $\mathbf{F} \times \mathbf{\Lambda}$, where $\mathbf{\Lambda}$ is a vector along the rod. Now we see a potential complication with the notation so far. We have measured the angle Θ_n relative to the previous rod, but it is more convenient to write θ_n to be the angle between the n^{th} rod and the direction of the external force (as shown in figure 3.2). Careful examination of the geometry of the rods tells us that

$$\Theta_n = \pi + (\theta_n - \theta_{n+1})(-1)^n$$

where the $(-1)^n$ term differentiates between the odd and even hinges. In addition, balancing the moments acting on the n^{th} rod $(n \neq 1)$ requires that, for equilibrium,

$$(-1)^n \left(K(\Theta_{n-1} - \phi) + K(\Theta_n - \phi)\right) = F\Lambda \sin\theta_n,$$

where once again we must differentiate between odd and even hinges. Hence we arrive at an equation necessary for the moments on the n^{th} rod to be balanced as

$$K\left(\theta_{n+1} - 2\theta_n + \theta_{n-1} - 2(-1)^n(\pi - \phi)\right) + F\Lambda \sin\theta_n = 0 \qquad \text{for } n = 2, \cdots, N-1.$$

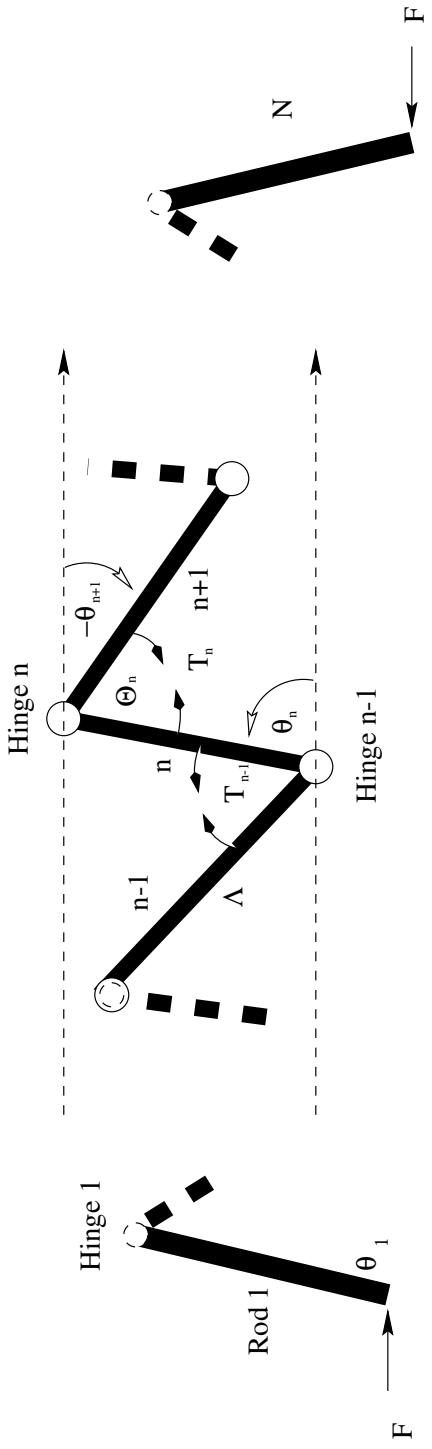


Figure 3.2: Hinged Rod configuration for an even number of rods (N)

Note that this does not apply to the end rods, where only one hinge exerts a torque. For these, we have the conditions

$$\begin{aligned} K\left(\theta_2 - \theta_1 + \pi - \phi\right) + F\Lambda \sin\theta_1 &= 0, \\ K\left(\theta_{N-1} - \theta_N - (-1)^N(\pi - \phi)\right) + F\Lambda \sin\theta_N &= 0. \end{aligned}$$

3.2.2 Non-dimensionalization

We can non-dimensionalize by writing

$$K = \frac{F\Lambda}{\kappa}$$

and dividing. We also write

$$\chi = \pi - \phi.$$

This gives the following system of equations with which we shall deal from now on

$$\begin{aligned} \theta_{n+1} - 2\theta_n + \theta_{n-1} + \kappa \sin\theta_n &= 2(-1)^n\chi \qquad (3.1) \\ &\quad \text{for } n = 2, \cdots, N-1 \\ \theta_2 - \theta_1 + \kappa \sin\theta_1 &= -\chi \qquad (3.2) \\ \theta_{N-1} - \theta_N + \kappa \sin\theta_N &= (-1)^N\chi. \qquad (3.3) \end{aligned}$$

3.2.3 Asymptotics

Equation (3.1) is a nonlinear second order difference equation, and, as such, is difficult to solve. In absence of the $(-1)^n$ term, we might be able to take a continuum limit as $\kappa \to 0$ to obtain an ODE for θ, but we do not expect it to be possible when the angle θ_n is both $O(1)$ and can change rapidly. Instead, we will make use of the assumption that[4] $\kappa \ll 1$ and seek a solution to (3.1) with boundary conditions (3.2) and (3.3) in the form

$$\theta_n = \theta_{0,n} + \kappa\theta_{1,n} + \kappa^2\theta_{2,n} + \cdots.$$

Expanding and collecting terms of the same magnitude we see that

- $O(1)$

$$\begin{aligned} \theta_{0,n+1} - 2\theta_{0,n} + \theta_{0,n-1} - 2(-1)^n\chi &= 0, && (3.4)\\ \theta_{0,2} - \theta_{0,1} + \chi &= 0, && (3.5)\\ \theta_{0,N-1} - \theta_{0,N} - (-1)^N\chi &= 0. && (3.6) \end{aligned}$$

- $O(\kappa)$

$$\begin{aligned} \theta_{1,n+1} - 2\theta_{1,n} + \theta_{1,n-1} + \sin\theta_{0,n} &= 0, && (3.7)\\ \theta_{1,2} - \theta_{1,1} + \sin\theta_{0,1} &= 0. && (3.8)\\ \theta_{1,N-1} - \theta_{1,N} + \sin\theta_{0,N} &= 0. && (3.9) \end{aligned}$$

- $O(\kappa^2)$

$$\begin{aligned} \theta_{2,n+1} - 2\theta_{2,n} + \theta_{2,n-1} + \theta_{1,n}\cos\theta_{0,n} &= 0, && (3.10)\\ \theta_{2,2} - \theta_{2,1} + \theta_{1,1}\cos\theta_{0,1} &= 0, && (3.11)\\ \theta_{2,N-1} - \theta_{2,N} + \theta_{1,N}\cos\theta_{0,N} &= 0. && (3.12) \end{aligned}$$

3.2.3.1 $O(1)$

The general solution to (3.4) is

$$\theta_{0,n} = \alpha_0 n + \beta_0 - (-1)^n\frac{\chi}{2}. \tag{3.13}$$

Applying boundary conditions (3.5) and (3.6) requires that

$$\alpha_0 = 0$$

but imposes no conditions on β_0, for which we will need to look to higher order terms.[5]

[4] Although it is difficult to estimate κ directly, we shall see later that this assumption leads to pysically relvant solutions

[5] A physical interpretation for this is that the O(1) problem corresponds to the case when no force is applied, and hence there is no direction imposed by the model

3.2.3.2 $O(\kappa)$

Applying this result to (3.7) we have

$$\theta_{1,n+1} - 2\theta_{1,n} + \theta_{1,n-1} + \sin\beta_0 \cos\frac{\chi}{2} - (-1)^n \sin\frac{\chi}{2}\cos\beta_0 = 0.$$

Now seeking a solution of the form

$$\theta_{1,n} = A_1(-1)^n + B_1 n^2 + \alpha_1 n + \beta_1 \tag{3.14}$$

and comparing like terms we see that

$$\begin{aligned} A_1 &= -\frac{1}{4}\sin\frac{\chi}{2}\cos\beta_0, \\ B_1 &= -\frac{1}{2}\cos\frac{\chi}{2}\sin\beta_0. \end{aligned}$$

Applying boundary conditions (3.8) and (3.9) gives

$$\begin{aligned} \alpha_1 - \frac{1}{2}\cos\frac{\chi}{2}\sin\beta_0 + \frac{1}{2}\sin\frac{\chi}{2}\cos\beta_0 &= 0, \\ -\alpha_1 - \frac{(-1)^N}{2}\sin\frac{\chi}{2}\cos\beta_0 + \frac{2N+1}{2}\cos\frac{\chi}{2}\sin\beta_0 &= 0. \end{aligned}$$

If N is even then

$$\begin{aligned} N\cos\frac{\chi}{2}\sin\beta_0 &= 0, \\ 2\alpha_1 + \sin\frac{\chi}{2}\cos\beta_0 - (N+1)\cos\frac{\chi}{2}\sin\beta_0 &= 0; \end{aligned}$$

otherwise

$$\begin{aligned} \sin\frac{\chi}{2}\cos\beta_0 + N\cos\frac{\chi}{2}\sin\beta_0 &= 0, \\ 2\alpha_1 - (N+1)\cos\frac{\chi}{2}\sin\beta_0 &= 0, \end{aligned}$$

giving the solutions

- N even

$$\beta_0 = 0, \tag{3.15}$$

$$\alpha_1 = -\frac{1}{2}\sin\frac{\chi}{2}. \tag{3.16}$$

- N odd

$$\tan\beta_0 = -\frac{1}{N}\tan\frac{\chi}{2}, \tag{3.17}$$

$$\alpha_1 = \frac{N+1}{2}\cos\frac{\chi}{2}\sin\beta_0. \tag{3.18}$$

3.2.3.3 $O(\kappa^2)$

Once again, we have been unable to determine the value of the constant β_1. Using our results so far, and applying them to equation (3.10) gives

$$\theta_{2,n+1} - 2\theta_{2,n} + \theta_{2,n-1} = \tag{3.19}$$
$$\cos\left(-\frac{\chi}{2}(-1)^n + \beta_0\right) \cdot \left(\alpha_1 n + \beta_1 - \frac{1}{4}\sin\frac{\chi}{2}\cos\beta_0(-1)^n - \frac{1}{2}\cos\frac{\chi}{2}\sin\beta_0 n^2\right).$$

Considering the solution to the associated homogeneous equation and boundary conditions (which is β_2) we see, by the Fredholm Alternative, (3.19) will only have a non-trivial solution if

$$\begin{aligned} 0 \;=\; & \beta_2 \sum_{n=1}^{N} \cos\left(-\frac{\chi}{2}(-1)^n + \beta_0\right) \cdot \\ & \left(\alpha_1 n + \beta_1 - \frac{1}{4}\sin\frac{\chi}{2}\cos\beta_0(-1)^n - \frac{1}{2}\cos\frac{\chi}{2}\sin\beta_0 n^2\right). \end{aligned}$$

Hence we find a value for β_1.

Note that these solutions are not valid unless $\kappa N^2 \ll 1$. In order to redress this problem, we will seek an alternative asymptotic procedure that will be uniformly valid as N increases.

3.2.4 A reformulation of the problem

We want to find an asymptotic solution to the equations that is uniformly valid for all N. We have seen that writing the solution as a series in κ is insufficient when $N^2 > O(\kappa^{-1})$. To understand the difficulty, let us consider the simpler difference equation

$$y_{n+1} - 2y_n + y_{n-1} + \kappa \sin y_n = 0. \tag{3.20}$$

Seeking a solution where $y = y_{0,n} + \kappa y_{1,n} + \cdots$ will only pick up the trivial solution $y \equiv 0$. Instead, we assume that y is sufficiently smooth that

$$y_{0,n} \simeq y_0(x) \qquad \text{where} \qquad x = \frac{n}{N} \text{ and } \kappa = \frac{1}{N^2}\kappa'$$

and hence

$$\frac{y_{0,n+1} - 2y_{0,n} + y_{0,n-1}}{1/N^2} \sim \frac{d^2 y_0}{dx^2} + O(\kappa).$$

For $\kappa N^2 = O(1)$ our difference equation can therefore be approximated as

$$y_0'' + \kappa' \sin y_0 = 0$$

which will have a non-trivial solution.

Unfortunately, the $(-1)^n$ term in (3.1) precludes such a procedure. Instead, let us take our inspiration from the form of the solutions encountered above ((3.13) and (3.14)) and write that

$$\theta_n = \Sigma_n - (-1)^n \Delta_n$$

for some functions Σ_n and Δ_n that are as yet undefined[6], but that we shall insist vary gradually in n. Now let us insert this into the equation (3.1) to give :

$$\begin{aligned}(\Sigma_{n+1} - 2\Sigma_n + \Sigma_{n-1}) + (-1)^n (\Delta_{n+1} + 2\Delta_n + \Delta_{n-1}) \\ +\kappa \cos\Delta_n \sin\Sigma_n - (-1)^n \kappa \cos\Sigma_n \sin\Delta_n = 2(-1)^n \chi.\end{aligned}$$

Grouping together terms of same type ($(-1)^n$ or 1) we define Σ_n, Δ_n by letting

$$\Sigma_{n+1} - 2\Sigma_n + \Sigma_{n-1} + \kappa \cos\Delta_n \sin\Sigma_n = 0 \qquad (3.21)$$

$$\text{and} \qquad \Delta_{n+1} + 2\Delta_n + \Delta_{n-1} - \kappa \cos\Sigma_n \sin\Delta_n = 2\chi. \qquad (3.22)$$

We now seek a solution that is valid when N is large and following our discussion of (3.20) assume that $\kappa N^2 \sim O(1)$. Writing[7]

$$\begin{aligned}\epsilon &= \frac{1}{N} \\ \kappa &= \epsilon^2 \kappa' \\ \Sigma_n &\sim \epsilon \Sigma_n^{(1)} + \epsilon^2 \Sigma_n^{(2)} + \cdots \\ \Delta_n &\sim \Delta_n^{(0)} + \epsilon \Delta_n^{(1)} + \cdots\end{aligned}$$

and inserting into our equations gives

- From equation (3.21)

$$\begin{aligned}\epsilon \left(\Sigma_{n+1}^{(1)} - 2\Sigma_n^{(1)} + \Sigma_{n-1}^{(1)}\right) + \epsilon^2 \left(\Sigma_{n+1}^{(2)} - 2\Sigma_n^{(2)} + \Sigma_{n-1}^{(2)}\right) + \\ \epsilon^3 \left(\Sigma_{n+1}^{(3)} - 2\Sigma_n^{(3)} + \Sigma_{n-1}^{(3)}\right) + \epsilon^3 \kappa' \cos\Delta_n^{(0)} \cdot \Sigma_n^{(1)} + \\ \epsilon^4 \kappa' \left(-\sin\Delta_n^{(0)} \cdot \Delta_n^{(1)} \Sigma_n^{(1)} + \cos\Delta_n^{(0)} \Sigma_n^{(2)}\right) = O(\epsilon^5). \qquad (3.23)\end{aligned}$$

[6]There are physical interpretations for this tactic. We can obtain the same pair of equations by writing the difference equation for odd and even hinges separately, or by combining the equations for hinge n and $n+1$ together. However, each of these forces choice of Σ_n and Δ_n. Our purpose in choosing to write θ in this way is that it be composed of smooth functions and that neither Σ_n nor Δ_n vary appreciably as n is increased to $n+1$

[7]If we were to take $\Sigma_n \sim O(1)$ then we would get an equation similar to (3.28) and with Neumann boundary data, giving the solution $\Sigma_n^{(0)} = 0$.

- From (3.22)

$$\left(\Delta_{n+1}^{(0)} + 2\Delta_n^{(0)} + \Delta_{n-1}^{(0)}\right) - 2\chi + \epsilon\left(\Delta_{n+1}^{(1)} + 2\Delta_n^{(1)} + \Delta_{n-1}^{(1)}\right) + \epsilon^2\left(\Delta_{n+1}^{(2)} + 2\Delta_n^{(2)} + \Delta_{n-1}^{(2)}\right) + \epsilon^3\left(\Delta_{n+1}^{(3)} + 2\Delta_n^{(3)} + \Delta_{n-1}^{(3)}\right) + \epsilon^4\left(\Delta_{n+1}^{(4)} + 2\Delta_n^{(4)} + \Delta_{n-1}^{(4)}\right) - \epsilon^2\kappa' \sin\Delta_n^{(0)} - \epsilon^3 \cos\Delta_n^{(0)} \cdot \Delta_n^{(1)} - \epsilon^4\kappa'\left(-\frac{1}{2}\sin\Delta_n^{(0)} \cdot (\Delta_n^{(1)})^2 + \cos\Delta_n^{(0)} \cdot \Delta_n^{(2)} - \frac{1}{2}\cos\Delta_n^{(0)} \cdot (\Sigma_n^{(1)})^2\right) = O(\epsilon^5). \tag{3.24}$$

- From the boundary condition at $n = 1$ (3.2)

$$-\left(\Delta_2^{(0)} + \Delta_1^{(0)}\right) + \chi + \epsilon\left(\Sigma_2^{(1)} - \Sigma_1^{(1)}\right) - \epsilon\left(\Delta_2^{(1)} + \Delta_1^{(1)}\right) + \epsilon^2\left(\Sigma_2^{(2)} - \Sigma_1^{(2)}\right) - \epsilon^2\left(\Delta_2^{(2)} + \Delta_1^{(2)}\right) + \epsilon^3\left(\Sigma_2^{(3)} - \Sigma_1^{(3)}\right) - \epsilon^3\left(\Delta_2^{(3)} + \Delta_1^{(3)}\right) + \epsilon^2\kappa' \sin\Delta_1^{(0)} + \epsilon^3\kappa' \cos\Delta_1^{(0)} \cdot (\Sigma_1^{(1)} + \Delta_1^{(1)}) + \epsilon^4\kappa'\left(\cos\Delta_1^{(0)} \cdot (\Sigma_1^{(2)} + \Delta_1^{(2)}) - \frac{1}{2}\sin\Delta_1^{(0)} \cdot (\Sigma_1^{(1)} + \Delta_1^{(1)})^2\right) = O(\epsilon^5). \tag{3.25}$$

- From the boundary condition at $n = N$ (3.3).

$$(-1)^N\left(\Delta_{N-1}^{(0)} + \Delta_N^{(0)}\right) - (-1)^N\chi + \epsilon\left(\Sigma_{N-1}^{(1)} - \Sigma_N^{(1)}\right) + (-1)^N\epsilon\left(\Delta_{N-1}^{(1)} + \Delta_N^{(1)}\right) + \epsilon^2\left(\Sigma_{N-1}^{(2)} - \Sigma_N^{(2)}\right) + (-1)^N\epsilon^2\left(\Delta_{N-1}^{(2)} + \Delta_N^{(2)}\right) + \epsilon^3\left(\Sigma_{N-1}^{(3)} - \Sigma_N^{(3)}\right) + (-1)^N\epsilon^3\left(\Delta_{N-1}^{(3)} + \Delta_N^{(3)}\right) - (-1)^N\epsilon^2\kappa' \sin\Delta_N^{(0)} + \epsilon^3\kappa' \cos\Delta_N^{(0)} \cdot (\Sigma_N^{(1)} - (-1)^N\Delta_N^{(1)}) + \epsilon^4\kappa'\left(\frac{(-1)^N}{2}\sin\Delta_N^{(0)} \cdot \left(\Sigma_N^{(1)} - (-1)^N\Delta_N^{(1)}\right)^2 + \cos\Delta_N^{(0)} \cdot \left(\Sigma_N^{(2)} - (-1)^N\Delta_N^{(2)}\right)\right) = O(\epsilon^5). \tag{3.26}$$

We now follow the example used for equation (3.20) and write

$$\Sigma_{n+1}^{(m)} - 2\Sigma_n^{(m)} + \Sigma_{n-1}^{(m)} \quad \sim \quad \epsilon^2\frac{d^2\Sigma^{(m)}}{ds^2}$$

$$\begin{aligned}\Sigma_{n+1}^{(m)} - \Sigma_n^{(m)} &\sim \epsilon \frac{d\Sigma^{(m)}}{ds} \\ \Delta_{n+1}^{(m)} + 2\Delta_n^{(m)} + \Delta_{n-1}^{(m)} &\sim 4\Delta^{(m)}(s) + O(\epsilon^2) \\ \Delta_{n+1}^{(m)} + \Delta_n^{(m)} &\sim 2\Delta^{(m)}(s) + O(\epsilon)\end{aligned}$$

where

$$s = \epsilon n \qquad\qquad \epsilon \leq s \leq 1$$

and group accordingly.[8] Hence we have

- From (3.24), (3.25) and (3.26) to $O(1)$

$$\begin{aligned}4\Delta^{(0)}(s) &= 2\chi \\ 2\Delta^{(0)}(0) &= \chi \\ 2\Delta^{(0)}(1) &= \chi\end{aligned}$$

which gives

$$\Delta^{(0)}(s) = \frac{\chi}{2} \tag{3.27}$$

Now looking at equation (3.23) to $O(\epsilon^3)$ we have

$$\frac{d^2\Sigma^{(1)}}{ds^2} + \kappa' \cos\frac{\chi}{2} \cdot \Sigma^{(1)}(s) = 0 \tag{3.28}$$

Solving (3.28) for $\Sigma^{(1)}(s)$ gives[9]

$$\Sigma^{(1)}(s) = A^{(1)} \sin\left(\lambda^{(1)} s - \omega^{(1)}\right) \tag{3.29}$$

where

$$\lambda^{(1)} = \sqrt{\kappa' \cos\frac{\chi}{2}}. \tag{3.30}$$

The boundary conditions come from the $O(\epsilon^2)$ from equations (3.24), (3.23), (3.25) and (3.26)

$$\begin{aligned}4\Delta^{(2)}(s) &= \kappa' \sin\Delta^{(0)}(s) \\ \frac{d\Sigma^{(1)}}{ds}_{s=0} - 2\Delta^{(2)}(0) &= -\kappa' \sin\Delta^{(0)}(0) \\ -\frac{d\Sigma^{(1)}}{ds}_{s=1} + 2(-1)^N \Delta^{(2)}(1) &= (-1)^N \kappa' \sin\Delta^{(0)}(1)\end{aligned}$$

[8] This is possible as we have the freedom to define Σ and Δ. It would not have worked if we had limited ourselves by writing (for example)

$$\Sigma_n = \frac{\theta_{n+1} + \theta_n}{2} \qquad\qquad \Delta_n = (-1)^n \frac{\theta_{n+1} - \theta_n}{2}.$$

[9] Notice the similarity to the Euler Strut equation. We will return to this idea later in this chapter

Hence

$$\Delta^{(2)}(s) = \kappa' \frac{1}{4} \sin \Delta^{(0)}(s) = \kappa' \frac{1}{4} \sin \frac{\chi}{2} \tag{3.31}$$

$$\frac{d\Sigma^{(1)}}{ds}_{s=0} = -\kappa' \frac{1}{2} \sin \frac{\chi}{2} \tag{3.32}$$

$$\text{and} \quad -\frac{d\Sigma^{(1)}}{ds}_{s=1} = (-1)^N \kappa' \frac{1}{2} \sin \frac{\chi}{2}. \tag{3.33}$$

Conditions (3.32), (3.33), when applied to equation (3.29) give different results depending on whether N is even or odd:

- N even

  We require that

  $$\frac{d\Sigma^{(1)}}{ds}_{s=0} = \frac{d\Sigma^{(1)}}{ds}_{s=1}$$

  and hence

  $$\sin \frac{\lambda^{(1)}}{2} \cdot \sin \left(\frac{\lambda^{(1)}}{2} - \omega^{(1)} \right) = 0,$$

  so we either have that

  $$\lambda^{(1)} = 0, \pm 2\pi, \pm 4\pi \text{ etc.}$$

  or

  $$\lambda^{(1)} - 2\omega^{(1)} = 0, \pm 2\pi, \pm 4\pi \text{ etc.}$$

- N odd

  This time, we need

  $$\frac{d\Sigma^{(1)}}{ds}_{s=0} = -\frac{d\Sigma^{(1)}}{ds}_{s=1}$$

  and hence

  $$\cos \frac{\lambda^{(1)}}{2} \cdot \cos \left(\frac{\lambda^{(1)}}{2} - \omega^{(1)} \right) = 0,$$

  so we either have that

  $$\lambda^{(1)} = \pm \pi, \pm 3\pi \text{ etc.}$$

  or

  $$\lambda^{(1)} - 2\omega^{(1)} = \pm \pi, \pm 3\pi \text{ etc.}$$

In addition, we have that

$$\frac{d\Sigma^{(1)}}{ds}_{s=0} = -\frac{\kappa'}{2} \sin \frac{\chi}{2}.$$

Since $\lambda^{(1)}$ is a physical parameter, this is sufficient to determine both $\omega^{(1)}$ and $A^{(1)}$ (although not uniquely) except when $\lambda^{(1)}$ is an appropriate multiple of π. Thus we could now plot a bifurcation diagram for $\Sigma^{(1)}$ in terms of parameter $\lambda^{(1)}$ and can expect that including nonlinear terms would produce pitchfork bifurcations at $\lambda^{(1)} = n\pi$.

3.2.5 Results of the asymptotic analysis

Our asymptotic analysis has produced the following results:

- Using a regular peturbation we predicted a unique solution for small κ. This was valid only when $N^2\kappa \ll O(1)$.

- We then showed that our equations could be rewritten as a pair of second-order difference equations for two smoothly varying functions. This allowed us to approximate these with an ordinary differential equation when $N >> 1$ and $N^2\kappa = O(1)$.

- The solution of these equations predicted that the observed behaviour depends upon whether the number of hinges is odd or even. In particular, there exist bifurcation points at values of $\lambda^{(1)}$ for which the linear solution is not uniquely defined. In dimensional variables these are located at

$$N^2\kappa \cos\frac{\chi}{2} = 4\pi^2, 16\pi^2 \text{ etc.} \tag{3.34}$$

when N is even, and

$$N^2\kappa \cos\frac{\chi}{2} = \pi^2, 9\pi^2 \text{ etc.} \tag{3.35}$$

when N is odd.

We will now compare these predictions with the numerical solution of equations (3.1), (3.2) and (3.3).

3.2.6 Numerical solution of the hinged rods model

Let us now consider the numerical solution of the full problem given by equations (3.1), (3.2) and (3.3). Our purpose in doing thus is to confirm (or otherwise) the predictions made by the asymptotic consideration discussed in the previous sections. The procedure we will adopt is very simple. We define a function $F(\theta_1; \kappa, N, \chi)$ in the following manner

1. Assume θ_1 for given κ, N and χ, then use (3.2) to calculate θ_2.
2. Now we can repeatedly apply (3.1) to obtain $\theta_3, \cdots \theta_N$.
3. Looking at the end condition (3.3), we set $F(\theta_1; \kappa, N)$ to be given by

$$F(\theta_1; \kappa, N) = \theta_{N-1} - \theta_N + \kappa \sin \theta_N - (-1)^N \chi. \tag{3.36}$$

The roots of the equation $F = 0$ are values of θ_1 that will generate valid solutions to the full problem. When implementing this procedure, we can consider two separate techniques to locate the zeros of this function. The simplest is to look at the surface generated by $F(\theta_1; \kappa, N)$ for fixed N and varying θ_1 and κ, and find the contours of $F = 0$. Such a scheme was implemented in Matlab, and typical results shown in figures 3.3 and 3.4

Alternatively, we can use a standard root finding algorithm for suitable starting guesses. This gives the position of the roots more accurately, and generates full solutions (sets of θ_n for $n = 1, \cdots N$) for plotting (see figures 3.5 and 3.7)

3.2.6.1 Comparisons and Observations

Having developed a procedure through which numerical solutions may be found, we are now in the position to make comparisons with the asymptotic solutions found previously. Figures 3.3 and 3.4 plot the values of θ_1 that correspond to solutions for

- the numerical solution (blue lines),
- the asymptotic expansion in powers of κ (red lines - given by (3.14) and (3.13)), and
- the asymptotic expansion in powers of ϵ (black lines - given by (3.27), (3.31) and (3.29)).

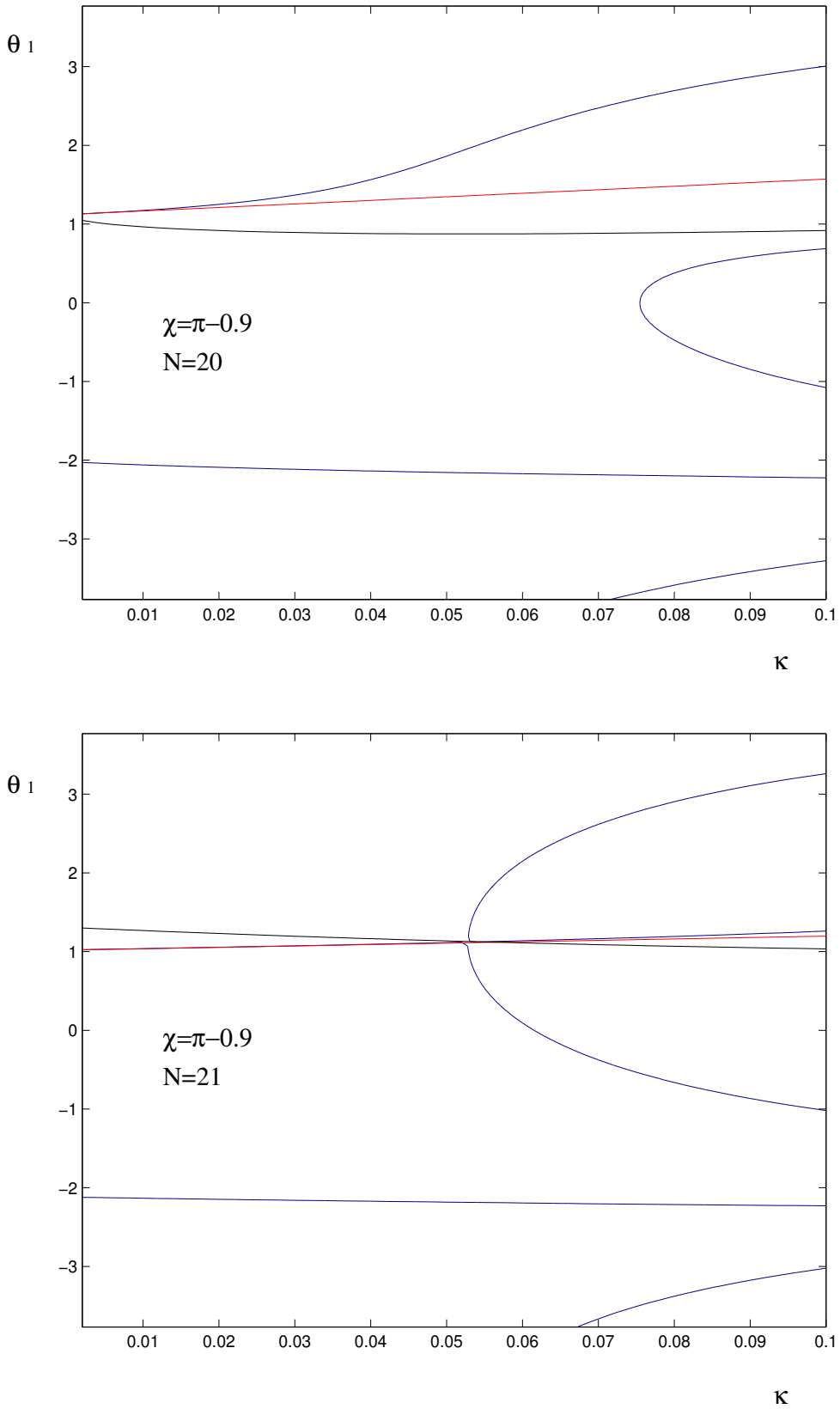


Figure 3.3: Comparison of asymptotics and Numerical Solution for $N = 20$ and $N = 21$

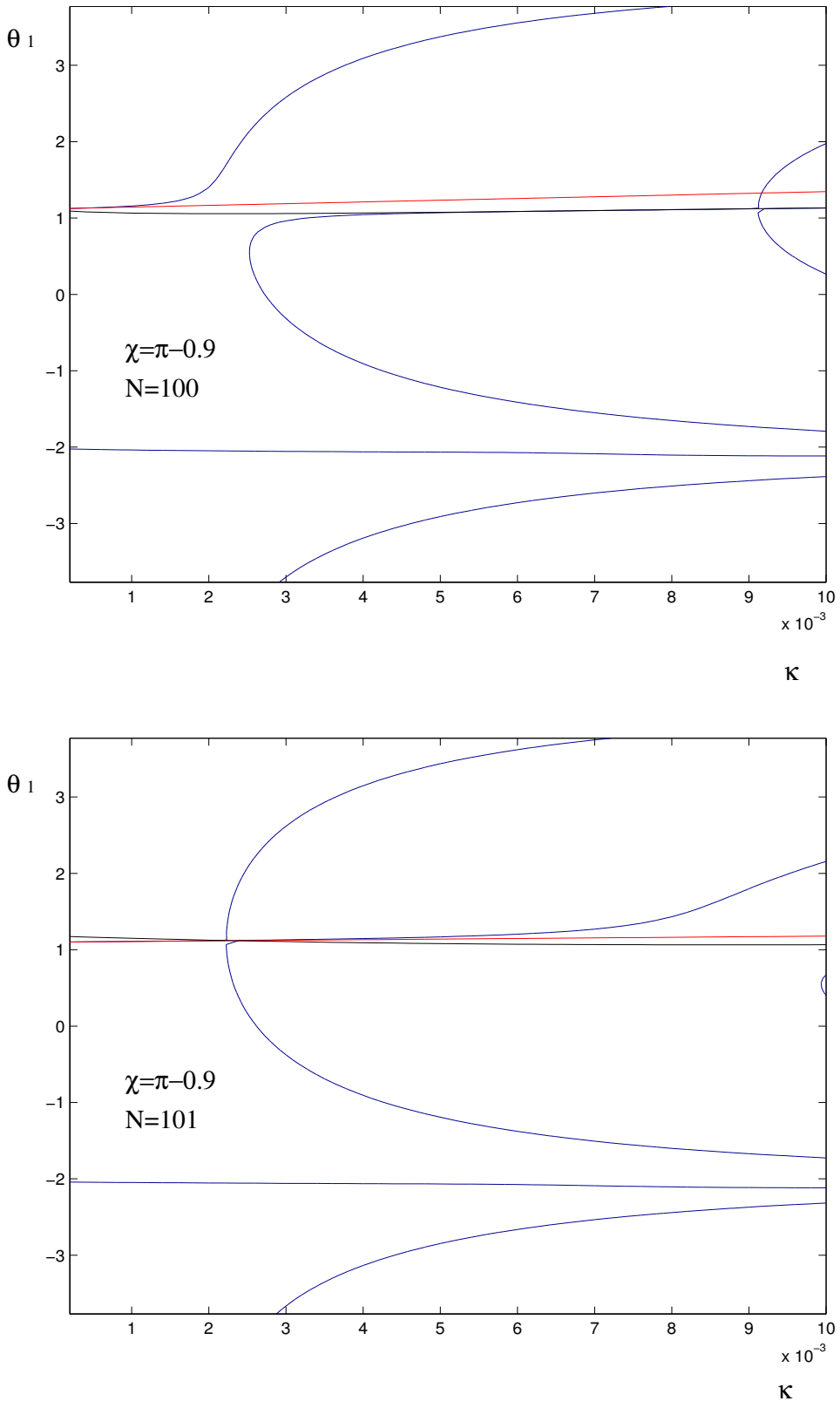


Figure 3.4: Comparison of asymptotics and Numerical Solution for $N = 100$ and $N = 101$

N	κ_{crit} *obtained numerically*	$\kappa = \frac{\pi^2}{N^2 \cos \chi/2}$
5	0.8412	0.9076
7	0.6482	0.4631
9	0.3351	0.2801
11	0.2092	0.1875
13	0.1447	0.1343
15	0.1065	0.1008
17	0.0819	0.0785
19	0.0651	0.0629
21	0.0531	0.0515
23	0.0441	0.0429
25	0.0372	0.0363
27	0.0316	0.0311
29	0.0274	0.0270

Table 3.1: Comparison of the numerically measured and the asymptotically predicted values of κ for the first bifurcation point for N rods

(Note that for all figures and table 3.1 we have taken χ to be $\pi - 0.9$).
Note the close correlation between the numerical and κ expansion solutions. For very small κ, we see a good match, much as we expected. However, the match between the numerical solution and the expansion in powers of ϵ is much worse, especially at small κ. This can be attributed to our assuming that $\kappa \sim \epsilon^2$ which limits the validity of this solution. Indeed, figure 3.4 (which has a smaller value of ϵ) shows a much better agreement.

Figures 3.3, 3.4, 3.5 and 3.7 all show bifurcations for certain values of κ. For N odd, we predicted that the first such bifurcation should occur when

$$\kappa = \frac{\pi^2}{N^2 \cos \chi/2}$$

(from equation (3.35)). Table 3.1 shows a comparison between measured (from plots such as 3.3) and asymptotic values of the critical value for κ. This shows good agreement between predicted and actual bifurcation points, especially as N increases.

Our numerical results also underline the important difference between odd and even numbers of rods. Firstly, we see that, as predicted, there are bifurcations near the predicted values of κ (when $\lambda^{(1)}$ is an odd multiple of π for N odd, and an even multiple of π when N is even). Secondly, the multiples of π for which there are no predicted bifurcations seem to have a fold bifurcation. This is similar to the symmetry breaking that is observed for the Euler strut when gravity is present.

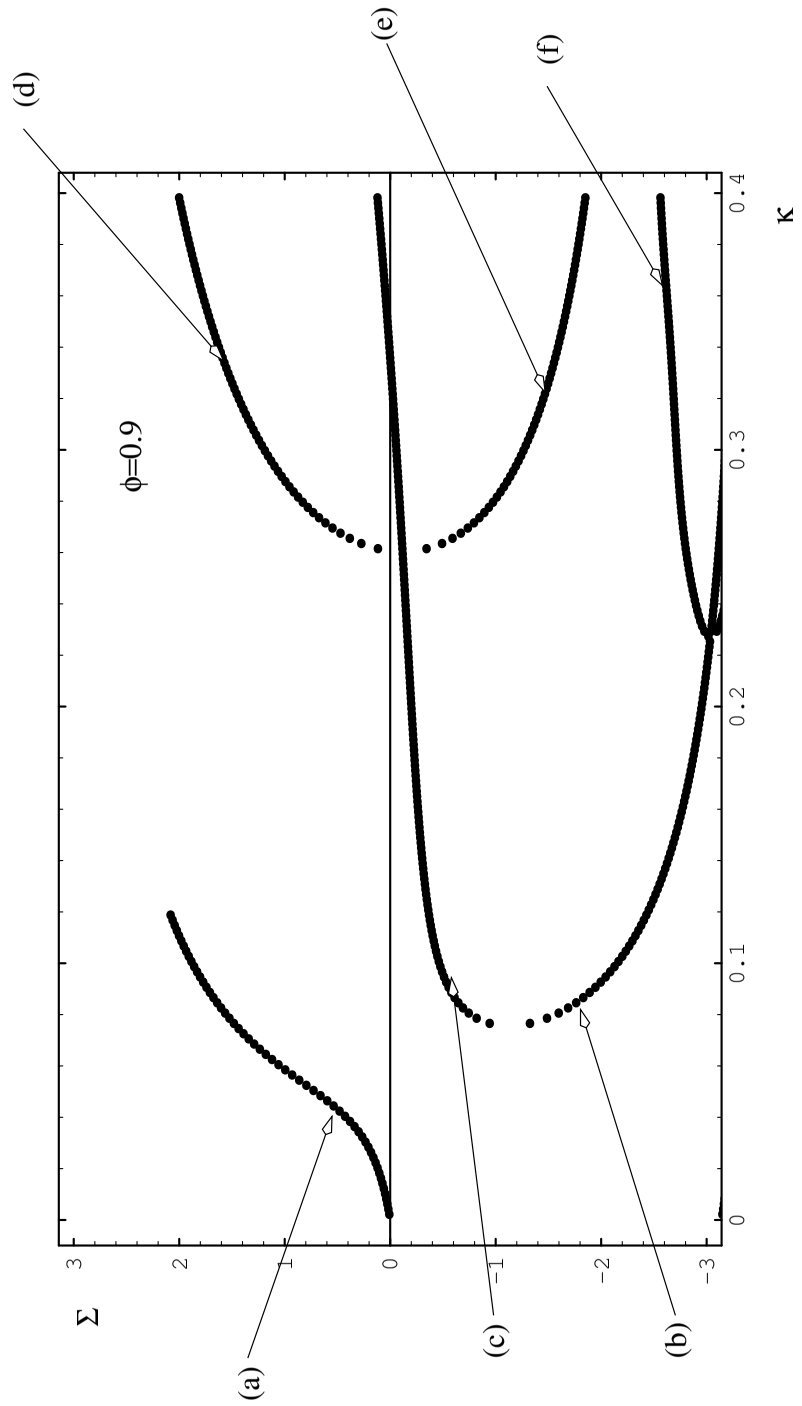


Figure 3.5: Σ_0 against κ in the case $N = 20$, $\phi = 0.9$

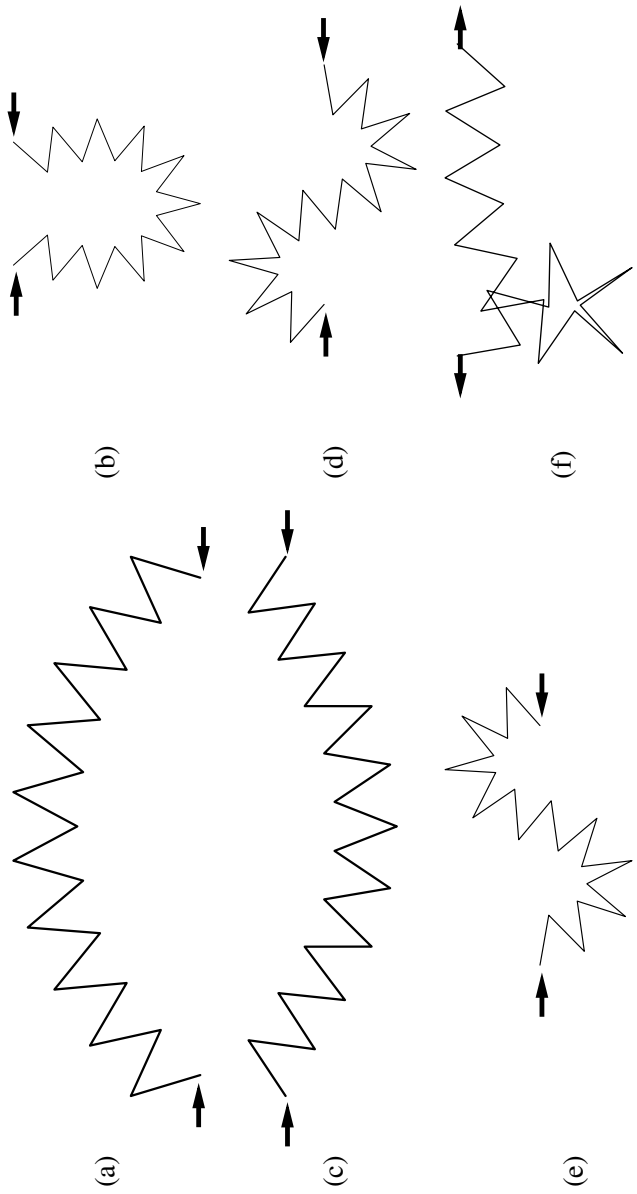


Figure 3.6: Key to Figure 3.5

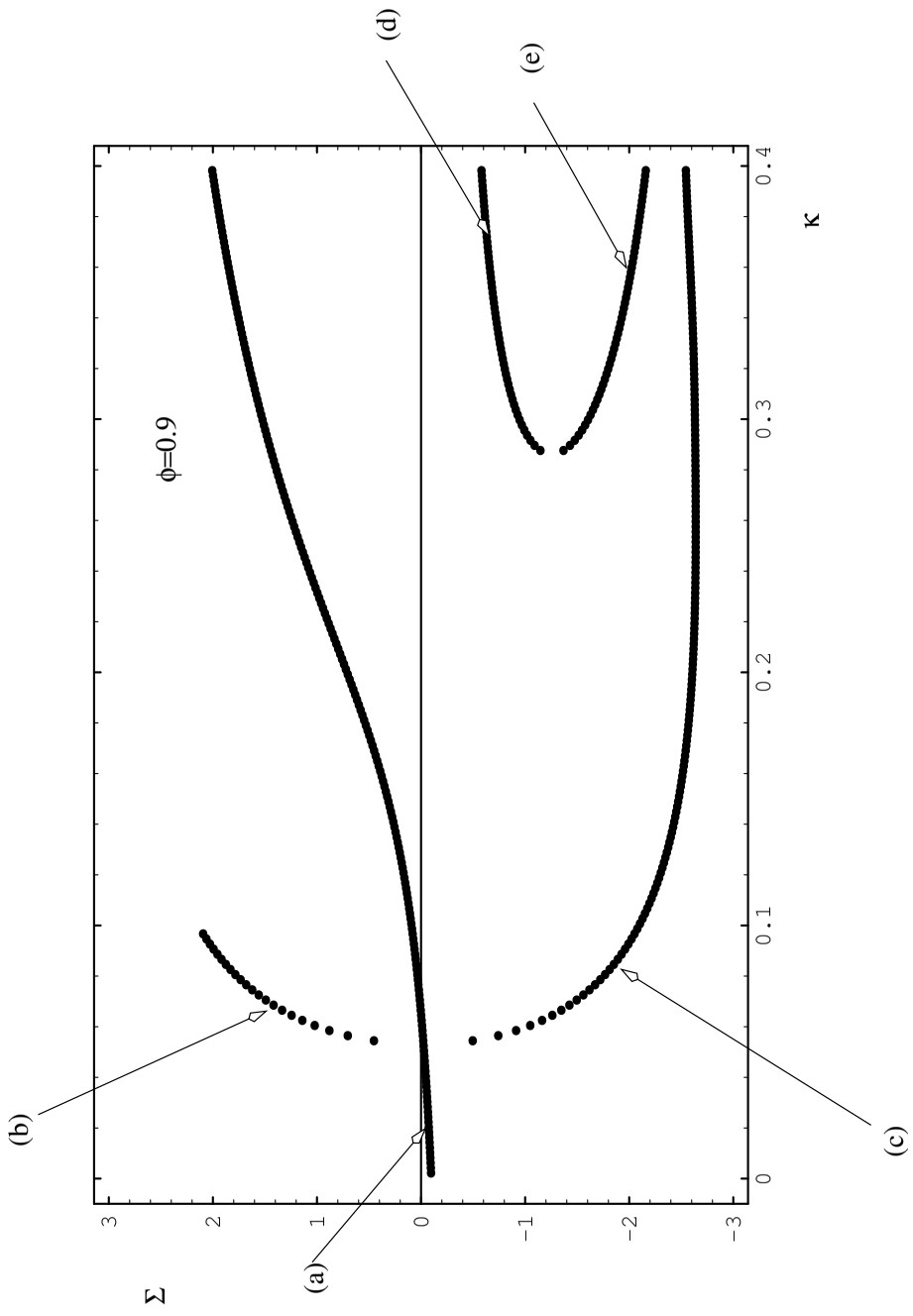


Figure 3.7: Σ_0 against κ in the case $N = 21$, $\phi = 0.9$

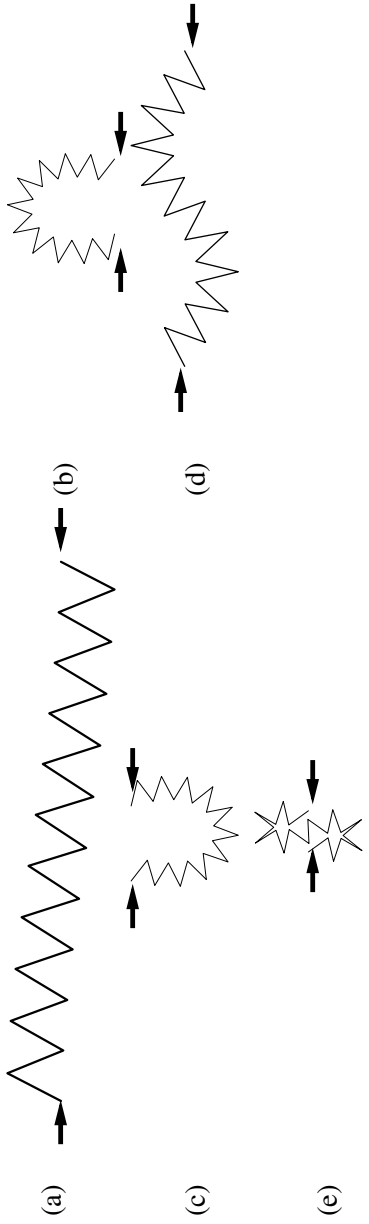


Figure 3.8: Key to Figure 3.7

3.3 Hinged Rods : Fitting Experimental Curves

The hinged rods model requires the following parameters with which to calculate the length of primary crimped material that will buckle

- Applied force F
- Rod length Λ
- Equilibrium Angle ϕ
- Hinge constant K

Of these, only the first two can be readily estimated in a practical situation, the force because it must be the same as that buckling the material at the nip and the rod length as that is half the primary crimp length (chapter 2). Only by modelling the plastic deformation of the fibres can we begin to get a theoretical understanding of how they depend on the past history.

The only realistic possibility is to use the results from experiments to fix these values for typical operating regimes, and then assume that they are constant over the parameter range we believe the crimper to work in. Suitable experiments are easy to propose. One of the simplest to perform is a force-extension measurement, for which the apparatus is available.

We apply the hinged rods model to the problem of a crimped tow under tension. Consider the tow as comprising M individual fibres, with each having N hinged rods. In terms of the angle made by the rods with the horizontal (θ) we see that the total length of the tow is given by

$$\text{Length of tow} = \sum_{n=1}^{n=N} \Lambda \cos\theta_n$$

We also know that if the rods are in equilibrium, then[10]

$$\theta_{n+1} - 2\theta_n + \theta_{n-1} - 2(-1)^n(\pi - \phi) - \frac{F\Lambda}{K}\sin\theta_n = 0. \tag{3.37}$$

Now let us look for a uniform solution where $\theta_{n+1} = -\theta_n = -(-1)^n\theta$. From (3.37) we have that

$$(-1)^n\left(-4\theta + 2(\pi - \phi) - \frac{F\Lambda}{K}\sin\theta\right) = 0$$

[10]Note that the tow is being elongated and hence the sign of the force F has changed

or

$$\frac{F\Lambda}{K}\sin\theta = -4\theta + 2(\pi - \phi).$$

The total tension in the tow is therefore

$$\frac{MK}{\Lambda}\frac{2(\pi-\phi)-4\theta}{\sin\theta}, \tag{3.38}$$

where M is the number of fibres in the tow. As the angles are constant, we also have that the extension is

$$N\Lambda\left(\cos\theta - \sin\frac{\phi}{2}\right), \tag{3.39}$$

and, when we apply no forces we have that

$$\theta = \frac{1}{2}(\pi - \phi).$$

3.3.1 Fitting Experimental Data

In contrast to the situation where the model is used as part of a larger description of an industrial crimper, when we consider an experimental run where we take a sample of tow and measure the extension against tension. In this case we only know the following[11]

- M From the specification of the fibre line
- a series of Force–Extension pairs.

We wish to find the parameters ϕ, $N\Lambda$ and K/Λ. A difficulty arises as our model gives tension and extension in terms of the parameter θ which is not measured in the experiment and so the normal curve fitting routines are not easy to apply. Instead we use information from (3.38) for special values of θ and (3.39).

Consider the situation as the parameter θ decreases. As it tends to 0, the tension approaches ∞ and the extension reaches its maximum value

$$N\Lambda\left(1 - \sin\frac{\phi}{2}\right).$$

Dividing through by the original length we get

$$\frac{\text{Maximum length}}{\text{Original length}} = \frac{1}{\sin\phi/2} - 1$$

[11] As the fibre is crimped, we do not know the total length ($N\Lambda$), nor the number of crimps N. The experiments were performed by Courtaulds using standard force-extension measuring devices.

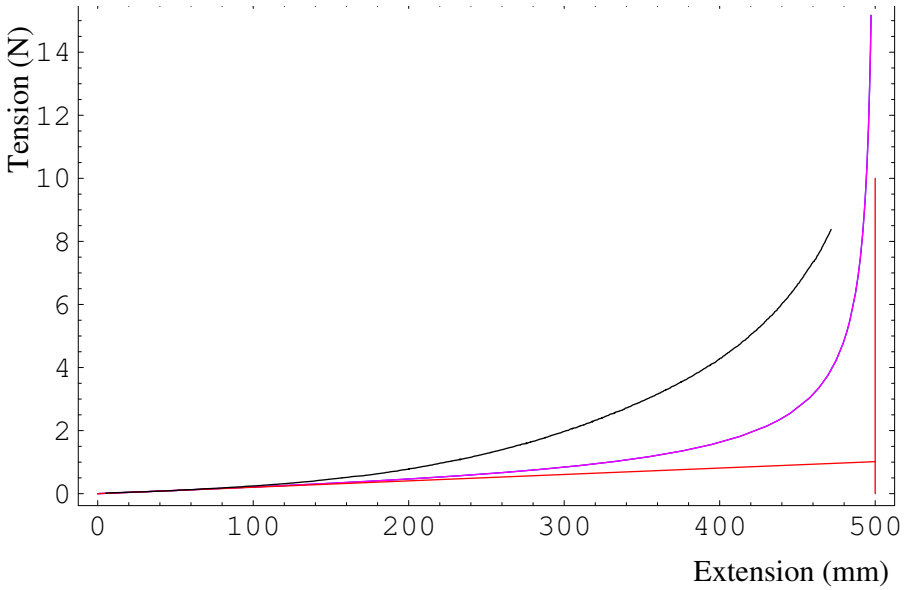


Figure 3.9: Fitting Data

from which we can deduce ϕ, and hence, from the original length, $N\Lambda$.

At the other extreme, consider the case when $\theta = (\pi - \phi)/2 - \epsilon$, where $\epsilon \ll 1$. Expanding (3.38) and (3.39) in powers of ϵ we get

$$\begin{aligned} \text{extension} &= N\Lambda\left(\epsilon\cos\frac{\phi}{2} - \frac{\epsilon^2}{2}\sin\frac{\phi}{2}\right) + O(\epsilon^3), \\ \text{tension} &= \frac{4MK}{\Lambda}\left(\frac{\epsilon}{\cos\phi/2} + \frac{\epsilon^2}{2}\tan\frac{\phi}{2}\right) + O(\epsilon^3). \end{aligned}$$

Thus we expect the slope of the tension-extension near the origin to be given by

$$\frac{4KM}{N\Lambda^2\cos^2\phi/2} + O(\epsilon).$$

This slope can be measured either graphically, or by fitting the data for low extension to a linear function. We now have sufficient information to infer K/Λ.

3.3.1.1 Typical Results

Figure 3.9 shows a typical set of experimental force-extension data (black line). The red lines correspond to the limiting value of extension and a fit to the slope of the curve for small force. The mauve line is the predicted shape based on the hinged rods model discussed above. Some points to note :

- The fit is very poor, especially for medium extension values

- Finding the maximum value of the extension is very difficult from this curve, as the tow had not been extended enough. The tow was discarded at the end of the experiment, preventing any further measurments being made.

Can we improve on this? Physically, we might expect the curve not to hold when the rods are nearly straight. In this situation, the assumption of rigidity (i.e. that they do not extend or bend) is far from the actual situation. This is particularly important for the fibres in tow, which are relatively elastic. The apparent "asymptote" of the experimental data is not vertical, so we expect that in practical secondary crimp, extension will become important.

3.3.2 Extensible, Unbending rods

Consider the tow comprising a number of unbending, extensible rods joined by elastic hinges. We suppose a linear relationship between tangential force and extension of the rod, such that if τ_n is the force along the rod and Λ_n the length, then

$$\Lambda_n = \Lambda_0 \left(1 + \frac{\tau_n}{E}\right)$$

for an elastic constant E. Once again, the hinges are such that the torque (T_n) is

$$K(\Theta_n - \phi).$$

Now consider the equilibrium of the rods. Balancing moments gives

$$\theta_{n+1} - 2\theta_n + \theta_{n-1} - 2(-1)^n(\pi - \phi) - \frac{F\Lambda_n}{K}\sin\theta_n = 0 \tag{3.40}$$

whilst a force balance gives

$$F\cos\theta_n = E\frac{\Lambda_n - \Lambda_0}{\Lambda_0}. \tag{3.41}$$

Let us now seek a solution such that

$$\begin{aligned} \Lambda_n &= \Lambda, \\ \theta_n &= -(-1)^n\theta. \end{aligned}$$

This transforms (3.40) into

$$4\theta - 2(\pi - \phi) + \frac{F\Lambda}{K}\sin\theta = 0.$$

Solving for the tension we get

$$F = \frac{K}{\Lambda}\frac{2(\pi - \phi) - 4\theta}{\sin\theta} \tag{3.42}$$

so that the tension is

$$\frac{MK}{\Lambda}\frac{2(\pi-\phi)-4\theta}{\sin\theta}.$$

A simple rearrangement of (3.41) gives

$$\Lambda = \Lambda_0\left(1+\frac{F\cos\theta}{E}\right) \tag{3.43}$$

and the extension is

$$N\left(\Lambda\cos\theta - \Lambda_0\cos\left(\frac{\pi}{2}-\frac{\phi}{2}\right)\right).$$

Eliminating F from (3.42) and (3.43) gives

$$\Lambda = \frac{\Lambda_0}{2} \pm \sqrt{\frac{\Lambda_0^2}{4}+\frac{\Lambda_0 K}{E}\left(\frac{(2(\pi-\phi)-4\theta)\cos\theta}{\sin\theta}\right)}$$

and we require the larger value (as we expect the rods to elongate). So, in summary we have that

$$\Lambda = \frac{\Lambda_0}{2} + \sqrt{\frac{\Lambda_0^2}{4}+\frac{\Lambda_0 K}{E}\left(\frac{(2(\pi-\phi)-4\theta)\cos\theta}{\sin\theta}\right)}, \tag{3.44}$$

$$\text{Tension} = \frac{MK}{\Lambda}\frac{2(\pi-\phi)-4\theta}{\sin\theta}, \tag{3.45}$$

$$\text{Extension} = N\left(\Lambda\cos\theta - \Lambda_0\cos\left(\frac{\pi}{2}-\frac{\phi}{2}\right)\right). \tag{3.46}$$

As E becomes large, $\Lambda \to \Lambda_0$ and we return to the original equations for the rigid rods.

3.3.3 Fitting the data

Let us consider the behaviour of (3.44)-(3.46) for the cases when θ is small and when θ is near to $\pi/2-\phi/2$.

3.3.3.1 Large Tension

We write $\theta \ll 1$ and expanding (3.44) we get

$$\Lambda \sim \sqrt{\frac{K\Lambda_0}{E}}\frac{\sqrt{2(\pi-\phi)}}{\sqrt{\theta}} + \frac{\Lambda_0}{2} + O(\sqrt{\theta}). \tag{3.47}$$

Using this, and substituting in (3.45) gives the tension as

$$\sim M\sqrt{\frac{2EK(\pi-\phi)}{\Lambda_0}}\frac{1}{\sqrt{\theta}} + \frac{EM}{2} + O(\sqrt{\theta}) \tag{3.48}$$

and (3.46) gives the extension as

$$\sim N\sqrt{\frac{2\Lambda_0 K(\pi-\phi)}{E}}\frac{1}{\sqrt{\theta}}+\frac{N\Lambda_0}{2}\left(1-\sin\frac{\phi}{2}\right)+O(\sqrt{\theta}). \tag{3.49}$$

Now we are in the position to be able to calculate the slope of the tension-extension graph for large values of extension which is

$$\frac{ME}{N\Lambda_0}+O(\sqrt{\theta}).$$

This suggests that for large forces, the slope is governed by the extensional properties of the fibre itself as one would expect on physical grounds.

Now consider the intercept of the asymptote given by (3.48) and (3.49). Simple manipulation gives that, as $\theta \to 0$, the intercept on the extension axis is

$$-\frac{N\Lambda_0}{2}\sin\frac{\phi}{2}$$

which gives us information about the equilibrium angle ϕ.

3.3.3.2 Small Tension ($\theta = \pi/2 - \phi/2 - \epsilon$)

We write $\theta = \pi/2-\phi/2-\epsilon$ where $\epsilon \ll 1$ and we again expand (3.44)-(3.46) in a series in powers of ϵ to get

$$\begin{aligned}
\Lambda &\sim \Lambda_0+\frac{4K}{E}\tan\frac{\phi}{2}\epsilon+O(\epsilon^2)\\
\text{Tension} &\sim \frac{4KM}{\Lambda_0}\sec\frac{\phi}{2}\epsilon+O(\epsilon^2) &(3.50)\\
\text{Extension} &\sim N\left(\Lambda_0\cos\frac{\phi}{2}+\frac{4K\sin^2\phi/2}{E\cos\phi/2}\right)\epsilon+O(\epsilon^2). &(3.51)
\end{aligned}$$

Hence the slope as $\theta \to \pi/2-\phi/2$ is given by

$$\frac{4KM}{\Lambda_0^2 N\left(\cos^2\phi/2+\frac{4K}{E\Lambda_0}\sin^2\phi/2\right)}$$

which again reverts to that for the inextensible rods when $K/(E\Lambda_0)$ is small.

3.3.3.3 Numerical Fitting

From the above analysis, we have found the following quantities

$$\text{End Slope} \sim \frac{ME}{N\Lambda_0} \tag{3.52}$$

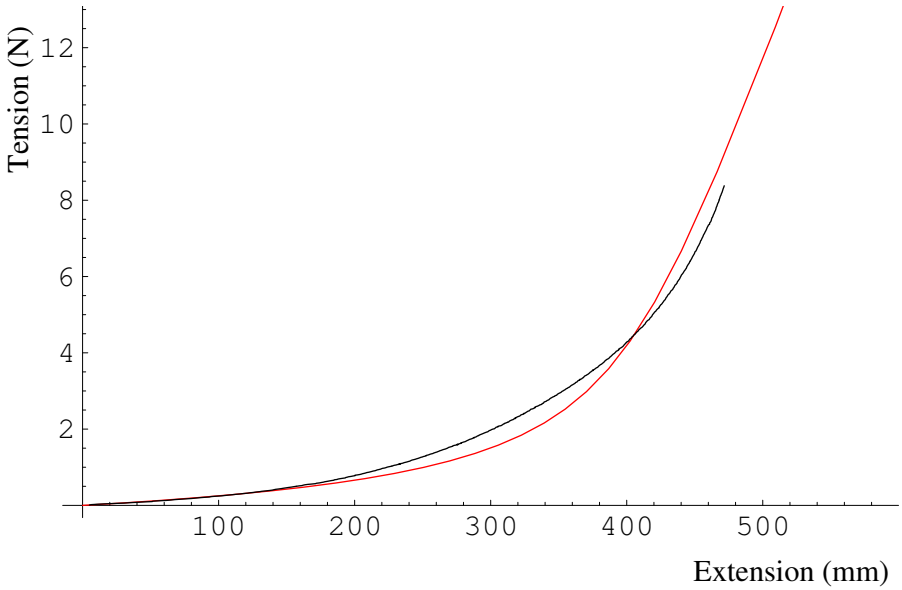


Figure 3.10: A comparison of a theoretical and experimental curve

$$\text{End Intercept} \sim ME\left(\sin\frac{\phi}{2} - 1\right) \tag{3.53}$$

$$\text{Start Slope} \sim \frac{4K}{\Lambda_0 E}\frac{\frac{ME}{N\Lambda_0}}{\cos^2\phi/2 + \frac{4K}{\Lambda_0 E}\sin^2\phi/2} \tag{3.54}$$

which can easily be estimated from the experimental data. We already know that if we now make a guess for the value of E, and use experimental values for (3.52), (3.53) and (3.54) we can evaluate $N\Lambda_0$, ϕ and $\frac{K}{\Lambda_0 E}$. We can now assess the accuracy of the model as follows :

1. Calculate pairs of tension–extension points for a range of θ from the extensible hinged rods model with the values of the parameters described above.

2. Construct an interpolating function $F(\text{extension})$ that passes through these points.

3. Define the error as
$$\sum_i \left(\text{tension}_i - F(\text{extension}_i)\right)^2$$
where $()_i$ denotes a data-point.

We can now treat this error as a nonlinear function of ME, and we can search for a minimum in this function. For our trial dataset, we find a minimum for $ME \simeq 1000$. A comparison of the predicted and dataset curve is shown in figure 3.10.

3.4 Naturally-curved Fibres

The second model of the crimped fibre that we will discuss treats the fibre as an elastica whose unstressed configuration is curved on a short length-scale (see figure 3.11). Let us denote $\theta(s) \sim 0(1)$ to be the angle between the tangent to the curve at point s and the direction of an externally applied force $\mathbf{F}$. In addition, we will describe the natural shape of the fibre by $\Xi(s)$ such that, when no forces are applied

$$\theta(s) = \Xi(s).$$

We consider the case when the natural shape varies over a very short length scale ϵ. If we let t be the distance along the fibre at this scale, then

$$t = \frac{s}{\epsilon} \text{ and we write } \Xi(s) = \alpha(t).$$

For convenience we will also choose α to be periodic in t, such that

$$\begin{aligned} \alpha(t) &= \alpha(t+1), \\ \int_0^1 \sin\alpha dt &= 0, \qquad (3.55) \\ \int_0^1 \cos\alpha dt &= \Upsilon, \qquad (3.56) \end{aligned}$$

where Υ is the ratio of the horizontal extent of the curved fibre to the fully extended length and the integral is taken over one period of the fibre. Equation (3.55) implies that, in the unstressed configuration, the fibre lies along the x-axis when viewed over a long length scale.

The relationship between the moment $M(s)$ and curvature is given by

$$M(s) = EI\left(\frac{d\theta}{ds} - \frac{d\Xi}{ds}\right),$$

where E and I are the Young's modulus and moment of area as in the usual Euler-strut notation. Balancing moments and forces, and writing

$$\lambda^2 = \frac{F}{EI}$$

as the non-dimensional force, we arrive at the equilibrium equation

$$\frac{d^2\theta}{ds^2} - \frac{d^2\Xi}{ds^2} + \lambda^2 \sin\theta = 0. \qquad (3.57)$$

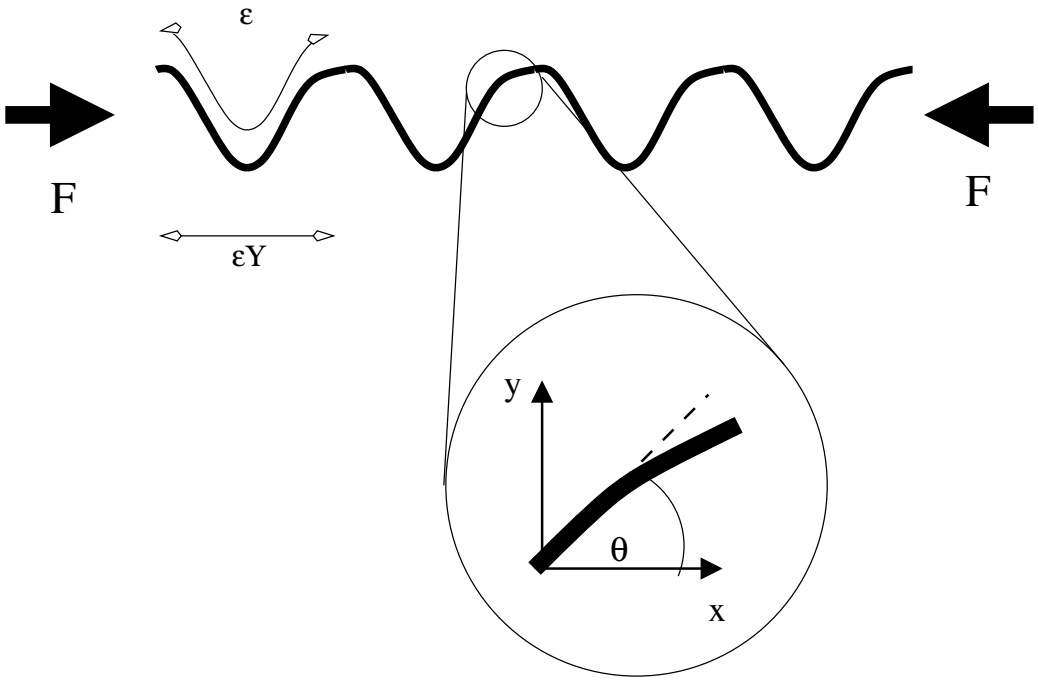


Figure 3.11: A smoothly curved fibre

3.4.1 Multiple scales analysis

Because there are two length scales s and t in this problem we can use the multiple scales method to analyse this problem (3.57). We write that

$$\frac{d}{ds} = \frac{\partial}{\partial s} + \frac{1}{\epsilon}\frac{\partial}{\partial t}$$

and seek a solution of the form

$$\theta(s) = \theta_0(s,t) + \epsilon\theta_1(s,t) + \epsilon^2\theta_2(s,t)$$

where we assume that $\theta_n(s,t)$ does not grow in t.
Expanding (3.57) as a series in ϵ and equating like powers of ϵ we have, (if $\lambda \sim O(1)$)

to $O(\epsilon^{-2})$

$$\theta_{0tt} - \alpha_{tt} = 0; \tag{3.58}$$

to $O(\epsilon^{-1})$

$$\theta_{1tt} + 2\theta_{0st} = 0; \tag{3.59}$$

to $O(1)$

$$\theta_{2tt} + 2\theta_{1st} + \theta_{0ss} + \lambda^2 \sin\theta_0 = 0. \tag{3.60}$$

After imposing that θ does not grow indefinitely as $t \to \infty$, (3.58) has the solution

$$\theta_0 = \alpha(t) + B_0(s).$$

Substituting into (3.59) we find

$$\theta_{1tt} = 0 \quad \Rightarrow \quad \theta_1 = A_1(s)t + B_1(s).$$

However, our desire that θ be periodic in t means that $A_1(s) = 0$. Substituting now into (3.60) we obtain

$$-\theta_{2tt} = B_{0ss} + \lambda^2 \sin B_0 \cos\alpha(t) + \lambda^2 \cos B_0 \sin\alpha(t) \tag{3.61}$$

By the Fredholm Alternative, if there is to be a non-trivial solution of (3.61) bounded as $t \to \infty$, then we require

$$\int_0^1 \left(B_{0ss} + \lambda^2 \sin B_0 \cos\alpha(t) + \lambda^2 \cos B_0 \sin\alpha(t)\right) dt = 0.$$

Applying (3.55) and (3.56) we deduce that

$$B_{0ss} + \Upsilon\lambda^2 \sin B_0 = 0.$$

If we now think in terms of a variable measuring the horizontal extent of the fibre in the natural state, rather than the distance along the fibre, we set $s' = \Upsilon s$ to give

$$B_{0s's'} + \frac{\lambda^2}{\Upsilon} \sin B_0 = 0. \tag{3.62}$$

This is the Euler Strut equation for a beam of stiffness $EI\Upsilon$, i.e. a less stiff beam than the original unbuckled material.

3.4.2 Hinged Rods revisited

Let us now cast our minds back to the hinged rods model we spent so much time considering in section 3.2. Through an appropriate asymptotic expansion, we found from (3.28) that

$$\frac{d^2\Sigma^{(1)}}{ds^2} + \kappa' \cos\frac{\chi}{2} \cdot \sin\Sigma^{(1)} = 0.$$

where $\Sigma^{(1)}$ is the inclination of the "concertina" to its mean direction. In this equation, $s = \frac{n}{N}$ and hence is equivalent to the distance measured along the rods. A simple change of variables to

$$s' = s\cos\frac{\chi}{2}$$

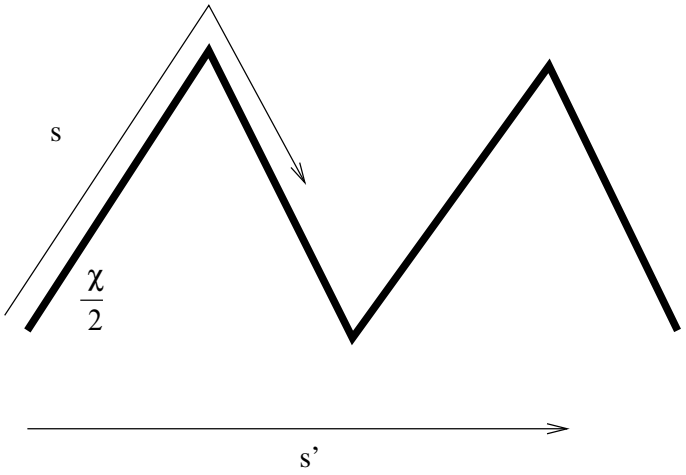


Figure 3.12: s and s' for the hinged rods model

leads to

$$\frac{d^2\Sigma^{(1)}}{ds'^2} + \frac{\kappa'}{\cos\chi/2}\sin\Sigma^{(1)} = 0 \tag{3.63}$$

where s' is the distance measured macroscopically (see figure 3.12).

Now consider the case when the unstressed configutation of the hinged rods model is straight (i.e. $\phi = \pi$). For this special case, equation (3.1) reduces to

$$\theta_{n+1} - 2\theta_n + \theta_{n-1} + \kappa\sin\theta_n = 0$$

Writing $s = \epsilon n$, and expanding as for equation (3.20) we get

$$\frac{d^2\theta}{ds^2} + \kappa'\sin\theta = 0 \tag{3.64}$$

where

$$\kappa' = \frac{\kappa}{\epsilon^2}.$$

Thus the hinged rods model and the naturally curved fibre models have both led to the same model which can be interpreted as an "equivalent" Euler Strut model. In each case, we have simplified the model by asymptotically separating the short and long scale variations. The resulting equations show the same behaviour as a less stiff system without the small scale variations. To summarise

Euler Strut			Hinged Rods		
$\frac{d^2\theta}{ds^2} + \lambda^2\sin\theta$	$=$	0	$\frac{d^2\theta}{ds^2} + \kappa'\sin\theta$	$=$	0
$\frac{d^2B_0}{ds'^2} + \frac{\lambda^2}{\Upsilon}\sin B_0$	$=$	0	$\frac{d^2\Sigma^{(1)}}{ds'^2} + \frac{\kappa'}{\cos\chi/2}\sin\Sigma^{(1)}$	$=$	0

We now have some understanding of the behaviour of the crimped fibre under compression and extension. This predicts that under certain circumstances a bifurcation can occur from a nearly flat configuration to an arched formation. This could be a model for secondary crimp formation. In the next chapter, we shall discuss the subsequent behaviour of the material as it moves through the hinged plates of the stuffer box.

Chapter 4

Modelling the Block Motion

4.1 Introduction

In this chapter we will discuss models for the material inside the stuffer box between the plates. As distinct from primary and secondary crimp, the orientation of the tow in this area undergoes no major changes but it is subject to compressive and small 'elastic' strains. The material in this region is therefore referred to as "the block". Although there are no major structural changes occurring in this region, the properties of the block change, as new material is introduced at one end after secondary crimp, and removed from the other end by a conveyor belt. The resulting flow of material through the block is resisted by frictional forces between the fibre and the plates and side walls.

The block is compressed between the top and bottom plates of the stuffer box. The upper plate is hinged at the end that the fibre enters (figure 4.2, and has a fixed moment applied to it by the addition of a weight on the top plate. This moment is one of the main control parameters for the stuffer box crimper. It will partly govern the magnitude of the frictional forces that oppose the motion of the block, and hence the force acting on the fibre in the nip that causes primary and secondary crimp. In this chapter we will show how simple models for the block can be coupled with models for the primary and secondary crimp to determine a complete model for the crimper. By doing so, we shall see how the choice of model for the block material alters the stability of the crimper, and that the work undertaken in chapters 2 and 3 need to be rethought in order to give physically realistic results for the modelling of the stuffer box.

4.2 Concept

Let us begin by considering the motion of the block in isolation. We must include a number of factors when modelling the stuffer box:

- **Properties of the material**
  The small scale structure of the material in the block is very complicated (see figure 4.1). Modelling all the interactions that take place between fibres would be excessively difficult. Instead, we shall treat the block as a homogenised material whose properties depend on the position along the stuffer box. In addition, although it is possible that plastic deformation and enviromental conditions[1] within the stuffer box could lead to fibre properties that change with time, we shall ignore these effects and concentrate on modelling the block as a quasi-static elastic material.

  We shall consider two different models for the material in the block. Firstly, we will use a greatly simplified picture of the material as a series of vertical springs. In contrast to this, the second model will imagine that the disordered jumble of fibre is equivalent to an isotropic elastic material. In each case, we shall have a number of parameters that must be determined. There are two main methods of doing this. The first is to measure them experimentally, and assume that their value does not depend on the small scale structure. An alternative technique is to look at a model for the micro-structure, and determine how this responds to certain applied forces. This can then be compared with the responses made by the homogenised material, and hence bulk properties deduced.

  Finally, our model for the block will require knowing the amount of material present at each point of the stuffer box. This will depend on the conditions under which the material entered between the plates, and the choice of secondary crimp model.

[1] As material passes through the stuffer box, it loses some of the solvents, resulting in a change in physical properties.

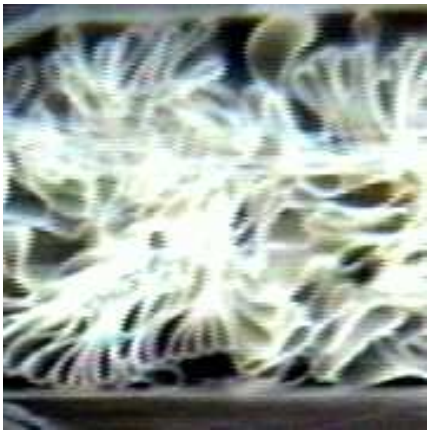


Figure 4.1: Video still of a section of the block.

- **Interaction between the block and stuffer box**
  The fibre interacts with walls of the stuffer box through two mechanisms : reaction forces and frictional forces. The reaction forces exert a moment on the hinged plate which, in equilibrium, must balance the externally applied moment. This condition will determine the angle the top plate makes with the horizontal. It is important to note that the block material can lose contact with a section of the upper plate of the stuffer box. When this occurs we have a free boundary problem for the point P in figure 4.2.

  The frictional forces in the stuffer box determine the compressive force applied to the fibres in the primary and secondary crimp regions. Unfortunately, frictional forces between elastic solids and rigid surfaces introduce many complications to otherwise simple contact problems. We consider two options in how we implement friction. The simplest is to assume that all points at the surface of the block are in limiting friction such that

  $$q = \mu p$$

  where p is the stress normal to the plate and q is the stress tangential to the boundary. A more physically realistic option is to divide the boundary into two regions. In the first, slip has occurred and

  $$u > 0 \qquad \text{and} \qquad q = \mu p$$

  where u is the displacement of the block parallel to the boundary relative to its orriginal position. In the second, no slip has occurred, and hence

  $$u = 0 \qquad \text{and} \qquad q \leq \mu p.$$

This adds another free boundary to the problem. Some solutions can be found for such problems (for example, see Spence [14] for a discussion of a Hertz contact problem with finite friction), but the problem is usually difficult. Thankfully, in our case we are interested in situations where the force is sufficient to move all the block, and hence the assumption that all contact points are in limiting friction can be justified.

- **Motion of material through the stuffer box**

  Consider the material labelled A at time t and at position x in figure 4.2. After a small time δt this has advanced through the box to A' due to material entering the box at position $x = 0$. Let $Q(t)$ be the rate of arrival of material at $x = 0$. If the material at A at time t entered the block at time t_0 then, in the absence of compression within the block, it is now at

$$\begin{aligned} x(t, t_0) &= \int_{t_0}^{t} Q(t')dt' \\ &= \int_{0}^{t} Q(t')dt' - \int_{0}^{t_0} Q(t')dt'. \end{aligned}$$

  If we make the reasonable assumption that $Q(t) \geq 0$ then it makes sense to write[2]

$$\chi = \int_{0}^{t} Q(t')dt'$$

  and hence

$$x = \chi - \chi_0, \tag{4.1}$$

  where χ_0 is the value of the Lagrangian variable χ when the material entered the stuffer box. If we let $f(\chi_0)$ be a property of the material when it enters the box then the property $F(x, t)$ of the material at position x at time t is given by

$$F(x, t) = f(\chi - x). \tag{4.2}$$

  This assumes that the rate of motion of material is proportional to the rate of arrival of material, and constant throughout the length of the box. Changes is the height of the material as it moves through the box are taken care of by vertical elasic expansion and compression. Furthermore, there is no horizontal compression. In the first model for the material entering the stufferbox (where we shall consider it composed of springs) this latter assumption is always valid.

[2]Note that χ is the amount of material which has entered the stuffer box in time t and so if material is fed in at a constant rate χ is proportional to t.

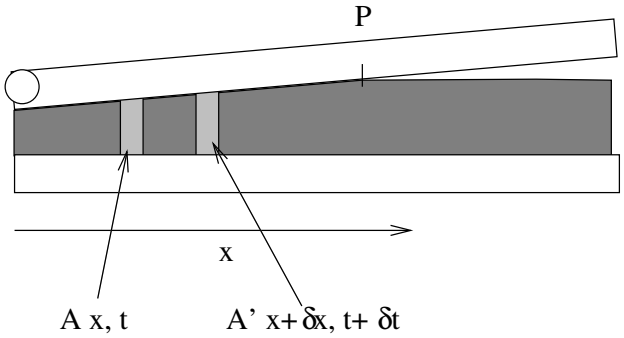


Figure 4.2: Diagram of the stuffer box, showing movement of material from A to A'

For the isotropic model, the horizontal compression is of the same magnitude as the vertical displacement, and hence the relationship between (say) $F(x,t)$ and $f(\chi - x)$ will only hold for small height changes.

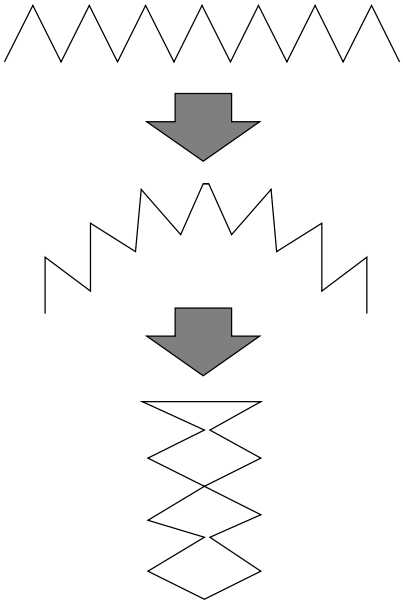


Figure 4.3: Formation of the block through secondary crimp

4.2.1 Models for the amount of material entering the block

We expect the amount of material entering the block to depend on the events occurring inside the nip of the stuffer box crimper. In chapter 2 we discussed how the peak force exerted on the block increases as more fibre is added. Our treatment of the secondary crimp in turn predicts that a buckle in the crimped material will occur when a critical condition is achieved. Our aim is to use these models to determine the amount of material entering the block at the hinged end and the force required to move the block. To this end we make the assumption, based on experimental evidence, that the length of crimped material that buckles to form secondary crimp is twice the equilibrium height of material entering the block (see figure 4.3). In addition we will equate the force associated with this buckle to the force required to move the block.

Under these assumptions, and recalling the discussions in chapter 3, we can write the equilibrium height of the block as either (from 3.35)

$$H_0 = \frac{\pi}{2}\sqrt{\frac{\Lambda K \cos\chi/2}{F}}$$

or

$$H_0 = \frac{\pi}{2}\sqrt{\frac{EI}{\Upsilon F}} \tag{4.3}$$

depending on whether we use the hinged rods or crimped elastica models for secondary crimp formation. Unfortunately we are still left with the undetermined parameters (Λ, K and χ or Υ). However, we can either deduce these from the primary crimp model or assume that they are independent of the operating conditions of the crimper.

4.2.2 Models for the micro-structure of the block

We will now consider two simplified models for the micro-structure of the block. Our aim is to understand the homogenised elastic properties. To this end, we shall consider two illustrative fibre arrangements (see figure 4.4). The first, a thought experiment, is a loop of fibre being compressed due to contact with other loops (I). The second is a folded elastica (II). Each will be modelled using the equations of the two dimensional elastica that we are familiar with from chapter 2. We shall then consider the response (i.e. deflection of the top surface) of these when acted on by a compressive force. This can then be compared with the results of applying the same force to an identical sized section of the block, and hence deducing the constants of the elastic model.

The problem of a hoop-shaped elastica under point contact has been extensively described in the literature [7]. We will briefly describe the analysis performed for this configuration before showing how it can be extended to

- A hoop touching others above and below
- A hoop touching others above, below and to each side
- A folded elastica (II) touching others above and below.

4.2.2.1 Loops of Elastica

Remember that the elastica obeys the equation

$$\begin{aligned} \frac{d^2\theta}{ds^2} + \frac{F_x}{EI}\sin\theta &= \frac{F_y}{EI}\cos\theta \\ \frac{dx}{ds} &= \cos\theta \\ \frac{dy}{ds} &= \sin\theta. \end{aligned}$$

We consider the half loop of material from A to B (total circumference $2L$) with boundary conditions

$$\begin{aligned} \theta(0) &= \pi \\ \theta(L) &= 0 \\ F_x &= 0 \\ F_y &= F, \end{aligned}$$

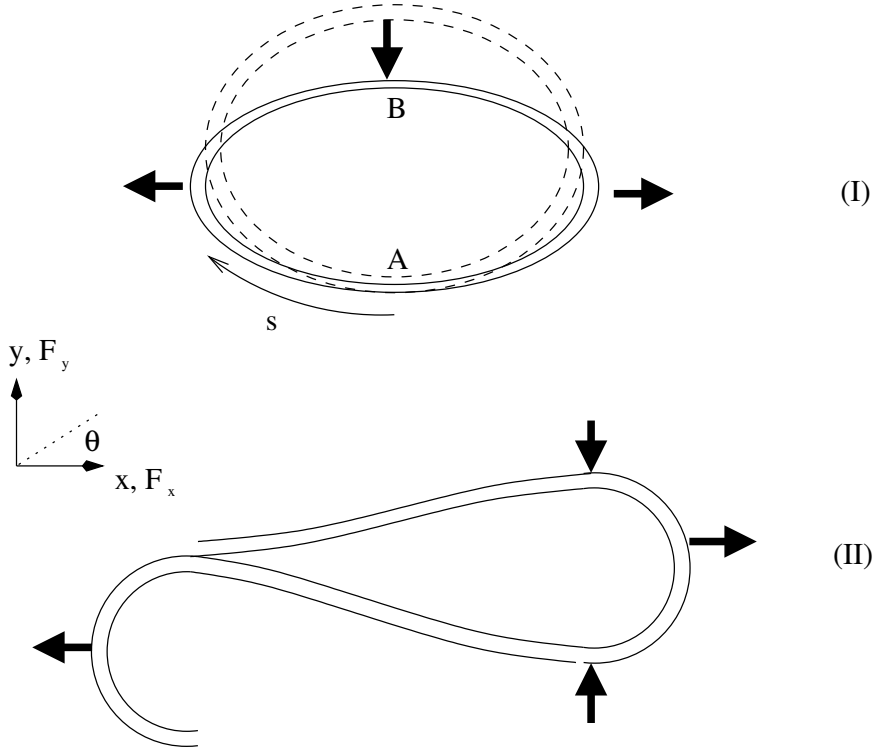


Figure 4.4: Two possible fibre arrangements

which assumes that the vertical force is F and that there is no horizontal external force. Non-dimensionalizing length such that

$$s = Ls'$$

rearranging and dropping the primes we find that

$$\begin{aligned} \frac{d^2\theta}{ds^2} - \lambda^2 \cos\theta &= 0 && (4.4) \\ \lambda^2 &= \frac{L^2 F_y}{EI} \\ \theta(0) &= \pi && (4.5) \\ \theta(1) &= 0. && (4.6) \end{aligned}$$

Integrating and rearranging leads to

$$\frac{d\theta}{\lambda\sqrt{\sin\theta + C}} = \pm ds\sqrt{2}$$

where C is the constant of integration. By making the substitutions

$$\begin{aligned} \theta &= -\frac{\pi}{2} + 2\alpha \\ C + 1 &= \frac{2}{\sin^2\beta} \end{aligned}$$

this can be rewritten as

$$\begin{aligned}\frac{\sin\beta d\alpha}{2\lambda\sqrt{1-\sin^2\beta\sin^2\alpha}} &= \pm ds\\ \alpha(0) &= \frac{3\pi}{4}\\ \alpha(1) &= \frac{\pi}{4}.\end{aligned}$$

Integrating over the length and taking $-$ sign since α is decreasing gives

$$\frac{\sin\beta}{2\lambda}\left(\text{EllipticF}\left(\frac{3\pi}{4},\beta\right)-\text{EllipticF}\left(\frac{\pi}{4},\beta\right)\right)=1 \tag{4.7}$$

where EllipticF is the elliptic integral of the first kind, defined by

$$\text{EllipticF}\left(\alpha,\beta\right)=\int_0^\alpha\frac{d\alpha'}{\sqrt{1-\sin^2\beta\sin^2\alpha}}.$$

Since

$$\theta'(0)=\lambda\frac{\sqrt{\cos 2\beta}}{\sin\beta},$$

the solution of (4.7) for $\beta(\lambda)$ has turned our boundary value equation into an initial value problem that is much more amenable to numerical solution. From this, it is a trivial matter to find computationally the shape ($x(s)$ and $y(s)$).

We are primarily interested in this loop of elastica as a model for the microstructure of the block. Take a small section of block of the same dimensions as the loop, and apply a compressive force to it (see figure 4.5). Now adjust the elastic properties of the block material until the response (movement of the top surface) is the same as that of the loop of elastica. In order to do this we need to know the response of the elastica to the same force. Figure 4.6 is a plot of the strain

$$\frac{\text{change in height}}{\text{original Height}}$$

against stress

$$\frac{\text{applied force}}{\text{projected area of loop normal to applied force}}$$

for a loop of elastica of unit width[3] in non-dimensional units. Notice that the graph is nearly linear, which will justify the assumptions we shall later make about the elastic properties of the material.

[3]Unit width in this case means that the elastica is of unit width, not the loop

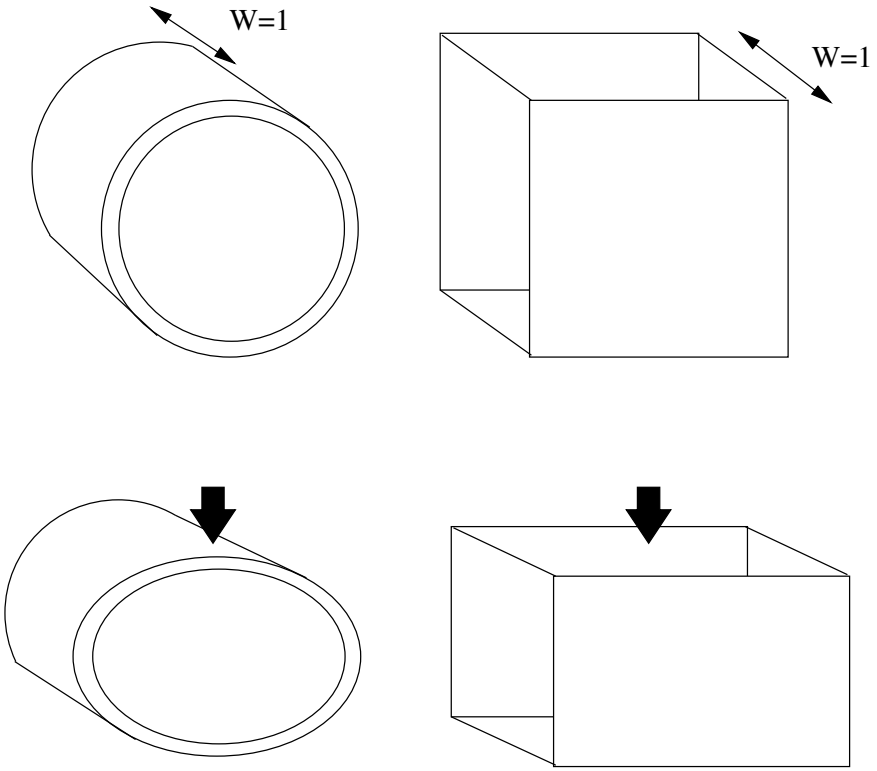


Figure 4.5: Comparison of loop microstructure with the material from the block

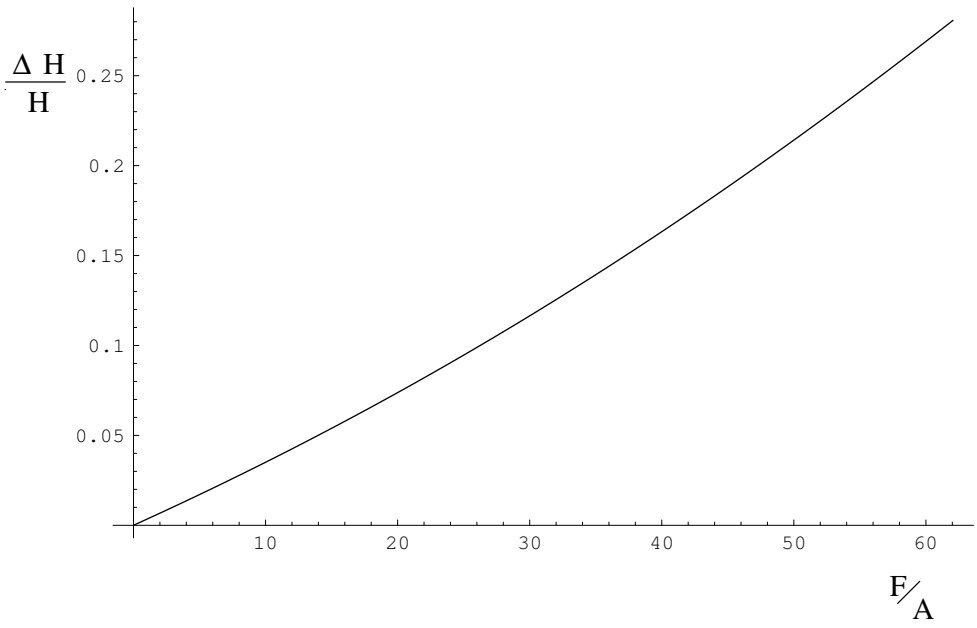


Figure 4.6: Strain vs. stress for a loop of elastica

4.2.2.2 Loop touching others above and below

This is identical to the above analysis, except that the fibre can be in continuous contact over a region. By symmetry, the contact region between the adjacent loops is flat, and there are no body forces acting, so we will be able to treat the contact in the same manner as the flat sections in chapter 2. If we this time denote z to be the length of the flat section, then the curved length is trivially given by $(1-z)$. The curved section has the boundary conditions

$$\begin{aligned} \theta(0) &= \pi \\ \theta'(0) &= 0 \\ \theta(1-z) &= 0 \\ \theta'(1-z) &= 0. \end{aligned}$$

Hence, identical analysis to that above, gives

$$\begin{aligned} \cos 2\beta &= 0 \\ \Rightarrow \beta &= \frac{\pi}{4} \\ \frac{\lambda(1-z)}{4} &= \text{EllipticF}\left(\frac{3\pi}{4}, \frac{\pi}{4}\right) - \text{EllipticF}\left(\frac{\pi}{4}, \frac{\pi}{4}\right). \end{aligned}$$

Once again, this will give us our initial condition to solve the problem numerically, and from which we can determine the elastic properties. Figure 4.7 shows the strain vs. stress graph for this elastica. It has a more pronounced curve, but has a similar slope.

4.2.2.3 Loop touching others above, below and to the sides

We now have forces being applied in both directions. Consider a quarter circle as shown in figure 4.8. The non-dimensional equations of the elastica can be written as

$$\begin{aligned} \frac{d^2\theta}{ds^2} + \lambda_x^2 \sin\theta &= \lambda_y^2 \cos\theta \\ \theta(0) &= \frac{\pi}{2} \\ \theta\left(\frac{1}{2}\right) &= 0. \end{aligned}$$

This can be rewritten

$$\frac{d^2\theta}{ds^2} + \lambda^2 \sin(\theta - \varphi) = 0$$

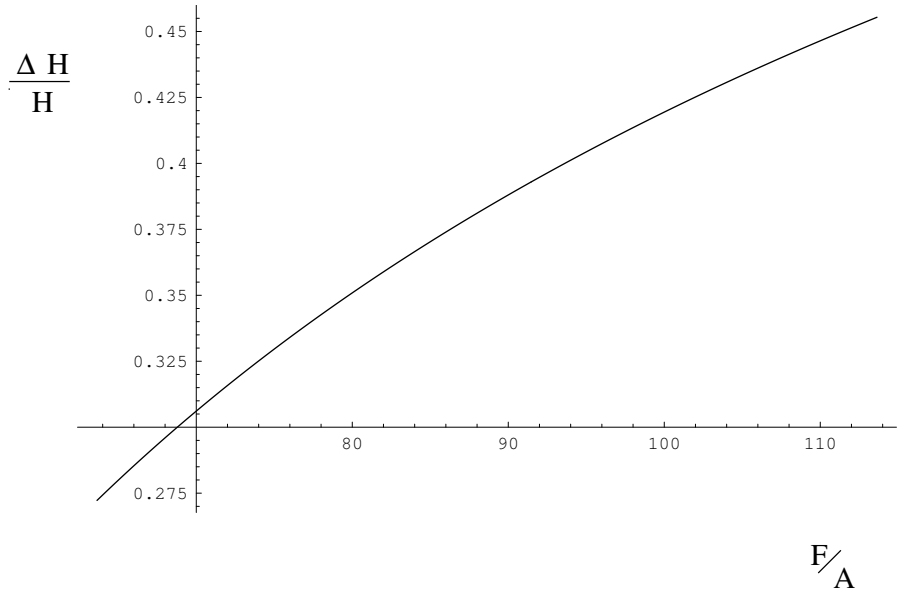


Figure 4.7: Strain vs. stress for a loop of elastica touching similar loops above and below

with

$$\begin{aligned} \lambda^2 &= \lambda_x^2 + \lambda_y^2 \\ \lambda_x^2 &= \lambda^2 \cos\varphi \\ \lambda_y^2 &= \lambda^2 \sin\varphi. \end{aligned}$$

Making the substitution $\psi = \theta - \varphi$ we obtain

$$\frac{d^2\psi}{ds^2} + \lambda^2 \sin\psi = 0 \tag{4.8}$$

subject to

$$\psi(0) = \frac{\pi}{2} - \varphi \tag{4.9}$$

$$\psi\left(\frac{1}{2}\right) = -\varphi. \tag{4.10}$$

Multiplying (4.8) by ψ' and integrating gives

$$\frac{d\psi}{\lambda\sqrt{C + \cos\psi}} = \pm ds\sqrt{2}$$

and the substitution $(C+1)\sin^2\beta = 2$ transforms this into

$$\frac{\sqrt{2}\sin\beta}{\lambda} \frac{d\psi}{\sqrt{1 - \sin^2\beta \sin^2\psi/2}} = \pm 2ds$$

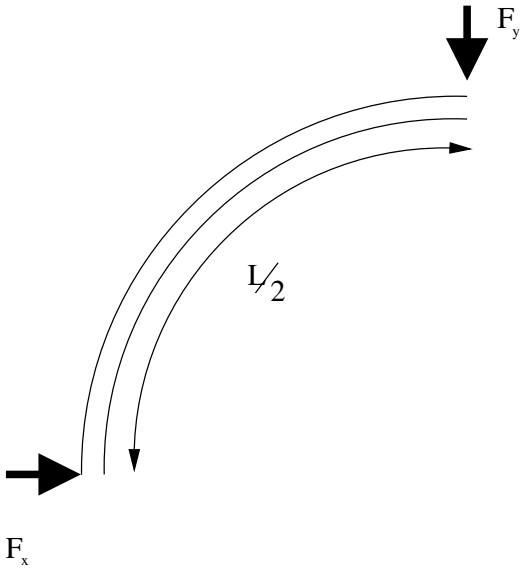


Figure 4.8: A loop touching others at four points

Integrating and applying the boundary conditions (4.9) and (4.10) results in

$$\text{EllipticF}\left(\frac{\pi}{4}-\frac{\varphi}{2},\beta\right)-\text{EllipticF}\left(-\frac{\varphi}{2},\beta\right)=\frac{2\lambda}{\sin\beta}.$$

The boundary conditions (e.g. prescribing the width and applied force on the loop) will determine the constants β and φ, and the deflection of the top surface, ΔH, can then be found. Note that for this configuration, we have a new experiment to carry out on our section of block material. As well as prescribing the vertical force, we can also imagine that the width of the block cannot change. Figure 4.9 shows the response of the loop under these conditions. Note two things in comparison with 4.6 and 4.7: firstly, the curve is very straight, and second that the slope is much less.

4.2.2.4 A folded Elastica touching others above and below

Perhaps a more realistic configuration for the block micro-structure is as a fold of elastica (see figure 4.4II). To describe this, we divide the folded elastica into two sections of non-dimensional length z and $1-z$ (see figure 4.10).

- **Semicircular Section**

$$\begin{aligned}\frac{d^2\theta_{sc}}{ds^2} &= \lambda_{sc}^2\cos\theta_{sc}\\ \theta_{sc}(0) &= \pi\\ \theta_{sc}(z) &= 0;\end{aligned}$$

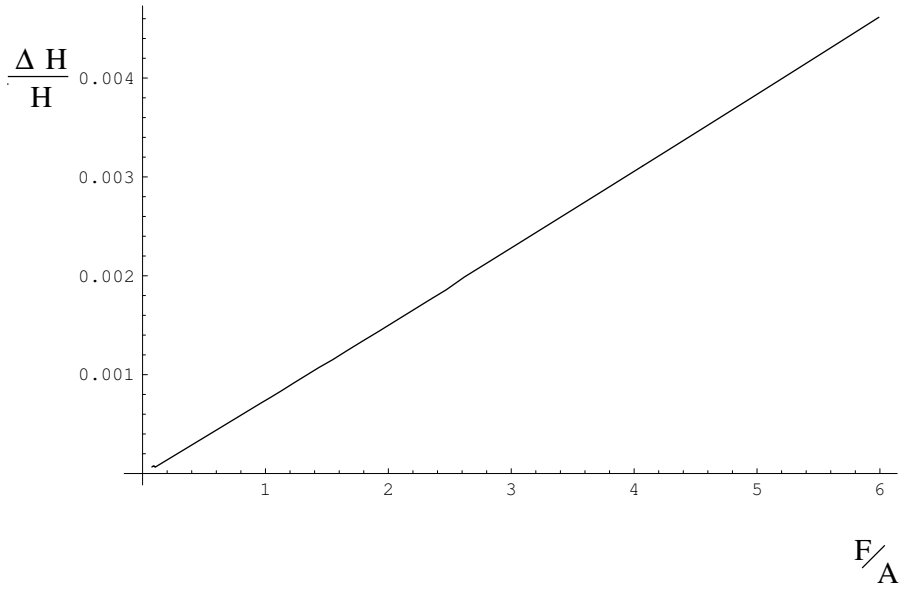


Figure 4.9: Strain vs. stress for a loop of elastica touching similar loops on four sides

- **Kinked Section**

$$\begin{aligned} \frac{d^2\theta_k}{ds^2} &= \lambda_k^2 \cos\theta_k \\ \theta_k(0) &= 0 \\ \theta_k(1-z) &= 0, \end{aligned}$$

where λ_{sc}^2 and λ_k^2 are the non-dimensional forces applied in the vertical direction in the semicircular and kinked sections respectively. Note that we are assuming that the elasticas only make point contact. We require that the moment be continuous, and so

$$\theta'(z) = \theta'(0) \tag{4.11}$$

and from symmetry we know that the height of the kink is half that of the semicircular section. Solving as before gives that

$$\begin{aligned} \frac{z\lambda_{sc}}{4\sqrt{2}\sin\beta_{sc}} &= \text{EllipticF}\left(\frac{3\pi}{4}, \beta_{sc}\right) - \text{EllipticF}\left(\frac{\pi}{4}, \beta_{sc}\right) \\ \frac{(1-z)\lambda_k}{4\sin\beta_k} &= \text{EllipticF}\left(\frac{\pi}{2}, \beta_k\right) - \text{EllipticF}\left(\frac{\phi_k}{2}, \beta_k\right), \end{aligned}$$

where β_k and ϕ_k are related by

$$\sin\left(\frac{\pi}{4}\right) = \sin\beta_k \sin\frac{\phi_k}{2}.$$

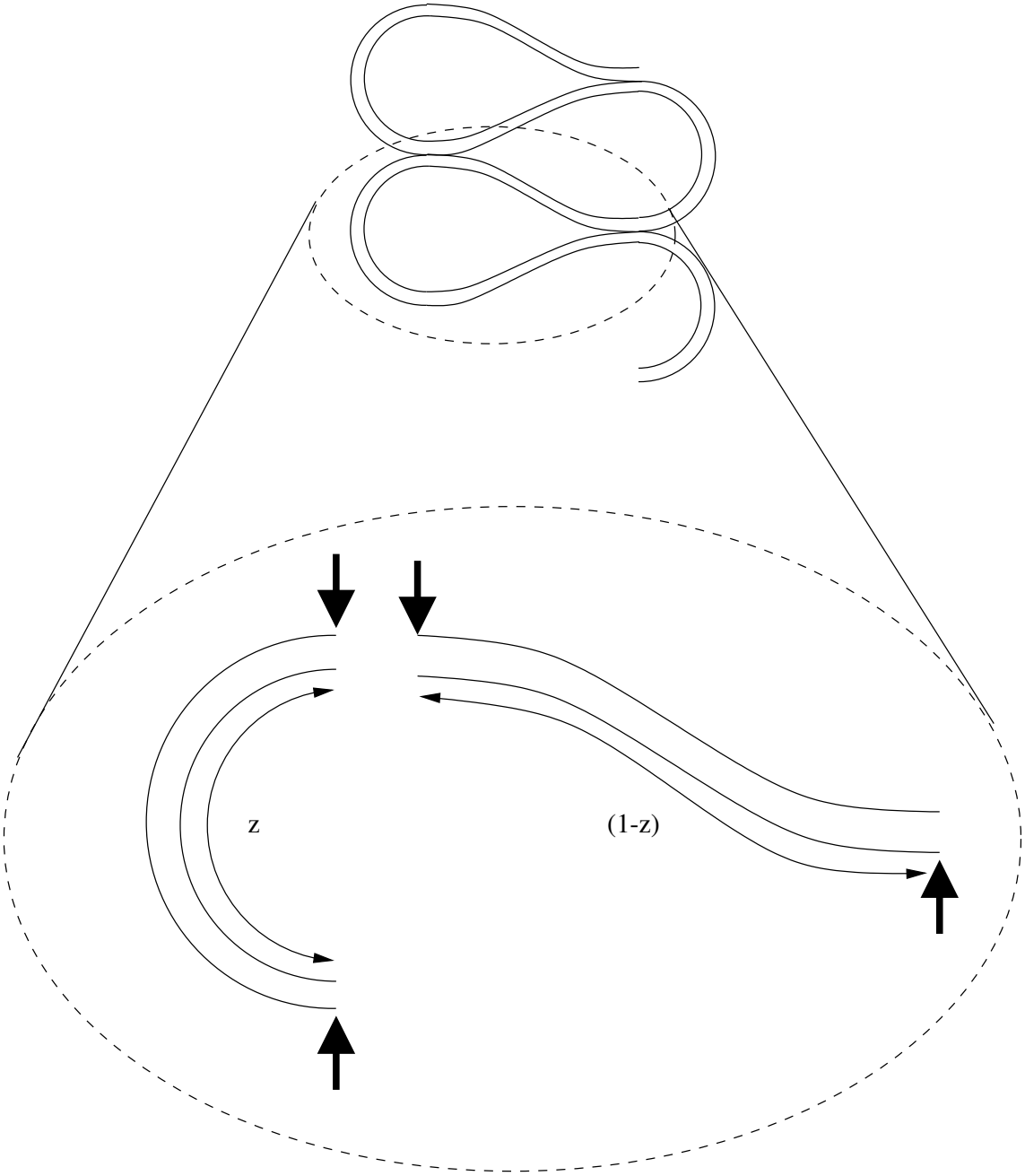


Figure 4.10: Structure of the folded Elastica

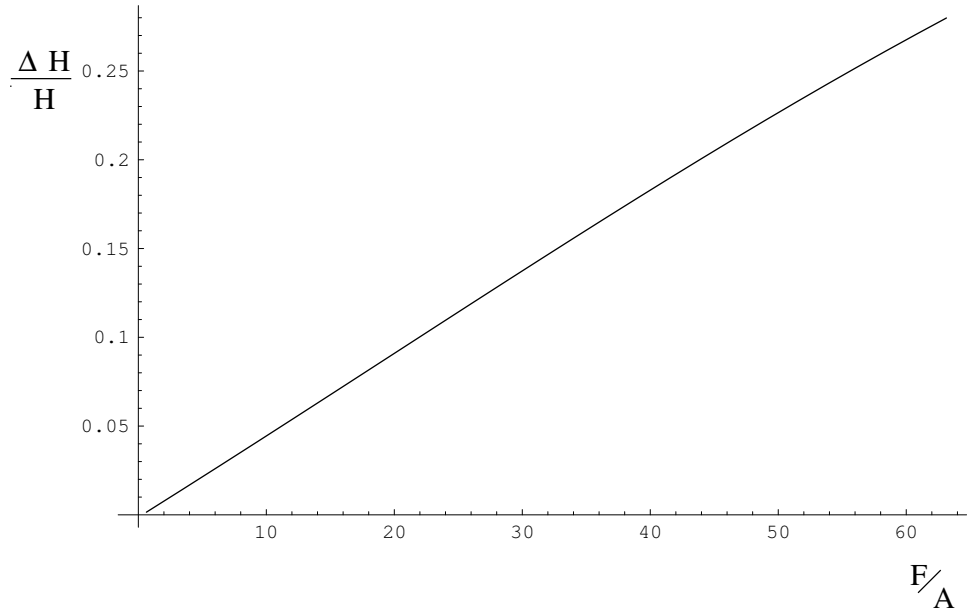


Figure 4.11: Strain vs. Stress for a folded elastica touching similar loops above and below

The continuity of curvature (4.11) requires that

$$\frac{2\lambda}{\sin\beta_{sc}}\sqrt{1-\sin^2\beta_{sc}\sin^2\frac{\pi}{4}} = \lambda_k\left(\sqrt{4\sin^2\beta_k - 2}\right)$$

and we have enough equations to determine β_{sc}, z, β_k and λ_{sc}, but note that we have an undetermined parameter ϕ_k. This is fixed by applying the condition that says that the height of the semicircular section is twice that of the kinked, and hence

$$\int_0^z \sin\theta_{sc} ds = 2\int_0^{1-z} \sin\theta_k ds.$$

Once again, we can compare the response of this elastica with that of a section of material from the block as shown in figure 4.11.

4.2.3 Stress, strain and nondimensionalisation

Figures 4.6, 4.7, 4.9 and 4.11 are all plots of strain against non-dimensional stress for elasticas of unit width. They all can be seen to be approximately straight (to one degree or another), and all but the confined loop have a similar slope. The elastic properties of the block we shall discuss shortly will be dimensional. Now is a good time to recall the relationship between these. Firstly, we rewrote all forces in terms of the natural force scale for the elastica

$$\frac{EI}{L^2}$$

where L is the primary crimp length (i.e. half the length of one loop or fold). Secondly, all the distances (with the exception of the width of the elastica) were nondimensionalised with the same length. The stress must therefore be nondimensionalised with the quantity

$$\frac{EI}{L^3}.$$

We must take care to remember that EI is the stiffness for an elastica of unit width, not the stiffness of the elastica fed into the stufferbox.

4.2.4 The primary crimp length and the force applied to the block

Recall the discussion at the end of chapter 2. There we compared the three, two dimensional models for primary crimp, and showed that for each

$$F_x \sim \pi^2 \frac{EIW}{X_b^2} M^2$$

where EI is the stiffness of the tow per unit width, W the width of the stufferbox, X_b the length of the region over which the primary crimp occurred and M the number of contact points. In addition, we found that the average crimp length was

$$L \sim \frac{2X_b}{M}.$$

Combining these we have that

$$L \sim 2\pi \sqrt{\frac{EIW}{F_x}}. \tag{4.12}$$

This will prove important when we consider how the material properties depend on the applied force.

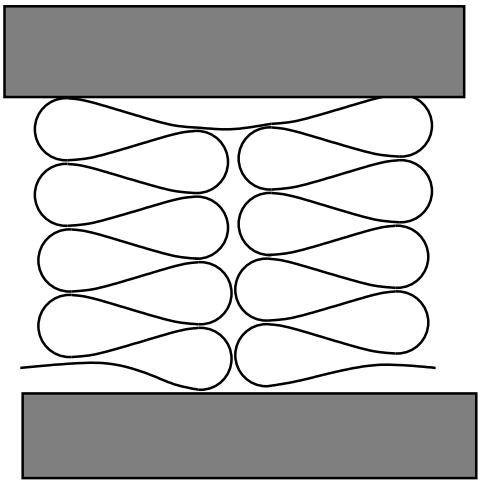


Figure 4.12: An idealized view of the crimped material in the stuffer box

4.3 First model of the Block : Vertical Springs

Let us take an idealised view of the block. We imagine it as being composed of a series of vertical springs (see figure 4.12) which have an equilibrium height ($h(x)$) and a spring constant $k(x)$, both depending on the position along the box (x). If the height of the block in the stuffer box is $H(x)$ then a section of the block of width δx exerts a normal force

$$\text{Normal Force} = P(x)W\delta x \tag{4.13}$$

where W is the width of the stufferbox and $P(x)$ is the pressure exerted, given by

$$P(x) = k(x)\left(\frac{h(x) - H(x)}{h(x)}\right). \tag{4.14}$$

Consider the forces acting on an elemental section of the block (See figure 4.13), and assume limiting friction. Let ψ be the angle made by the plate with the horizontal. Balancing the pressures acting on the trapezoidal element and requiring that, for stability, the total force exerted on the top plate by the block must balance the external moment applied we find that

$$P_1 = \frac{P}{\cos\psi + \mu\sin\psi}$$

and

$$M = \frac{W}{\cos\psi + \mu\sin\psi}\int_0^L xk(x)\left(\frac{h(x) - H(x)}{h(x)}\right)dx, \tag{4.15}$$

where L is the length of the plates. Similarily, if we assume that no horizontal force is exerted on the block at the exit from the box, the total force at the entrance (F)

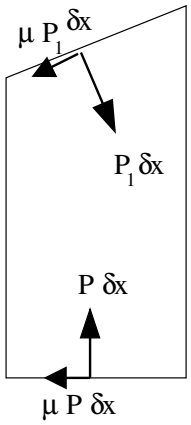


Figure 4.13: Forces acting on an elemental section of the block

can be shown to be given by

$$F = W\left(\mu + \frac{\mu\cos\psi - \sin\psi}{\cos\psi + \mu\sin\psi}\right)\int_0^L k(x)\left(\frac{h(x) - H(x)}{h(x)}\right)dx. \tag{4.16}$$

4.3.1 Contact

So far we have only said that $H(x)$ is the height of the block in the stufferbox. The precise form of this depends on what boundary conditions we apply. We must have that

$$H(x) \leq H_0 + x\sin\psi$$

where H_0 is the height of the top plate at its left most end. Secondly, if the block is not stuck to the top plate, we must require that

$$H(x) \leq h(x)$$

This is the same as saying that the block can only be compressed by the top plate, not elongated.

We will consider two cases here

- Full contact
$$H(x) = H_0 + x\sin\psi$$
- Loss of contact
$$H(x) = \min\left(H_0 + x\sin\psi, h(x)\right)$$

4.3.2 Time varying Parameters

If we let the properties $h(x)$ and $k(x)$ change with time in the manner discussed in section 4.2 then the equations of the system become from (4.15) and (4.16)

$$\begin{aligned} M &= \frac{W}{\cos\psi(\chi)+\mu\sin\psi(\chi)} \\ &\qquad \int_0^L x\cdot k(\chi-x)\left(\frac{h(\chi-x)-H(\chi,x)}{h(\chi-x)}\right)dx, \qquad (4.17) \\ F(\chi) &= W\left(\mu+\frac{\mu\cos\psi(\chi)-\sin\psi(\chi)}{\cos\psi(\chi)+\mu\sin\psi(\chi)}\right). \\ &\qquad \int_0^L k(\chi-x)\left(\frac{h(\chi-x)-H(\chi,x)}{h(\chi-x)}\right)dx, \qquad (4.18) \end{aligned}$$

where χ is the amount of material which has entered the box in time t.

4.3.3 Non-dimensionalization

The following non-dimensionalisations are appropriate for the system

$$\begin{aligned} x &= L\bar{x}, \\ H_0 &= L\epsilon, \\ \psi(\chi) &= \epsilon\bar{\psi}(\bar{\chi}), \\ k &= K_0\bar{k}, \\ M &= WL^2K_0\bar{M}, \\ \chi &= L\bar{\chi}, \\ h(\chi) &= \frac{L\epsilon}{g(\bar{\chi})}, \\ H(\chi,x) &= \epsilon L\bar{H}(\bar{\chi},\bar{x}), \end{aligned}$$

and introduce the small parameter ϵ, the aspect ratio of the box. If the force at the entrance to the stuffer-box is denoted F, then by considering equation (4.18), a suitable non-dimensionalisation is

$$F = \mu WLK_0\bar{F}.$$

After dropping the $^-$'s, the moments and force balances((4.17) and (4.18)), give the following system to describe the state of the stuffer-box at any instance in time

$$\begin{aligned} M &= \frac{1}{\cos\epsilon\psi + \mu\sin\epsilon\psi} \\ &\qquad \int_0^1 xk(\chi - x)\left(1 - H(\chi, x)g(\chi - x)\right)dx \qquad (4.19) \\ F &= \left(1 + \frac{\mu\cos\epsilon\psi - \sin\epsilon\psi}{\mu\cos\epsilon\psi + \mu^2\sin\epsilon\psi}\right) \\ &\qquad \int_0^1 k(\chi - x)\left(1 - H(\chi, x)g(\chi - x)\right)dx. \qquad (4.20) \end{aligned}$$

4.3.4 Linearization

We now linearize equations (4.19) and (4.20) by making the assumption that the height of the block varies slowly, in such a way that loss of contact occurs only for $\psi > 0$ and at a point $x_C(\chi)$. We therefore have that

$$H(\chi, x) = \begin{cases} 1 + \frac{x}{\epsilon}\sin\epsilon\psi & 0 < x < x_C(\chi) \\ \frac{1}{g(\chi - x)} & x_C(\chi) \le x \le 1 \end{cases}.$$

Expanding equations (4.19) and (4.20) in powers of ϵ gives, to zeroth order

$$\begin{aligned} M &= \int_0^{x_C} xk(\chi - x)\left(1 - (1 + x\psi)g(\chi - x)\right)dx, \qquad (4.21) \\ F &= 2\int_0^{x_C} k(\chi - x)\left(1 - (1 + x\psi)g(\chi - x)\right)dx. \qquad (4.22) \end{aligned}$$

4.3.5 Closing the model

We now have a model for the block that predicts the force required to move it in terms of the properties of the material that entered in the past. In order to close the model, we shall need to know how the properties of the material now entering the block depend on this force (the box marked "?" in figure 4.14). In a later section, we shall show how we can use our model of the primary and secondary crimp regions to give this information, but for ease of exposition we shall concentrate on the general case where we have that

$$\begin{aligned} F(\chi) &= \hat{F}(g(\chi)) \\ k(\chi) &= \hat{k}(g(\chi)). \end{aligned}$$

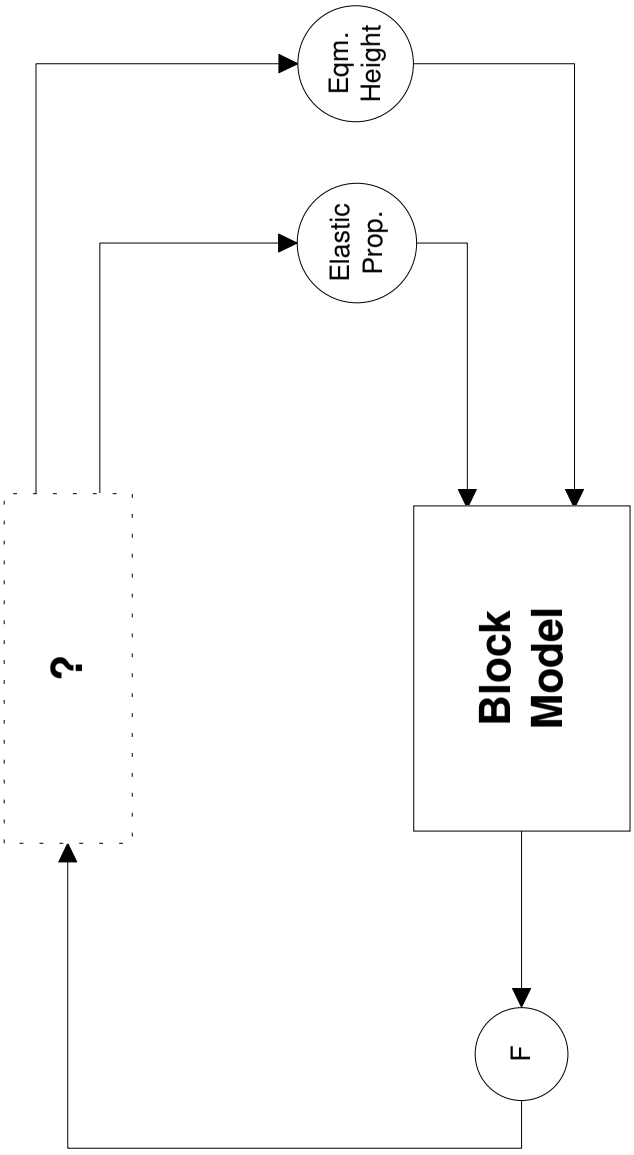


Figure 4.14: Closing the springs model

4.3.6 Uniform equilibrium states and their stability

Observation of the stuffer box crimper sugguests that under most operating conditions, the angle made by the plate is constant in time, and the crimp regular. However, when the box is nearing the end of its useful life, the system seems to become unstable, and exhibits large temporal oscillations. To help understand this, we shall now seek a solution of the form

$$\begin{aligned} g(\chi) &= g_0 + \varepsilon g_1(\chi) \\ x_C &= x_0 + \varepsilon x_1 \\ \psi(\chi) &= \psi_0 + \varepsilon \psi_1(\chi) \\ F(\chi) &= F_0 + \varepsilon F_1(\chi) \\ &= \hat{F}_0(g_0) + \varepsilon F_1(\chi) \\ k(\chi) &= k_0 + \varepsilon k_1(\chi) \\ &= \hat{k}_0(g_0) + \varepsilon k_1(\chi) \end{aligned}$$

where g_0, F_0, x_0, k_0 and ψ_0 relate to the uniform equilibrium state. Realizing that

$$F_1(\chi) = \frac{d\hat{F}}{dg} g_1(\chi) = \alpha g_1(\chi)$$

and

$$k_1(\chi) = \frac{d\hat{k}}{dg} g_1(\chi) = \beta g_1(\chi),$$

we can expand the equations (4.21) and (4.22) to obtain both stationary solutions and information about their stability.

To zeroth order we have that

$$\psi_0 = \frac{3}{x_0 g_0} \left(\frac{1}{2} - \frac{M}{x_0^2 \hat{k}_0(g_0)} - \frac{g_0}{2} \right), \tag{4.23}$$

$$\hat{F}_0(g_0) = 2\hat{k}_0(g_0) \left(x_0 - \frac{\psi_0 g_0 x_0^2}{2} - g_0 x_0 \right) \tag{4.24}$$

where

$$\begin{aligned} \text{either} \quad & x_0 \leq 1 \quad \text{and} \quad (1 + x_0\psi_0) g_0 = 1 \\ \text{or} \quad & x_0 = 1 \quad \text{and} \quad (1 + \psi_0) g_0 \leq 1 \end{aligned}$$

These will give us any uniform stationary states. To find their stability, we must continue to first order, where we arrive at

$$\begin{aligned} k_0\psi_1 g_0\frac{x_0^3}{3} &= (\beta(1-g_0)-k_0)\int_0^{x_0} xg_1(\chi-x)dx \\ &\quad -\psi_0(k_0+\beta g_0)\int_0^{x_0} x^2 g_1(\chi-x)dx \\ \text{and}\quad \frac{\alpha}{2}g_1(\chi) &= (\beta(1-g_0)-k_0)\int_0^{x_0} g_1(\chi-x)dx \\ &\quad -\psi_0(\beta g_0+k_0)\int_0^{x_0} xg_1(\chi-x)dx - k_0\psi_1 g_0\frac{x_0^2}{2} \end{aligned}$$

Eliminating ψ_1, we obtain

$$\begin{aligned} \frac{\alpha}{2}g_1(\chi) &= A_1\int_0^{x_0} g_1(\chi-x)dx - A_2\int_0^{x_0} xg_1(\chi-x)dx \\ &\quad -\frac{3}{2x_0}\left(A_1\int_0^{x_0} xg_1(\chi-x)dx\right. \\ &\quad \left. -A_2\int_0^{x_0} x^2 g_1(\chi-x)dx\right) \end{aligned} \tag{4.25}$$

where

$$\begin{aligned} A_1 &= \beta(1-g_0)-k_0 \\ A_2 &= \psi_0(\beta g_0+k_0). \end{aligned}$$

We will now seek a trial solution to this of the form

$$g_1(\chi) = Ce^{\lambda\chi}.$$

Inserting into (4.25) gives the following equation for λ

$$\begin{aligned} &\frac{\alpha}{2}\lambda^3 - A_1\lambda^2 + \left(\frac{3A_1}{2x_0}+A_2\right)\lambda - \frac{3A_2}{x_0} = \\ &\qquad \left(\frac{A_1 - x_0A_2}{2}\lambda^2 + \left(\frac{3A_1}{2x_0}-2A_2\right)\lambda - \frac{3A_2}{x_0}\right)e^{-\lambda x_0} \end{aligned} \tag{4.26}$$

Note that λ will, in general, be complex, and the sign of the real part will determine if the steady state is stable or not. Specifically, the system will be unstable for

$$\Re(\lambda) > 0.$$

4.3.6.1 Finding the roots

The infinity of roots of the trancendental equation (4.26) are difficult to find, although we can asymptotically find the location of those well away from the origin, these all lie well into the negative real half plane[4] and hence correspond to stable solutions. This means that any roots with positive real part will be found for $O(1)$ values of λ, and hence will need to be found numerically.

Our method to do this will involve locating roots near the origin for a given value of the parameters, and then tracking where they move for small changes in the parameters. To make this simpler, we can start by dividing (4.26) by A_1, and hence writing

$$B_1\lambda^3 + \lambda^2 - \left(\frac{3}{2x_0} - B_2\right)\lambda - \frac{3B_2}{x_0} = \\ -\left(\frac{1+B_2x_0}{2}\lambda^2 + \left(\frac{3}{2x_0} + 2B_2\right)\lambda + \frac{3B_2}{x_0}\right)e^{-\lambda x_0}$$

where

$$B_1 = -\frac{\alpha}{2A_1} \qquad\qquad B_2 = -\frac{A_2}{A_1}.$$

The roots were found using *Mathematica*'s inbuilt **FindRoot** command, using the root for the previous parameter values as the seed. Figures 4.15 and 4.16 show the regions of stability (black) and instability (white) for a range of control parameters (B_1, B_2 and x_0).

[4]Consider equation (4.26) when we write that

$$\lambda = \frac{X + IY}{\epsilon}$$

for some small constant ϵ. Inserting into the equation, and dividing through by λ^2 we have

$$\frac{\alpha}{2\epsilon}(X + IY) + O(1) = \exp -(\frac{X}{\epsilon} + I\frac{Y}{\epsilon})(\frac{A_1 - x_0A_2}{2} + O(\epsilon))$$

Taking the modulus of this and squaring, we have that

$$\left(\frac{\alpha}{2\epsilon}\right)^2(X^2 + Y^2) + O(1) = e^{-2X/\epsilon}(\frac{A_1 - x_0A_2}{2} + O(\epsilon))^2$$

Rearranging, this becomes

$$\left(\frac{\alpha}{A_1 - x_0A_2}\right)^2 Y^2 = \epsilon^2 e^{-2X/\epsilon} - \left(\frac{\alpha}{A_1 - x_0A_2}\right)^2 X^2$$

which only has real roots for large negative X.

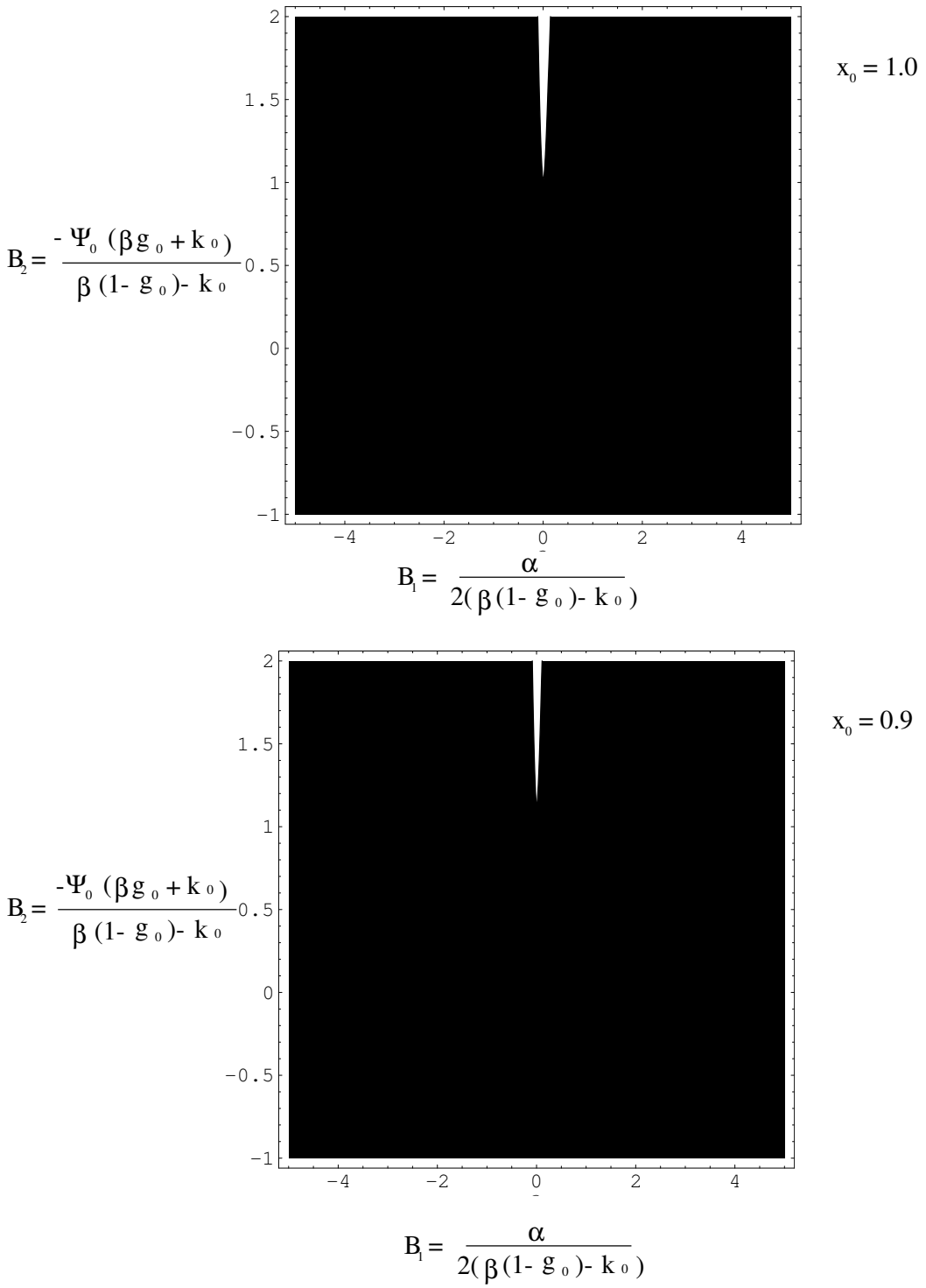


Figure 4.15: Regions of stability (black) and instability (white) for the springs model, with $x_0 = 1.0$ and 0.9

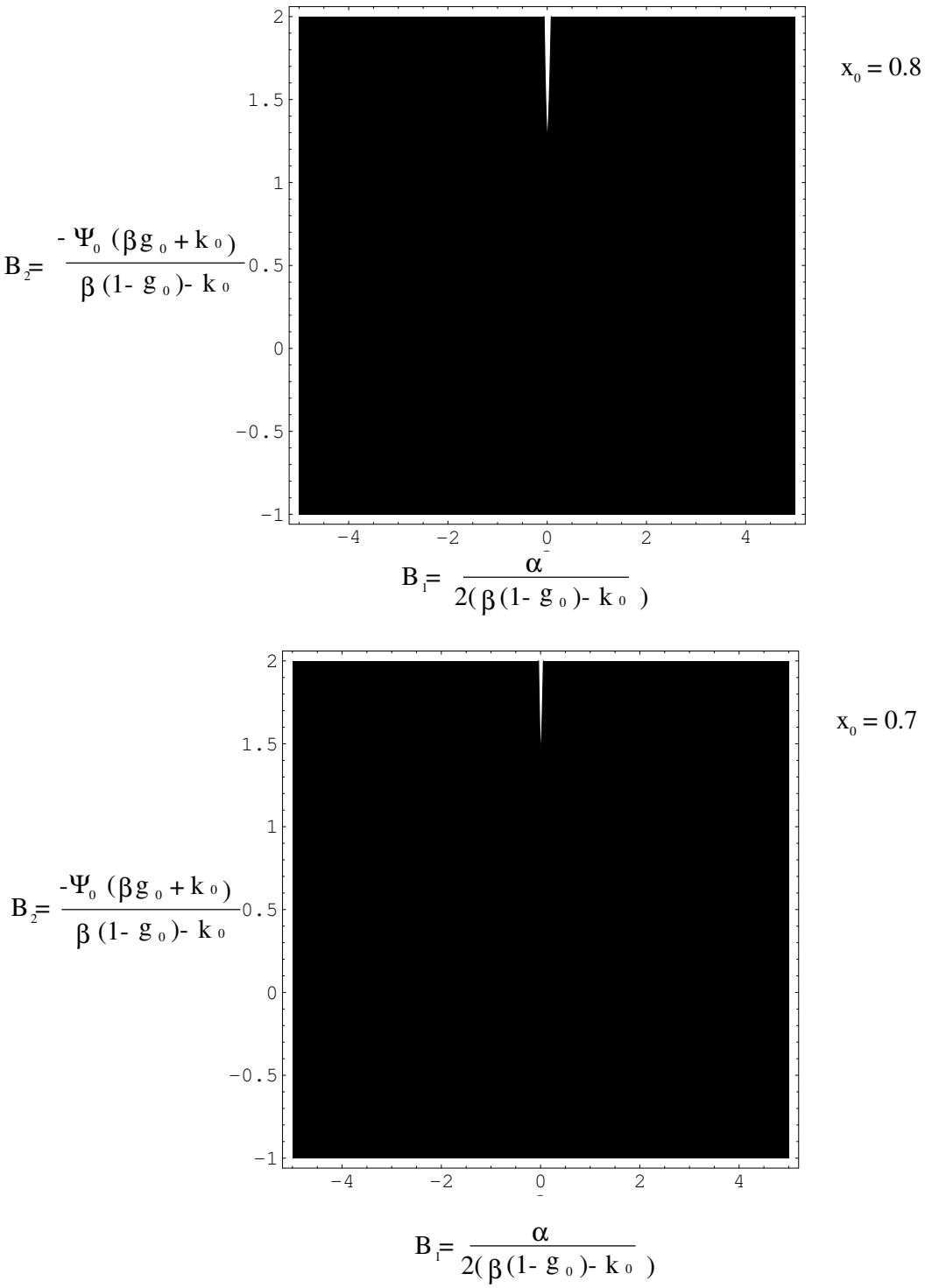


Figure 4.16: Regions of stability (black) and instability (white) for the springs model, with $x_0 = 0.8$ and 0.7

Note first that, contrary to what one might expect, the presence of the free boundary ($x_0 < 1$) makes the system more stable. One can attribute this to small variations having a lesser effect on the angle of the top plate due to decreased leaverage (acting closer to the pivot point as x_0 decreases). We can also see that instabilities occur for values of $B_2 > 1$. Remembering the definition,

$$\begin{aligned} B_2 &= -\frac{\psi_0(\beta g_0 + k_0)}{\beta(1-g_0) - k_0} \\ &= \psi_0 \left(1 - \frac{\beta}{\beta(1-g_0) - k_0}\right), \end{aligned}$$

we observe that one situation where instability may occur corresponds to a positive equilibrium angle ψ_0 and

- Either (for positive β)
$$g_0 > 1 - \frac{k_0}{\beta}$$
- or
$$g_0 < -\frac{k_0}{\beta}$$

for negative β. This can be interpreted as saying that unstable solutions can occur when the angle is large and positive, and where the equilibrium height of the block is less than the height of the stufferbox. These two situations are mutualy exclusive. Instability could also occur when $\beta(1-g_0)$ is very close to k_0 from below. Until we obtain values of the constants, we will be unable to determine whether this situation is likely.

The second condition for instability is that of small $|B_1|$, when

$$\left| \frac{\alpha}{2(\beta(1-g_0) - k_0)} \right|$$

is small, which occurs when α is small and $\beta(1-g_0) - k_0$ is large. Small α implies that small changes in the force gives rise to large changes in the equilibrium height (which one would expect physically to be more unstable), whilst a large β implies that small changes in force give rise to large changes in the block properties. Again, we might intuitively expect this to be an unstable situation.

From this model, we would not, in general, expect the block to be unstable. Any instability observed would need to be attributed to factors we have left out. A test of the model's accuracy would be to see if it predicts the equilibrium angle of the stuffer box plate correctly. This we shall now discuss.

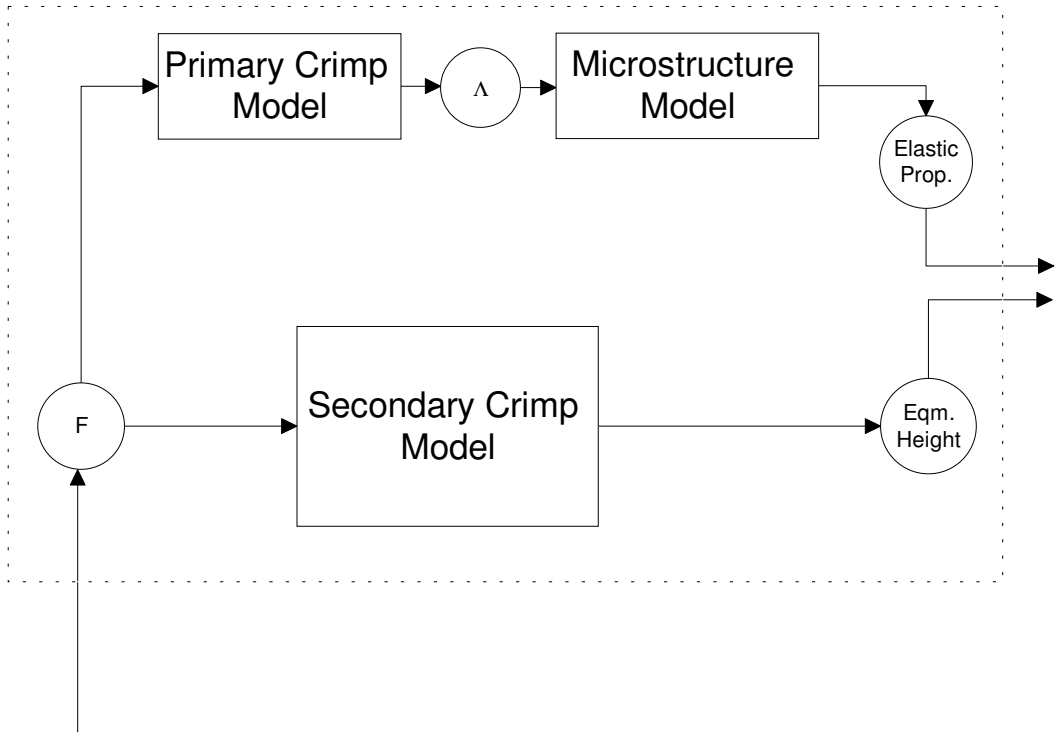


Figure 4.17: Closing the springs model

4.3.7 Predicting the equilibrium state

We shall now consider a specific example of the feedback between the current state of the block (represented by the force required to move it) and the properties of the fibre. To do so, we shall combine the models of the microstructure as looped or folded elastica, with the models of primary and secondary crimp discussed in chapters 2 and 3 (See figure 4.17). Firstly, let us consider the response of a small section of the spring material to a compressive force. It was an assumption of equations (4.13) and (4.14) that there was a linear relation between stress and strain (as was borne out in section 4.2.2). If we nondimensionalise stress and strain as discussed in section 4.2.3, we can write the linear relationship as

$$\text{stress} = \frac{\Lambda^3 k}{EI}\ \text{strain},$$

where Λ is the primary crimp length. Reading the slopes from figures 4.6 and 4.11 gives that

$$k = \frac{EI}{L^3}C, \tag{4.27}$$

where $C = C_{loop} = 285$ for a loop of elastica, and $C = C_{fold} = 230$ for a fold. We can also relate this to the applied force through equation (4.12) to give

$$k = C\frac{1}{\pi^3 8\sqrt{EI}W^{3/2}}F^{3/2}. \tag{4.28}$$

When we nondimensionalised the spring constant in section 4.3.3, we did so using an unspecified scale K_0. We can now choose the value of this such that (4.28) becomes

$$\bar{k} = \bar{F}^{3/2} \tag{4.29}$$

which requires that

$$K_0 = \frac{64EI\pi^6}{C^2\mu^3 L^3},$$

(remember that in this case EI is the stiffness of the tow per unit width, and L is the length of the plates).

In addition, we can recall the earlier discussion on the height of the material entering the stufferbox (4.3) to write

$$h = \frac{\pi}{2}\sqrt{\frac{EIW}{\Upsilon F}},$$

and hence, when nondimensionalised,

$$g = \frac{16\pi^2\epsilon\sqrt{\Upsilon}}{C\mu}\sqrt{\bar{F}}. \tag{4.30}$$

Combining this with the equation for $\bar{k}$ (4.29) we have

$$\bar{k} = \left(\frac{C\mu}{16\pi^2\epsilon\sqrt{\Upsilon}}\right)^3 \bar{g}^3. \tag{4.31}$$

4.3.7.1 Steady State Solutions

We shall now solve equations (4.23) and (4.24) using the relationships (4.30) and (4.31) to close the model, to find ψ_0, g_0, F_0 and k_0. We should first note that there are two possible cases. Either

$$x_0 < 1 \quad \text{and} \quad g_0(1 + x_0\psi_0) = 1$$

or

$$x_0 = 1 \quad \text{and} \quad g_0(1 + x_0\psi_0) < 1.$$

We shall start by considering the first of these. We start by solving for

$$\psi_0 = \frac{1 - g_0}{g_0 x_0}$$

and hence obtain from (4.23)

$$3\bar{M} = \frac{x_0^2}{2}(1 - g_0)\bar{k_0} \tag{4.32}$$

and from (4.24)

$$\bar{F_0} = \bar{k_0} x_0 (1 - g_0) \tag{4.33}$$

Now we write

$$\bar{k_0} = \bar{F_0}^{3/2}$$

from (4.29) and

$$\bar{k_0} = \alpha^3 g_0^3$$

from (4.31) where

$$\alpha = \frac{C\mu}{16\pi^2 \epsilon \sqrt{\Upsilon}}.$$

Eliminating x_0 from (4.32) and (4.33) we have that

$$g_0 = \frac{6M}{\alpha + 6M}.$$

In order that $x_0 < 1$ we require that

$$\frac{(\alpha + 6M)^2}{6M\alpha^2} \leq 1$$

or

$$\alpha^2 + 6M\alpha(2 - \alpha) + 36M^2 \leq 1.$$

This can be rewritten as

$$36(M - \lambda_1)(M - \lambda_2) \leq 0$$

where

$$\lambda_{1,2} = \frac{1}{36}\left[3\alpha(\alpha - 2) \pm 3\alpha\sqrt{(\alpha - 2)^2 - 4}\right].$$

$\lambda_{1,2}$ will be real if $\alpha > 4$ and then a solution will exist if M is between λ_1 and λ_2. Taking some approximate values for the constants[5]:

[5] A note on measurements.
Quantities such as Length, Height and Width are all easily measured. This is not the case for the coefficient of friction, applied moment and stiffness of paper. Hence, these quantities are more an indication of order of magnitude rather than exact values. The quantity Υ (the shortening of the tow due to primary crimp) can only ever be an estimate.

Length of Stuffer box	L	=	0.20 m
Height of Stuffer box	H_0	=	0.015 m
Width of Stuffer box	W	=	0.03 m
Coefficient of Friction	μ	=	0.2
Applied Moment	M	=	0.8 N m
Stiffness of paper p.u.w.	EI	=	0.44 N m
Shortening due to crimp	Υ	=	0.2 (a guess)

We have that

$$\alpha \sim 10 \quad \Rightarrow \quad \lambda_{1,2} \sim 0.222, 13.1$$

and

$$\bar{M} = 0.13$$

which does not satisfy the condition. The second possibility for the solution of (4.23) and (4.24) is that

$$x_0 = 1 \qquad \text{and} \qquad g_0(1 + x_0\psi_0) < 1.$$

Using the previous relationship for $\bar{k}_0$ and $\bar{F}_0$ leads to

$$\alpha^3 g_0^4 - \alpha^3 g_0^3 + 2\alpha^2 g_0^2 - 6\bar{M} = 0 \tag{4.34}$$

This has at least one positive real root and one negative real root, and may have 3 positive real roots depending on the relative sizes of $\bar{M}$ and α. When $\alpha \sim 10$ (as for the above values of the parameters), there is a single positive root, which gives

$$g_0 \sim 0.77.$$

Using this value, we can calculate ψ_0 to be ~ 0.34. Unfortunately, this means that

$$g_0(1 + \psi_0) \sim 1.03$$

which violates our inequality. For the values of the parameters given above, we have been unable to find a leading order solution. It is worth remembering the assumptions that we have made in reaching this point. In doing so, we hope to consider alternative models that may explain the behaviour of the stuffer box:

- **Modelling the block as springs**
  It is always possible that the block does not behave in any way like the springs model would predict. Later in this chapter, we will consider two further options : the block as an isotropic elastic material, and the block as an anisotropic elastic material. The choice of model will then be discussed. For now, we shall continue to discuss the spring model.

- **Relationship between force and equilibrium height of the block**
  When we discussed secondary crimp formation, we assumed that the crimp formed without any constraints. In the stuffer box crimper, this is not the case, as the secondary crimp occurs in the nip region, and it may be possible that under these conditions the model we chose does not hold. In addition, we looked at the case when we had a fixed number of rods and applied a force until the collection buckled. In reality, we are increasing the applied force and also adding new rods. Whether this will behave in the same way is open to question. Indeed, qualitative arguments made by observing the paper crimper suggest that as the force required to move the block increases (for example, when the paper gets caught between the roller and the top plate), the equilibrium height of the block material also increases. This is the opposite to the result predicted by both the hinged rods and small scale elastica models, where an increase in force decreased the secondary crimp length.[6]

- **Relationship between force and primary crimp length**
  Our discussion on how the force exerted on the secondary crimp region (and by implication the block) depended on the excess of fibre within the nip region made the assumption that the aspect ration of the channel was small, and hence we could linearise the equations of the elastica. Indeed, when we compared our results with the solutions to the full equations given by Domokos, Holmes and Royce [8] we saw very similar graphs. Observations from the video suggest that the crimp length depends on the geometry of the nip and this has not yet been taken into account in our models.

- **Models of the microstructure**
  There may also be problems with the models for the microstructure. In both the loop and the folded elastica we assumed that the lengthscale of the shape was that of the crimp length. If this is not the case, for example if there were large regions of contact such that the majoritory of the load was supported by small regions of elastica (that do not scale with the primary crimp length), then the analysis would need to be redone.

[6] Both the models for secondary crimp predict that

$$F \propto g^2 \propto \frac{1}{\bar{h}_0^2}$$

(where $\bar{h}_0$ is the equilibrium height of the material). Hence as we increase F the equilibrium height must decrease.

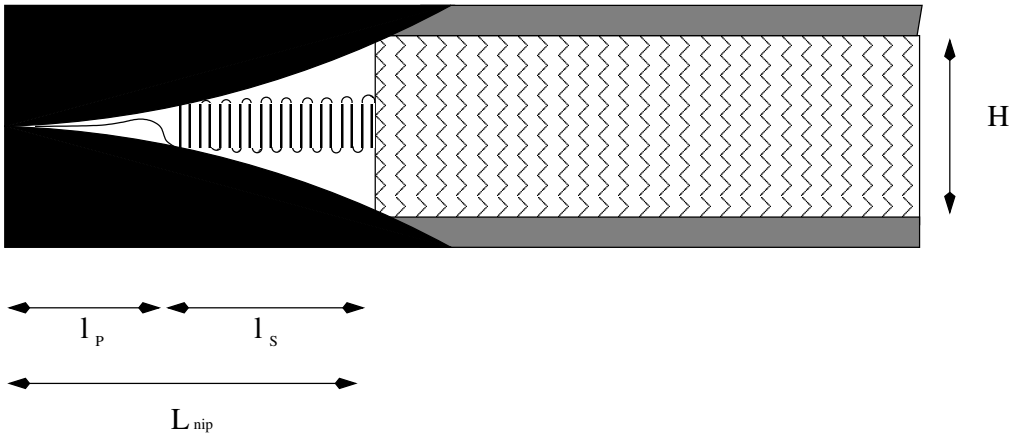


Figure 4.18: Geometry for the new model for secondary crimp

We shall now discuss in more detail the relationship between the primary and secondary crimp lengths, and the force required to move the block to take into account the geometry of the nip.

4.3.7.2 A new model for secondary crimp

Suppose that the primary and secondary crimp regions lie in a well defined region of the stuffer box within the nip (see figure 4.18). Let L_{nip} denote the length of this region, and H_0 the distance between the plates. A trivial application of geometry allows us to write that

$$L_{nip} = \sqrt{H_0 R - \frac{H_0^2}{4}}$$

where R is the radius of the roller. In addition, let the primary crimp occur in a region of length l_P and the secondary in a region l_S such that

$$L_{nip} = l_P + l_S.$$

As primary crimp occurs, the amount of crimped material increases. However, we suppose that no secondary crimp can occur until the block has moved and space to accept it in the block region has been created. If we imagine that the fibre in the primary crimp region is an Euler strut of length l_P and stiffness EIW then the force required to buckle it is given by

$$F_{buckle} = \frac{\pi^2 EIW}{l_P^2}. \tag{4.35}$$

Primary crimp will continue to occur until this force is greater than that required to move the block. At this point, the block moves up and the fibre in the secondary

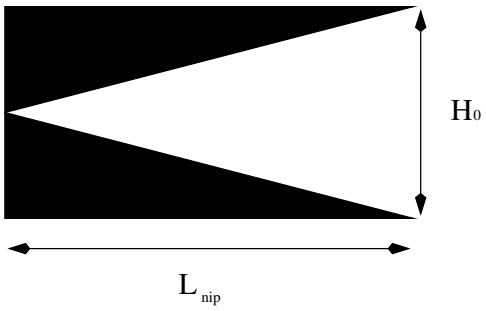


Figure 4.19: The nip as a wedge

crimp region folds to become the new block material.

Now think of the material in the secondary crimp region. When the block is about to move, it is being compressed by a force F_{buckle}, and is taking up a length $l_S = L_{nip} - l_P$. In a moment, this material is going to be entering the block, and so let us use the same "springs" model for it now. Hence if Λ denotes the primary crimp length, then

$$\frac{F_{buckle}}{\Lambda W} = k\frac{l_0 - l_S}{l_0}.$$

where l_0 is the equilibrium length of the secondary crimp region. We can also relate k to the primary crimp length using the relationship derived before (4.27), and hence

$$F_{buckle} = C\frac{EIW}{\Lambda^2}\frac{l_0 - l_S}{l_0}. \tag{4.36}$$

l_0 can be related to the equilibrium height of the material by the simple assumption that

$$l_0 = 2h_0$$

Finally, we need to consider how the primary crimp length Λ depends on the applied force. Let us imagine that the crimp is forming in a wedge of length L_{nip} and width H_0 (see figure 4.19). We imagine that primary crimp forms at the end of the length l_P and hence has a crimp length of

$$\Lambda = \frac{H_0 l_P}{L_{nip}} \tag{4.37}$$

Now we can put all this together. Eliminating l_P from (4.35) and solving for l_S we have

$$l_S = L_{nip} - \pi\sqrt{\frac{EIW}{F_{buckle}}}.$$

Combining this with (4.36) and (4.37) we get

$$h_0 = \frac{1}{2}\left(\frac{\pi^2 H_0^2}{C L_{nip}^2} + 1\right)\left(L_{nip} - \pi\sqrt{\frac{EIW}{F_{buckle}}}\right)$$

and

$$\Lambda = \pi\sqrt{\frac{EIW}{F_{buckle}}}\frac{H_0}{L_{nip}}$$

4.3.7.3 Nondimensionalisation

We can now apply the necessary nondimensionalisations. In the same manner as before, we see that

$$\bar{k} = \bar{F}^{3/2}$$

where k is now nondimensionalised by

$$K_0 = \frac{\pi^6 EI\gamma^6}{\mu^3 L^3 C^2}$$

and

$$\gamma = \frac{H_0}{L_{nip}}$$

In addition, we can nondimensionalise the equation for the equilibrium height of the block, and rearrange to get

$$\bar{F} = \frac{C^4\mu^2}{\pi^4\gamma^4\epsilon^2}\frac{g^2}{\left(C(g-2\gamma) - 2g\pi^2\gamma^2\right)^2}$$

Notice that, as desired, F decreases as g increases (for sufficiently large values of g). This is all the information we shall need to find the equilbrium position of the plate. Unfortunately, solving equations (4.23) and (4.24) with these relationships between $\bar{F}$, k and g requires finding the roots of a sixth order polynomial. Thankfully, modern computer algebra systems can easily find approximate roots to such problems, and it proves easy to get *Mathematica* to find all six for suitable values of the constants (as used before, but also including the radius of the rollers ($R = 0.10m$). Of the six, only one is realisitc, and this gives a value of

$$\psi = 0.017\epsilon$$

where ϵ is the aspect ratio of the block. This gives us a solution to the problem (with $x_0 = 1$). We now have a second model for how the primary / secondary crimp properties depend on the force acting on the block. We shall now consider how the model for the material of the block affects the results.



Figure 4.20: The block composed of an isotropic elastic solid

4.4 The Block as an Isotropic Elastic Material

We shall now discuss our second model for the block, where we imagine that it consists of an isotropic elastic material. Unlike the springs model, in an elastic material a vertical stress can give rise to a horizontal strain. In this section, we will derive the equations for the block under these assumptions, and in the same geometry as the springs model. We shall then look for steady state solutions and consider the stability. We can then proceed to look for specific solutions when we couple the block model to models for primary and secondary crimp.

4.4.1 Constitutive relations

We shall use the standard, quasi-static equations for an isotropic linear elastic solid, written in terms of an Airy stress function $A(x, y)$ such that

$$\frac{\partial^2 A}{\partial y^2} = \sigma_{xx} = \lambda(u_x + v_y) + 2\mu u_x, \tag{4.38}$$

$$-\frac{\partial^2 A}{\partial x \partial y} = \sigma_{xy} = \mu(u_y + v_x), \tag{4.39}$$

$$\frac{\partial^2 A}{\partial x^2} = \sigma_{yy} = \lambda(u_x + v_y) + 2\mu v_y, \tag{4.40}$$

Here, u is the displacement in the x direction and v that in the y (see figure 4.20). On the bottom plate, we apply the boundary conditions

$$v = 0$$

$$\text{and} \quad \tau_{xy} = 0.$$

(where τ is the stress). These can be rewritten in terms of the stress function as

$$u_y = 0 \tag{4.41}$$
$$v = 0 \tag{4.42}$$
$$A_y = 0 \tag{4.43}$$

(which corresponds to no vertical displacement, no friction), whilst at the upper surface, we prescribe the normal and tangential stresses to be

$$A_{xy} = f \tag{4.44}$$
$$A_{xx} = -P \tag{4.45}$$

(with f the horizontal shear stress and P the pressure exerted by the plate). Note that these only hold exactly if the top plate is horizontal, otherwise they are an approximation valid for the nearly horizontal case.

4.4.1.1 Nondimensionalisation

We will now nondimensionalise the equations and boundary conditions (4.38)-(4.43) using the following scalings

$$\begin{aligned} x &= L\bar{x} \\ u &= L\bar{u} \\ y &= \epsilon L\bar{y} \\ v &= \epsilon L\bar{v} \\ \lambda &= \Lambda\bar{\lambda} \\ A &= \Lambda L^2\bar{A} \\ P &= \Lambda\bar{P} \\ f &= \Lambda\bar{f} \\ \mu &= \Lambda\bar{\mu} \end{aligned}$$

where

$$\epsilon = \frac{H_0}{L}$$

the aspect ratio of the box. Inserting into our equations, and dropping the bars gives

$$A_{yy} = \epsilon^2 \left[\lambda(u_x + v_y) + 2\mu u_x\right] \tag{4.46}$$
$$-A_{xy} = \mu\left(u_y + \epsilon^2 v_x\right) \tag{4.47}$$
$$A_{xx} = \lambda(u_x + v_y) + 2\mu v_y \tag{4.48}$$

with

$$u_y = 0 \tag{4.49}$$

$$v = 0 \tag{4.50}$$

$$A_y = 0 \tag{4.51}$$

on $y = 0$ and

$$A_{xy} = \epsilon f \tag{4.52}$$

$$A_{xx} = -P \tag{4.53}$$

on $y = 1 + \frac{x}{\epsilon}\sin\psi$. We can now proceed to linearise the problem. Writing

$$A \sim A^{(0)} + \epsilon^2 A^{(1)} + \cdots \qquad \text{and} \qquad \psi = \epsilon\bar{\psi}$$

we get from (4.46) and (4.51)

$$A^{(0)} = A^{(0)}(x)$$

and hence from (4.53)

$$A^{(0)}_{xx} = -P$$

From (4.47) this implies that

$$\mu u^{(0)}_y = -A^{(0)}_{xy} = 0 \qquad \Rightarrow \qquad u^{(0)} = u^{(0)}(x,t)$$

and then by using (4.48)

$$v^{(0)} = \frac{-y}{\lambda + 2\mu}\left(P + \lambda u^{(0)}_x\right) \tag{4.54}$$

Now look at (4.46) to $O(\epsilon^2)$

$$A^{(1)}_{yy} = (\lambda + 2\mu)u^{(0)}_x + \lambda v^{(0)}_y = \frac{4\mu(\lambda+\mu)u^{(0)}_x - \lambda P}{\lambda + 2\mu}$$

with boundary conditions

$$A^{(1)}_y = 0 \qquad \text{on} \qquad y = 0$$

$$A^{(1)}_{xy} = \frac{f}{\epsilon} \qquad \text{on} \qquad y = 1 + \psi x$$

Note the ϵ^{-1} term on the top boundary condition. This arises due to an $O(1)$ change in the shear force occuring over an $O(\epsilon)$ distance. In order to balance this, we will require that the shear stress is $O(\epsilon)$ ($f = \epsilon\bar{f}$). Now the total force per unit width on a section of the block will be

$$T(x) = \int_0^{1+x\psi} A^{(1)}_{yy} dy.$$

Hence

$$T(x) = \frac{4\mu(\lambda+\mu)u_x^{(0)} - \lambda P}{\lambda+2\mu}(1+\psi x) \tag{4.55}$$

and

$$\frac{dT}{dx} = \bar{f} + \psi\frac{4\mu(\lambda+\mu)u_x^{(0)} - \lambda P}{\lambda+2\mu}. \tag{4.56}$$

(This last equation comes from the $O(\epsilon^2)$ terms in (4.47)). Now we are in the position to close the model. Firstly, we shall prescribe the displacement on the top surface (V, measured downwards) to be

$$V = (1+\beta(x) - (1+\psi x))$$

where $\beta(x)$ is the "excess" height of the block in equilibrium at position x, and will be determined by the model for secondary crimp formation. Secondly, we will assume that the block is in limiting friction everywhere (as must be the case prior to the block moving). From this, we can say that

$$\bar{f} = \xi P$$

where ξ is a coefficient of friction. Combining this with equations (4.54), (4.55) and (4.56) allow us to eliminate $u_x^{(0)}$ to give

$$\frac{dT}{dx} = \left(\xi - \psi\frac{\lambda+2\mu}{\lambda}\right)P - \frac{4\mu(\lambda+\mu)\psi}{\lambda}\frac{x\psi-\beta}{1+x\psi} \tag{4.57}$$

$$T = -\frac{\lambda+2\mu}{\lambda}(1+x\psi)P - \frac{4\mu(\lambda+\mu)}{\lambda}(x\psi-\beta) \tag{4.58}$$

Comparing (4.57) with the differential of (4.58) gives, assuming constant μ and λ[7]

$$\xi P + \frac{\lambda+2\mu}{\lambda}(1+x\psi)\frac{dP}{dx} = \frac{4\mu(\lambda+\mu)\psi}{\lambda(1+\psi x)}\left((x\psi-\beta) + \frac{1+x\psi}{\psi}\left(\psi - \frac{d\beta}{dx}\right)\right)$$

Writing

$$A1 = \frac{\xi\lambda}{\lambda+2\mu} \quad \text{and} \quad A2 = \frac{4\mu(\lambda+\mu)}{\lambda+2\mu}$$

this can be transformed using an integrating factor to

$$\frac{d}{dx}\left((1+x\psi)^{A1/\psi}P(x)\right) = -A2\psi(1+x\psi)^{(A1/\psi-2)}\frac{d}{dx}\left(\frac{1+x\psi}{\psi}(x\psi-\beta)\right) \tag{4.59}$$

and hence solved to find P in terms of the excess height of the block and ψ. In order to do so, we need to fix the constant this introduces. This is obtained by remembering

[7]We shall look only at the case of constant coefficients, as to do otherwise would make the resulting equations increasingly difficult to solve

that the block loses contact at $x = x_0$, and at this point $P = 0$. The position of x_0 must be determined by the requirement that we apply no force on the block at the exit of the system, and hence can say that $T(x_0) = 0$, and hence from (4.58)

$$x_0 = \text{Max}\left(\frac{\beta}{\psi}, 1\right) \tag{4.60}$$

We also know that the pressure supports the applied moment, and so

$$\int_0^{x_0} Px dx = M \tag{4.61}$$

where M is the nondimensionalised moment. This is now sufficient information to determine both $P(x)$ and ψ for a given $\beta(x)$. In turn, if we equate

$$-T = \text{Force required to form primary crimp}$$

then we can close the model and describe the evolution of the stuffer box.

4.4.1.2 Steady State Solution

We shall begin by looking for a steady state solution where β, μ and λ are constant. Under these circumstances (4.59) simplifies to

$$\frac{d}{dx}\left((1 + x\psi)^{A1/\psi} P(x)\right) = A2\psi(1 + x\psi)^{(A1/\psi - 2)}(1 + 2x\psi - \beta)$$

This can be integrated to give $P(x)$ and then inserted into (4.61) to give an equation relating ψ, $A1$, $A2$ and M. Unfortunately, this cannot be inverted, so we shall need to use root finding techniques to find ψ.

4.4.1.3 Relationship between micro-structure and elastic properties

We shall now consider how the elastic properties of the block depend on the micro-structure. Consider two simple experiments carried out on a cube of the block material. In the first, we simply apply a uniform pressure to the top surface, letting the sides expand as required. In the second, we apply a similar uniform pressure, but prevent the block expanding by adding walls. The equations for a linear, isotropic elastic medium are easy to solve in each case. For the block with free sides,

$$\frac{\text{Stress}}{\text{Strain}} = \frac{4\mu(\lambda + \mu)}{\lambda + 2\mu}$$

whilst when the sides are fixed

$$\frac{\text{Stress}}{\text{Strain}} = \lambda + 2\mu$$

Comparing these with the graphs of stress vs. strain for the loop of elastica under the same conditions (figures 4.6 and 4.9) gives, in dimensional variables

$$\frac{4\mu(\lambda+\mu)}{\lambda+2\mu} = \frac{EI}{L_p^3} C_{Free}$$

and

$$\lambda + 2\mu = \frac{EI}{L_p^3} C_{Confined}$$

where (reading the slopes off the graph)

$$C_{Free} \sim 285 \qquad \text{and} \qquad C_{Confined} \sim 1250$$

and L_p is the primary crimp length. We can then solve for λ and μ to get

$$\begin{aligned} \lambda &= \frac{EI}{L_p^3}\sqrt{C_{Confined}^2 - C_{Confined}C_{Free}} \\ &\sim 1100\frac{EI}{L_p^3} \\ \mu &= \frac{1}{2}\left(\frac{1250EI}{L_p^3} - \lambda\right) \\ &\sim 75\frac{EI}{L_p^3} \end{aligned}$$

We are more interested in the quantities $A1$ and $A2$, which become in dimensional variables

$$\begin{aligned} A1 = &\quad \tfrac{\xi\lambda}{\lambda+2\mu} &&\sim 0.9\xi \\ A2 = &\quad \tfrac{4\mu(\lambda+\mu)}{\lambda+2\mu} &&\sim \frac{EI}{L_p^3} C_{Free} \end{aligned}$$

This will influence our choice of scalings for λ, M, P and f, as we wish $A2$ to be an $O(1)$ quantity, and therefore must choose a scale for Λ appropriately. The exact scaling will depend on the relationship we choose between T and the primary crimp length. We shall once again compare two choices. The first uses the results of the chapters on primary (2) and secondary (3) crimp. The second will be the new model we introduced to improved model allowing for variation in the nip region (section 4.3.7.2).

- **Basic models for Primary and Secondary crimps**

  Recall that, for the primary crimp model as discussed in chapter 2[8]

$$L_p = 4\pi\sqrt{\frac{EIW}{TW}}$$

  giving

$$A2 = \frac{1}{64\pi^3\sqrt{EI}}C_{Free}T^{3/2}$$

  in dimensional terms. We now realise that

$$A2 = \Lambda\bar{A}2 \qquad \text{and} \qquad T = \Lambda\epsilon L\bar{T}$$

  and hence

$$\bar{A}2 = \frac{1}{64\pi^3\sqrt{EI}}C_{Free}\epsilon^{3/2}L^{3/2}\Lambda^{1/2}\bar{T}^{3/2}$$

  We now choose Λ such that

$$\bar{A}2 = \bar{T}^{3/2}$$

  and so

$$\Lambda = \frac{4096\pi^6 EI}{L^3\epsilon^3 C_{Free}^2}$$

  From the work on secondary crimp formation (chapter 3, (3.62)) we had that

$$\epsilon L(1+\beta) = \frac{\pi}{2}\sqrt{\frac{EIW}{\Upsilon WT}}$$

  and so

$$(1+\beta) = \frac{\pi}{2}\sqrt{\frac{EI}{\Upsilon\epsilon^3 L^3\Lambda\bar{T}}}$$

  Hence

$$\beta = \frac{C_{Free}}{128\pi^2}\frac{1}{\sqrt{\Upsilon\bar{T}}} - 1$$

  We can now use these relationships, coupled with the equations for ψ (4.59-4.61) to solve the problem and seek equilibrium values of ψ and β. Unfortunately, we find that there is no solution satisfying the constants of this problem.

- **New model for Primary and Secondary crimp**

  We shall now attempt to find solutions by using the second model for primary and secondary crimp we derived for the springs model. The analysis needed is

[8]This equation comes from combining equations (2.91) and (2.92), and noting that in the notation of this chapter (where we discuss a problem in terms of a sheet of unit width), $F_x \Rightarrow TW$, and $EI \Rightarrow EIW$.

the same as that performed in section 4.3.7.2, but with k replaced by $A2$, in keeping with the model for the material in the block. This gives us

$$\epsilon L(1+\beta) = \frac{1}{2}\left(\frac{\pi^2 H_0^2}{C_{Free}L_{nip}^2}+1\right)\left(L_{nip}-\pi\sqrt{\frac{EI}{T}}\right) \tag{4.62}$$

$$A2 = \frac{C_{Free}L_{nip}^3}{\epsilon^3\pi^3 L^3}\sqrt{EI}T^{3/2} \tag{4.63}$$

This allows us to suitably nondimensionalise our equations to

$$\bar{A}2 = \bar{T}^{3/2}$$

which requires

$$\Lambda = \frac{\pi^6 EI\gamma^6}{C_{Free}^2 L^3\epsilon^3}$$

and

$$\beta = \frac{1}{2}\left(\frac{\pi^2\gamma^2}{C_{Free}}+1\right)\left(\frac{1}{\gamma}-\frac{C_{Free}}{\gamma^3\pi^2}\frac{1}{\sqrt{T}}\right)$$

where γ is again defined by

$$L_{nip} = \frac{\epsilon L}{\gamma}$$

For suitable values of the constants (see page 152), this gives an equilibrium angle of

$$\psi \sim -0.42\epsilon$$

Although this is negative, it might be a possible value. Unfortunately, this corresponds to an equilibrium height of

$$h \sim 0.67H_0$$

which is < 1 and hence outside the range of validity for the model (which only makes physical sense if the pressure on the plate is positive everywhere. Seeing the effect of changing parameters, we qualitatively observe that γ (the aspect ratio of the nip) plays an important role whereas M does not. This suggests that the geometry of the stuffer box has a very important role to play.

4.4.2 Stability of the stuffer box

The set of equations that govern the stuffer box ((4.58), (4.59), (4.60) and (4.61)) are very difficult to work with. Indeed, when we attempt to do an expansion for a small peturbation, the number of terms rapidly increases, and it becomes increasingly



Figure 4.21: An alternative design of stuffer box

difficult to make progress, even when taking advantage of computer algebra packages. This is primarily due to the terms of the form

$$(1 + x\psi)^{A1/\psi}$$

that appear. In an attempt to overcome this problem, let us begin by considering the case when the top plate is nearly horizontal, i.e.

$$\psi = O(\epsilon^2).$$

This has two effects. Firstly, we will find it difficult to balance the applied moment, and so we must either consider

- The case when the system is designed to run with the plate nearly horizontal. This prescribes what M should be. Note that for a nearly flat plate, contact is made throughout the length (i.e. from $x_0 = 1$.)
- The alternative design of stuffer box, where the top plate is horizontal and a hinged flap at $x = 1$ provides extra resistance to the motion and control. (see figure 4.21))[9]

We shall now consider the stability of these two special cases of the stuffer box.

4.4.2.1 Stability of the stuffer box with a nearly horizontal upper plate

When the upper plate is nearly horizontal, we can write that

$$\begin{aligned} P &= P_0(x) + \varepsilon P_1(x) \\ \psi &= 0 + \varepsilon\psi_1 \\ \beta &= \beta_0 + \varepsilon\beta(x) \\ T &= T_0(x) + \varepsilon T_1(x) \end{aligned}$$

[9]The effect of adding the hinged flap can be modelled by writing

$$T(1) = T_{control}$$

(instead of $T(1) = 0$) where $T_{control}$ represents the effect of the flap applied at $x = 1$.

where ε is the size of the disturbance, and insert into our equations for the stuffer box ((4.58)-(4.61)). Expanding to $O(1)$ gives

$$\begin{aligned} T_0 &= -\frac{\lambda+2\mu}{\lambda}P_0 + \frac{4\mu(\lambda+\mu)}{\lambda}\beta_0 \\ 0 &= \frac{\lambda\xi}{\lambda+2\mu}P_0 + \frac{dP_0}{dx} \\ M &= \int_0^1 xP_0(x)dx \end{aligned}$$

with the boundary condition

$$T_0(1) = 0$$

Solving these gives

$$P_0 = A2\beta_0 e^{A1(1-x)}$$

where $A1$ and $A2$ are as defined on page 160. This can then be used to calculate the required value of M. If the functional relationship between the excess material in the stuffer box (β) and the force needed to move the block $-T(0)$ can be written as

$$T(0) = f(\beta)$$

then we can close the model and write

$$f(\beta_0) = \frac{A2\xi}{A1}\left(e^{A1} - 1\right)\beta_0$$

which can then be solved to find β_0. The stability will require us to consider how the material moves through the stuffer box, and so applying the ideas in section 4.2 we have

$$\beta_1(x) = \hat{\beta}_1(\chi - x)$$

and so, expanding to $O(\varepsilon)$ we have

$$\begin{aligned} T_1(x,\chi) &= -\frac{\xi}{A1}(x\psi_1 P_0(x) + P_1(x,\chi)) - \frac{A2\xi}{A1}(x\psi_1(\chi) - \beta_1(\chi - x)) \\ A1P_1(x,\chi) + \frac{dP_1}{dx} &= A2\psi_1(1-\beta_0) - x\psi_1\frac{dP_0}{dx} - A2\frac{d\beta_1}{dx} \\ 0 &= \int_0^1 xP_1(x,\chi)dx \end{aligned} \tag{4.64}$$

with the boundary condition

$$T_0(1,\chi) = 0$$

We shall now seek a solution where

$$\beta_1 = e^{z(\chi - x)}$$

for an unknown z. Solving for P_1 we find

$$\begin{aligned} P_1(x,\chi) &= \frac{A2}{2}\left(2e^{z(\chi-1)} + 2(e^{z(\chi-x)} - e^{z(\chi-1)})\, z \right. \\ &\qquad \left. -\psi_1(2 + 2\beta_0 + A1\beta_0 - A1\beta_0 x^2 e^{A1(1-x)})\right) \end{aligned}$$

The value of ψ can be deduced from this by balancing the moments (4.64). With this knowledge, we can now apply our closing condition, by writing that

$$T_1(\chi, 0) = \left.\frac{df}{d\beta}\right|_{\beta_0} \beta_1(\chi)$$

We now proceed to seek values of z which satisfy this condition. Once again, this analysis gives a transcendental equation for z, and so in the same manner as before we shall use a numerical technique to track the roots as control parameters are changed. Looking at the form of the equation that forms, we see that by writing

$$\alpha = \frac{A1}{A2\xi}\left.\frac{df}{d\beta}\right|_{\beta_0}$$

then there are three main parameters we can vary:

α	which measures the sensitivity of the coupling between the block and the secondary crimp region,
β_0	the equilibrium excess height of the block,
and $A1$	which measures the friction between the block and the stuffer box.

Figures 4.22 and 4.23 show the contours of stability for eight values of $A1$ and a range of β_0 and α. Note that for large $A1$ the system becomes unstable for large β_0. We shall discuss the importance of this later.

4.4.2.2 Stability of the Alternative Stuffer box design

The equations for this case are much simpler, as we have the condition that $\psi = 0$. Equation (4.59) becomes

$$\frac{dP}{dx} + A1P = A2\frac{d\beta}{dx} \tag{4.65}$$

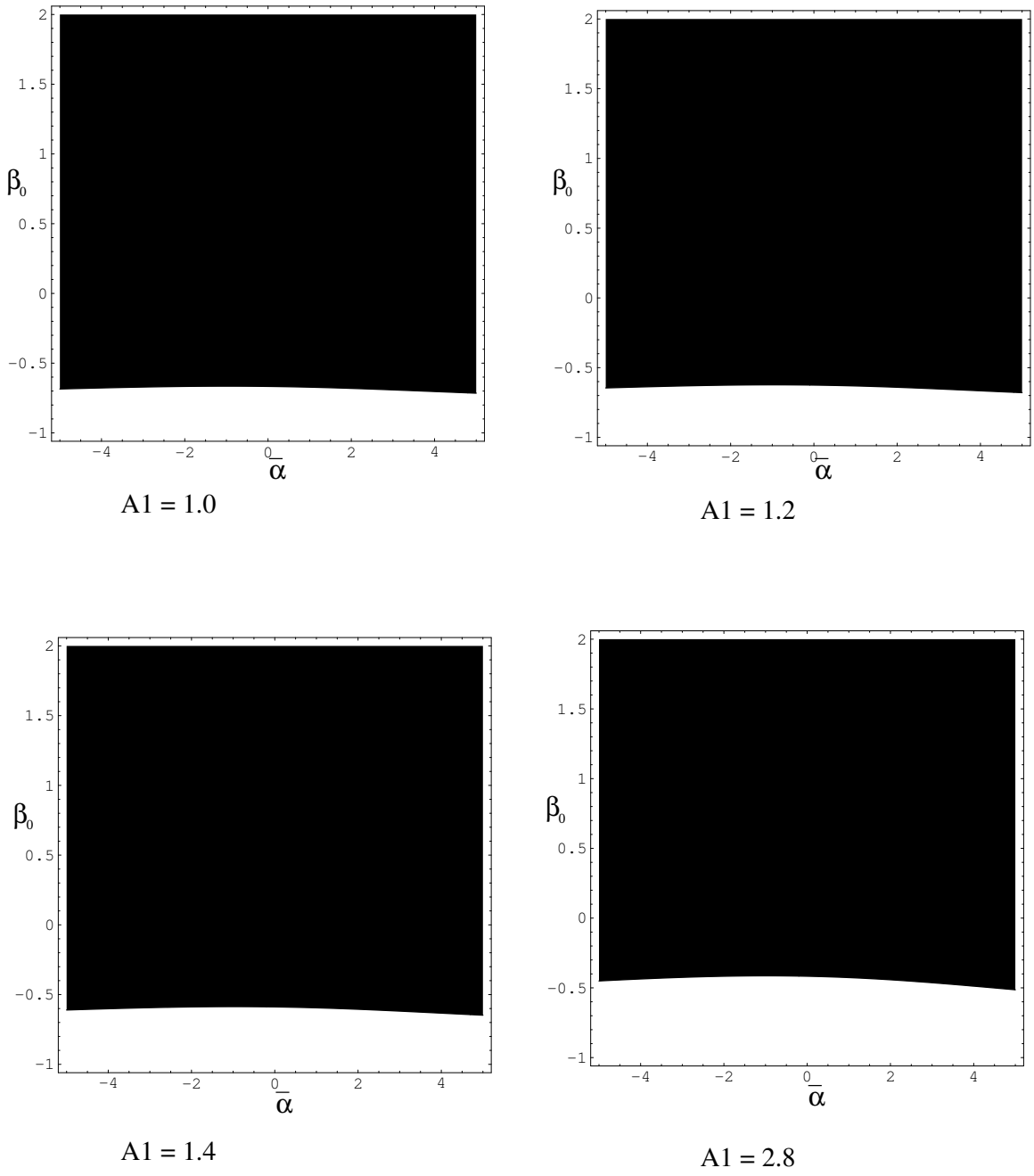
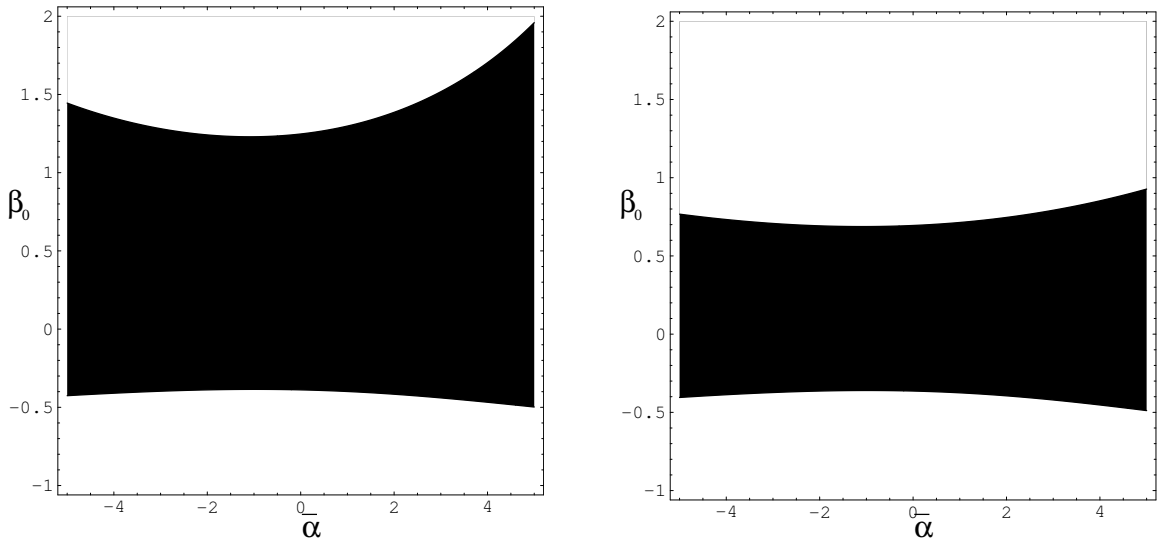


Figure 4.22: Stability contours for the stuffer box crimper with isotropic elastic block and nearly flat top plate



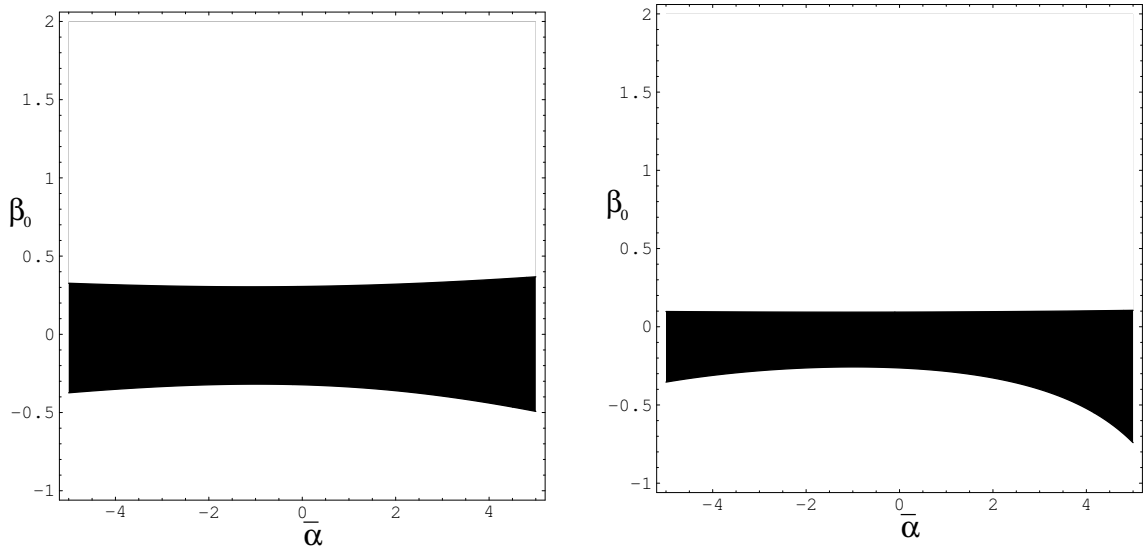


Figure 4.23: Stability contours for the stuffer box crimper with isotropic elastic block and nearly flat top plate

with boundary conditions at $x = 0$ and $x = 1$ of

$$T_{control} = \frac{A2\xi}{A1}\beta(1) - \frac{\xi}{A1}P(1) \tag{4.66}$$

$$F(\beta(0)) = \frac{A2\xi}{A1}\beta(0) - \frac{\xi}{A1}P(0) \tag{4.67}$$

The first two of which can be readily solved to give

$$P(x) = A2\beta(x) + A2A1e^{-A1x}\int_x^1 \beta(x')e^{A1x'}dx' - \frac{A1T_{control}}{\xi}e^{A1(1-x)}$$

and hence

$$F(\beta(0)) = e^{A1}T_{control} - \xi A2\int_0^1 \beta(x)e^{A1x}dx \tag{4.68}$$

Now we shall seek a solution where material moves through the stuffer box and hence

$$\beta(x) = \beta(\chi - x)$$

and look for a solution of the form

$$\beta = \beta_0 + \varepsilon\beta_1(\chi - x) + \cdots \qquad \text{and} \qquad F = F(\beta_0) + \varepsilon\left.\frac{dF}{d\beta}\right|_{\beta_0}\beta_1 + \cdots$$

Inserting into (4.68) we find

$$F(\beta_0) = e^{A1}T_{control} - \frac{\xi A2}{A1}\beta_0\left(e^{A1} - 1\right)$$

$$\left.\frac{dF}{d\beta}\right|_{\beta_0}\beta_1(\chi) = -A2\xi\int_0^1 \beta_1(\chi - x)e^{A1x}dx.$$

Seeking a solution where

$$\beta_1(\chi - x) = e^{z(\chi - x)}$$

we find that z must satisfy

$$\gamma = -\frac{1}{A1 - z}\left(e^{A1-z} - 1\right) \tag{4.69}$$

where

$$\gamma = \frac{1}{A2\xi}\left.\frac{dF}{d\beta}\right|_{\beta_0}.$$

We shall return to discuss the relative stability of this equation shortly, after we have first discussed the behaviour of the original springs model when contained within the "alternative" design of stufferbox.

4.4.3 Springs model revisited

Recall the springs model for the block. If we have the springs material filling the alternative stuffer box, with a control force $F_{control}$ applied at the right hand end then the (dimensional) force required to move it would be given by

$$F_{control} + \int_0^1 \frac{\beta(\chi - x)}{1 + \beta(\chi - x)} dx$$

Expanding as

$$F = F_0(\beta_0) + \varepsilon \left.\frac{dF}{d\beta}\right|_{\beta_0} \beta_1(\chi) \qquad \text{and} \qquad \beta = \beta_0 + \varepsilon\beta_1(\chi)$$

and seeking a solution of the form

$$\beta_1 = e^{z(\chi - x)}$$

requires that

$$F_0(\beta_0) = F_{control} + \beta_0$$

and

$$\left.\frac{dF}{d\beta}\right|_{\beta_0} = \frac{\beta_0}{(1+\beta_0)^2}\frac{1}{z}\left(e^{-z} - 1\right).$$

Let us compare this with the equation obtained for the stability with an isotropic elastic material (4.69). Direct comparisons of the stability of the two models is difficult as the β_0 will be different in each case, however if we realise that by choosing our scalings such that

$$A2 = 1 \qquad \text{and} \qquad k = 1$$

we can show that the equations determining stability can be written as

$$\gamma = \frac{1}{z - A1}\left(e^{A1 - z} - 1\right) \qquad \text{and} \qquad \frac{1 + \beta_0}{2\beta_0}\gamma = \frac{1}{z}\left(e^{-z} - 1\right) \tag{4.70}$$

Stability corresponds to the real parts of the roots of z being negative. Making the transformation

$$z = Z + A1$$

we can reduce both problems (4.70) to finding the roots of the equation

$$Z' e^{Z'} = a \tag{4.71}$$

where $Z' = Z - \gamma'^{-1}$ and $a^{-1} = \gamma' e^{1/\gamma'}$ for appropriate γ' (as defined previously). If $Z'_{min,a}$ is the root of (4.71) with the largest real part then the blocks are stable if

- Springs model:

$$\Re(Z'_{min,a}) < -\frac{2\beta_0}{1+\beta_0}\frac{1}{\gamma}$$

or

- Isotropic Elastic model:

$$\Re(Z'_{min,a}) < -\frac{1}{\gamma} - A1$$

For the same a, the latter of these is the more restrictive (assuming that $A1 > 0$, see footnote), and hence we have predicted that the springs model will be more stable. In addition, we can observe that small a favours stability, and hence (if $\beta_0 < 1$) we again see that the springs model is more stable. Note that this will not necessarily be the case for large heights ($\beta_0 > 1$) and materials where $A1 < 0$.[10] Finally, we should note that stability is improved for both models by having $a < 0$, i.e. increasing force giving decreasing height of material. In contrast, observe from figures 4.15 and 4.16 that in the stability analysis of the springs model with hinged top, the stability diagrams are very nearly symmetric around the line $B_1 = 0$. As B_1 is proportional to α, this result is in contrast to the predictions of the alternative stuffer box design. We could attribute this to the presence of the hinged lid stabilising the system (indeed, the lid will lift if the amount of material becomes too large, reducing the force). When we look at the stability diagrams for the small angle isotropic elastic model (figures 4.22 and 4.23), we see a slight asymmetry along the line $\alpha = 0$, as one may expect from the

[10] What sort of materials have $A1 < 0$? Remember that

$$A1 = \frac{\lambda}{\lambda + 2\mu}\xi$$

and it would be unphysical to have $\xi < 0$ (i.e. a negative coefficient of friction). Therefor $A1 < 0$ needs

$$\frac{\lambda}{\lambda + 2\mu} < 0$$

Remembering the definition of the poisson's ratio (σ) of

$$\sigma = \frac{1}{2}\frac{3K - 2\mu}{3K + \mu}$$

where

$$K = \lambda - \frac{2}{3}\mu > 0$$

we see that

$$A1 = \frac{3K + \mu}{3K + 4\mu}\sigma\xi$$

and hence $A1 < 0$ requires that the poisson's ratio of the block be negative.

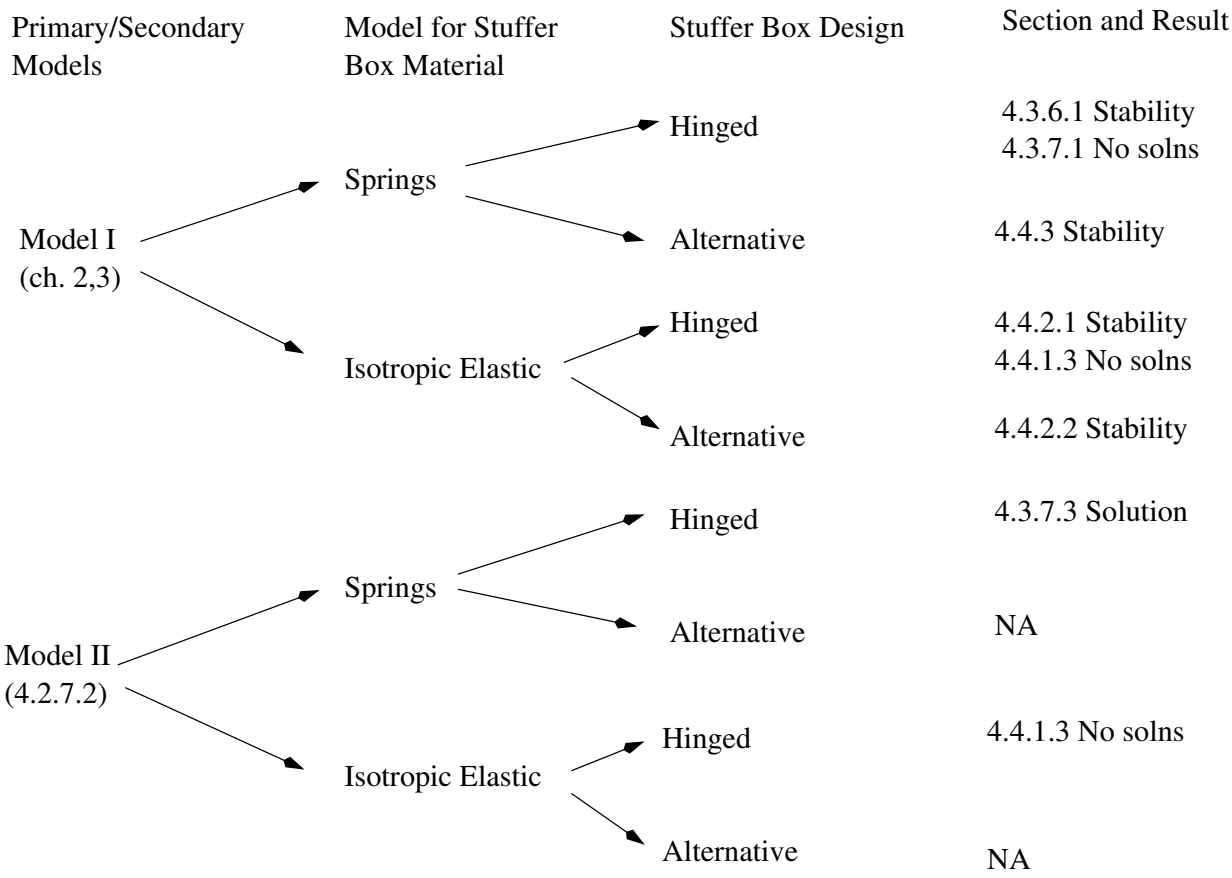


Figure 4.24: The different models considered in this chapter

action of a stabalising hinged lid. Note that all these observations must be qualitative only, as there are no direct correlations between the parameters plotted in each figure.

4.5 Summary

In this chapter we have looked at

- 2 models for the material the block is made from,
- 2 models for the coupling between primary/secondary crimp regions and the properties of the block, and
- 2 models for the design of stuffer box.

The results are summarised below in figure 4.24

Chapter 5

Conclusions

In this thesis, we have shown the rich seam of interesting mathematics that underlies the crimping process. As we progressed along our journey through the stuffer box crimper, we needed to look at the process on different scales. At each stage, we have needed to derive new models to describe the process, and new mathematics to seek solutions. When we looked at the crimper as a whole, we were forced to think about the intermediate processes, and the boundaries between the models on the different scales. Indeed, when we sought solutions for the systems as a whole, we found that these transition processes governed the whole system. We presented a number of different models at each stage, and followed them through to show how the predictions of each case compared with experimental results.

5.1 Primary Crimp

We began our stroll where the fibre enters the crimper, in the nip region between the rollers. In chapter 2 we model this as an increasing length of elastica being forced into a narrow channel of fixed dimensions. To make progress in what was a potentially complicated problem, we began by considering a quasi-static elastica confined to two dimensions. In addition, in order to see more of the details of the solutions, we took advantage of the narrowness of the channel to linearise the equations of the system.

Even though the equations were linear, the problem was still nonlinear, as the confining channel could give rise to numerous contact points. Thankfully, in the regions between the contact points the equations for the elastica were simple to solve. This enabled us to divide the elastica into a series of sections, and from symmetries of the confining box, classify these sections based on the type of contact at each end. The boundary conditions at the ends of the box, and knowledge of the physics of

the contact, allowed us to write down both global conditions on these sections, and continuity conditions which must be satisfied at the joins. This gave us sufficient information to solve the problem.

Previous attempts at solving the problem in two dimensions had required assumptions to be made about the overall shape of the elastica. The technique we had used overcame this, and by combining all possible section types, we could find all possible fibre configurations for a given number of contact points. This gave rise to rich bifurcation diagrams. To determine what would be observed experimentally, we needed to use energy arguments, supposing that the observed solution minimises the energy stored in the system. This enabled us to describe the evolution of shape, contact and confining force as more fibre was added in.

This progression was found to depend on the boundary conditions imposed at the ends, especially the amount of freedom at the entrance to the stuffer box. If fibre was added at the base, then extra contact points formed through the growth of a "dimple"[1]. This dimple grew out of a flat section of fibre. If the fibre entered half way up the wall, then these flat sections never formed, and extra contact points involved a change in the direction of curvature of the fibre.

The shape of the channel was also found to influence the behaviour of the fibre, as expected. For a fibre entering a rectangular channel, the formation of another contact point involved an increase in force followed by a sudden decrease as either the dimple began to form, or the direction of the fibre changed. This was observed not to be the case for a fibre entering a wedge, where the force was observed to only increase.

5.1.1 Crimp in three dimensions

The work on an elastica confined in two dimensions is certainly applicable to the paper crimper, however when the stuffer box is part of the fibre manufacturing process, three dimensional effects are an observed feature. Indeed, for some industrial uses (such as use in filters), the increased tortuosity of the filaments is a welcome feature. In the second section of chapter 2 we discussed the equations of an elastica in three

[1] A section of fibre that goes between two contact points on the same wall

dimensions, and linearised for the case of small deflections.

When the deformations were small, we saw that the deflections in each of the two principal directions uncoupled. Under these circumstances, we considered an elastica confined to a channel, with the principle directions held at a fixed alignment. We then applied a thrust to the ends of the fibre, and allowed it to buckle. As expected, the fibre buckled first in one of its principal directions. However once the fibre touched a confining surface, we observed more interesting behaviour. If the principal direction was normal to the surface, then the fibre behaved like the two dimensional case, up to a critical value of the applied thrust. At this point, it became possible for the fibre to "escape" from the plane it had deformed in, by buckling along the second principal direction. Energy arguments showed that this configuration was favoured.

When the principal direction of the elastica was not normal to the confining surface, more complicated behaviour was observed. The boundary conditions that the fibre be tangential to the surfaces coupled together the deformations in each of the principal directions, meaning that it was no longer possible to satisfy the boundary conditions with a planar solution. Instead, the fibre immediately took on a three dimensional shape. Unfortunately, with only one contact point, the fibre never exhibited the helical structure observed in the tow.

5.2 Secondary Crimp

Continuing our saunter through the stuffer box crimper, we arrived at the secondary crimp region, where the primary crimped fibre buckled again, before entering the region between the plates. In chapter 3 we considered two models that captured the highly oscillatory nature of the tow. The first, the *hinged rods model* supposed that the crimped fibre was comprised of a series of rigid rods, joined by elastic hinges where all deformation occurred. In contrast, the second model thought of it as an elastica whose natural configuration was oscillatory or crimped, and where deformation could occur throughout.

5.2.1 The hinged rods model

Once again we considered the static case and we derived a difference equation describing the relationship between the angles θ_n of the different rods. This had two features that made solution difficult. Firstly, it was nonlinear, and secondly, it had a large driving term that oscillated rapidly. This meant that the usual techniques of linearisation could not work.

To overcome these problems, we started by looking for solutions when the applied force, κ, was asymptotically small. This proved successful, except when the total number of rods N was such that

$$N \cdot \kappa = O(1),$$

at which point our expansion broke down. We noted that the series in κ had two types of terms, those proportional to $(-1)^n$ (where n is the number of the rod) and those which were not. We decided to make use of this fact when we looked for a solution that was uniformly valid for all n.

We started by seeking a solution of the form

$$\theta_n = \Sigma_n - (-1)^n \Delta_n$$

where Σ and Δ would vary smoothly. This enabled us to rewrite the difference equation as a pair of coupled difference equations, which we then proceeded to solve by approximating them by smooth functions of ϵn (where $\epsilon = N^{-1}$). Under these assumptions, we were able to change the difference equations into an ordinary differential equation. This analysis predicted that there were critical values of force for which there was a bifurcation from a flat solution to an arched one, and that these values satisfied different equations depending on whether N was odd or even. When we proceeded to solve the equations numerically, this difference between odd and even was observed.

The final work on the hinged rods model attempted to fit experimental force extension curves. This proved difficult with the model as presented, and in order to improve the fit, we allowed the individual rods to extend slightly. This gave much better agreement to the experimental curves, and allowed us to determine the parameters for the hinged rods model. Another application for this was to model

the tow under tension, which is of importance when handling the tow (see "Open Problems" below).

5.2.2 Curved fibre model

The second model had the crimped fibre described as an elastica with a highly oscillatory natural shape. We considered the behaviour of this under an applied thrust along its length. The equation was solved approximately by carrying out a multiple scales analysis, the result of which was that the elastica behaved as an Euler strut of lower stiffness than the original fibre.

When we compared this model to the differential equation formulation of the hinged rods problem we noticed a similarity. In each case, the effect of the oscillatory nature of the tow led to it behaving as a less stiff version of the straight elastica (of the same macroscopic length). The ratio of the stiffness of the oscillatory fibre to that of the straight was the same as the ratio of the macroscopic length of the fibre to its arc length[2].

5.3 The Block

Our journey through the stuffer box crimper now brought us to the largest scale of the machine, the plates. In this region, the shape of the fibre was observed to vary little (although some compression did occur) and hence we referred to the material as the block. Our modelling of the block had two main avenues. Firstly, we needed a description of the material contained within. Secondly, we had to relate the properties of the material currently entering the block to that currently found within. These together would allow us to describe the evolution of the stuffer box crimper as more fibre was fed in.

We considered two models for the material contained in the block - a springs model where the compression of the tow caused only a vertical force, and an isotropic elastic model, where the compression resulted in a horizontal force. Certain aspects of the modelling was the same for each:

[2]The length measured including all the oscillations

- *Motion of material through the stuffer box*
  The material was assumed to move uniformly through the stuffer box so that the current state of the block depended on the past history.

- *Friction between plates and block*
  Frictional forces acted between the plates and the block, such that the block was in limiting friction all along its length. This assumption was justified as we were interested only in the peak force exerted.

- *Boundary conditions*
  We applied boundary conditions that required no force exerted on the block at the exit from the stuffer box, and that the torque exerted by the compression of the block must balance the externally applied moment.

- *Contact*
  The upper plate was assumed to not be attached to the block, and thus unable to stretch the material, only compress it. This meant that there was a free boundary in the problem where contact was lost.

As well as a model for the material contained within the block, we needed to relate the properties of the material entering to the block's current state, in particular to the current force needed to move the block. In both the springs and isotropic elastic models, we had two attributes to consider, the elastic constants of the material and its unstressed height.

To determine values for the elastic constants, we began by proposing a grossly simplified micro-structure for the material, with it being composed of either loops of elastica, or folded elasticas. Having written down the necessary equations and nondimensionalised, we then considered the deformation each shape would exhibit under simple applied forces. These could then be compared with the response of the block material to the same stresses, and hence elastic constants deduced. Our principal result come from the dimensional analysis, that predicted that the elastic properties would be proportional to Λ^{-3}, where Λ was the primary crimp length. Our original intention was to use the results of chapter 2 to give a value for Λ in terms of the force required to move the block. Later it became necessary to use a different primary crimp length (see next section).

The natural place to start when modelling how the height of the material entering the block was influenced by the force need to move the block was with the discussion of secondary crimp from chapter 3. For both of the models, this predicted that for an applied force F, the length that would buckle was proportional to $F^{-1/2}$. Unfortunately, we could not find any steady state solutions. We proposed that this could be because the model did not include any effects from the geometry of the nip region. To overcome this limitation, we introduced a new model for primary and secondary crimp.

Closing the models of the block (both as springs and isotropic elastic material) using models derived by considering primary and secondary crimp separately proved inadequate. Instead, we began to consider the two processes in the nip region as linked. Our starting point was to imagine that the nip consisted of two parts, a section of fibre that would buckle to form primary crimp, and a section of crimped tow that would eventually fold to form secondary crimp. The same forces acted on each. The block was assumed to advance when the force required to buckle the fibre into primary crimp was greater than that required to move the block. At this point, we assumed that the block would move, and the crimped fibre fold to form secondary crimp.

This model had the advantage over the previous in that it predicted that as the force increased, the size of the secondary crimp would increase, as was qualitatively observed in the experimental paper crimper. When we used this model to close the springs and elastic material models, we found that we could find solutions (which were physically realistic for the springs model, but not for the other).

5.3.1 Stability of the stuffer box

As well as predicting the equilibrium states of the stuffer box, we were also interested in the stability of those states. We investigated this by considering a small perturbation of the state, and seeing if it grew or shrank as fibre went through. We found that the springs model was almost always stable, except under conditions which were unlikely to occur in reality. The stability of the isotropic elastic block model was more difficult to determine, and so we concentrated on a more limited class of solution, those where the equilibrium angle of the plate was zero. This could occur for one of two reasons. Firstly, because of the operating conditions, and secondly due to the

design of stuffer box.

If the plate was free to move (i.e. the plate was horizontal due to the running conditions), then the stuffer box could become unstable if the coefficient of friction was large enough, and the equilibrium height of the material large. This was in contrast to the springs model which was almost always stable.

A second design of stuffer box, which exerted a fixed force at the exit, was easier to analyse for stability. We compared the springs and isotropic elastic material models, and noted that the latter was always more unstable, except when the Poisson's Ratio for the material was negative. We attributed this instability to the added coupling between the stresses over the springs model. As an interesting aside, we also noted that the springs model could become unstable in this case, unlike the prediction from the model when the hinged lid was present. We postulated that the hinged lid adds to the stability.

This thesis cannot claim to have solved the problem of the stuffer box crimper, although it has extended the areas of research to examine both the individual sections of the process and the system as a whole. The discussion in chapter 5 shows that the coupling between the systems requires much more work before any definite predictions can be made, but shows that there are some promising avenues to explore. Of the models for the individual processes, those for the secondary crimp region are least satisfactory, for it is unclear whether they would apply in the case when more fibre is being added, nor when the tow was constrained by the top surfaces.

5.4 Open Problems

There are a number of problems that can be considered "open", either because they require a considerable extension to the work, or they have not been considered at all. Some have direct application to the crimping problem, others have arisen as part of the work.

- **Tow under tension**
  During the use of crimped fibres, it is necessary to transport the tow. This is often results in crimped fibres hanging between rollers. One example when this occurs is when fibre is removed from a box by being pulled over a roller above (see figure 5.1). This problem is similar to that of the periodic folding of thin

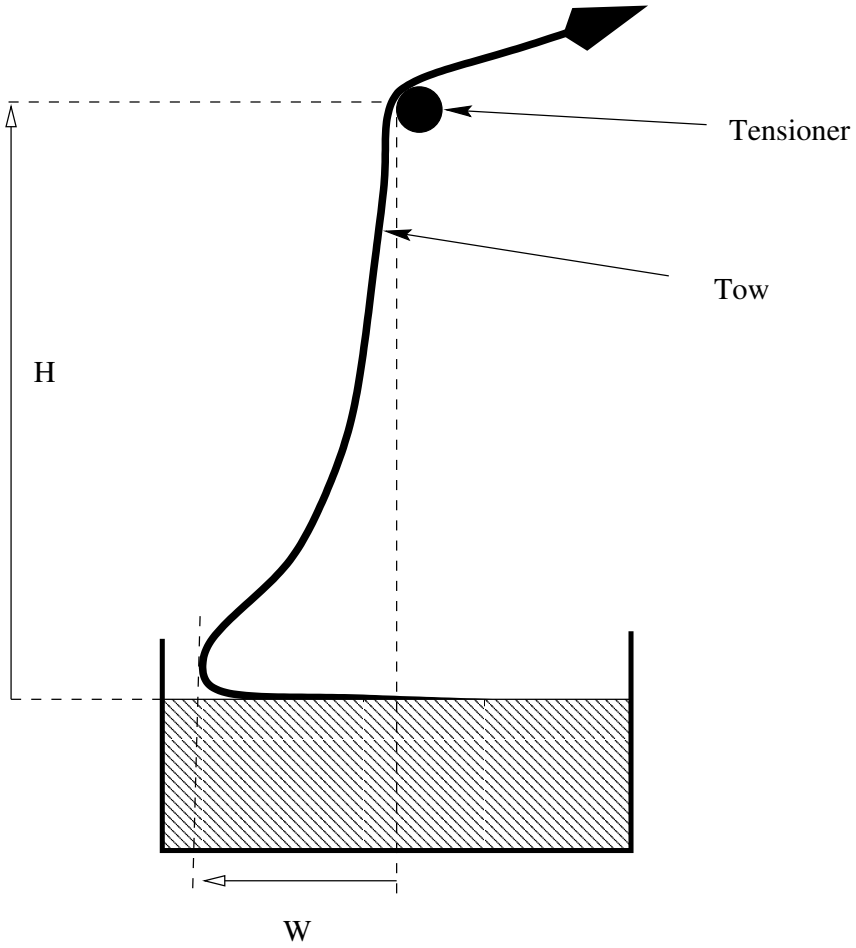


Figure 5.1: Tow being removed from a box

sheets [11], but has the added complication that the fibre might stretch under its own weight.

- **Buckling of the block**
  While carrying out experimental runs with the paper crimper, it was observed that, under heavy loading, the block could buckle. This could prove an interesting free boundary problem to study. The block is in compression only where it touches the plate (and must support the applied load). When the buckle occurs, some of the block moves whilst other regions don't (a second free boundary). The contact will be over a region, and hence it may not be appropriate to use the elastica equations.

- **Primary crimp in a nip**
  All the work done on primary crimp assumed thin aspect ratios so the deformations were small. This is not the case in reality, as the crimp occurs in the

nip, and often results in the fibre going vertical.

- **Plastic deformation of fibres in the stuffer box**
  The fibres in the stuffer box have all been modelled as elasticas. This is not the case in reality, as there must be some permanent deformation in order for the crimp to take. How to include this into our model could prove an interesting topic for discussion.

- **Multiple fibre effects**
  All the work has concentrated on modelling the tow as a sheet, and therefore has not considered the interaction between the fibres. This could be an important step in understanding effects such as the three dimensional crimp observed in practice.

- **Dynamic effects**
  We have assumed throughout that inertia could be ignored. In reality, the fibre enters rapidly, and the boundary of the nip is moving. Both of these effects may be important.

References

[1] *Reports on the 22nd European Study Group with Industry*, 1989.

[2] *26th European Study Group with Industry*, 1993.

[3] G. G. Adams and R. C. Benson. Postbuckling of an elastic plate in a rigid channel. *International Journal of Mechanical Science*, 28(3):153–162, 1986.

[4] Warrick Cooke. Buckling in the crimping process, 1997. (Transfer thesis).

[5] C. M. Elliot and J. R. Ockendon. *Weak and Variational Methods for Moving Boundary Problems*. Number 59 in Pitman Advanced Publishing Program. Pitman, 1982.

[6] Avner Friedman. *Mathematics in Industrial Problems Part 4*, volume 38 of *IMA Volumes in Mathematics and its Application*, chapter 1. Springer-Verlag, 1988-1997.

[7] Robert Frisch-Fay. *Flexible Bars*. Butterworths, 1962.

[8] P. Holmes G. Domokos and B. Royce. Constrained euler buckling. *Journal of Nonlinear Science*, 7:281–314, 1997.

[9] D. H. Hodges and P. R. Bless. Analysis of beam contact problems via optimal control theory. *AIAA Journal*, 33(3):551–556, 1995.

[10] A. E. H. Love. *A Treatise on the Mathematical Theory of Elasticity*. Dover Publications, 4 edition, 1944.

[11] L. Mahadevan and J. B. Keller. Periodic folding of thin sheets. *SIAM Journal of Applied Mathematics*, 55(6):1609–1624, 1995.

[12] L. Mahadevan and Joseph B. Keller. Coiling of flexible ropes. *Proc. R. Soc. Lond. (A)*, 452:1679–1694, 1996.

[13] T.C. Soong and Injae Choi. An elastica that involves continuous and multiple discrete contacts with a boundary. *Int. J. Mech. Sci.*, 28:1–10, 1986.

[14] D. A. Spence. The hertz contact problem with finite friction. *Journal of Elasticity*, 5(3-4):297–319, 1975.

[15] D. P. Vailette and G. G. Adams. An elastic beam contained in a frictionless channel. *Journal of Applied Mechanics*, 50(3):693–694, 1983.

[16] D. R. Westbrook. Contact problems for elastic beams. *Computers and Structures*, 15(4):473–479, 1982.

[17] D. R. Westbrook. The obstacle problem for beams and plates. *Journal of Computational and Applied Mathematics*, 30(3):295–311, 1990.